TU Delft

Delft University of Technology

Document Version
Final published version

Citation (APA)
Anand, S. (2026). *Analytical and semi-analytical models for crashworthiness in preliminary design.* [Dissertation (TU Delft), Delft University of Technology]. https://doi.org/10.4233/uuid:17165193-522b-4d62-a163-d668a5479872

Important note
To cite this publication, please use the final published version (if applicable).
Please check the document version above.

Copyright
In case the licence states “Dutch Copyright Act (Article 25fa)”, this publication was made available Green Open Access via the TU Delft Institutional Repository pursuant to Dutch Copyright Act (Article 25fa, the Taverne amendment). This provision does not affect copyright ownership.
Unless copyright is transferred by contract or statute, it remains with the copyright holder.

Sharing and reuse
Other than for strictly personal use, it is not permitted to download, forward or distribute the text or part of it, without the consent of the author(s) and/or copyright holder(s), unless the work is under an open content license such as Creative Commons.

Takedown policy
Please contact us and provide details if you believe this document breaches copyrights.
We will remove access to the work immediately and investigate your claim.

This work is downloaded from Delft University of Technology.

Analytical and semi-analytical models for crashworthiness in preliminary design

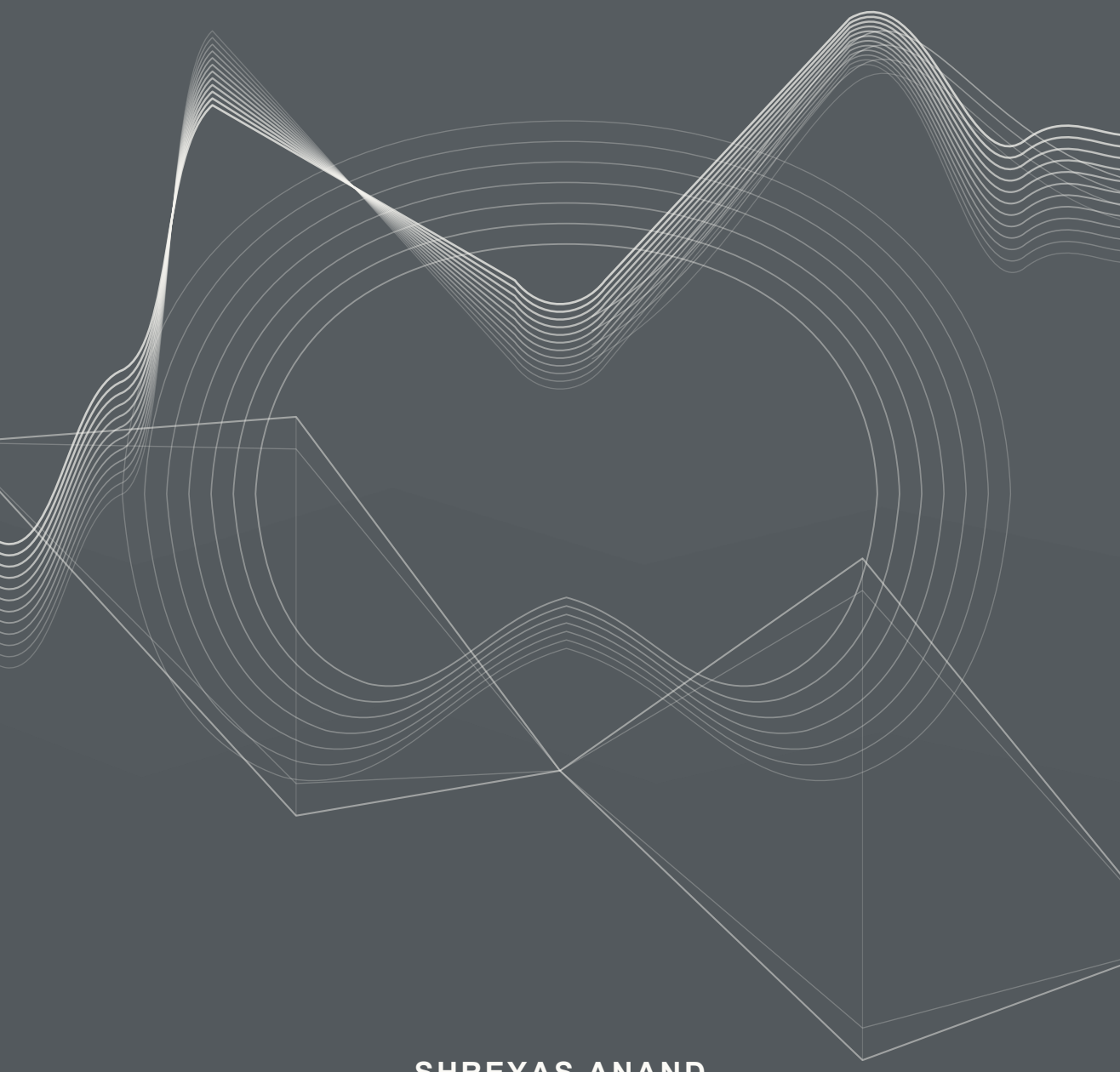

SHREYAS ANAND

Analytical and semi-analytical models for crashworthiness in preliminary design

Analytical and semi-analytical models for crashworthiness in preliminary design

Dissertation

for the purpose of obtaining the degree of doctor
at Delft University of Technology
by the authority of the Rector Magnificus, Prof. dr. ir. H. Bijl,
chair of the Board for Doctorates
to be defended publicly on
Wednesday, 9 September 2026 at 12:30

by

Shreyas ANAND

This dissertation has been approved by the promotors.

Composition of the doctoral committee:

Rector Magnificus,	chairperson
Prof. dr. ir. R. C. Alderliesten	Delft University of Technology , *Promotor*
Dr. ir. S. Giovani Pereira Castro	Delft University of Technology, *Promotor*
Independent members:	
Prof. dr. ir. R. Benedictus	Delft University of Technology
Prof. dr. J. Ambrósio	Instituto Superior Técnico, Universidade de Lisboa, Portugal
Prof. dr. S. Rivallant	Institut Supérieur de l'Aéronautique et de l'Espace, France
Prof. dr. S. Tabacu	National University of Science and Technology POLITEHNICA Bucharest, Romania
Prof. C.A. Dransfeld,	Delft University of Technology, reserve member



Keywords: Crashworthiness, Mean crushing force, Glare laminates, Bending, Metallic tubes, Preliminary design, 3-point bending, Analytical models, Square and rectangular tubes, Circular tubes, Spring-linkage model

Version: Electronic version

Cover by: Shreyas Anand

Copyright © 2026 by S. Anand

ISBN 978-94-6518-412-8

An electronic copy of this dissertation is available at
https://repository.tudelft.nl/.

Contents

Summary **xv**

Samenvatting **xvii**

1. Introduction **1**
1.1. Motivation for Computationally Efficient Crash Models 2
1.2. Existing Approaches and research gap 3

2. Axial crushing of metallic tubular structures **7**
2.1. Introduction 8
2.2. Analytical model parameters 12
2.3. Analytical models for mean crushing force (P_{mean}) 13
2.4. Sensitivity of analytical models to geometrical and material parameters 20
2.5. Strain rate effects 22
2.6. Experimental and numerical datasets 23
2.6.1. Experimental dataset from literature 23
2.6.2. Numerical dataset 23
2.6.3. Validation of numerical model 25
2.7. Results 26
2.7.1. Extensional crushing of circular tubular structures 27
2.7.2. Inextensional crushing of square tubular structures 27
2.7.3. Inextensional crushing of hexagonal tubular structures 33
2.7.4. Inextensional crushing of octagonal tubular structures 33
2.7.5. Extensional crushing of hexagonal and octagonal tubular structures 33
2.8. Modification to the model from Abramowicz et al. [26] 39
2.9. Tabacu et al.'s model [29] for circular structures 41
2.10. Calibration of Zhang and Zhang's model [42] with our dataset 43
2.11. Generalized mean crushing force expression for axial crushing of metallic tubular structures 47
2.12. Discussion 51
2.13. Conclusions 53

3. Bending collapse of square and rectangular structures **57**
3.1. Introduction 58
3.2. Analytical models for bending collapse of square and rectangular tubular structures 61
3.2.1. Analytical model from Kecman 61

3.2.2. Wierzbicki model 63
3.2.3. Kim and Reid 63
3.3. Materials and Methods 67
3.3.1. Material data 67
3.3.2. Numerical dataset for bending simulations: Square and rectangular tubes 67
3.4. Elastic and Elasto-plastic deformation stage (Stage-I and II) 70
3.4.1. Calculation of M versus rotation curve for an element of length dx 70
3.4.2. Use of spring linkage method to predict elastic and elasto-plastic deformation stage 71
3.5. Collapse stage (Stage-III) 75
3.5.1. Flow stress 75
3.5.2. Estimation of maximum moment 75
3.5.3. Model from Kecman for collapse beyond 20 degrees 90
3.5.4. Transition between spring-linkage model and Kecman model 90
3.6. Results and discussions 93
3.6.1. Comparison with existing analytical models 93
3.6.2. Comparison between dataset and semi-analytical model for square tubular structures 96
3.6.3. Comparison between dataset and semi-analytical model for rectangular tubular structures 103
3.6.4. Peak force and absorbed energy 103
3.6.5. Comparison between dataset and experimental results from literature 103
3.7. Conclusions 109

4. Three-point bending of GLARE laminates 111
4.1. Introduction 112
4.2. Materials and Methods 114
4.2.1. Material data 114
4.2.2. Experimental setup 116
4.2.3. Semi-analytical model 118
4.3. Results 122
4.3.1. Experimental results 122
4.3.2. Repeatability of experimental results 123
4.3.3. Results from semi-analytical model for central cracking 125
4.4. Discussion 125
4.4.1. Failure mechanisms 128
4.4.2. Effect of stacking sequence 130
4.4.3. Effect of displacement rate 138
4.4.4. Effect of aluminum rolling direction 138
4.4.5. Results from semi-analytical model 141
4.4.6. Sensitivity of force-displacement curve to span 147
4.5. Conclusions 147

5. Discussion **151**
5.1. Axial crushing of metallic tubular structures 151
5.2. Plastic bending for metallic tubular structures 153
5.3. Bending of GLARE laminates 155

6. Conclusion **157**

7. Recommendations **159**
7.1. Axial crushing of open sections 159
7.2. Post-peak response for stockier tubes with $t/b > 0.1$ 159
7.3. Bending for varied cross sections 162
7.4. Oblique impact 162
7.5. Inclusion of shear for GLARE bending 163
7.6. Extension of GLARE bending model to other composite materials . . 164
7.7. Analytical models for axial crushing of composite structures 164
7.8. Extension towards full-aircraft crashworthiness assessment 164

A. Appendix: Chapter 2 **169**
A.1. Experimental dataset from literature 169
A.1.1. Hexagonal tubular structures 169
A.1.2. Octagonal tubular structures 169
A.1.3. Square tubular structures 170
A.1.4. Circular tubular structures 171
A.2. Material data 172
A.3. Numerical dataset 173
A.3.1. Square and circular tubular structures 173
A.3.2. Hexagonal and octagonal tubular structures (Inextensional) . 174
A.3.3. Hexagonal and octagonal tubular structures (Extensional) . . 175

B. Appendix: Chapter 3 **177**
B.0.1. Derivation for the baseline moment-rotation curve 177
B.0.2. Comparison between numerical data and semi-analytical model for square cross-sections 181

C. Appendix: Chapter 4 **189**
C.1. Configurations tested at displacement rate = 1 mm/min 190
C.2. Configurations tested at displacement rate = 10 mm/min 191
C.3. Configurations tested at displacement rate = 100 mm/min 192
C.4. Configurations tested at displacement rate = 1000 mm/min 193
C.5. Specific Energy Absorption (SEA), Peak force (kN) and Bending modulus (GPa) for experimental 3-point bending 194
C.6. Comparison of results from semi-analytical model to experimental results 197

Bibliography **207**

List of Publications **219**

Acknowledgements **221**

Curriculum Vitæ **223**

List of Figures

1.1. IATA strategy for net zero emissions by 2050 [7] 2
1.2. Comparison between Airbus A350 (left) [9] and Flying-V fuselage cross section (right) [8] 3

2.1. Nomenclature reference schematics adapted from [29] and [25] . . . 9
2.2. Comparison between Airbus A350 (left) [9] and Flying-V fuselage cross section (right) [8] 10
2.3. Ideal force versus displacement curve for a tubular structure 11
2.4. Basic collapse elements for (a) Inextensional crushing mechanism and (b) Extensional crushing mechanism 14
2.5. Fitting a curve to the dataset obtained using the analytical model from Abramowicz et al. [26]) 17
2.6. Geometrical parameters for the model from Tabacu et al. [29] 19
2.7. Sensitivity of analytical models for predicting mean crushing force to radius/ edge length and thickness for (a) circular tubular structures and (b) polygonal tubular structures 21
2.8. Numerical model for a hexagonal tubular structure 26
2.9. Correlation between experimental dataset and results from numerical model 27
2.10. Comparison between analytical models and dataset for circular tubular structures: (a) Alexander [22], (b) Abramowicz et al. [24], (c) Wierzbicki et al. [38], (d) Singace et al. [39] and (e) Tabacu et al. [29] 30
2.11. Comparison between analytical models and dataset for square tubular structures: (a) Magee and Thornton [23], (b) Abramowicz et al. [25] and (c) Tabacu et al. [29] 32
2.12. Comparison between analytical models and dataset for hexagonal tubular structures: (a) Abramowicz et al. [26], (b) Zhang and Zhang [42] and (c) Tabacu et al. [29] 35
2.13. Comparison between analytical models and dataset for octagonal tubular structures: (a) Abramowicz et al. [26], (b) Zhang and Zhang [42], (c) Tabacu et al. [29]. 37
2.14. Comparison between analytical model from Tabacu et al. [29] and extensional mean crushing force dataset for (a) Hexagonal tubular structures and (b) Octagonal tubular structures 38
2.15. Superfolding element proposed by Abramowicz et al. [26] (Phase-I) . 40
2.16. (a) Comparison of model from Abramowicz et al. [26] (Modified) for hexagonal tubular structures; (b) Comparison of model from Abramowicz et al. [26] (Modified) for octagonal tubular structures 42

2.17. Comparison of the modified Tabacu's model [29] for circular tubular structures. 44
2.18. Comparison of the Zhang and Zhang's model [42] for square tubular structures. 45
2.19. Curve fit for our dataset using Eq. 2.60. 46
2.20. Comparison of numerical (FEM results from Zhang and Zhang [42]) and analytical mean crushing force obtained using Zhang and Zhang's model calibrated with (a) Our dataset (b) Magee and Thornton's dataset 48
2.21. Comparison of model from Zhang and Zhang [42] (calibrated with our dataset, Eq. 2.63) for (a) hexagonal tubular structures and (b) octagonal tubular structures 49
2.22. Comparison between generalized expression for mean crushing force and mean crushing force dataset 51

3.1. General moment-rotation (θ) curve showing three stages of bending, adapted from [76] 60
3.2. Comparison of moment-rotation curves from literature [30] and our implementation of the model 62
3.3. Wierzbicki attempt-1: Comparison of moment-rotation curves from Wierzbicki et al. [31] and our implementation of the model 64
3.4. Wierzbicki attempt-2: Comparison of moment-rotation curves from Wierzbicki et al. [31] and our implementation of the model 65
3.5. Comparison of moment-rotation curves from Kim and Reid [32] and our implementation of the model 66
3.6. Comparison between experimental force-displacement curves from literature [76, 85] and the numerical model 68
3.7. 3-point bending setup schematic, adapted from [76] 70
3.8. Composite method to get moment-rotation curve for a cross-section . 72
3.9. Spring-linkage method used to calculate the force-displacement response for the elastic and elasto-plastic deformation stages. 76
3.10. Comparison of force-displacement curve from numerical simulation and spring-linkage model 78
3.11. Comparison of numerical force-displacement curve and maximum moment (Case-1) 80
3.12. Comparison of numerical force-displacement curve and maximum moment (Case-2) 82
3.13. Comparison of numerical force-displacement curve and maximum moment (Case-2: Peak force obtained from semi-analytical model) . 85
3.14. Comparison of numerical force-displacement curve and maximum moment (Case-3) 87
3.15. Comparison of numerical force-displacement curve and maximum moment (Case-3: Peak force obtained from semi-analytical model) . 89
3.16. Comparison of force-displacement curve from numerical simulation and spring-linkage model 92

3.17. Comparison of force-displacement curve from numerical simulation and spring-linkage model 94
3.18. Examples for transition case-1 and case-2 95
3.19. Comparison of numerical force-displacement curve and force-displacement curve from analytical models 99
3.20. Comparison of numerical force-displacement curve and force-displacement curve from proposed semi-analytical model for square tubular structures 102
3.21. Comparison of numerical force-displacement curve and force-displacement curve from proposed semi-analytical model for rectangular tubular structures 105
3.22. Comparison between peak force and absorbed energy between semi-analytical model and numerical results 106
3.23. Comparison of experimental force-displacement curve from literature and force-displacement curve from proposed semi-analytical model . 108

4.1. Comparison between Airbus A350 (left) [9] and Flying-V fuselage cross section (right) [8] 113
4.2. Schematic diagrams for glass fiber and aluminum layers 116
4.3. True stress-strain curve for AL2024-T3 in laminated(L) and transverse(LT) directions, plotted using digitized data from [102] 116
4.4. 3-Point Bending Test Setup 118
4.5. Infographic: Semi-analytical prediction of bending strength of GLARE laminates 119
4.6. Example force versus displacement curve with vertical drops after transverse failure of layers indicated with dotted lines 121
4.7. Experimental force versus displacement for GLARE laminates subjected to 3-point bending 124
4.8. Minimum, mean and maximum area between curves versus configuration for normalized experimental dataset 126
4.9. Comparison of experimental force-versus-displacement curves with predictions from semi-analytical model 127
4.10. Failure modes observed GLARE laminates subjected to 3 point bending 129
4.11. Typical force versus displacement curves for central-cracking failure mechanisms 131
4.12. Typical force versus displacement curves for shear dominated failure mechanisms 132
4.13. Effect of stacking sequence on failure mode and specific energy absorption (SEA) 137
4.14. Comparison of experimental force-versus-displacement envelopes for specimens with change in displacement rate 139
4.15. Effect of displacement rate on failure modes 140
4.16. Comparison of experimental force-versus-displacement envelopes for specimens with change in aluminum rolling direction 142
4.17. Comparison of experimental force-versus-displacement curves with predictions from semi-analytical model 145

4.18. Comparison of analytical and experimental values for peak force and total energy absorbed, only central cracking cases are considered. Dotted lines represent ideal correlation, experimental=analytical. . . . 146
4.19. Sensitivity of force versus displacement curves to span 149

5.1. Comparison between analytical and numerical peak crushing force . 152

7.1. Deformed c-shaped sections submitted to axial crushing, different fold widths can be clearly observed indicating varying fold wavelength . . 160
7.2. Force-displacement plots for c-shaped section 161
7.3. Deformed cross-section for a tube with t/b<0.1 and a tube with t/b>0.1 at loading pin displacement of 20mm 163
7.4. Crushing front development in composite tube under axial loading. Reprinted from *Stacking sequence optimization of composite tubes submitted to crushing using the discrete ply model (DPM)*, S. Anand, J.-E. Chambe, C. Bouvet, and S. Rivallant, *Composite Structures*, © 2022 Informa UK Limited, trading as Taylor & Francis Group. Reprinted by permission of Informa UK Limited, trading as Taylor & Francis Group, `http://www.tandfonline.com`. [113] 165

B.1. Tri-linear approximation of the stress-strain curve 177
B.2. Comparison of numerical and semi-analytical force–displacement responses. 187

C.1. Specific Energy Absorption (SEA), Peak force (kN) and Bending modulus (GPa) for GLARE-2 194
C.2. Specific Energy Absorption (SEA), Peak force (kN) and Bending modulus (GPa) for GLARE-3 195
C.3. Specific Energy Absorption (SEA), Peak force (kN) and Bending modulus (GPa) for GLARE-4 196
C.4. Force versus displacement curves: Experiment versus semi-analytical model 205

List of Tables

2.1. Values of X, Y and Z for specific cases (Eq. 2.70) 50
2.2. Coefficient of determination (R^2), Average error ($\overline{E}$) and Interquartile range for various analytical models 54

3.1. Configurations used for numerical test campaign (dimensions are in mm) 69

4.1. Configurations of the tested GLARE specimens 115
4.2. Material properties for S2-glass fiber/ FM94-epoxy resin 116
4.3. Failure modes observed for GLARE-2 specimens. 130
4.4. Failure modes observed for GLARE-3 specimens. 133
4.5. Failure modes observed for GLARE-4 specimens. 134
4.6. Effect of span variation on maximum force and total energy absorbed. Values in parentheses represent percentage change relative to the 0% span. 147

7.1. Experimental results for mean crushing force of C-shaped sections . 162

C.1. Configurations tested at a displacement rate of 1 mm/min. 190
C.2. Configurations tested at a displacement rate of 10 mm/min. 191
C.3. Configurations tested at a displacement rate of 100 mm/min. 192
C.4. Configurations tested at a displacement rate of 1000 mm/min. 193

Summary

The aviation sector is responsible for approximately 2.5% of global CO_2 emissions. While the CO_2 emissions reduced at a compound annual growth rate (CAGR) of 2.8% between 2000 and 2019, the passenger demand is projected to more than double by 2044 as compared to 2024 at a CAGR of about 4.2%, outpacing the reduction in emissions. Unconventional aircraft (for example blended wing body aircraft) are projected to reduce emissions by more than 20% as compared to widebody aircraft of comparable mission and size, making them instrumental for reducing aviation emissions. However, these novel configurations also introduce new crashworthiness challenges that must be addressed early in the design process to prevent cost overruns and delays at later stages of the design process.

Historically, preliminary crashworthiness analysis has relied on linkage-kinematic joint representation of the aircraft, with characteristic curves for the kinematic joints derived using experimental or numerical campaigns. Even the most recent multi-body and FEM-kinematic joint hybrid models still depend on characteristic curves derived through simulations or experiments. Consequently, while these models are fast and ideal for preliminary crashworthiness analysis, design exploration is limited by the amount of component level test/simulation data, highlighting a clear research gap for analytical/semi-analytical models that can inform such multi-body models on the go with material and geometry data as inputs.

This thesis addresses that gap by focusing on the two dominant energy absorption mechanisms in metallic fuselage structures: axial crushing and plastic bending. For axial crushing of closed-section metallic tubular structures, existing models are evaluated and a generalized expression for various cross-section shapes is proposed. For bending collapse, a semi-analytical framework combining spring-linkage based elasto-plastic stage prediction, transition algorithm, and Kecman model for collapse stage prediction is proposed to obtain complete force–displacement curves. Although aircraft structures commonly use open sections, the scope of the present work is limited to closed sections in order to establish a robust and consistent methodological foundation within the available time frame.

Finally, the bending framework is extended to hybrid materials, specifically GLARE (Glass Laminate Aluminium Reinforced Epoxy). A maximum strain-based damage model based on the spring-linkage method is proposed, the approach predicts stiffness degradation and progressive central cracking failure for GLARE laminates. The results demonstrate that analytical and semi-analytical models can be further extended to hybrid systems, enabling fast, early-stage crashworthiness evaluation of unconventional aircraft designs utilizing hybrid materials.

Samenvatting

De luchtvaartsector is verantwoordelijk voor ongeveer 2,5% van de wereldwijde CO_2-uitstoot. Hoewel de CO_2-emissies tussen 2000 en 2019 daalden met een samengesteld jaarlijks groeipercentage (CAGR) van 2,8%, wordt verwacht dat de vraag naar passagiersvervoer tegen 2044 meer dan zal verdubbelen ten opzichte van 2024 met een CAGR van ongeveer 4,2%, waarmee de groei de reductie in emissies overstijgt. Onconventionele vliegtuigen (bijvoorbeeld *blended wing body* vliegtuigen) zullen naar verwachting de uitstoot met meer dan 20% verminderen in vergelijking met *widebody* vliegtuigen met een vergelijkbare missie en omvang, waardoor zij een belangrijke bijdrage kunnen leveren aan het terugdringen van de luchtvaartemissies. Deze innovatieve configuraties introduceren echter ook nieuwe uitdagingen op het gebied van crashbestendigheid (*crashworthiness*) die vroeg in het ontwerpproces moeten worden geadresseerd om kostenoverschrijdingen en vertragingen in latere stadia van het ontwerpproces te voorkomen.

Historisch gezien vertrouwde de vroege crashbestendigheidsanalyse op de weergave van het vliegtuig middels mechanische koppelingen en kinematische verbindingen, waarbij de karakteristieke curven voor deze verbindingen werden afgeleid uit experimentele of numerieke campagnes. Zelfs de meest recente hybride modellen, waarin *multi-body*-systemen worden gecombineerd met op FEM gebaseerde kinematische verbindingen, zijn nog steeds afhankelijk van karakteristieke curven verkregen via simulaties of experimenten. Bijgevolg is de verkenning van ontwerpen beperkt door de hoeveelheid beschikbare test- of simulatiedata op componentniveau. Hoewel deze modellen snel en ideaal zijn voor vroege crashbestendigheidsanalyses, duidt dit op een duidelijke kennislacune voor analytische of semi-analytische modellen die dergelijke *multi-body*-modellen direct kunnen voeden op basis van materiaal- en geometriegegevens.

Dit proefschrift richt zich op dit hiaat door te focussen op de twee dominante energie-absorptiemechanismen in metalen rompstructuren: axiaal bezwijken door verbrijzeling en plastische buiging. Voor het axiale bezwijken van metalen kokerstructuren met gesloten secties worden bestaande modellen geëvalueerd en wordt een gegeneraliseerde uitdrukking voor verschillende dwarsdoorsnedevormen voorgesteld. Voor bezwijken door buiging wordt een semi-analytisch raamwerk voorgesteld dat een op veren en schakelelementen gebaseerde voorspelling van de elastoplastische fase, een transitie-algoritme en het Kecman-model voor de voorspelling van de bezwijkfase combineert om volledige kracht–verplaatsingscurven te verkrijgen. Hoewel vliegtuigstructuren doorgaans gebruikmaken van open secties, is de reikwijdte van dit werk beperkt tot gesloten secties om binnen het beschikbare tijdsbestek een robuuste en consistente methodologische basis te vestigen.

Ten slotte wordt het buigingsraamwerk uitgebreid naar hybride materialen, specifiek GLARE (*Glass Laminate Aluminium Reinforced Epoxy*). Een op maximale rek gebaseerd schademodel, gebruikmakend van de veer-schakelmethode, wordt voorgesteld. Deze aanpak voorspelt stijfheidsdegradatie en progressief bezwijken door centrale scheurvorming in GLARE-laminaten. De resultaten tonen aan dat analytische en semi-analytische modellen verder kunnen worden uitgebreid naar hybride systemen, wat een snelle evaluatie van de crashbestendigheid van onconventionele vliegtuigontwerpen met hybride materialen in een vroeg stadium mogelijk maakt.

1 Introduction

By 2050, CO_2 emissions have been estimated to double if no efforts are made. Unconventional aircraft, for example blended wing body (BWB) aircraft, are projected to cut emissions by more than 20% as compared to similarly sized widebody tube and wing configurations. However, these configurations pose unique challenges in terms of crashworthiness including the ovalized cross-section due to combination of the wing-fuselage structure which leads to a significant decrease in available stroke length between the passenger floor and the ground. To avoid drastic cost overruns and evaluate the feasibility of a design from crashworthiness perspective, it is necessary to have fast running crashworthiness prediction models which can be used to evaluate the design space. In this thesis, an effort has been made to collect, compare, improve and also propose new analytical and semi-analytical models for prediction of energy absorption by components in early stages of the design process.

To address this challenge, this thesis is structured around three principal scientific contributions, focusing on the two primary energy-absorbing mechanisms in the crashworthiness of metallic fuselage structures: axial crushing and plastic bending followed by bending collapse. Chapter 2 deals with axial crushing of metallic tubular structures, a generalized equation for closed section metallic tubular structures has been proposed. Chapter 3 deals with plastic bending of metallic tubular structures and a semi-analytical approach using a combination of the spring-linkage model, transition algorithm and Kecman model for bending collapse [1] has been proposed to predict Moment-rotation and force-displacement curves for bending of square and rectangular tubular structures. Finally, in chapter 4, the spring-linkage model has been further adapted and used to predict the force-displacement curve for GLAss fiber REinforced laminates (GLARE), employing a maximum strain based damage model to further predict degradation for GLARE laminates that fail with central cracking.

1

1.1. Motivation for Computationally Efficient Crash Models

The aviation sector contributes roughly about 2.5% of all global emissions [2]. Per Boeing commercial market outlook, 2025 [3], Revenue Passenger Kilometers (RPKs) are expected to grow at a compound annual growth rate (CAGR) of 4.2% in the following decades, nearly doubling the current value by 2044. On the other hand, for conventional tube and wing configurations, the gains in emission reduction happened at a modest rate of 2.8% per annum between the year 2000 and 2019 (RPKs (2000) = 3381 billion [4], RPKs (2019)=8913.4 billion [5], CO_2 emissions (2000) = 672.96 Mt [6] and CO_2 emissions (2019) = 1035.83 Mt [6]). Given the difference between rising passenger demand and the rate of reduction in emissions, the IATA net zero goal by 2050 seems distant. If the goal has to be met, more disruptive changes are required both in terms of operations and design. IATA net zero strategy [7] attributes a 13% reduction in emissions by 2050 (Figure 1.1) to new designs and hydrogen/electric propulsion.

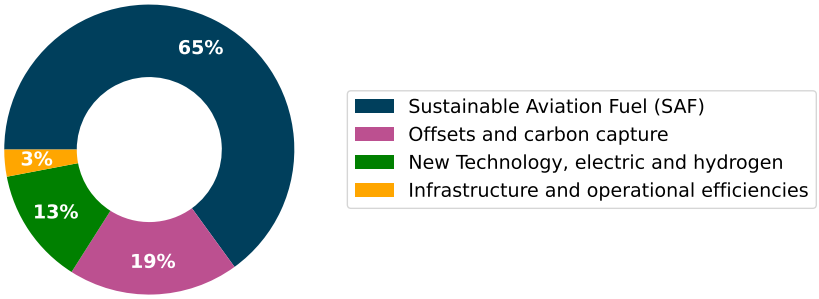

Figure 1.1.: IATA strategy for net zero emissions by 2050 [7]

Unconventional configurations like Blended-Wing-Body can play a significant role in this regard, with Oosterom and Vos [8] predicting a potential reduction of upto 22% in emissions as compared to comparable widebody tube-and-wing aircraft. However, these designs also pose new challenges in terms of crashworthiness, one of them being the ovalized cross-section of the fuselage which leads to a much shorter stroke length for subfloor energy absorbing structures (Figure 1.2). For such unconventional designs, to avoid rework at later stages and therefore cost overruns, it is important to study design feasibility with respect to crashworthiness in early stages of the design process. The next section, therefore, focuses on methods that are fast running and can be used in early stages of the design process to predict crash response of an early-stage aircraft design.

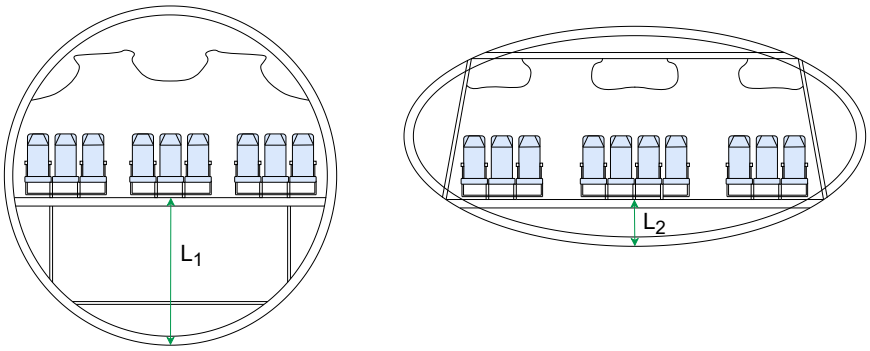

Figure 1.2.: Comparison between Airbus A350 (left) [9] and Flying-V fuselage cross section (right) [8]

1.2. Existing Approaches and research gap

The most widely used model for crashworthiness in preliminary design was KRASH, which was originally developed in the early 1970s. This model utilized a set of beams with pinned or clamped boundary conditions along with non-linear behavior modeled using springs, non-linear beams or plastic hinges. The non-linear behavior was introduced via experimental tests or numerical analyses [10]. The model was used widely starting from 1970s to 2000s [10–16] and was used by many organizations including Airbus, Bell-Helicopters, Fokker, Eurocopter, NASA-LANGLEY and others [16]. The author was however unable to find any recent literature using KRASH. In 1992, Burrows [14] notes that a lot of component level testing has to be conducted by designers to get good crush initiators, energy attenuation and rectangular force-displacement curves. Burrows [14], therefore suggests development of a database for all the crash tests and increased use of analytical models to permit component formulations in less time and cost.

An early plastic-hinge approach for vehicle crash simulation was presented by Nikravesh et al. [17], in which a structure was divided into components connected using joint-spring combinations. Bending deformation was represented using revolute joints and torsional springs, with the required moment-rotation characteristics obtained from experimental data. The plastic-hinge approach was subsequently extended within a multibody dynamics framework by Ambrósio and Nikravesh [18]. Sousa et al. [19] proposed a model for automobiles using a variety of kinematic joints based on different loading conditions: one-axis bending, two-axis bending, torsion and crushing. The constitutive models for the kinematic joints were obtained from finite element models. In their hybrid multi-body approach for crashworthiness analysis of a fuselage section, Tay et al. [20] used a spring-linkage approach to model frame sections, with bending stiffness characteristics obtained using component level numerical simulations. Close agreement was observed between deceleration versus time curves obtained using multi-body model and numerical analysis for various locations along the fuselage. The multibody model

from Tay et al. [20] was implemented in the MADYMO environment.

A similar hybrid methodology was proposed by Schatrow et al. [21] for composite fuselage sections. the fuselage section was modeled utilizing a set of macro elements informed with force-displacement and moment-rotation curves obtained using experimental tests or numerical simulations.

Across the spring-linkage and multi-body models discussed above, a common limitation is the reliance on numerical simulations or experimental testing to obtain the characteristic force–displacement curves.

Consequently, the present thesis investigates the development of fast-running analytical and semi-analytical models capable of generating force–displacement relationships for use in kinematic joint formulations.

While aircraft frame structures usually employ open-section metallic members, this thesis focuses on closed-section metallic tubular structures as a starting point. The idea of the thesis was to first address axial crushing and bending collapse of tubular structures, as their symmetry leads to a more predictable response, and then to extend the work to investigate crushing and bending collapse of open-section metallic structures. However, during the course of the project, it was realized that even axial crushing and collapse of closed-section structures require more detailed investigation and therefore due to timing constraints only closed sections are addressed in the current work. The gaps identified for axial crushing and bending collapse of closed section metallic structures are listed below:

1. Numerous models [22–29] have been proposed for the axial crushing of metallic tubular structures, each claiming reasonably accurate predictions based on their corresponding experimental or numerical datasets. Since the end goal is to use such models to obtain force–displacement curves during the early stages of the design process, it is important to evaluate the existing models across a wide range of materials and geometries.

2. The proposed bending-collapse models [1, 30–32] do not account for the elastic and elasto-plastic stages of deformation. Most existing models were developed with a focus on steel specimens. However, since the present application is aimed at aircraft structures, which predominantly use aluminium alloys, the models should be capable of predicting moment–rotation curves for cases in which the material exhibits pronounced plastic deformation. In addition, similar to the case of axial crushing, it is important to assess the accuracy of the various models against multi-material and multi-geometry datasets.

Furthermore, the bending framework was extended to GLARE laminates to investigate the applicability of analytical and semi-analytical models to hybrid material systems. This investigation provides an initial basis for extending such modelling approaches to more complex geometries and additional classes of composite materials.

Therefore, to address these gaps, the following **research questions** are formulated and addressed in this work:

1. What computationally inexpensive methods suitable for early-stage design can be developed to predict force–displacement curves for the axial crushing of metallic structures?
2. What computationally inexpensive methods suitable for early-stage design can be developed to predict force–displacement curves for the bending collapse of metallic structures?
3. How can analytical and semi-analytical models be extended to hybrid structures?

Chapters 2, 3, and 4 address the research questions outlined above. Although the three chapters consider different loading mechanisms and material systems, they are linked by the common objective of developing computationally efficient methods for crashworthiness assessment during the early stages of structural design. Detailed finite element models can represent complex deformation and failure mechanisms, but their computational cost limits their use when a large number of structural configurations need to be assessed. Analytical models are considerably faster, but are generally developed for specific geometries, materials, or deformation mechanisms. The work presented in this thesis therefore investigates how such models can be assessed, modified, generalized, or combined with low-order modelling methods to extend their applicability while retaining a low computational cost.

Chapter 2 focuses on the axial crushing of metallic tubular structures. Analytical models available in literature are first reviewed and assessed for circular, square, hexagonal, and octagonal cross-sections using experimental data supplemented by a validated numerical dataset. Their sensitivity to geometrical and material parameters is studied in order to identify their range of applicability and the reasons for deviations between different formulations and the dataset. Based on the observed trends, modifications to selected models are investigated and a generalized expression for prediction of the mean crushing force of metallic tubular structures is proposed. The chapter therefore investigates whether the mechanics contained within existing cross-section-specific formulations can be used to obtain a more general expression suitable for rapid assessment of different tubular geometries.

Chapter 3 extends the study from axial crushing to bending and bending collapse of square and rectangular metallic tubular structures. Unlike axial crushing, where the mean crushing force can be used as a representative parameter for much of the response, bending requires the evolution of structural resistance with deformation to be predicted. Existing analytical models primarily describe the collapse stage and, in spring-linkage or multibody approaches, the required moment-rotation characteristics are often obtained from experiments [17] or finite element simulations. To reduce this dependence, a semi-analytical method is developed to calculate the moment-rotation response directly from the material stress-strain curve and

cross-sectional geometry. This response is introduced into a spring-linkage model to predict the elastic and elasto-plastic stages. The subsequent collapse response is described using the model from Kecman, and a transition method is developed to connect the two regions and obtain the complete force-displacement curve. The resulting framework is assessed against numerical simulations covering different materials and geometries and is subsequently compared with experimental results available in literature. Chapter 3 therefore extends the low-order modelling approach from prediction of a characteristic crushing parameter to prediction of the complete bending response without requiring finite element simulations to generate the rotational spring characteristics.

Chapter 4 considers three-point bending of GLARE laminates. This introduces additional complexity compared with the metallic structures considered in the preceding chapters, since the response depends on the interaction between aluminium layers, glass-fibre reinforced layers, and their interfaces, with several possible failure mechanisms. An experimental campaign is therefore first used to characterize the bending response and to study the influence of laminate configuration, displacement rate, and aluminium rolling direction on the observed failure mechanisms, force-displacement response, and energy absorption. Based on these observations, a semi-analytical model is developed for specimens exhibiting a central-cracking failure mechanism and is assessed against the experimental force-displacement curves, peak force, and absorbed energy. This chapter therefore investigates the extent to which the computationally efficient modelling approach can be extended from metallic structures to a hybrid laminated material, while also identifying the limitations introduced by interacting failure mechanisms.

The three technical chapters consequently form a progression in both the response being predicted and the complexity of the structure being considered. Chapter 2 addresses prediction of mean crushing force during axial collapse, Chapter 3 extends this to the complete force-displacement response during metallic bending and collapse, and Chapter 4 considers bending of a hybrid laminate with multiple interacting failure mechanisms. In each case, the objective is to retain the mechanics required to describe the dominant structural response while reducing the computational effort required for its prediction.

The results obtained from these investigations are brought together and discussed in chapter 5. The main conclusions are presented in chapter 6 and related back to the research questions introduced in this chapter. Recommendations for future research, informed by the limitations identified and experience gained throughout this work, are provided in chapter 7.

2

Axial crushing of metallic tubular structures

To design crash structures for disruptive aircraft designs, it is required to have fast and accurate methods that can predict crashworthiness of aircraft structures early in the design phase. Axial crushing is one of the key energy absorbing mechanisms during a crash event. In this study, various analytical models proposed for calculation of mean crushing force for thin-walled tubular structures are compared with a database of numerical and experimental values to ascertain their accuracy. Improvements to some of the models have also been proposed. Finally a generalized model based on the studied and improved analytical models for prediction of mean crushing force for closed section thin-walled tubular structures is introduced. The generalized model demonstrates high accuracy when compared against experimental/numerical dataset as evidenced by a high coefficient of determination (R^2) value of 0.97 and can therefore be used to estimate the mean crushing force for closed-section thin-walled metallic tubular structures with various cross-sectional shapes and crushing modes early in the design phase.

This chapter has been copied verbatim from the paper published in International Journal of Impact Engineering, "Crashworthiness in preliminary design: Mean crushing force prediction for closed-section thin-walled metallic structures", **Volume 188**, (June, 2024) [33]. Changes have been made for relevant portions based on the corrigendum, **Volume 194**, (December, 2024) [34]. Some additions have also been made based on the recommendations of thesis review committee.

Nomenclature

c	Edge length of cross-section in polygonal tubular structures
$2H$	Initial distance between plastic hinges at top and bottom of a basic folding element (Fig. 12, Reference [25])
κ	Effective crushing length
N_c	Number of corners for a polygonal or star shaped cross-section (Reference [29])
P_{mean}	Mean crushing force
R	Mean radius of cross-section in circular tubular structures
h	Wall thickness for the metallic structures
M_0	Fully plastic bending moment per unit length
σ_0	Flow stress (MPa)
ε_u	Ultimate strain
θ_e	External angle (Fig. 2, Reference [29])
θ_i	Internal angle (Fig. 2, Reference [29])
b	Radius of the toroidal surface (Fig. A1, Reference [26])
$2\psi_0$	π - central angle of a corner element
α	timelike parameter (Fig. 2.15)
$\overline{\alpha}$	Switching point parameter
R^2	Coefficient of determination
$\overline{E}$	Average error
θ	Enclosed angle for an angle element
B	Edge length of an angle element
IQR	Inter Quartile Range

2.1. Introduction

Aviation was responsible for approximately 12% of the total greenhouse gas emissions from the transportation sector in 2020 [35]. At the current rate, if no improvements are made, carbon emissions from the aviation sector are expected to reach 1.8 gigatonnes per year by 2050 [36]. This figure would constitute 4.2% of the aggregate carbon emissions for 2050 [37]. Therefore, the International Air Transport Association(IATA) proposed a strategy for achieving carbon neutrality by the year 2050 [36]. The proposed strategy consists of 4 components: (a) Sustainable Aviation Fuel(SAF), (b) new technologies, (c) infrastructure /operations, and (d) offsetting /carbon capture. Amongst these components, 13% of the reductions are expected to come from new technologies which include more efficient aircraft designs as well as electric and hydrogen propulsion technologies.

To fulfill the demand for more efficient aircraft, more disruptive configurations have been conceptualized. Prime examples of such designs include the Flying-V

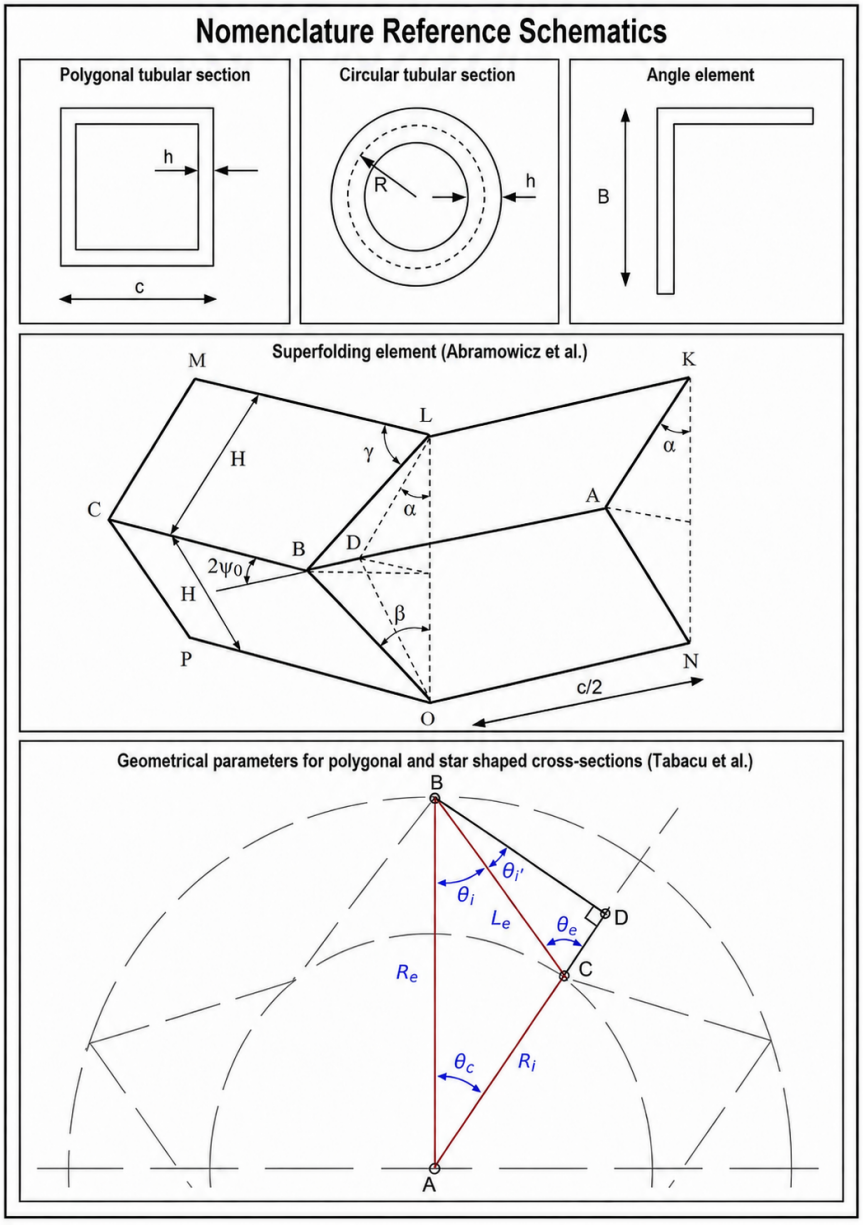

Figure 2.1.: Nomenclature reference schematics adapted from [29] and [25]

and the Airbus Maveric. Oosterom and Vos [8] predict a 22% decrease in fuel burn for some versions of the Flying-V compared to an Airbus A350. However, the Flying-V combines the lifting function of the aircraft (wing) with the load-carrying

function (fuselage) into a single wing-fuselage structure, resulting in an ovalized fuselage cross-section which leads to a significant decrease in distance between the cabin floor and the ground ($L_1 > L_2$, Figure 2.2). As a consequence of this decrease in the available crushing distance, crashworthiness for such disruptive aircraft configurations becomes more challenging as compared to a conventional aircraft configuration. Therefore, to avoid cost overruns and drastic design changes in the later stages of the design process, it is necessary that crashworthiness is assessed early on in the design phase for such disruptive aircraft configurations.

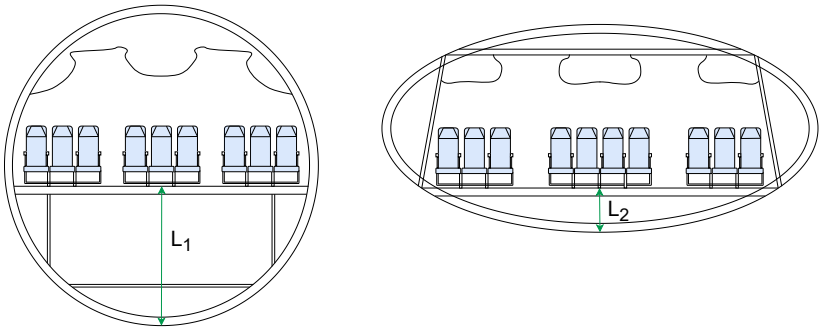

Figure 2.2.: Comparison between Airbus A350 (left) [9] and Flying-V fuselage cross section (right) [8]

The main challenges involved with an early crashworthiness assessment are related to the unavailability of high-fidelity models that are compatible with current methods based on implicit or explicit dynamic finite-element analyses. The dependence of such models on more detailed geometry definitions makes high-level structural layout trade-offs difficult to implement and computationally costly. Therefore, we propose the use of reduced-order models that are fast and easy to parameterize, allowing iteration through various structural layout configurations. In our research, it is proposed a low-fidelity model consisting of user elements enriched using analytical equations for the various energy absorbing mechanisms, namely axial crushing, plastic bending, and failure of joints. In this paper, the quasi-static analytical modelling of axial crushing for metallic thin-walled structures is explored in detail. The results from these quasi-static analytical models can then be extended to the case of dynamic loading by considering the strain rate effects (section 2.5).

To model the axial crushing behaviour of metallic thin-walled structures, it is important to be able to predict the force versus displacement curve for a member subjected to axial loads. Metallic structures submitted to axial crushing typically display a progressive folding behavior. An ideal force versus displacement graph for axial crushing of a tubular structure is shown in Figure 2.3. When the tubular structure comes into contact with the rigid plane, a force P starts to increase until it reaches a peak (P_{peak}), at this point plastic failure sets in and the crushing transitions into a mechanism of progressive folding corresponding to a mean force

(P_{mean}) denoted by a dashed line in Figure 2.3.

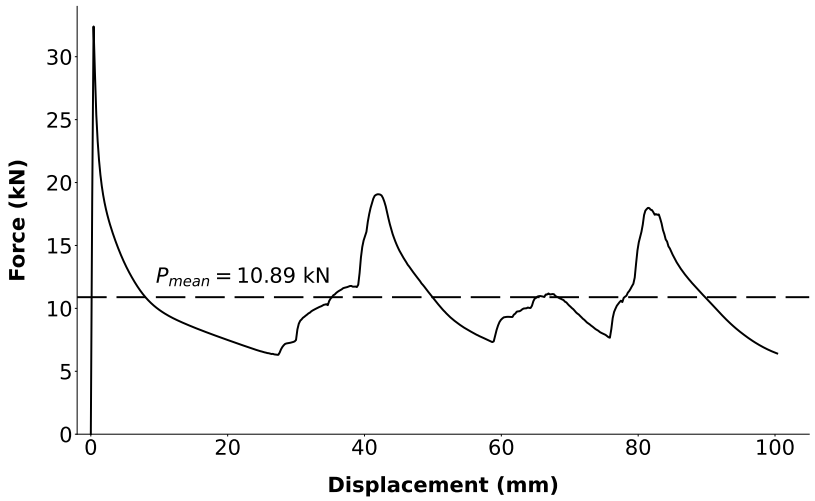

Figure 2.3.: Ideal force versus displacement curve for a tubular structure

The prediction of the mean crushing force requires a detailed analysis of the crushing mechanism. Various analytical models have been proposed in the literature for predicting the mean crushing force (P_{mean}) for thin-walled metallic structures submitted to axial crushing. Alexander [22] proposed in 1960 an approximate theory for calculating the mean crushing force for cylindrical thin-walled tubular structures. In 1978, Magee and Thornton proposed empirical equations for circular and square tubular structures. In the 1980s, Abramowicz et al. proposed a kinematics-based model for square [25], circular [24] and multi-corner [26] tubular structures. Subsequently, in 1992, Wierzbicki et al. [38] revisited Alexander's model and proposed a model using super-folding elements to reproduce the whole crushing process. Singace et al. [39] proposed in 1995 a modification to the eccentricity factor in Weirzbicki's model [38]. In 2007, Liu and Day [40, 41] used the methodology from Abramowicz et al. [26] to propose an equation for calculating the mean crushing force for octagonal tubular structures. In 2012, an analytical model for angle elements was proposed by Zhang and Zhang [42]. In 2014, Maalej et al. proposed a closed form solution for calculating P_{mean} for polygonal tubular structures based on the work of Abramowicz et al. [26]. More recently, in 2019, Tabacu et al. [29] proposed a generalized analytical model for polygonal and star-shaped cross-sections based on the membrane energy calculations from Zhang and Zhang [43].

The aforementioned analytical models claimed to correspond well with experimental findings. Therefore, to select the most suitable models for the present study, we decided to evaluate these analytical models against a dataset that includes various materials, geometries, and cross-sections. This dataset includes experimental results compiled from the literature, and simulation results obtained

from a shell-based finite element (FE) model.

Four different cross-sectional shapes (circular, square, hexagonal and octagonal) were considered for this study. Square and circular cross-sections are the most commonly studied cross-sections for axial crushing applications. While square tubular structures are better in terms of practicality and ease of manufacturing [44], circular tubular structures have been shown to have better energy absorption characteristics [44–46]. Mamalis et al. [44] note that polygonal tubular structures can lend themselves to easier fabrication while displaying crushing characteristics closer to that of circular tubular structures. It was observed by Yamashita et al. [46] and Fan et al. [47] that for polygonal tubular structures specific energy absorption increases with increase in the number of sides. However, Tarlochan et al. [45] recorded a decrease in specific energy absorption for octagonal tubular structures as compared to hexagonal tubular structures. Yamashita et al. [46] also state that polygonal cross-sections with less than six sides should generally be avoided as they are more susceptible to disordered deformation patterns. Since we want to assess crashworthiness early in the design phase, having the ability to account for different cross-sectional shapes is a significant advantage. Therefore, analytical models for estimating the mean crushing force of circular, square and polygonal tubular structures have been considered in this study.

2.2. Analytical model parameters

For the considered analytical models, the parameters used for the calculation of the mean crushing force can be divided into two categories: geometrical parameters and material parameters.

Geometrical parameters

1. Wall thickness (h)
2. Side length (c)
3. Mean Radius (R)
4. Number of sides of the polygon / angle enclosed between two edges

Material parameters

1. **Effective crushing length (κ):** Effective crushing length is a key parameter that characterizes the energy absorption capability of a tubular structure during an impact event. For the purposes of this paper, effective crushing length is defined as the proportion of the crushed length to the initial length, with the former being the length of the tubular structure subsequent to full-scale crushing:

$$\text{Effective crushing length, } \kappa = \frac{Crushed\ length}{Initial\ length} \tag{2.1}$$

2. **Flow stress (σ_0):** Pertaining to the axial crushing of metallic tubular structures, flow stress is the level of stress needed to sustain plastic deformation of the material. The identification of this flow stress is crucial to the calculation of mean crushing force for these metallic structures. Various formulas for calculating flow stress, denoted as σ_0, are available in the published literature:

   a) Alexander [22]:
   $$\sigma_0 = \frac{2}{\sqrt{3}}\sigma_y \tag{2.2}$$

   b) Wierzbicki et al. [38]:
   $$\sigma_0 = 0.92 \cdot \sigma_u \tag{2.3}$$

   c) Wierzbicki et al. [48]:
   $$\sigma_0 = 0.70 \cdot \sigma_u \tag{2.4}$$

   d) Langseth and Hopperstad [49], Zhang and Zhang [43], Hannsen et al. [50], and Yang and Caldwell [51] use the expression:
   $$\sigma_0 = \frac{\sigma_y + \sigma_u}{2} \tag{2.5}$$

   e) Tabacu et al. [29]:
   $$\sigma_0 = \frac{1}{\varepsilon_u} \cdot \int_0^{\varepsilon_u} \sigma \cdot d\varepsilon \tag{2.6}$$

2.3. Analytical models for mean crushing force (P_{mean})

When submitted to axial crushing, metallic tubular structures crush either with an extensional or an inextensional crushing mechanism [25, 29]. In extensional crushing mechanism, both sides of a corner element move outwards creating an extension about the edge whereas during inextensional crushing, one side moves outward while the other side moves inward with the material flowing across the edge (plastic hinge line). Both these crushing mechanisms are illustrated in Figure 2.4.

Equations proposed by various authors for inextensional and extensional crushing of polygonal tubular structures (concertina crushing for circular tubular structures) are presented in this section. These equations are either obtained by calibration with experimental data [23, 42] or by equating mean force times the displacement required for one complete fold with the amount of energy consumed to create the fold (Eq. 2.7).

$$P_{mean}.\delta = \text{Energy absorbed for creation of one fold} \tag{2.7}$$

Where δ is the crushed distance for one complete fold and is generally given by $2H.\kappa$. Energy absorbed for creation of one fold is computed using two different

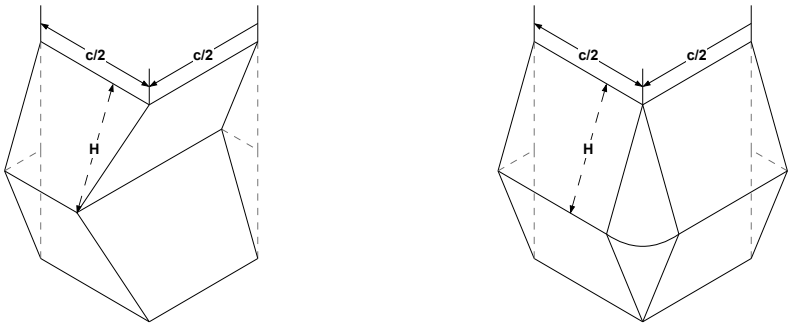

(a) (b)

Figure 2.4.: Basic collapse elements for (a) Inextensional crushing mechanism and (b) Extensional crushing mechanism

approaches in the presented analytical models. The first approach is more rigorous and considers the finite rotations and deformations that take place during formation of a fold [24–26] while the second approach considers the sum of bending and membrane energy required for creation of a fold [29]. For a detailed treatment of energy absorbed in creation of one fold, readers should consult the work of respective authors. However, for completeness one example of the governing equation for each approach is presented below:

1. **Quasi inextensional crushing of polygonal tubular structures per Abramowicz et al. [26]:** The energy required for the creation of one fold is given as a sum of energy absorbed by plastic flow over the toroidal surface (E_1), energy absorbed by bending along the horizontal hinge lines (E_2 and E_5), energy absorbed by bending along the inclined hinge lines (E_3 and E_6), and energy absorbed by stretching of the conical zone (E_4). Energies $E_1 \rightarrow E_6$ are given as functions of fully plastic bending moment (M_0), wavelength of folding ($2H$), radius of toroidal surface (b), side length (c), wall thickness (h), angle of corner element (ψ_0), angle of rotation of sides (α), terminal value of angle of rotation (α_f), switching angle after which the crushing turns extensional ($\bar{\alpha}$) and integrals $I_1 \rightarrow I_6$ (functions of ψ_0 and $\bar{\alpha}$):

$$E_1 = 16M_0\frac{Hb}{h}I_1;\ E_2 + E_5 = 4M_0c\alpha_f;\ E_3 = 4M_0\frac{H^2}{b}I_3;$$
$$E_4 = 8M_0\frac{H^2}{h}I_4 \text{ and } E_6 = 2M_0HI_6 \tag{2.8}$$

The equation for mean crushing force (P_{mean}) is then written as:

$$P_{mean}.2H.\kappa = 16M_0\frac{Hb}{h}I_1 + 4M_0c\alpha_f + 4M_0\frac{H^2}{b}I_3 + 8M_0\frac{H^2}{h}I_4 + 2M_0HI_6 \tag{2.9}$$

Equation 2.9 can then be further simplified and value of mean crushing force obtained by minimizing with respect to the three unknowns ($\partial P_m/\partial\chi = 0,$ where $\chi = [H, b, \bar{\alpha}]$).

2. **Extensional crushing of square tube per Tabacu et al. [29]:** The energy required for creation of one fold is given as a sum of membrane and bending energies. The bending energy is the amount of energy absorbed by bending along the plastic hinge lines while the membrane energy accounts for extension or compression of the material during fold formation. The bending and membrane energies for a corner element can be given as:

$$E_{bending} = 2.\pi.L.M_0 \text{ and } E_{membrane} = 2.\pi.M_0.H^2/h \tag{2.10}$$

For a square tubular structure, this leads to:

$$P_{mean}.2H.\kappa = 2.\pi.4c.M_0 + 2.\pi.M_0.\frac{H^2}{h} \tag{2.11}$$

The expression for H can then be obtained by putting the partial differential of mean crushing force with H ($\partial P_m/\partial H$) equal to 0 (since the mean crushing force is constant). Final expression of mean crushing force can then be obtained by substituting the expression of H in Eq. 2.11.

Concertina crushing of circular tubular structures per Alexander (1960) [22]:

$$P_{mean} = K\sigma_0 h^{1.5}\sqrt{2R} \tag{2.12}$$

where: $K = 6.08$

Concertina crushing of circular tubular structures per Abramowicz et al. (1984) [24]:

$$\frac{P_{\text{mean}}}{M_0}\cdot\kappa = 2\sqrt{3}\pi\left(\frac{R}{h}\right)\left(\frac{H}{R}\right) + \frac{2}{\sqrt{3}}\pi\left(\frac{R}{h}\right)\left(\frac{H}{R}\right)^2 + 2\pi^2\left(\frac{R}{H}\right) + 2\pi \tag{2.13}$$

where:

$$\frac{H}{R} = \left(\frac{\pi h}{\sqrt{3}R}\left[1 + \frac{2}{3}\left(\frac{H}{R}\right)\right]^{-1}\right)^{\frac{1}{2}} \text{ and } M_0 = \frac{2\sigma_0 h^2}{4\sqrt{3}}$$

Concertina crushing of circular tubular structures per Wierzbicki et al. (1992) [38]:

$$\frac{P_m}{M_0} = 31.74\sqrt{\frac{2R}{h}} \tag{2.14}$$

where: $M_0 = \frac{\sigma_0 h^2}{4}$

Concertina crushing of circular tubular structures per Singace et al. (1995) [39]:

$$\frac{P_m}{M_0} \cdot \kappa = 22.27\sqrt{\frac{2R}{h}} + 5.632 \tag{2.15}$$

where: $M_0 = \frac{\sigma_0 h^2}{4}$

Square tubular structures per Magee and Thornton (1978) [23]:

Magee and Thornton obtained an empirical equation for the mean crushing force of square tubular structures:

$$P_m = 17 \cdot \sigma_0 \cdot c^{0.2} \cdot h^{1.8} \tag{2.16}$$

Inextensional crushing of square tubular structures per Abramowicz et al. (1984) [25]:

Abramowicz et al. gave an expression for inextensional crushing of square tubular structures:

$$\frac{P_{\text{mean}}}{M_0} \cdot \kappa = 17.76\left(\frac{b}{h}\right) + 4\pi\left(\frac{c}{h}\right)\left(\frac{h}{H}\right) + 9.184\left(\frac{H}{h}\right)\left(\frac{h}{b}\right) \tag{2.17}$$

where:

$$\frac{b}{h} = 0.72\left(\frac{c}{h}\right)^{\frac{1}{3}};\ \frac{H}{h} = 0.99\left(\frac{c}{h}\right)^{\frac{2}{3}} \text{ and } M_0 = \frac{\sigma_0 h^2}{4}$$

Quasi inextensional crushing of polygonal tubular structures per Abramowicz et al. (1988, 1989, 1992) [26, 52, 53]:

$$\frac{P_m \cdot \delta_{eff}}{M_0 \cdot 2H} = A_1\frac{b}{h} + (A_2 + A_5)\frac{c}{H} + A_3\frac{H}{b} + A_4\frac{H}{h} + A_6 \tag{2.18}$$

where M_0 is calculated as $\sigma_0 h^2/4$, A_i (i=1 to 6) is a function of the angle between two edges of a corner element ($\pi - 2\psi_0$) and a time-like parameter (α), b and $2H$ are bending radius and wavelength of the buckling wave respectively. A switching point parameter ($\overline{\alpha}$) is also used in the calculation, the crushing is inextensional

below $\overline{\alpha}$ and extensional after $\overline{\alpha}$. The term $\delta_{eff}/2H$ indicates effective crushing length and can be used interchangeably with κ. Since the mean crushing force should remain constant throughout the crushing process, the values of unknowns (b, H, $\overline{\alpha}$) can be obtained by equating the partial differentiation of the mean force with respect to each unknown equal to zero.

For a specific type of cross-section, it is convenient to solve Eq. 2.18 in terms of the mean crushing force (P_m) for different values of M_0 and c/h. These results will give a set of points in a graph of c/h versus P_m/M_0, for which a simpler curve can be fit, Figure 2.5. For the case of mild steel, κ =0.73 [26]:

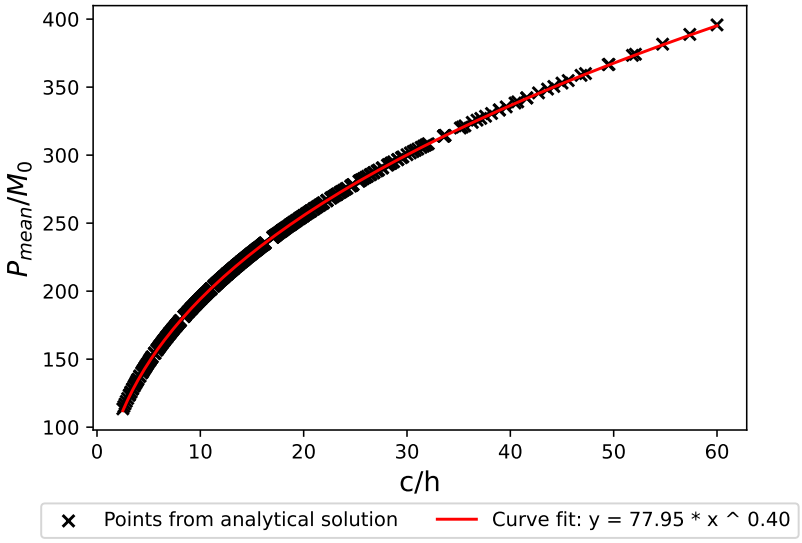

Figure 2.5.: Fitting a curve to the dataset obtained using the analytical model from Abramowicz et al. [26])

- For hexagonal tubular structures:

$$\frac{P_m}{M_0} = 80.92\left(\frac{c}{h}\right)^{0.4} \tag{2.19}$$

However, in our implementation, we obtain a slightly lower coefficient :

$$\frac{P_m}{M_0} = 77.95\left(\frac{c}{h}\right)^{0.4} \tag{2.20}$$

The discrepancy in the coefficient value may arise from variations in the selected (c/h) range. Additionally, rounding inaccuracies might also cause a deviation in the value of the coefficient.

- For octagonal tubular structures, following the procedure presented in the paper, we obtain a similar equation:

$$\frac{P_m}{M_0} = 110.24\left(\frac{c}{h}\right)^{0.4} \tag{2.21}$$

These results are obtained assuming $\kappa = 0.73$, for other kappa values, mean force should therefore be multiplied by $0.73/\kappa$. The same holds true for other models that are based on this model (Eq. 2.22 and 2.25).

Quasi inextensional crushing of polygonal tubular structures per Maalej et al. (2014) [28]:

Maalej et al. [28] used the model from Abramowicz et al. [26] to derive with an empirical closed form solution:

$$\frac{P_m}{M_0} = N_c \cdot (2.13 + 9.44\phi - 2\phi^2)\left(\frac{c}{h}\right)^{\frac{1}{3}+0.06\left(\phi-\frac{\pi}{3}\right)} \tag{2.22}$$

where:
N_c= Number of corners; ϕ=Corner element angle and $M_0 = \frac{\sigma_0 h^2}{4}$
This equation for specific cases are given below:

- For Hexagonal tubular structures:

$$\frac{P_m}{M_0} = 78.77\left(\frac{c}{h}\right)^{0.4} \tag{2.23}$$

- For Octagonal tubular structures:

$$\frac{P_m}{M_0} = 106.15\left(\frac{c}{h}\right)^{0.41} \tag{2.24}$$

Quasi inextensional crushing of octagonal tubular structures per Liu and Day (2007) [40, 41]:

$$\frac{P_m}{M_0} = 97.77\left(\frac{c}{h}\right)^{0.4} \tag{2.25}$$

where: $M_0 = \frac{\sigma_0 h^2}{4}$

This equation is obtained using the model from Abramowicz et al. [26]. However, it is very different from the equation that we obtain in our implementation of Abramowicz et al.'s model (Eq. 2.21) and the equation obtained by Maalej et al. [28] (Eq. 2.22). During the development of the present study, we were able to identify the source of this deviation, which is a printing error in the work of Abramowicz et al. [26]. The equation for integral I_3 is supposed to be:

$$I_3(\psi_0, \overline{\alpha}) = cot^2\psi_0 \int_0^{\overline{\alpha}} cos\alpha \sqrt{tan^2\psi_0 + sin^2\alpha} d\alpha \tag{2.26}$$

Extensional crushing of polygonal and star-shaped cross sections per Tabacu et al.(2019) [29]:

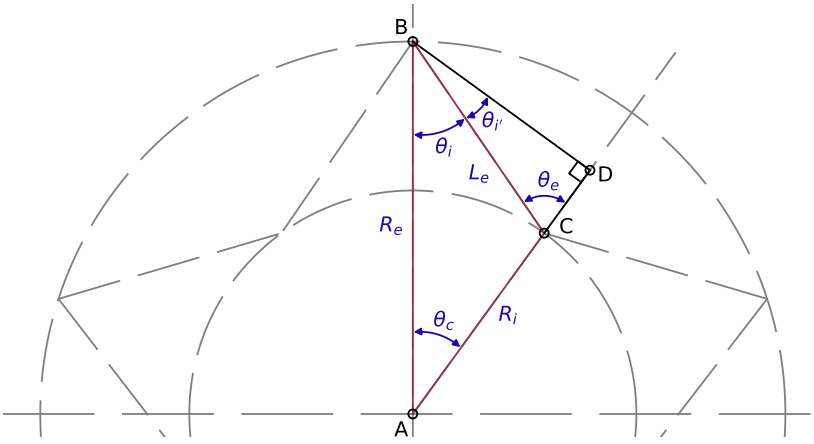

Figure 2.6.: Geometrical parameters for the model from Tabacu et al. [29]

Tabacu et al. proposed a model for extensional crushing of polygonal and star-shaped cross-sections. The equation for the model from Tabacu et al. [29] takes the form:

$$P_m \cdot \kappa = \sigma_0 \cdot h \cdot N_c \cdot \sqrt{[2\pi - 2(\theta_i + \theta_e)] \cdot \pi \cdot L_e \cdot h} \tag{2.27}$$

The parameters θ_i, θ_e, L_e and N_c come from the cross-sectional geometry (Figure 2.6). The equation for specific cases derived by Tabacu et al. [29] are given below:

- For rectangular tubular structures:

$$P_m \cdot \kappa = 8.88 \cdot \sigma_0 \cdot L_e^{\frac{1}{2}} \cdot h^{\frac{3}{2}} \tag{2.28}$$

- For circular tubular structures:

$$P_m \cdot \kappa = 22.27 \cdot \frac{\sigma_0 \cdot h^2}{4} \sqrt{\frac{2 \cdot R}{h}} \tag{2.29}$$

- For convex polygon with N_c corners:

Equation 2.27 can be further simplified for the case of convex polygons. For convex polygons, $\theta_c = \pi/N_c$ and $\theta_e = \pi/2$. If "c" is the side length of the polygon, then substituting the values of θ_c and θ_e in equation 2.27 result in:

$$P_m \cdot \kappa = \pi \cdot \sigma_0 \cdot N_c^{\frac{1}{2}} \cdot c^{\frac{1}{2}} \cdot h^{\frac{3}{2}} \tag{2.30}$$

Equation 2.30 is very interesting because it indicates that for tubular structures with convex polygonal shapes, the mean crushing force is directly proportional to the square root of the number of sides/corners given by $N_c^{0.5}$. Abramowicz et al. [26] proposed in their work that the inextensional crushing mode is infact a quasi inextensional mode and involves a combination of extensional and inextensional crushing with extensional crushing becoming the dominant mode for obtuse angle elements. Therefore, while the equation from Tabacu et al. [29] specifically deals with extensional crushing, it is also interesting to compare its results with inextensional mean crushing force dataset.

Inextensional crushing of angle elements per Zhang and Zhang (2013) [42]:

Zhang and Zhang proposed a general equation for angle elements with a central angle θ by calibrating a general expression for the mean crushing force with the empirical equation for square tubular structures from Magee and Thornton [23].

$$P_m = \frac{\sigma_0}{2 \cdot \kappa} \cdot (B)^{0.2} \cdot h^{1.8} \cdot \sqrt{\frac{2\pi \cdot tan(\theta/2)}{0.082(tan(\theta/2) + 0.06/tan(\theta/2))}} \tag{2.31}$$

2.4. Sensitivity of analytical models to geometrical and material parameters

For the present work, experimental data from literature (Section 2.6) and numerical simulation data were used to evaluate the accuracy of various analytical models. The analytical models presented in Section 2.3 use various geometrical and material parameters to estimate the value of the mean crushing force (P_{mean}). which means that an error in the input parameters can lead to a significant error in the estimated value of mean crushing force. Potential sources of error are experimental measurement discrepancies, fabrication inconsistencies, and data reporting approximations.

To understand the amount of error that each of the input parameters can cause while estimating the mean crushing force, a sensitivity analysis is conducted for the various models. For all the models, the mean crushing force is directly proportional to the flow stress (σ_0), therefore, a percentage (%) change in flow stress causes the mean force to change by the same percentage.

Figure 2.7.: Sensitivity of analytical models for predicting mean crushing force to radius/ edge length and thickness for (a) circular tubular structures and (b) polygonal tubular structures

The sensitivity analyses shown in Figures 2.7a and 2.7b only investigate the effect of the edge length (radius for circular tubular structures) and thickness. It is evident that the calculations of mean crushing force exhibit a high sensitivity to variations in thickness, meaning that significant errors would be reasonably expected when comparing the analytical models against the experimental dataset obtained from literature, because minor inaccuracies in the reported geometry would result in significant discrepancies in the mean crushing force calculated using the analytical models. Therefore, it becomes imperative for users of these analytical models to remain cognizant of the high sensitivity of such models to thickness variations. Furthermore, since P_{mean} is directly proportional to the flow stress, ensuring high accuracy in the stress-strain data becomes crucial before utilizing these analytical models for comparison against experimental data.

2.5. Strain rate effects

Since we intend to use the analytical models for impact loading scenarios (aircraft crash), it is essential to adapt results from quasi-static analytical models presented in this paper to take strain rate effects into account. While a detailed study of strain rate effects is outside the scope of this paper, a brief summary of methods from literature which can be used to obtain the dynamic mean crushing force (P_m^d) from the quasi-static mean crushing force (P_m) are presented in this section.

Okhubo et al. [54] proposed an empirical equation (Eq. 2.32) by comparing the static and dynamic mean crushing force for closed-hat sections and Wimmer [55] proposed an empirical equation for square box columns (Eq. 2.33).

$$P_m^d = P_m\,(1 + 0.068V)\,;\ \text{where V is velocity in } m.s^{-1} \tag{2.32}$$

$$P_m^d = P_m\left(1 + 0.07V^{0.82}\right);\ \text{where V is velocity in } m.s^{-1} \tag{2.33}$$

Since these methods are empirical and are not suitable for preliminary design, a dynamic correction factor based on viscoplastic analysis was proposed by Akerstorm [56]:

$$P_m^d = P_m\left(1 + 0.11V^{0.714}\right);\ \text{where V is velocity in } m.s^{-}1 \tag{2.34}$$

Abramowicz et al. [25] proposed to account for strain rate effects using the Cowper-Symonds constitutive relationship which gives dynamic flow stress (σ_0^d) as a function of flow stress (σ_0) and strain rate ($\dot{\varepsilon}$).

$$\frac{\sigma_0^d}{\sigma_0} = 1 + \left(\frac{\dot{\varepsilon}}{D}\right)^{\frac{1}{p}} \tag{2.35}$$

where D and p are strain-rate parameters for the Cowper-Symonds material model

Since mean crushing force (P_m) is directly proportional to flow stress, dynamic mean crushing force (P_m^d) is then obtained by using the following expression:

$$P_m^d = P_m \left[1 + \left(\frac{\dot{\varepsilon}}{D} \right)^{\frac{1}{p}} \right] \tag{2.36}$$

Cowper-Symonds relationship is the most commonly used method [24, 25, 28, 49, 57–60] to make a correlation between dynamic mean crushing force (P_m^d) and static mean crushing force (P_m).

2.6. Experimental and numerical datasets

Section 2.3 presented various analytical models available in the literature for calculating the mean crushing force for metallic tubular structures. To select an appropriate analytical model to be used in the reduced-order crashworthiness simulation, the output of these models is compared against experimental data from literature, presented in Section 2.6.1. To augment this dataset, numerical simulations using a shell-based finite element model were also conducted, and the results are presented in Section 2.6.2. All input files along with the extracted force-displacement results corresponding to the numerical dataset were made available in a public dataset by the authors [61].

2.6.1. Experimental dataset from literature

The experimental dataset is compiled using data points collected from literature for closed-section thin-walled metallic structures, as detailed below. The dataset for different cross-sections is given in Appendix A.1, while the corresponding material data in Appendix A.2.

1. **Circular tubular structures:** 44 data points from 5 sources, consisting of 7 different materials
2. **Square tubular structures:** 42 data points from 6 sources, consisting of 11 different materials
3. **Hexagonal tubular structures:** 9 data points from 4 sources, consisting of 4 different materials
4. **Octagonal tubular structures:** 5 data points from 3 sources, consisting of 3 different materials

2.6.2. Numerical dataset

At an initial glance, the dataset sourced from the literature appears sufficiently extensive; however, it exhibits certain limitations. Many data points in the collected experimental dataset have the same geometry and material, for example the data

from Nia and Hamedani includes 5 square tubular samples made from Al3003-H12 with $c = 47.1mm$ and $h = 1.5mm$. Furthermore, the dataset has few data points for hexagonal and octagonal tubular structures.

Shell based crushing models are frequently used to simulate the crushing response of thin-walled metallic structures and have been shown to be very accurate [28, 29, 40, 62, 63]. Therefore, to augment the experimental dataset previously presented, a shell-based finite element model is developed in Abaqus [64], using quadrilateral shell elements with reduced integration (S4R). All models consist of a tubular structure placed between two rigid planes, where a vertical displacement is applied to the top rigid plane, while the bottom plane is encastred and the nodes at the bottom of the tubular structure were connected to the bottom rigid plane.

To induce a more controlled and progressive failure, two types of triggers have been used based on the literature [29, 42, 63]. For inextensional crushing mode, an indentation trigger is introduced on alternate faces (type-I trigger) whereas an indentation trigger is introduced on all the faces to trigger the extensional crushing mode (type-II trigger). A trigger mechanism initiates the structure into a progressive folding sequence by creating local weakness, ensuring a stable crushing zone and preventing other failure modes like global bending which can lead to a significantly lower energy absorption [45, 65, 66]. Employing a trigger mechanism also results in a reduction of peak crushing force which is especially desirable for crash applications as the human body is susceptible to severe injury when exposed to high deceleration magnitude and onset rates [67]. Trigger mechanisms have been evaluated for a variety of applications including automotive crash box [45, 65], helicopter structures [68], and landing gear [69].

Finally, to obtain the force versus displacement curves (cf. Figure 2.3), a reference node is placed at the center of the top rigid plane where both the reaction force and the displacement are measured. The numerical dataset is presented in Appendix A.3. Figure 2.8 illustrates a finite element model used for hexagonal tubular structures. The numerical simulation campaign consisted of:

1. **Circular tubular structures:** 32 simulations with 2 different materials (20 simulations using AA6060-T4 and 12 simulations using AISI-316). For AA6060-T4, the combinations considered were composed of Radius, R (mm) =[15, 20, 25, 30] and thickness, h (mm) = [1, 1.25, 1.5, 1.75, 2]. For AISI-316, the combinations considered were composed of Radius, R (mm) = [15, 20, 25, 30] and thickness, t (mm) = [1, 1.25, 1.5]. All the simulations are triggered for an extensional crushing mode as all the models for circular tubular structures presented in this paper deal with this mode of crushing.

2. **Square tubular structures:** 40 simulations with 2 different materials (28 simulations using AA6060-T4 and 12 simulations using AISI-316). For AA6060-T4, the combinations considered were composed of Side length, c (mm) = [30, 40, 50, 60] and thickness, h (mm) = [1, 1.25, 1.5, 1.75, 2, 2.25, 2.5]. For AISI-316, the combinations considered were composed of Side length, c (mm) =[30, 40, 50, 60] and thickness, t (mm)= [1, 1.25, 1.5]. All the simulations are triggered for an inextensional crushing mode as this mode is

predominant in the crushing of square tubular structures.

3. **Hexagonal tubular structures:**

   Extensional crushing simulations

   20 simulations with 2 different materials (12 simulations using AA6060-T4 and 8 simulations using AISI-316). For AA6060-T4, the combinations considered were composed of Side length, c (mm) = [30, 40, 50, 60] and thickness, h (mm) = [1, 1.5, 2]. For AISI-316, the combinations considered were composed of Side length, c (mm) =[30, 40, 50, 60] and thickness, t (mm)= [1, 1.5].

   Inextensional crushing simulations

   40 simulations with 2 different materials (20 simulations using AA6060-T4 and 20 simulations using AISI-316). For AA6060-T4, the combinations considered were composed of Side length, c (mm) = [30, 40, 50, 60] and thickness, h (mm) = [1, 1.25, 1.5, 1.75, 2]. For AISI-316, the combinations considered were composed of Side length, c (mm) =[30, 40, 50, 60] and thickness, t (mm)= [1, 1.12, 1.25, 1.37, 1.5].

4. **Octagonal tubular structures**

   Extensional crushing simulations

   20 simulations with 2 different materials (12 simulations using AA6060-T4 and 8 simulations using AISI-316). For AA6060-T4, the combinations considered were composed of Side length, c (mm) = [30, 40, 50, 60] and thickness, h (mm) = [1, 1.5, 2]. For AISI-316, the combinations considered were composed of Side length, c (mm) =[30, 40, 50, 60] and thickness, t (mm)= [1, 1.5].

   Inextensional crushing simulations

   A total of 40 simulations were launched with 2 different materials (20 simulations using AA6060-T4 and 20 simulations using AISI-316) and type-I (inextensional) trigger. However, it was observed that tubular structures with $c/h \leq 30$ have a tendency to crush under extensional or mixed crushing mode even when type-I trigger (Inextensional trigger) is used. Therefore, only 26 tubes that crushed with an inextensional crushing mode are considered. For AA6060-T4, the combinations considered were composed of Side length, c (mm) = [30, 40, 50, 60] and thickness, h (mm) = [1, 1.25, 1.5, 1.75, 2]. For AISI-316, the combinations considered were composed of Side length, c (mm) =[30, 40, 50, 60] and thickness, t (mm)= [1, 1.12, 1.25, 1.37, 1.5].

2.6.3. Validation of numerical model

To validate the numerical shell model, datapoints from the collected experimental dataset were simulated using the numerical model and a comparison was made. Material data for the respective experimental datapoints was obtained by digitizing the published stress-strain curves. The results obtained show a very good correlation between numerical and experimental data, as evidenced by a high

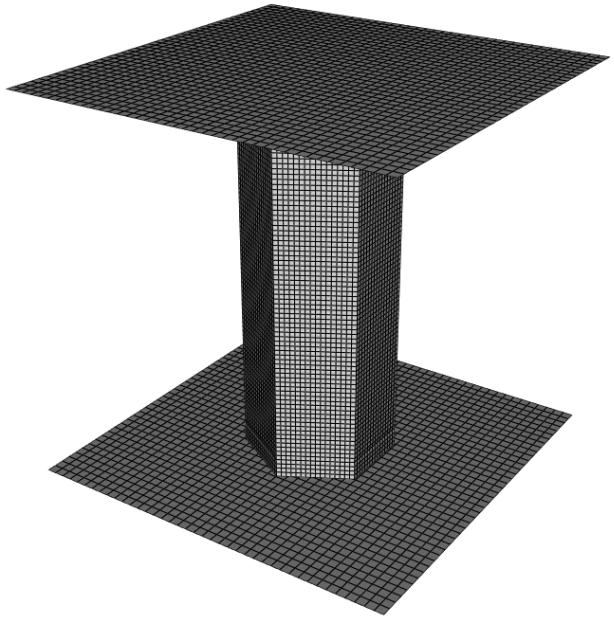

Figure 2.8.: Numerical model for a hexagonal tubular structure

coefficient of correlation ($R^2 = 0.97$), reinforcing the ability of numerical model to simulate axial crushing of metallic tubular structures. The correlation between experimental dataset and obtained numerical results is presented in Figure 2.9.

2.7. Results

The accuracy of various analytical models is evaluated comparing the mean crushing force predictions against the combined dataset including the experimental data from literature and numerical simulations. The following sub-sections present these comparisons for varying cross-sectional shapes.

For the models presented in this work, different equations to compute flow stress have been proposed by the respective authors. However, since we want to use these analytical models to study crashworthiness early in the design phase, it is important that the considered models can be used for different metallic materials and therefore, calculating flow stress solely based on yield and ultimate stress values will not be appropriate. To ensure that the comparison between analytical models is relevant for different materials, flow stress for all the models presented in this section has been calculated using equation 2.6 which considers the entire stress-strain curve for computation of flow stress. It was also observed by Abramowicz et al. [70] that flow stress obtained using Eq. 2.6 can be used for theoretical predictions over a wider range of materials.

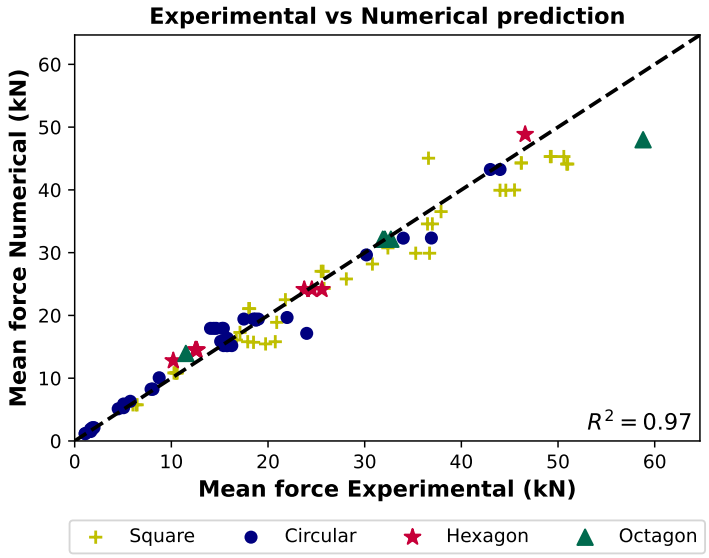

Figure 2.9.: Correlation between experimental dataset and results from numerical model

2.7.1. Extensional crushing of circular tubular structures

Figures 2.10a to 2.10e show the comparisons for circular tubular structures. The model from Alexander (Eq. 2.12) underpredicts significantly, reaching $R^2 = 0.73$. A very good agreement is observed for the model from Abramowicz et al. (Eq. 2.13), $R^2 = 0.98$. The revisited Alexander's model from Wierzbicki et al. (Eq. 2.14) and the subsequent revisit of Weirzbicki from Singace et al. (Eq. 2.15) also show good agreement with the dataset, reaching $R^2 = 0.95$ and $R^2 = 0.94$ respectively for these two cases. Finally, for the model from Tabacu et al. (Eq. 2.29), a slight under-prediction is observed, with $R^2 = 0.91$. The reason for the underestimation of mean crushing force using the equation from Tabacu et al. (2.29) is discussed further in section 2.9.

2.7.2. Inextensional crushing of square tubular structures

As shown in Figure 2.11a, for square tubular structures the model from Magee and Thornton (Eq. 2.16) slightly underpredicts the mean crushing force. Figure 2.11b presents the comparison based on the model from Abramowicz et al. (Eq. 2.17), a good correlation fit is observed between the model and the dataset, with $R^2 = 0.91$. Finally, the extensional crushing model from Tabacu et al. (Eq. 2.28) overpredicts the inextensional mean force by a large margin, reaching $R^2 = 0.50$, the comparison is presented in Figure 2.11c.

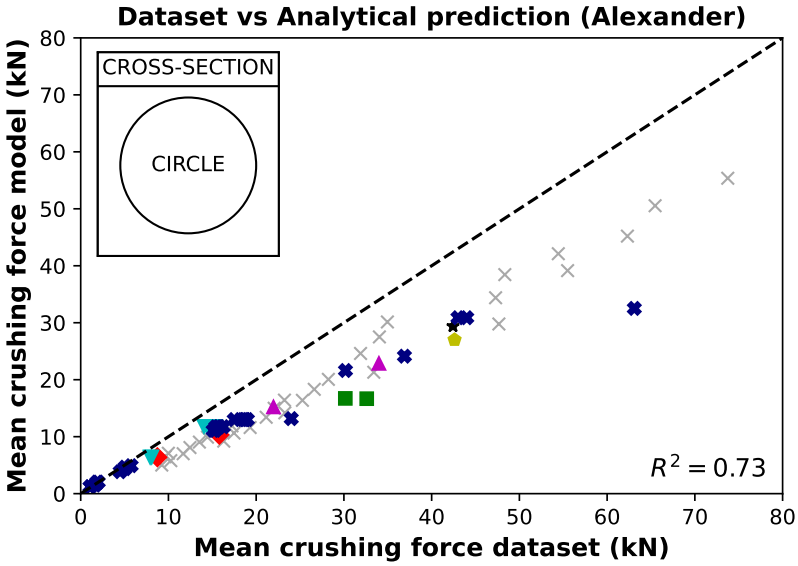

(a)

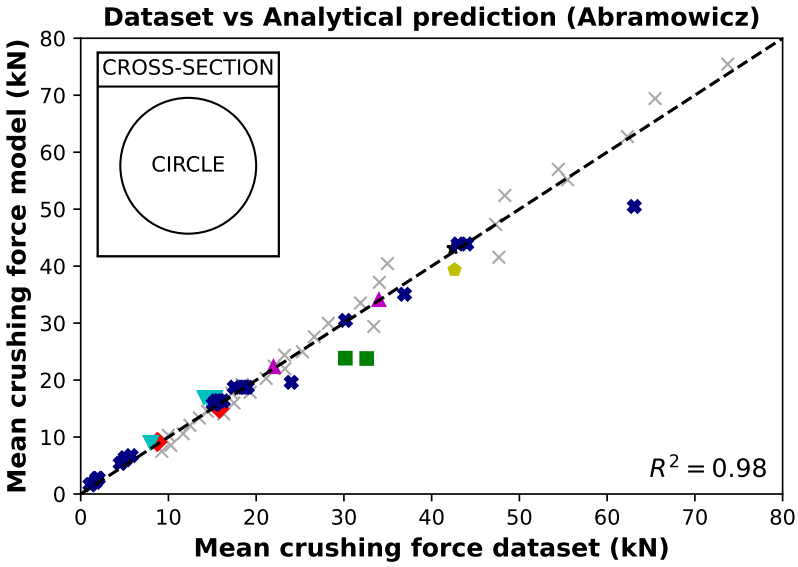

(b)

Figure 2.10.: Comparison between analytical models and dataset for circular tubular structures: (a) Alexander [22], (b) Abramowicz et al. [24], (c) Wierzbicki et al. [38], (d) Singace et al. [39] and (e) Tabacu et al. [29] – **continued on next page**

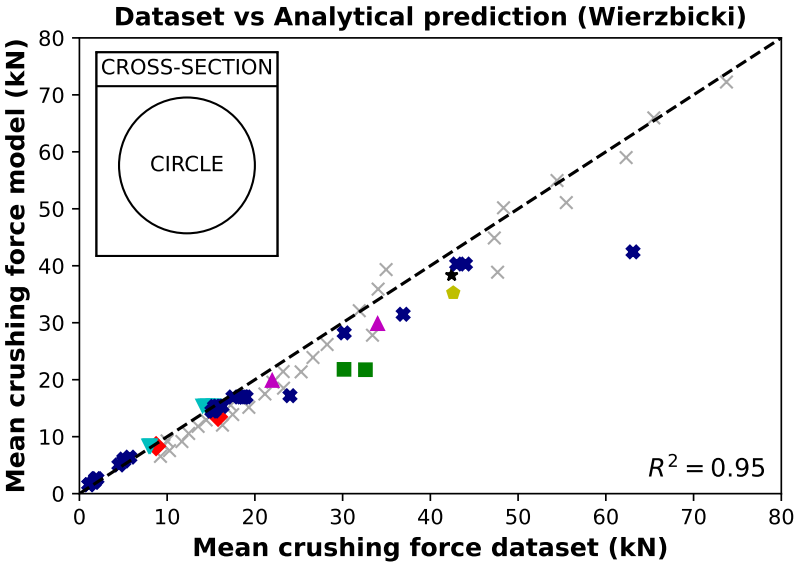

(c)

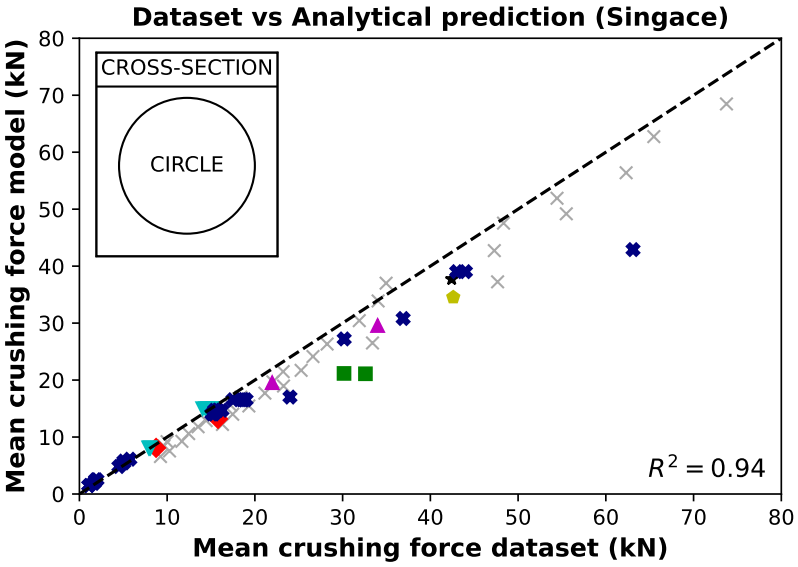

(d)

Figure 2.10.: Comparison between analytical models and dataset for circular tubular structures: (a) Alexander [22], (b) Abramowicz et al. [24], (c) Wierzbicki et al. [38], (d) Singace et al. [39] and (e) Tabacu et al. [29] – **continued on next page**

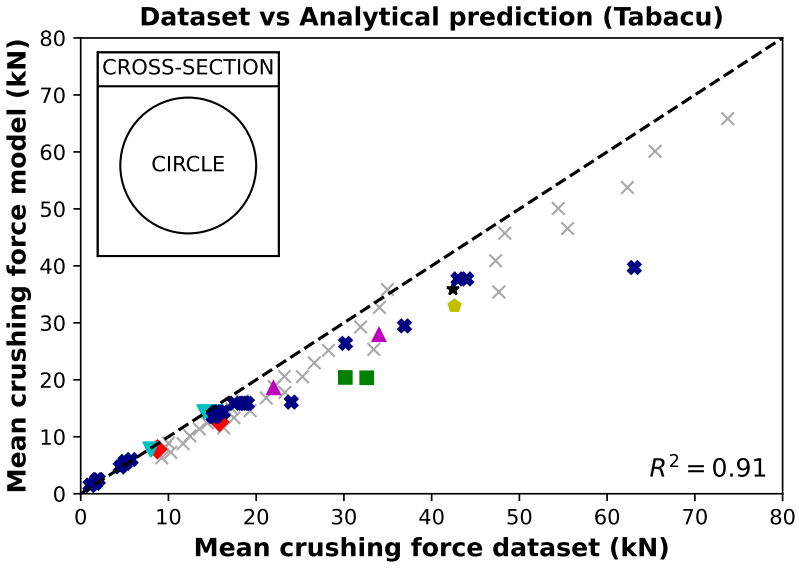

(e)



Figure 2.10.: Comparison between analytical models and dataset for circular tubular structures: (a) Alexander [22], (b) Abramowicz et al. [24], (c) Wierzbicki et al. [38], (d) Singace et al. [39] and (e) Tabacu et al. [29]

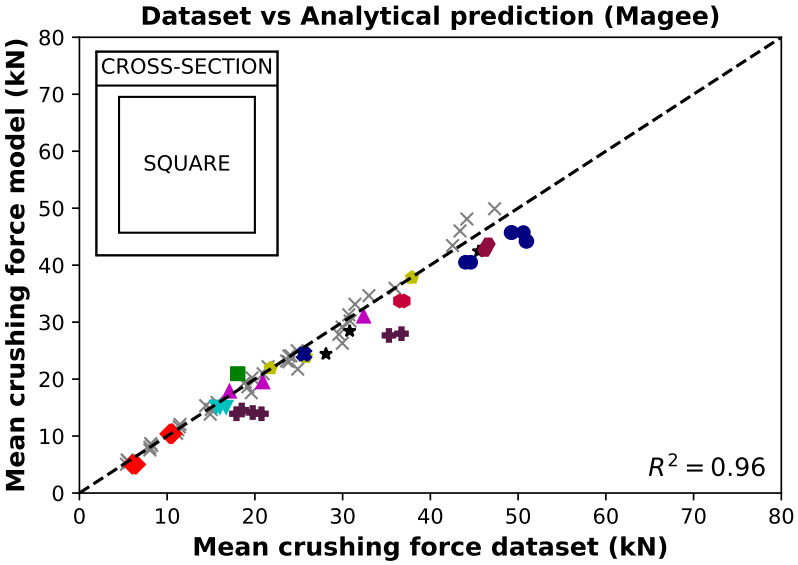

(a)

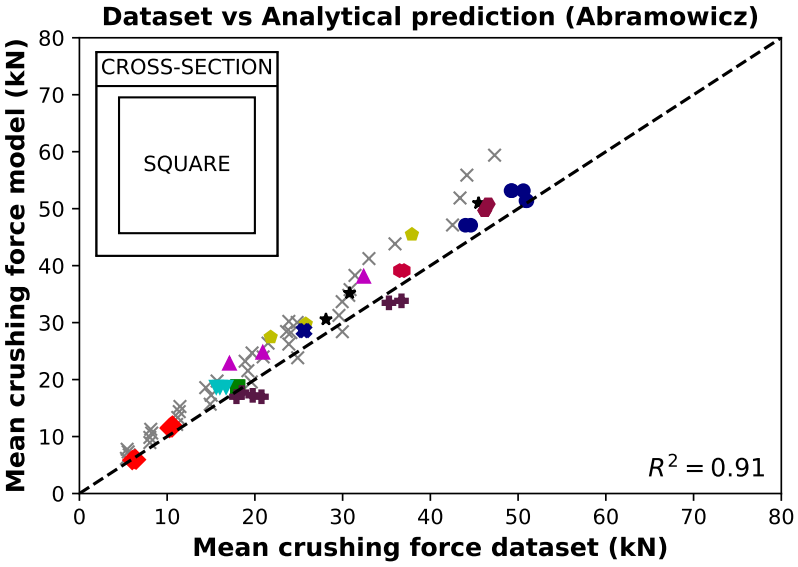

(b)

Figure 2.11.: Comparison between analytical models and dataset for square tubular structures: (a) Magee and Thornton [23], (b) Abramowicz et al. [25] and (c) Tabacu et al. [29] – **continued on next page**

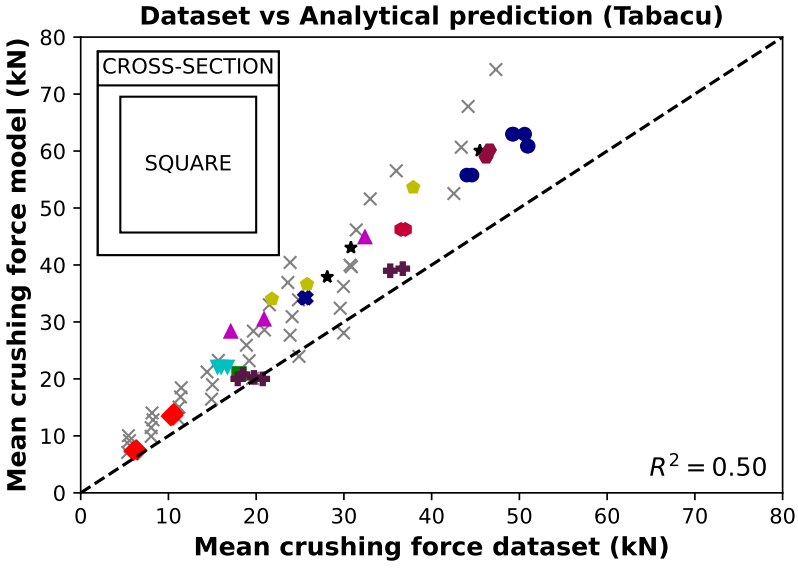

(c)

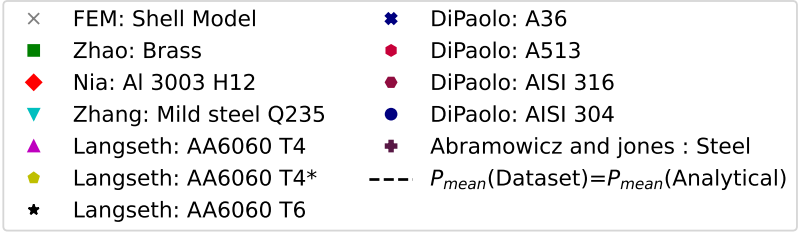

Figure 2.11.: Comparison between analytical models and dataset for square tubular structures: (a) Magee and Thornton [23], (b) Abramowicz et al. [25] and (c) Tabacu et al. [29]

2.7.3. Inextensional crushing of hexagonal tubular structures

For hexagonal tubular structures, the model from Abramowicz et al. (Eq. 2.19) for multi-corner sheet metal columns, the model from Zhang and Zhang (Eq. 2.31) for angle elements, and the model from Tabacu et al. (Eq. 2.30), are used in the comparison.The model from Zhang and Zhang shows reasonable agreement with the inextensional mean crushing force dataset ($R^2 = 0.86$), however, the model from Abramowicz et al. overpredicts the mean crushing force by a very large margin ($R^2 = -0.29$). The negative value indicates that the model produces a larger squared prediction error than a constant prediction based on the mean of the reference dataset; it does not imply a negative physical correlation. The results obtained are presented in Figures 2.12a and 2.12b.

Interestingly, the extensional crushing model from Tabacu et al. also shows reasonable agreement with the inextensional mean crushing force dataset ($R^2 = 0.86$), which seems to be in line with Abramowicz et al.'s observation that the extensional crushing becomes the dominant mode for quasi inextensional crushing of obtuse angle elements (Fig. 2.12c).

2.7.4. Inextensional crushing of octagonal tubular structures

Again, the models from Abramowicz et al. (Eq. 2.21), the model from Zhang and Zhang (Eq. 2.31) for angle elements and the model from Tabacu et al. (Eq. 2.30) are compared against experimental/numerical database. As in the case of hexagonal tubular structures, the model from Abramowicz et al. significantly overestimates the mean crushing force ($R^2 = -0.41$).The negative value indicates that the model produces a larger squared prediction error than a constant prediction based on the mean of the reference dataset; it does not imply a negative physical correlation. The model from Zhang and Zhang also over-predicts the mean crushing force, although by a much smaller margin as compared to the model from Abramowicz et al. ($R^2 = 0.90$). The results for these two cases are presented in Figures 2.13a and 2.13b.

The extensional crushing model from Tabacu et al. also shows very good agreement with inextensional mean crushing force dataset for octagonal tubular structures (Fig. 2.13c), with R^2 of 0.98.

2.7.5. Extensional crushing of hexagonal and octagonal tubular structures

The dataset for extensional crushing for hexagonal and octagonal tubular structures was compared against the model from Tabacu et al. (Eq. 2.30). The results are presented in Fig. 2.14a and 2.14b, for both the cases the model from Tabacu et al. was shown to have a good accuracy with an R^2 of 0.99 for hexagonal tubular structures and an R^2 of 0.93 for octagonal tubular structures.

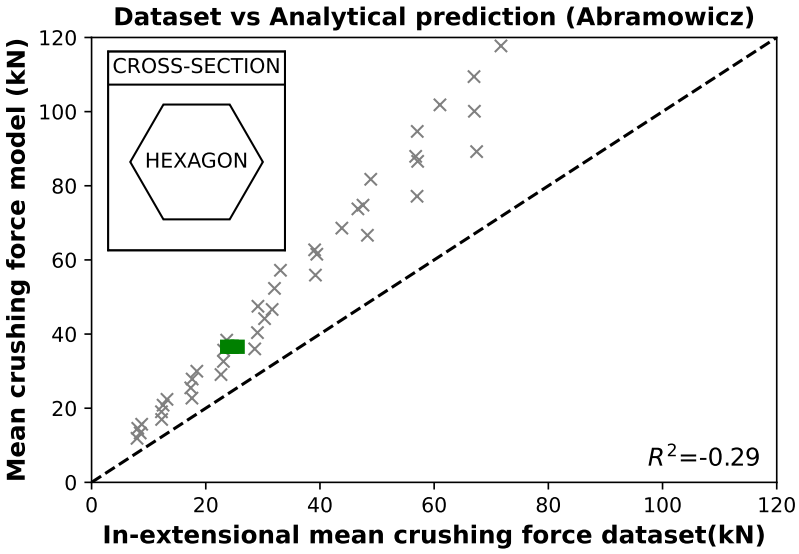

(a)

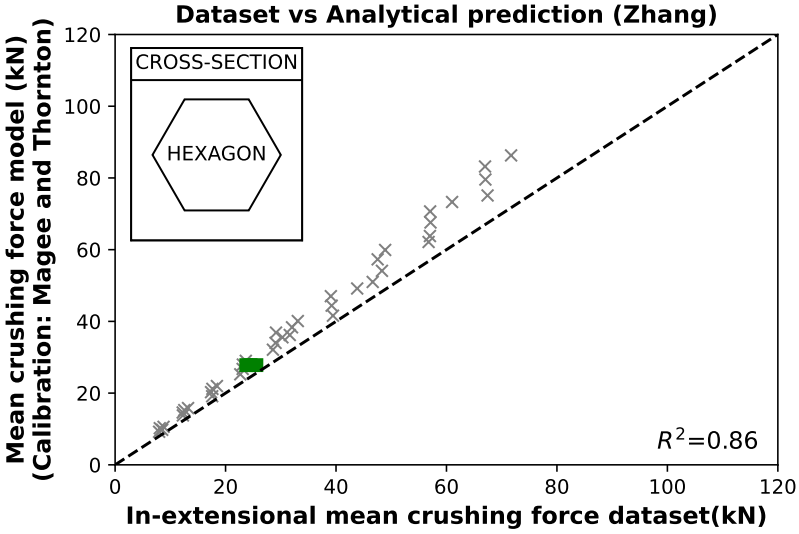

(b)

Figure 2.12.: Comparison between analytical models and dataset for hexagonal tubular structures: (a) Abramowicz et al. [26], (b) Zhang and Zhang [42] and (c) Tabacu et al. [29] – **continued on next page**

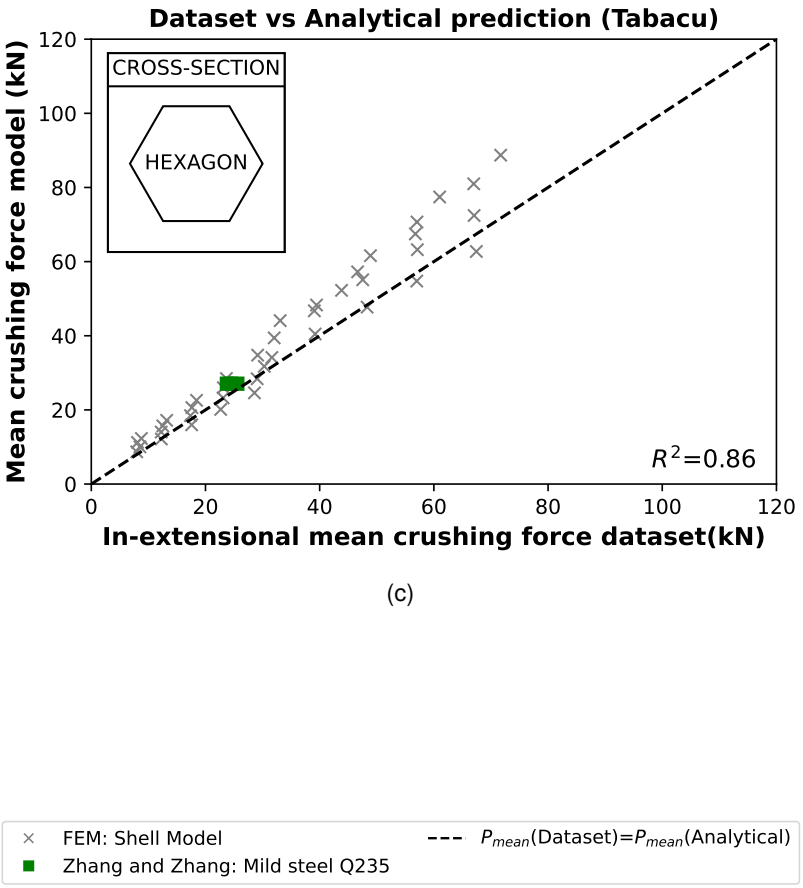

(c)

Figure 2.12.: Comparison between analytical models and dataset for hexagonal tubular structures: (a) Abramowicz et al. [26], (b) Zhang and Zhang [42] and (c) Tabacu et al. [29]

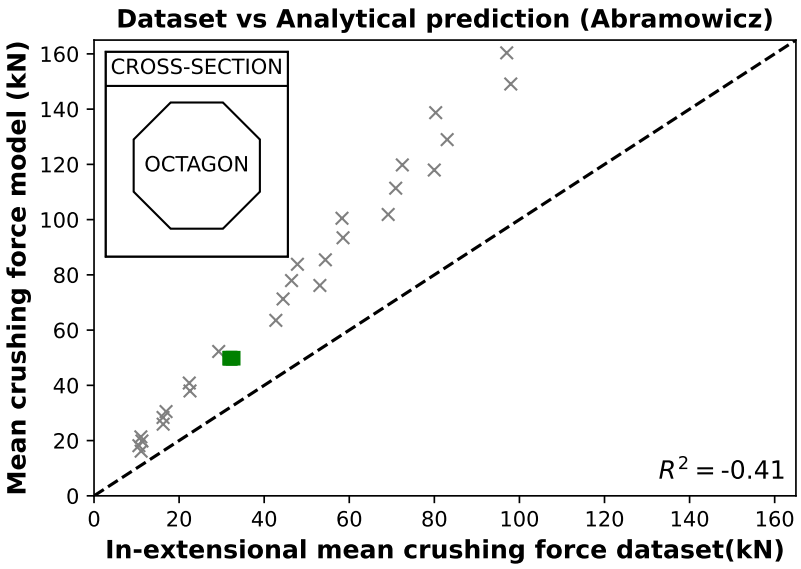

(a)

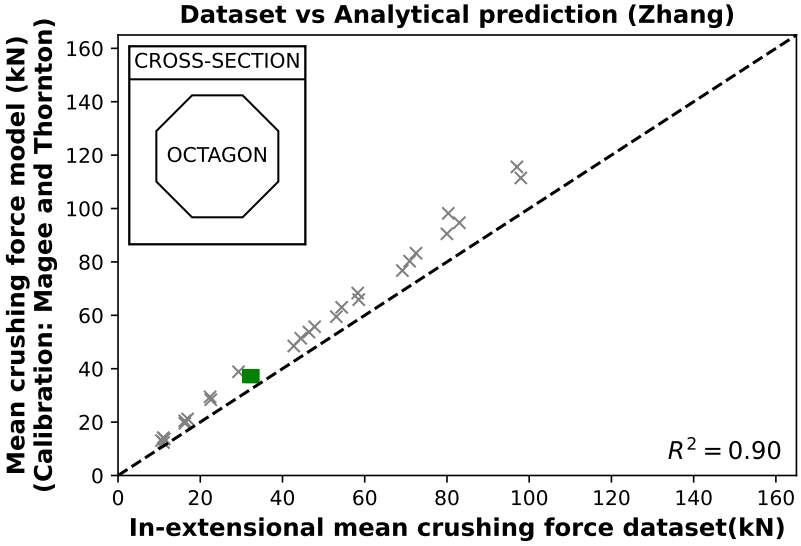

(b)

Figure 2.13.: Comparison between analytical models and dataset for octagonal tubular structures: (a) Abramowicz et al. [26], (b) Zhang and Zhang [42], (c) Tabacu et al. [29] – **continued on next page**

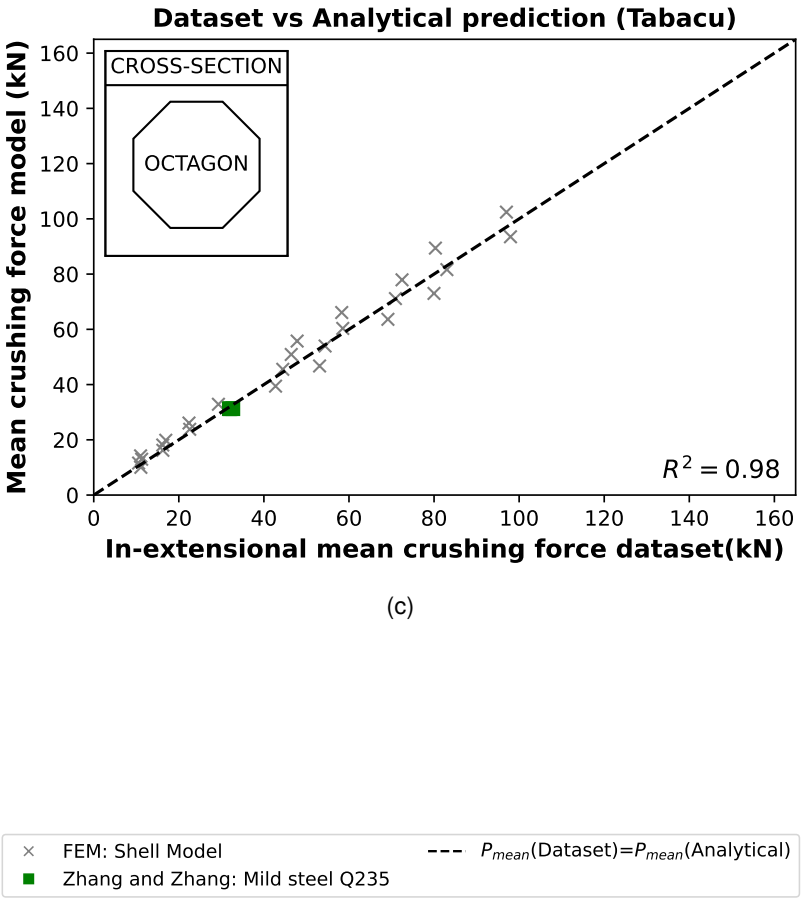

(c)

Figure 2.13.: Comparison between analytical models and dataset for octagonal tubular structures: (a) Abramowicz et al. [26], (b) Zhang and Zhang [42], (c) Tabacu et al. [29].

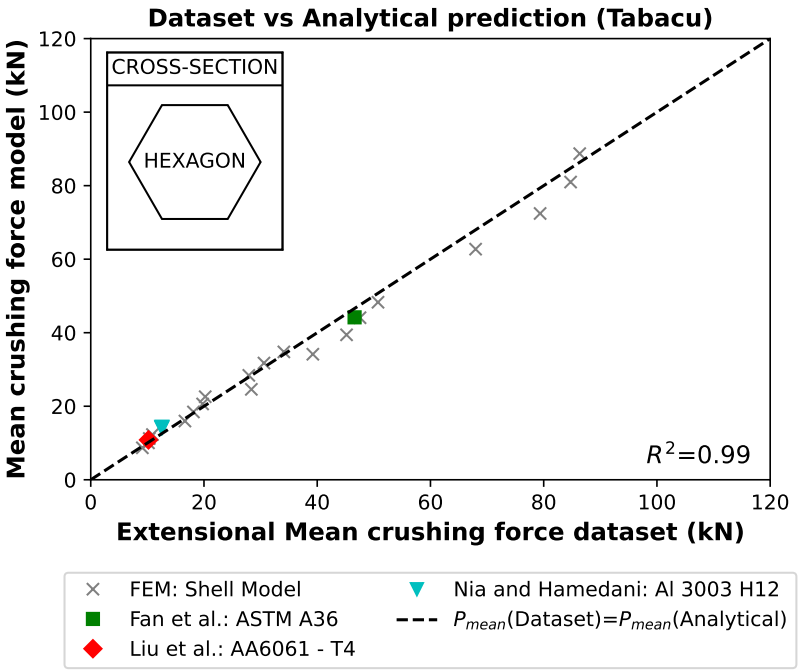

(a)

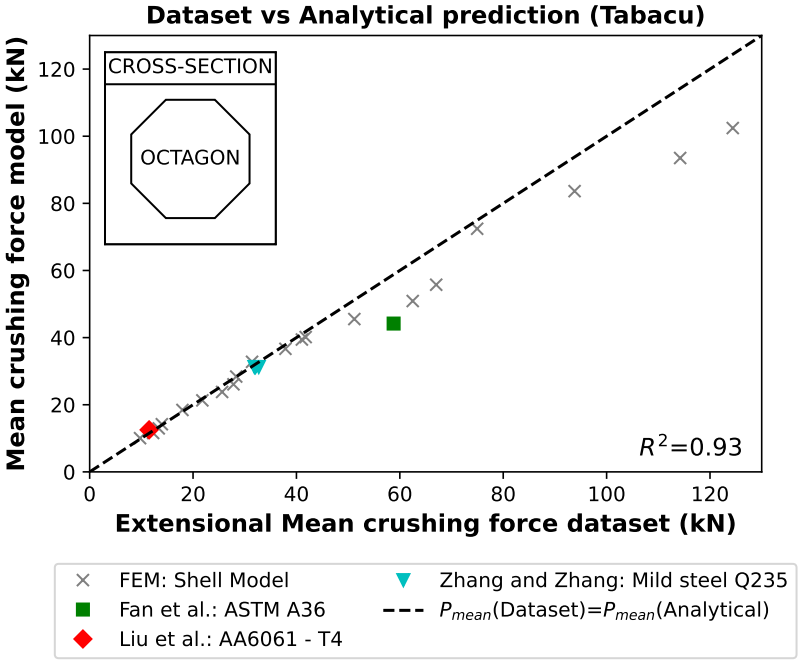

(b)

Figure 2.14.: Comparison between analytical model from Tabacu et al. [29] and extensional mean crushing force dataset for (a) Hexagonal tubular structures and (b) Octagonal tubular structures

2.8. Modification to the model from Abramowicz et al. [26]

As seen in section 2.7, the superfolding element model from Abramowicz et al. over-predicts by a very large margin for both hexagonal and octagonal tubular structures. In this section, we propose a slightly altered set of equations to better estimate the mean crushing force. The main equation for the model remains the same (Eq. 2.18):

$$\frac{P_m \cdot \delta_{eff}}{M_0 \cdot 2H} = A_1 \frac{b}{h} + (A_2 + A_5)\frac{c}{H} + A_3 \frac{H}{b} + A_4 \frac{H}{h} + A_6 \tag{2.37}$$

where:
$A_1 = 8 \cdot I_1(\psi_0, \overline{\alpha})$
$A_2 + A_5 = 2 \cdot \alpha_f$, where $\alpha_f = \frac{\pi}{2}$
$A_3 = 2 \cdot I_3(\psi_0, \overline{\alpha})$
$A_4 = 4 \cdot I_4(\psi_0, \overline{\alpha})$
$A_6 = I_6(\psi_0, \overline{\alpha})$

Integral $I_1(\psi_0, \overline{\alpha})$ comes from Weirzbicki and Abramowicz [71], the limits are changed from $(0 \rightarrow \pi/2)$ to $\left(0 \rightarrow \overline{\alpha}\right)$:

$$I_1(\alpha_m, \psi_0) = \frac{\pi}{\pi - 2\psi_0} \int_0^{\overline{\alpha}} \cos(\alpha) \left\{ \sin(\psi_0) \sin\left(\frac{\pi - 2\psi_0}{\pi}\beta\right) + \cos(\psi_0)\left[1 - \cos\left(\frac{\pi - 2\psi_0}{\pi}\beta\right)\right]\right\} d\alpha \tag{2.38}$$

where: $\beta = tan^{-1}\left\{\frac{tan(\alpha)}{sin(\psi_0)}\right\}$

Integral I_3 in the original model is calculated by multiplying the rate of rotation $\dot{\omega}$ with the length of the inclined hinge line $l = 2H/sin(\gamma)$, where γ is related to α and ψ_0 by the relation:.

$$\gamma = tan^{-1}\left\{\frac{tan(\psi_0)}{sin(\alpha)}\right\} \tag{2.39}$$

The term $\dot{\omega}$ is related to the tangential velocity (V_t) and radius of toroid (b) as:

$$\dot{\omega} = \frac{V_t}{b} \tag{2.40}$$

where V_t is computed as the rate of change of length of line BD (Fig. 2.15), and is given by the expression:

$$V_t = \frac{H \cdot cos(\alpha)}{tan(\psi_0)} \cdot \dot{\alpha} \tag{2.41}$$

Subsequently the equation for the rate of change of energy, $\dot{E_3}$ is obtained by

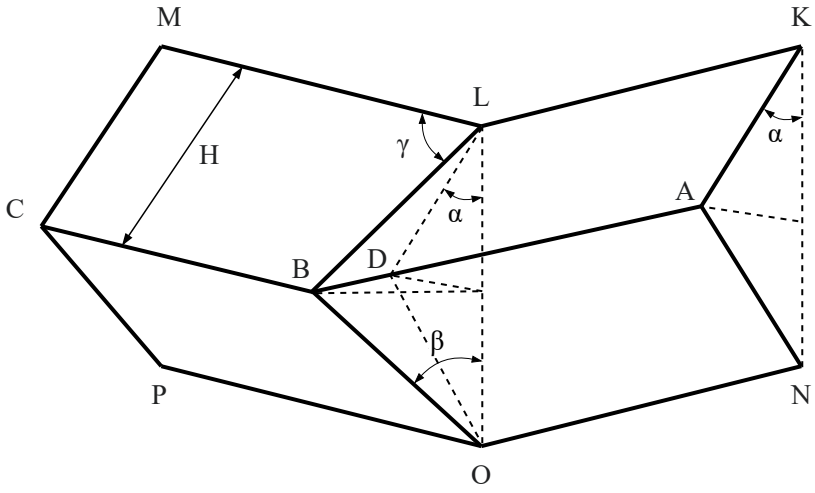

Figure 2.15.: Superfolding element proposed by Abramowicz et al. [26] (Phase-I)

substituting the values of l and $\dot{\omega}$ into the equation:

$$\dot{E_3} = 2 \cdot M_0 \cdot l \cdot \dot{\omega} = \frac{4 \cdot M_0 \cdot H^2 \cdot cos(\alpha)}{b \cdot sin(\gamma) \cdot tan(\psi_0)} \cdot \dot{\alpha} \tag{2.42}$$

However, it is interesting to note here that the velocity is assumed to be constant all along the inclined hinge lines. Instead of making this assumption, it is possible to express the rate of energy in terms of the rate of change of area of the triangles LBD and OBD (Fig. 2.15).

$$\dot{E_3} = 2 \cdot M_0 \cdot \frac{dS}{b} \tag{2.43}$$

Since the length of LD and OD remain constant, dS can be expressed in terms of the rate of change of BD, which leads to the expression:

$$\dot{E_3} = \frac{2 \cdot M_0 \cdot H^2 \cdot cos(\alpha)}{b \cdot tan(\psi_0)} \cdot d\alpha \tag{2.44}$$

and E_3 can then be written as:

$$E_3 = \frac{4 \cdot M_0 \cdot H^2}{b} \cdot I_3(\psi_0, \overline{\alpha}) \tag{2.45}$$

where integral I_3 is:

$$I_3(\psi_0, \overline{\alpha}) = \frac{1}{2} \int_0^{\overline{\alpha}} \frac{cos(\alpha)}{tan(\psi_0)} \cdot d\alpha \tag{2.46}$$

The expressions for integrals I_4 and I_6 remain the same as in the work of Abramowicz et al. [26]:

$$I_4(\psi_0, \overline{\alpha}) = \int_{\overline{\alpha}}^{\alpha_f} \frac{\sin\overline{\alpha}\tan\psi_0 \sin 2\alpha}{2\left(\sin^2\overline{\alpha} + \tan^2\psi_0 \sin^2\alpha\right)} d\alpha + \int_{\overline{\alpha}}^{\alpha_f} \left[\tan^{-1}\left(\frac{\sin\alpha\tan\psi_0}{\sin\overline{\alpha}}\right) - \psi_0\right]\cos\alpha\, d\alpha \tag{2.47}$$

$$I_6(\psi_0, \overline{\alpha}) = \frac{2}{tan\psi_0}\int_{\overline{\alpha}}^{\alpha_f} \frac{sin\overline{\alpha}(sin^2\overline{\alpha} + tan^2\psi_0)}{sin^2\overline{\alpha} + tan^2\psi_0 sin^2\alpha} \cdot d\alpha \tag{2.48}$$

Using the integrals above and following the procedure presented by Abramowicz et al. [26], we obtained the following equations for Hexagonal and Octagonal tubular structures:

$$\text{Hexagon}: \frac{P_m}{M_0}\cdot\kappa = 50.72\left(\frac{c}{h}\right)^{0.36} \tag{2.49}$$

$$\text{Octagon}: \frac{P_m}{M_0}\cdot\kappa = 71.43\left(\frac{c}{h}\right)^{0.36} \tag{2.50}$$

Equations 2.49 and 2.50 result in a significant decrease in over-prediction. The new equation results in much more reasonable predictions of mean crushing force for hexagonal tubular structures (Fig. 2.16a). However, the model still significantly overestimates the mean crushing force for octagonal tubular structures (Fig. 2.16b).

2.9. Tabacu et al.'s model [29] for circular structures

For the purposes of the present work, the model from Tabacu et al. is very desirable due to its ability to handle various types of cross-sectional shapes. However, we observed an under-prediction for the case of circular tubular structures, a slight modification which improves the prediction is presented in this section.

For circular tubular structures, Tabacu et al. [29] propose using Eq. 2.27 with a high value of N_c ($N_c \approx 999$) which leads to Eq. 2.29. From the results presented in Figure 2.10e, we can observe that Eq. 2.29 slightly underpredicts the mean crushing force. Tabacu et al. derive the equation for mean crushing force using $\sigma_0 \cdot h^2/4$ as the value of fully plastic bending moment, M_0. While the value of $\sigma_0 \cdot h^2/4$ can be used for polygonal tubular structures, this value is not well suited for circular tubular structures because the geometry of circular tubular structures can be considered as an infinitely wide beam which leads to largely plane strain and incompressible conditions, as observed by Alexander [22]. Under such conditions, if Von-Mises criterion is used the stress will be raised to $2/\sqrt{3}\sigma_0$ and subsequently M_0 is given by the equation:

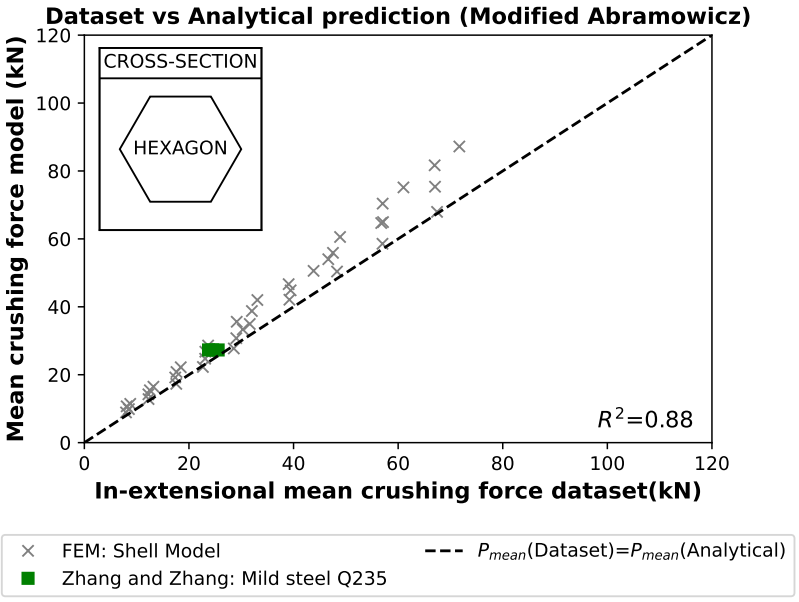

(a)

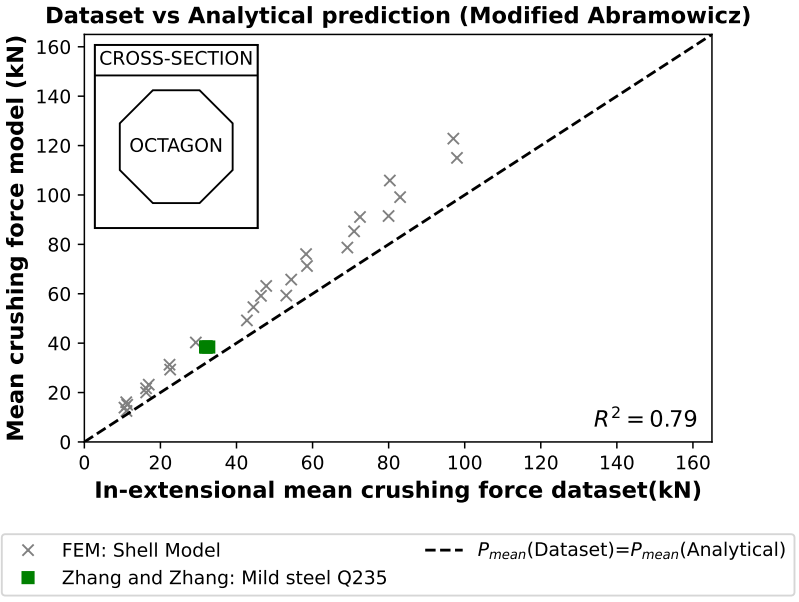

(b)

Figure 2.16.: (a) Comparison of model from Abramowicz et al. [26] (Modified) for hexagonal tubular structures; (b) Comparison of model from Abramowicz et al. [26] (Modified) for octagonal tubular structures

$$M_0 = \frac{2}{\sqrt{3}} \cdot \frac{\sigma_0 \cdot h^2}{4} \tag{2.51}$$

Taking this value of M_0 into account, and following the procedure presented by Tabacu et al. [29], the bending energy takes the form:

$$E_b = 4\pi^2 R M_0 \tag{2.52}$$

while the membrane energy takes the form:

$$E_m = \frac{4\sqrt{3}\pi H^2 M_0}{h} \tag{2.53}$$

The mean force is then given by the equation:

$$\frac{P_m}{M_0} \cdot \kappa = \frac{2\pi^2 R}{H} + \frac{2\sqrt{3}\pi H}{h} \tag{2.54}$$

Finally, minimizing with respect to H to obtain the value of H and then substituting it back into Eq. 2.54, we obtain the equation for mean force:

$$P_m \cdot \kappa = \frac{2 \cdot \sigma_0 \cdot \pi^{\frac{3}{2}} \cdot h^{\frac{3}{2}} R^{\frac{1}{2}}}{3^{\frac{1}{4}}} \tag{2.55}$$

Equation 2.55 led to an improvement in the correlation between the analytically obtained mean crushing force and the dataset, as illustrated in Figure 2.17, where R^2 increases from 0.91 to 0.94.

2.10. Calibration of Zhang and Zhang's model [42] with our dataset

In their work Zhang and Zhang [42, 43] gave a general expression of the inextensional membrane energy for a corner element with enclosed angle θ and corner element edge length B:

$$E_m(\theta) = \frac{2 \cdot M_0 \cdot H^2 \cdot tan\left(\frac{\theta}{2}\right)}{0.082 \cdot h \cdot \left(\frac{B}{h}\right)^{0.6} \cdot \left(tan\left(\frac{\theta}{2}\right) + \frac{0.06}{tan\left(\frac{\theta}{2}\right)}\right)} \tag{2.56}$$

Equation 2.56 for membrane energy is derived by assuming an equation for rolling radius, P_{mean} for an angle element is then expressed in the form:

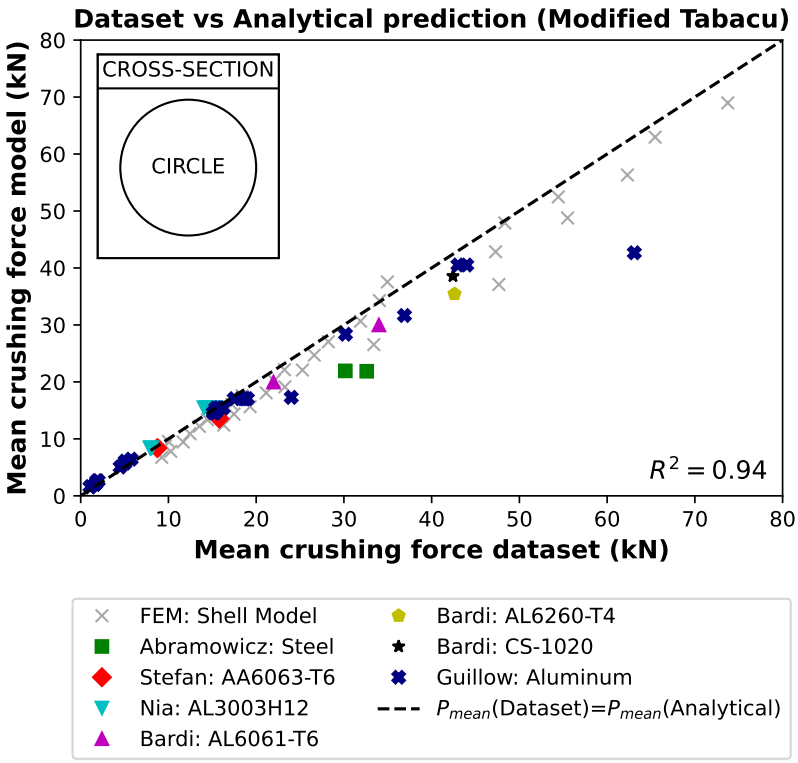

Figure 2.17.: Comparison of the modified Tabacu's model [29] for circular tubular structures.

$$P_m = \frac{\sigma_0}{2 \cdot \kappa} \cdot (B)^{0.5} \cdot h^2 \cdot \sqrt{\frac{2\pi \cdot tan(\theta/2)}{a_1 \cdot B^{a_2} \cdot h^{1-a_2}(tan(\theta/2) + a_3/tan(\theta/2))}} \tag{2.57}$$

The unknowns of Eq. 2.57 are then calculated by calibrating Eq. 2.57 to be equivalent to a quarter of Eq. 2.16, from Magee and Thornton [23] for square tubular structures:

$$P_m = \frac{\sigma_0}{2 \cdot \kappa} \cdot (B)^{0.2} \cdot h^{1.8} \cdot \sqrt{\frac{2\pi \cdot tan(\theta/2)}{0.082(tan(\theta/2) + 0.06/tan(\theta/2))}} \tag{2.58}$$

In the course of our investigation, we determined that, for $\theta = 90°$ and $\kappa = 0.73$, the value of a_1 must be 0.116 to ensure equivalence between Eq. 2.58 and Eq. 2.16. Nevertheless, as the precise methodology used to determine $a_1 = 0.082$

has not been detailed, we kept the value $a_1 = 0.082$ for subsequent calculations. Putting $\theta = \pi/2$ in equation 2.58, replacing B with $c/2$, where c is the edge length of the square tubular structure and multiplying by $N_c = 4$, we get:

$$P_m = \frac{14.80}{\kappa} \cdot \sigma_0 \cdot c^{0.2} \cdot h^{1.8} \tag{2.59}$$

Since the procedure followed by Tabacu et al. and Zhang and Zhang are identical, substituting the expression for the inextensional membrane energy (2.56) in place of the extensional membrane energy in the model from Tabacu et al., will also lead to Eq. 2.59. Using this equation from Zhang and Zhang, results in a good fit with experimental/numerical data with an R^2 of 0.92. The results using Eq. 2.59 are presented in Figure 2.18.

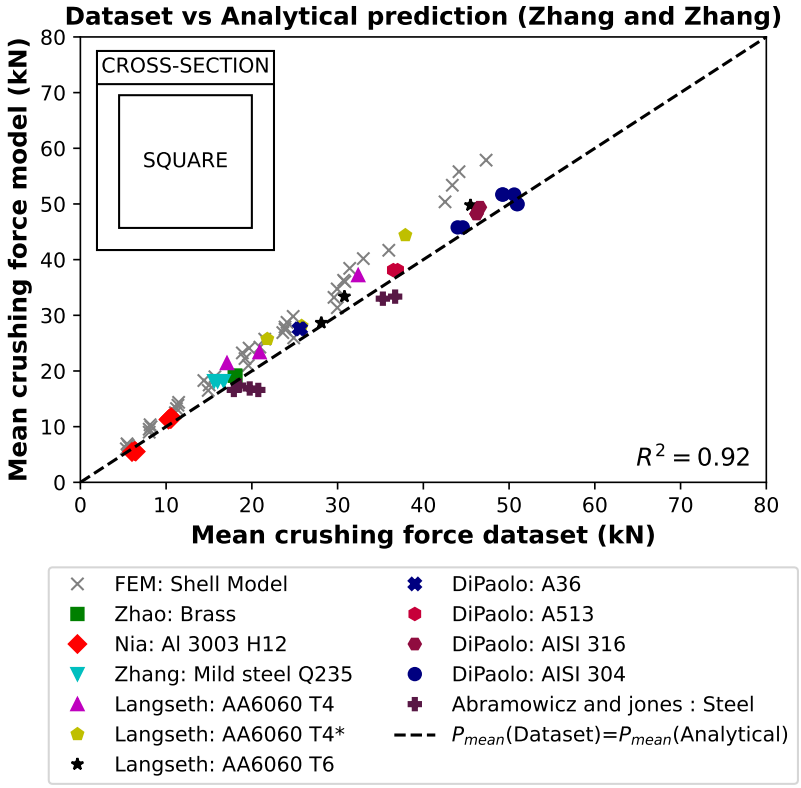

Figure 2.18.: Comparison of the Zhang and Zhang's model [42] for square tubular structures.

As mentioned in sub-section 2.7.2, the empirical model from Magee and Thornton [23] slightly underpredicts the mean crushing force for our dataset. The empirical relation by Magee and Thornton was obtained by fitting a power law to the

experimental data. Since our dataset is larger than the one used by Magee and Thornton, it is interesting to obtain an empirical equation based on our dataset. The following expression, relating the mean crushing force to the c/h ratio, is utilized for the curve fitting:

$$\frac{P_m}{M_0} \cdot \kappa = a \cdot \left(\frac{c}{h}\right)^b \tag{2.60}$$

Assuming a constant effective crushing length of $\kappa = 0.73$, the equation from Magee and Thornton can also be transformed to a similar form:

$$\frac{P_m}{M_0} \cdot \kappa = 49.64 \cdot \left(\frac{c}{h}\right)^{0.2} \tag{2.61}$$

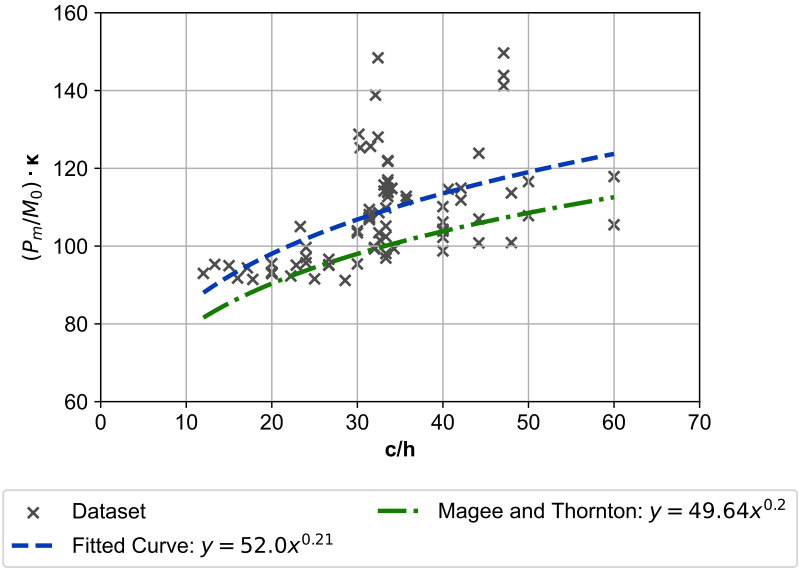

Figure 2.19.: Curve fit for our dataset using Eq. 2.60.

Figure 2.19 illustrates the curve fit obtained for our dataset, the equation from Magee and Thornton is also plotted for comparison. From the curve fitting, the parameters a and b were determined to be 52.00 and 0.21 respectively, which indicates a slightly greater sensitivity of the mean crushing force to the edge length for a square tubular structure. Rewriting Eq. 2.60 based on the obtained values of a and b:

$$\frac{P_m}{M_0} \cdot \kappa = 52 \cdot \left(\frac{c}{h}\right)^{0.21} \tag{2.62}$$

It is also of interest to use this new expression of Eq. 2.62 to calibrate the model

from Zhang and Zhang (Eq. 2.57), aiming to obtain an expression for inextensional crushing of angle elements. Following the procedure given by Zhang and Zhang [42], the following equation for an angle element is obtained:

$$P_m = \frac{\sigma_0}{2\kappa} \cdot B^{0.21} \cdot h^{1.79} \cdot \sqrt{\frac{2\pi \cdot tan(\theta/2)}{0.105(tan(\theta/2) + 0.06/tan(\theta/2))}} \tag{2.63}$$

Using the material data from [63], a value of 146 MPa for σ_0 is obtained using Eq. 2.6. Figure 2.20 presents a comparison between the numerical results from Zhang and Zhang (Table 1 in [42]) with the results obtained using Eq. 2.63. For comparison, the results obtained using Eq. 2.59 are also plotted, for this equation $\sigma_0 = 106$MPa is retained from the original work. After calibration with our dataset, an even better correlation is observed between the numerical and analytical values, with R^2 increasing from 0.987 for calibration using Magee and Thornton's dataset to 0.988 for calibration using our dataset. The R^2 value, when only considering elements with $\theta = 90°$, also increases from 0.986 to 0.992.

Further, this new expression based on Zhang and Zhang's model 2.63 can be used to estimate the mean crushing force for inextensional crushing of hexagonal and octagonal tubular structures (Fig. 2.21a and Fig. 2.21b). For hexagonal tubular structures, the R^2 value increased from 0.86 to 0.97 and for the octagonal tubular structures, the R^2 value increased from 0.90 to 0.98.

2.11. Generalized mean crushing force expression for axial crushing of metallic tubular structures

Based on the results presented in the previous sections, we find that the following models demonstrate a good agreement with the experimental/numerical mean crushing force dataset and can also be rewritten in a simpler form:

1. Model from Tabacu et al. with modified M_0 for circular tubular structures, further simplifying Eq. 2.55:

$$\frac{P_m}{M_0} \cdot \kappa = 33.85 \cdot N_c^0 \cdot \left(\frac{R}{h}\right)^{0.5} \tag{2.64}$$

   The N_c term is added to maintain similarity with the other two models presented in this section.

2. Model from Tabacu et al. for extensional crushing of polygonal tubular structures, further simplifying Eq. 2.30:

$$\frac{P_m}{M_0} \cdot \kappa = 12.56 \cdot N_c^{0.5} \cdot \left(\frac{c}{h}\right)^{0.5} \tag{2.65}$$

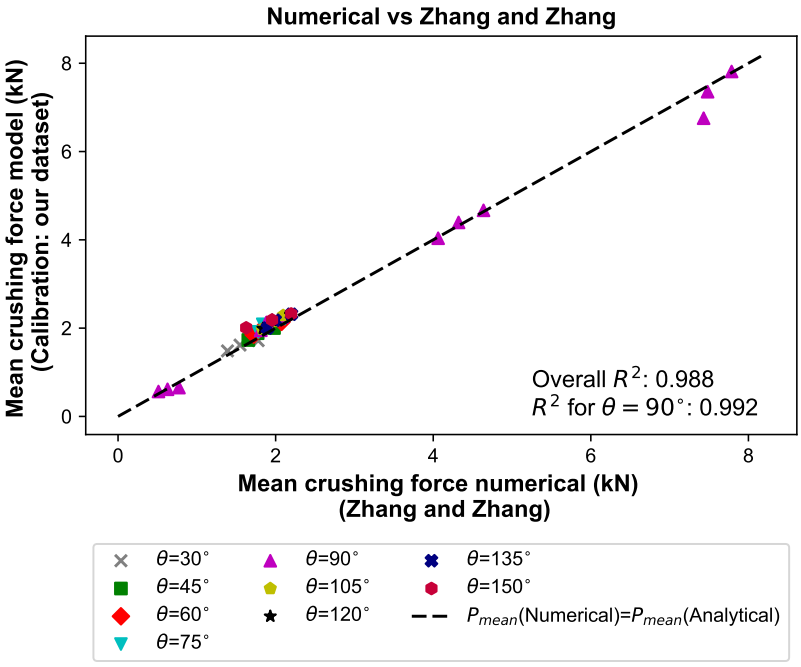

(a)

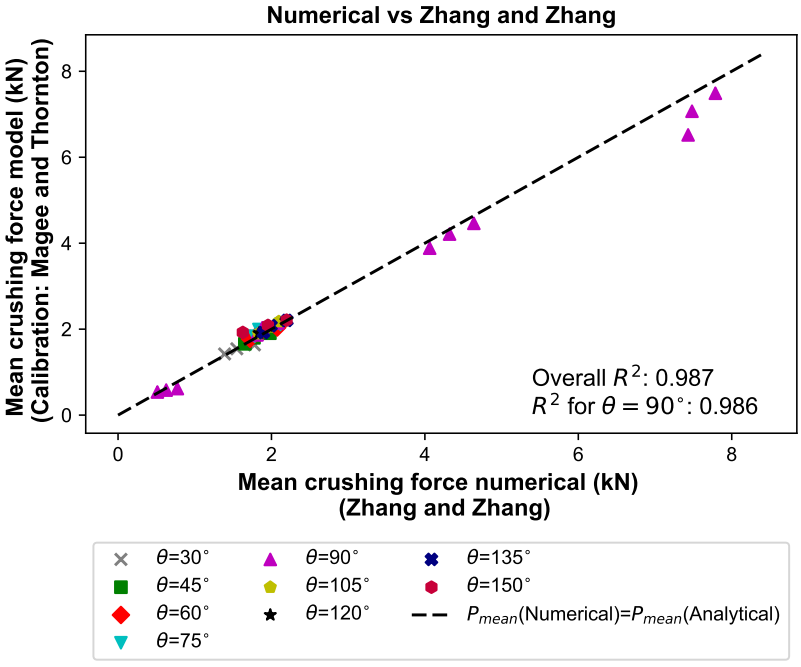

(b)

Figure 2.20.: Comparison of numerical (FEM results from Zhang and Zhang [42]) and analytical mean crushing force obtained using Zhang and Zhang's model calibrated with (a) Our dataset (b) Magee and Thornton's dataset

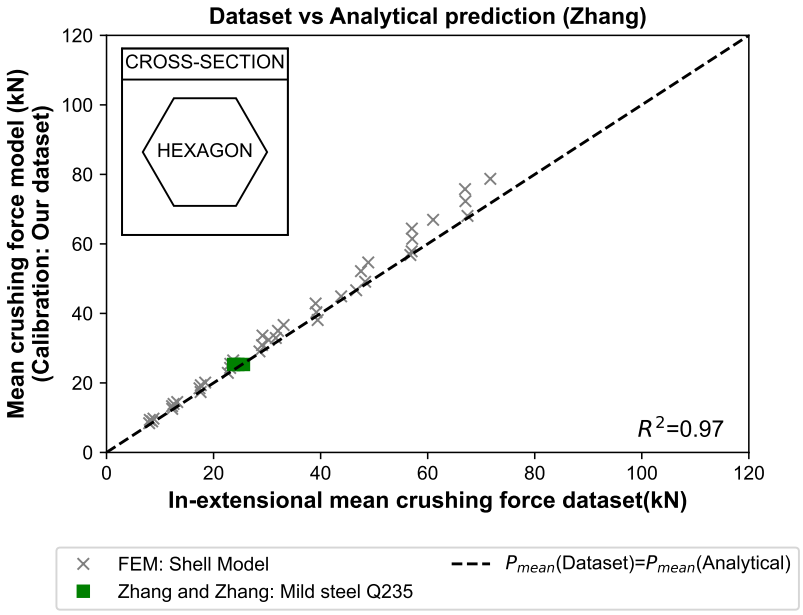

(a)

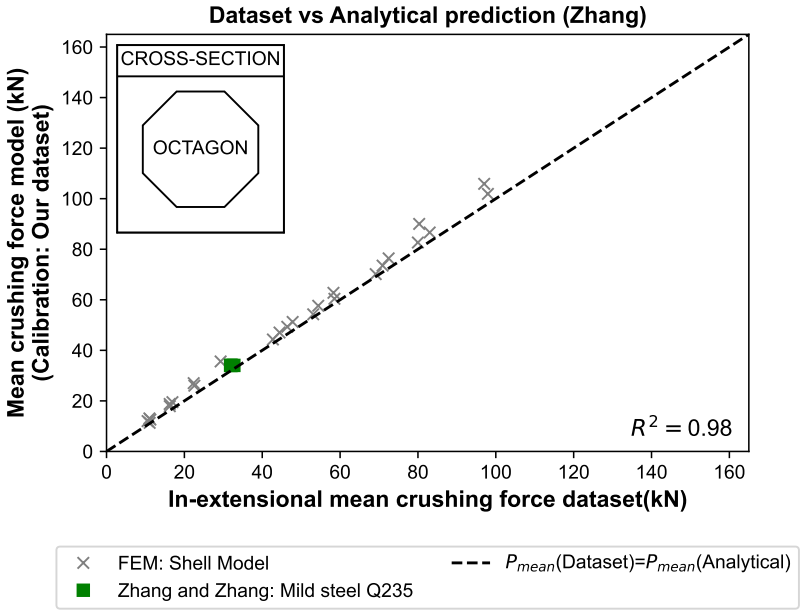

(b)

Figure 2.21.: Comparison of model from Zhang and Zhang [42] (calibrated with our dataset, Eq. 2.63) for (a) hexagonal tubular structures and (b) octagonal tubular structures

3. Model from Zhang and Zhang for inextensional crushing of polygonal tubular structures calibrated to our dataset (Eq. 2.63):

$$P_m = \frac{N_c \cdot \sigma_0}{2\kappa} \cdot B^{0.21} \cdot h^{1.79} \cdot \sqrt{\frac{2\pi \cdot tan(\theta/2)}{0.105(tan(\theta/2) + 0.06/tan(\theta/2))}} \quad (2.66)$$

Putting $B = c/2$, moving M_0 to the left side of the equation and further simplifying:

$$\frac{P_m}{M_0} \cdot \kappa = 13.37 \left(\frac{c}{h}\right)^{0.21} \cdot \sqrt{\frac{N_c^2 \cdot tan(\theta/2)}{(tan(\theta/2) + 0.06/tan(\theta/2))}} \quad (2.67)$$

The term under the root can be rewritten as a function of N_c, since the central angle θ is a function of N_c. For $4 \leq N_c \leq 8$, the term under the root can be approximated very accurately (mean absolute percentage error = 0.23%) by a power law of the form $i.N_c^j$, where i and j are unknowns:

$$\sqrt{\frac{N_c^2 \cdot tan(\theta/2)}{(tan(\theta/2) + 0.06/tan(\theta/2))}} \approx 0.94 \cdot N_c^{1.03} \quad (2.68)$$

The final equation then takes a form similar to Eq. 2.64 and 2.65:

$$\frac{P_m}{M_0} \cdot \kappa = 12.57 \cdot N_c^{1.03} \cdot \left(\frac{c}{h}\right)^{0.21} \quad (2.69)$$

Based on equations 2.64, 2.65 and 2.69, a general equation for mean crushing force of metallic tubular structures can be written in the form:

$$\frac{P_m}{M_0} \cdot \kappa = X \cdot N_c^Y \cdot \left(\frac{c}{h}\right)^Z \text{; c/h is replaced with R/h for circular tubular structures} \quad (2.70)$$

S.No.	Case	X	Y	Z
1	Circular	33.85	0	0.5
2	Polygon (Extensional crushing mode)	12.56	0.5	0.5
3	Polygon (Inextensional crushing mode)	12.57	1.03	0.21

Table 2.1.: Values of X, Y and Z for specific cases (Eq. 2.70)

where, X, Y and Z vary based on the shape and crushing mode of the tubular structures. This form is especially interesting for preliminary design where various geometries and materials must be compared. The values of X,Y and Z for different

cases have been presented in table 2.1. A very good agreement between the analytical mean crushing force and the mean crushing dataset (comprising of all cross-sections and both the crushing modes) was obtained ($R^2 = 0.97$), the comparison is presented in Fig. 2.22.

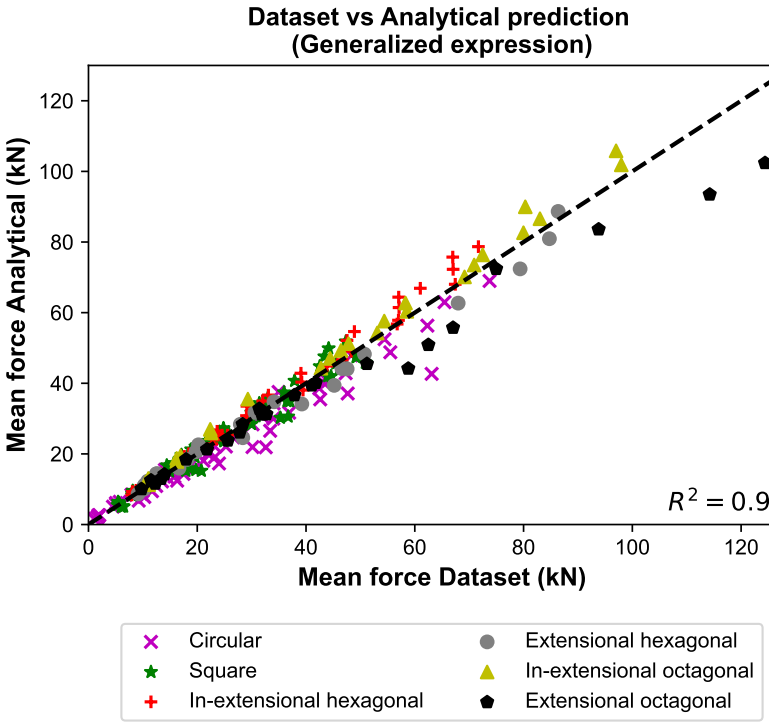

Figure 2.22.: Comparison between generalized expression for mean crushing force and mean crushing force dataset

2.12. Discussion

A summary indicating the average error of each model is provided in table 2.2. Additionally, to better comprehend the distribution of errors throughout the entire dataset, the Inter-Quartile Range (IQR) is also given for all the models. IQR is a valuable measure in this context as it quantifies the spread of the middle 50% of the errors, providing insight into the reliability of these predictions. From table 2.2, it can be noted that while the presented analytical models are a great way of quickly determining the mean crushing force, the spread of errors even for the best-fitting model is about 6%. Such models should therefore be used with caution, keeping the error ranges in mind.

For circular tubular structures, the model from Abramowicz et al. [24] was found

to be the most accurate with a R^2 value of 0.98. The models from Weirzbicki et al. [38] and Singace et al. [39] were found to have similar accuracy (R^2 of 0.95 and 0.94 respectively). An underestimation ($\overline{E} = 26.4\%$) of the mean force is observed for the model from Alexander [22] which stems from the absence of an effective crushing length parameter. Similarly, the model from Tabacu et al. [24] also underestimates the mean crushing force, and the accuracy of the model is significantly improved when the fully plastic bending moment (M_0) is multiplied by $2/\sqrt{3}$, to account for the largely plain strain conditions.

For square tubular structures, the models from Magee and Thornton [23], and Abramowicz et al. [25] both show good agreement with experimental/numerical dataset. The model from Zhang and Zhang [42] calibrated to the model from Magee and Thronton (Eq. 2.58) predicts the mean crushing force for polygonal tubular structures with R^2 value of 0.86 for hexagonal tubular structure and R^2 value of 0.9 for octagonal tubular structures. A calibration of Zhang and Zhang's model based on our dataset has also been proposed, which further improves the accuracy of Zhang and Zhang's model for polygonal tubular structures (R^2 (hexagonal) $= 0.97$ and R^2 (octagonal) $= 0.98$).

The quasi inextensional crushing model proposed by Abramowicz et al. for multicorner sheet metal columns (polygonal tubular structures) is found to overestimate the mean crushing force values by very large margins (hexagonal tubular structures: $\overline{E} = -53.5\%$ and octagonal tubular structures: $\overline{E} = -63.5\%$). The method attempts to model a mixed crushing mode using a timelike α and a switching point parameter $\overline{\alpha}$ by assuming that the crushing from $\alpha = 0$ to $\overline{\alpha}$ is inextensional while the crushing from $\overline{\alpha}$ to $\pi/2$ is extensional. Abramowicz's approach requires an accurate determination of the switching point parameter ($\overline{\alpha}$), which needs to be calculated alongside two other unknowns, namely: the radius of the torus b, and the crushing wavelength $2H$; and the model is very sensitive to slight changes of b or $2H$. In the present study, an attempt is made to correct the model by using the rate of change of area in place of the rate of plastic flow along the inclined hinge lines (section 2.8). The equations obtained from the modified set of integrals provide a much more reasonable estimate of the mean crushing force compared to the original model, however, the model still overestimates the mean crushing force. (hexagonal tubular structures: $\overline{E} = -14.6\%$ and octagonal tubular structures: $\overline{E} = -25.3\%$)

For hexagonal and octagonal tubular structures, the results from Tabacu et al.'s model [29] are found to be quite accurate for extensional crushing (for hexagonal tubular structures: $R^2 = 0.99$ and for octagonal tubular structures:$R^2 = 0.93$). For inextensional crushing of hexagonal and octagonal tubular structures, Zhang and Zhang's model [42] calibrated to our dataset (Eq. 2.63) predicted the mean crushing force with a better accuracy compared to other models ($R^2 = 0.95$ for hexagonal tubular structures and $R^2 = 0.97$ for octagonal tubular structures). The extensional crushing model from Tabacu et al. gives an R^2 of 0.86 for inextensional crushing of hexagonal tubular structures and 0.98 for inextensional crushing of octagonal tubular structures, reinforcing the observation made by Abramowicz et al. [26] that for quasi-inextensional crushing mode, the contribution of energy absorption due to

extension is more dominant for obtuse angle elements.

Finally, a generalized equation (Eq. 2.70) for axial crushing of tubular structures based on the models from Tabacu et al. (Eq. 2.55 and 2.30) and Zhang and Zhang (Eq. 2.63) is proposed which can be used to determine the mean crushing force for different cross-sectional shapes as well as crushing modes, demonstrating a high coefficient of determination (R^2) of 0.97, which underscores its predictive strength.

2.13. Conclusions

The purpose of this work was to identify and improve analytical models that can be employed to calculate the mean crushing force of metallic tubular structures, with the goal of reaching models that are fast and accurate to be applied in the preliminary design of structures taking crashworthiness into account. The existing and improved models were compared against experimental data from the literature, and numerical data generated with finite elements.

For circular tubular structures the model from Abramowicz et al. [24] demonstrates the best accuracy. The model from Tabacu et al. [29] in its original form consistently underestimates the P_{mean} for circular tubular structures. However, with the improvements herein proposed for circular tubular structures, the accuracy of the model is improved as evidenced by the improvement in the coefficient of determination (R^2) from 0.91 to 0.94, and a reduction in the average error ($\overline{E}$) from 9.9% to 3.5%. For inextensional crushing of square tubular structures, it is recommended to utilize the model proposed by Abramowicz et al. [25] (Eq. 2.17) or the model proposed by Zhang and Zhang [42] (Eq. 2.59 and 2.63). For inextensional crushing of polygonal tubular structures, the model from Zhang and Zhang calibrated to our dataset (Eq. 2.63) for square tubular structures gives the best overall accuracy (R^2 (hexagonal) $= 0.97$ and R^2 (octagonal) $= 0.98$). And for extensional collapse of polygonal tubular structures, the model from Tabacu et al. [29] gives an R^2 of 0.99 for hexagonal tubular structures and an R^2 of 0.93 for octagonal tubular structures.

The model for quasi inextensional crushing of polygonal tubular structures from Abramowicz et al. [26], along with the models derived using Abramowicz et al.'s model (Maalej et al. [28], Liu and Day [40, 41]), overestimated the mean crushing force by a large margin for both hexagonal and octagonal tubular structures ($\overline{E}$ (hexagon)=53.5% and $\overline{E}$ (octagon)=63.5%). An improvement was suggested to reduce the over-prediction, however, the model still overestimates the mean crushing force with an $\overline{E}$ of 14.6% for hexagonal tubular structures and 25.3% for octagonal tubular structures.

Based on the dataset of experimental results, we also observed that polygonal tubular structures with $N_c = 4$ have a tendency to crush in the inextensional crushing mode, while polygonal columns with $N_c \geq 8$ have a tendency to collapse in mixed or extensional collapse modes. It was also observed from the finite element results that as N_c approaches a value of 8, the tubular structures with $c/h \leq 30$ have a tendency to crush under extensional or mixed crushing mode, even when a type-I trigger (i.e. an inextensional trigger) is used. Therefore, for preliminary design,

Model	Equation	R^2	$\overline{E}$(%)	Interquartile range		
				Q_1	Q_3	Δ
Circular tubular structures						
Alexander	2.12	0.73	26.4	20.6	33.5	12.9
Abramowicz et al.	2.13	0.98	-4.9	-10.4	1.5	11.8
Wierzbicki et al.	2.14	0.95	3.9	-3.6	13.2	16.8
Singace et al.	2.15	0.94	6.5	1.3	13.3	11.9
Tabacu et al.	2.29	0.91	9.9	5	18	13.0
Modified Tabacu et al.	2.55	0.94	3.5	-0.9	12.2	13.1
Square tubular structures						
Magee and Thornton	2.16	0.96	4.5	-1.1	7.7	8.8
Abramowicz et al.	2.17	0.91	-13.0	-20.8	-6.1	14.8
Tabacu et al.	2.30	0.50	-32.9	-43.9	-21.3	22.6
Hexagonal tubular structures (Inextensional)						
Abramowicz et al.	2.19	-0.29	-53.5	-63.2	-44.4	18.8
Abramowicz et al. (Mod.)	2.49	0.88	-14.6	-21.3	-8.7	12.6
Zhang and Zhang (Magee and Thornton)	2.58	0.86	-16.9	-20.5	-12.3	8.2
Zhang and Zhang (Our Calibration)	2.63	0.97	-6.6	-9.8	-2.3	7.5
Tabacu et al. (Extensional model)	2.30	0.86	-13.6	-22.6	-5.3	17.3
Hexagonal tubular structures (Extensional)						
Tabacu et al.	2.30	0.99	-0.9	-8.0	5.1	13.1
Octagonal tubular structures (Inextensional)						
Abramowicz et al.	2.21	-0.41	-63.5	-72.7	-55.3	17.4
Abramowicz et al. (Mod.)	2.50	0.79	-25.3	-31.8	-19.4	12.4
Zhang and Zhang (Magee and Thornton)	2.58	0.90	-32.5	-22.3	-13.8	8.5
Zhang and Zhang (Our Calibration)	2.63	0.98	-8.52	-12.1	-4.0	8.1
Tabacu et al. (Extensional model)	2.30	0.98	-4.3	-11.7	2.6	14.3
Octagonal tubular structures (Extensional)						
Tabacu et al.	2.30	0.93	5.8	1.9	10.8	8.9

Table 2.2.: Coefficient of determination (R^2), Average error ($\overline{E}$) and Interquartile range for various analytical models

it can be considered that the crushing mode is inextensional for $N_c = 4$; however, for $N_c > 4$, both extensional and inextensional crushing modes need to be considered.

Based on the accuracy and similarity of some of these models (Eq. 2.55, 2.30 and 2.63), a generalized form for the crushing of metallic tubular structures is

also presented, which is shown to have a good accuracy for predicting the mean crushing force of circular and polygonal tubular structures ($R^2 = 0.97$).

The generalized model suggested for calculating the mean crushing force demonstrates high accuracy, evidenced by an R^2 value of 0.97. However, the coefficients applied for the inextensional crushing of polygonal tubular structures are derived from empirical calculations. Consequently, additional research is necessary to deepen the understanding of the inextensional crushing mechanism and enable the development of a mechanism-based approach for determining the mean crushing force for inextensional crushing of polygonal tubular structures.

3

Bending collapse of square and rectangular structures

For unconventional aircraft designs, accurate and computationally cheap methods are required to predict crashworthiness in early stages of the design process. In metallic fuselage sections, plastic bending is a key contributor to the overall energy absorption. This paper investigates plastic bending and bending collapse response of square and rectangular tubular structures. A review of the existing analytical models has been conducted. And subsequently, a semi-analytical model for use in early stages of the design process, based on a combination of spring-linkage method, Kecman model and a transition algorithm is presented. The framework was observed to be much faster (average ≈3 seconds for a given configuration) than finite element models. The proposed semi-analytical model has been verified against numerical simulations and the corresponding results are presented. A fast n-linear stress-strain curve based equation is also presented to predict $M - \theta$ response which can be used in the spring-linkage model for prediction of elastic deformation stage and elastic-plastic deformation stage.

This chapter is based on the paper titled "Crashworthiness in preliminary design: Semi-analytical modeling for bending collapse of square and rectangular tubular structures". The manuscript material has been revised and extended for inclusion in this thesis.

Nomenclature

a	Cross-section width
b	Cross-section height
t	Thickness of specimen
l_s	Span for 3-point bending tests
dx	Length of element in spring linkage model
θ	Rotation angle in 3-point bending tests
ε_{max}	Strain at farthest fiber from neutral axis
z_{max}	Distance of fiber farthest from the neutral axis
ρ	Radius of curvature
σ_{flow}	Flow stress
σ_y	Yield stress
σ_{cr}	Critical stress
F_{max}	Peak force

3.1. Introduction

Aviation is responsible for roughly 2.5% of the global carbon emissions [2]. Projected growth indicates that passenger traffic numbers will continue to rise in the coming years. According to Boeing commercial market outlook 2025 [3], Revenue Passenger Kilometers(RPKs) in 2044 is expected to more than double in 2044 as compared to 2024, corresponding to a compound annual growth rate (CAGR) of about 4.2% . This increased passenger demand will inevitably lead to an increase in the total number of flights per day. On the other hand CO_2 emissions per Revenue Passenger Kilometers (RPKs) reduced at a CAGR of 2.8% from the year 2000 to 2019 (RPKs (2000) = 3381 billion [4], RPKs (2019)=8913.4 billion [3], CO_2 emissions (2000) = 672.96 Mt [6] and CO_2 emissions (2019) = 1035.83 Mt [6]). More efficient aircraft designs and configurations are therefore necessary in order to reduce emissions. In this regard, blended wing body (BWB) aircraft have been proposed, with some estimates indicating up to a 20% reduction in fuel emissions compared with conventional twin-aisle passenger aircraft of a comparable role [8].

The fuselage structure of a passenger aircraft must be able to absorb the impact energy associated with a potentially survivable crash scenario in order to be certified for commercial operations. However, crashworthiness for BWB and similar aircraft designs poses several new challenges due to the ovalization of the fuselage structure that reduces the distance between the passenger floor and the ground, when compared to conventional aircraft of similar passenger capacity and role, leading to high accelerations for passengers already in case of vertical impact [72], and even more for the case of inclined impact attitudes [73]. Furthermore, there is no historical crash data, and energy absorbing structures for these configurations are not as well studied and documented as for conventional aircraft. For these reasons, fast-running models capable of predicting crash response of fuselage structures is a crucial need. During a crash scenario, metallic fuselage structures absorb energy through two main failure mechanisms: axial crushing and plastic

bending. This paper focuses on semi-analytical modeling of plastic bending, to achieve faster prediction of bending response.

A common low-fidelity approach to modeling plastic bending is the representation of the structure using rigid linkages connected using kinematic joints. The approach has been widely studied in literature. Nikravesh et al. [17] employed the plastic-hinge approach for vehicle crash simulation, representing localized bending deformation using revolute joints and torsional springs. The spring characteristics were obtained from experimental results and modified to account for the represented element length and dynamic effects. A model to study the bending forces on a bonding wire was proposed by Lo et al. [74, 75]. Sousa et al. [19] developed a vehicle crashworthiness model with help of kinematic joints, with the constitutive relationships derived via Finite Element Method (FEM). A multi-body modelling approach was proposed by Tay et al. [20] for crashworthiness modelling of a fuselage section, the model was shown to be in close agreement with numerical and experimental results. The frame sections in the model from Tay et al. were represented using a spring-linkage approach, with characteristic curves obtained from FEM simulations. A similar methodology was used by Schatrow et al. [21] for modelling the crash of composite fuselage sections. While these works reinforce the viability of using spring-linkage/multibody based methods for crashworthiness predictions in early stages of the design process, numerical simulations are still required to obtain the characteristic curves for the kinematic joints. This work, therefore focuses on developing a computationally cheap method for determining force-displacement response of square and rectangular tubular structures in bending, which can be used to inform multibody/spring-linkage based models.

The collapse behavior (M-θ) curve for any section generally consists of three stages: elastic deformation stage, plastic deformation stage and the collapse stage [76]. While the elastic deformation stage can be predicted using classical beam formulations like Euler-Bernoulli beam theory or Timoshenko beam theory [77], analytical prediction of elastic-plastic deformation stage and collapse phase are more challenging.

In their work dated 1979 and 1983, Kecman [1, 30] performed a study on the bending collapse mechanism for square hollow tubular structures to assess the energy absorption of roll-over and falling object protective structures and also proposed a theoretical bending collapse model relating the moment at plastic hinge with the associated rotation angle. In their work, Kecman proposed a collapse mechanism based on experimental observations and summed together the contribution of each plastic hinge towards the total energy absorbed. The theory from Kecman is semi-empirical as it uses an empirical relation for rolling radius based on experimental observations. Later in 1993, Wierzbicki et al. [31] with the aim of addressing the semi-empirical deficiency of Kecman model, extended the concept of Super-Folding Element (SFE) used in axial crushing to the concept of bending collapse and proposed a kinematically admissible model, deriving closed form solutions for moment-rotation characteristics.

In 2001, Kim and Reid [32] studied both the models from Kecman and Wierzbicki, highlighting the deficiencies in the two models and proposed an improvement

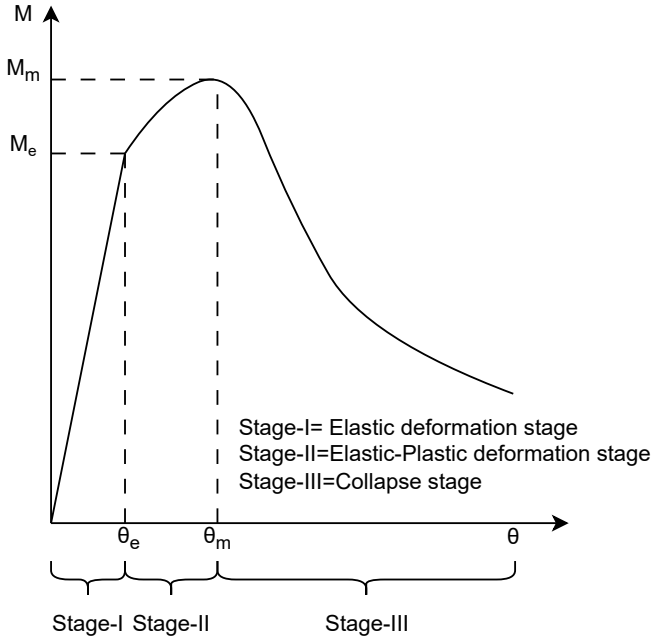

Figure 3.1.: General moment-rotation (θ) curve showing three stages of bending, adapted from [76]

on Kecman bending collapse model. In 2006, Liu and Day [78] proposed a theoretical bending collapse model based on the work of Wierzbicki et al. [31] to predict bending resistance of channel cross-sections, they also applied the derived resistance to simplified thin-walled channel beam model which they developed using a non-linear spring element along with a beam element. Later in 2008, Liu and Day [79] extended their method to thin-walled circular tubular structures. More recently, in their 2021 work Farfan et al. [76] proposed a curve fit based method to obtain input parameters which improve predictions using Kecman model.

While it is evident from the state of the art that multi-body/spring-linkage crashworthiness models have been studied in detail, multiple gaps still remain, especially when considering application of such models to aerospace structures in early stages of the design process:

1. Multiple modelling approaches for bending resistance exist, but most of them focus on steel specimens. Therefore it is important to compare the prediction of these models against a multi-material dataset (literature and numerical), consisting of both aluminum and steel specimens, to ascertain if they can be used to generate characteristic curves for a low fidelity model intended to be used in the preliminary design phase of aircraft.

2. The most recent update to the model from [76] relies on curve fitting of

parameters for collapse stage and a parabolic fit between M_e and M_m for elastic-plastic stage. Although the obtained results are in close agreement with numerical/experimental results, this is not ideal for early stages of design as it requires calibration from a numerical/experimental campaign.

3. Some of the most recent multi-body models in aircraft crash, such as the work of Tay et al. from 2019 [20], use FEM to generate the input Moment-Rotation curves. An analytical/semi-analytical approach can help create automated design space exploration pipelines.

4. Analytical models in the literature deal specifically with the bending collapse phase and do not present a modelling method for the elastic and elastic-plastic deformation stages except the model from Farfan et al. [76].

This paper aims to address these gaps, first by comparing the various models for bending resistance against each other, and subsequently providing a semi-analytical model that can produce reasonable force-displacement curves using material stress-strain response curve as the sole input.

3.2. Analytical models for bending collapse of square and rectangular tubular structures

This section provides an overview of some of the bending collapse models available in the literature. Python based implementation of all of these models has been made available [80].

3.2.1. Analytical model from Kecman

Kecman [1, 30] observed the bending collapse in rectangular tubes across 27 different sections through experiments and divided the bending collapse into four distinct phases: the initial phase where a bulge forms in the webs but there is no rolling deformation, second phase with rolling along hinge lines, third phase with "jamming" of rolling with subsequent creation of a secondary hinge and fourth phase being the development of secondary hinge. Kecman further observed that each collapse phase displays a different mechanism. The first mechanism (which lasts for the initial 5-10°) is obtained by joining the point of maximum strength to a point on the bending collapse curve such that the joining line becomes a tangent to the collapse curve. The model proposed by Kecman is based on the mechanism observed in the second phase (next 20-30° after the first phase). Kecman also noted that the third stage has a similar bending strength variation as compared to the second stage.

The model from Kecman was implemented in the present work and the implementation was verified against two cross-sections reported in the literature [30], see (Figure 3.2).

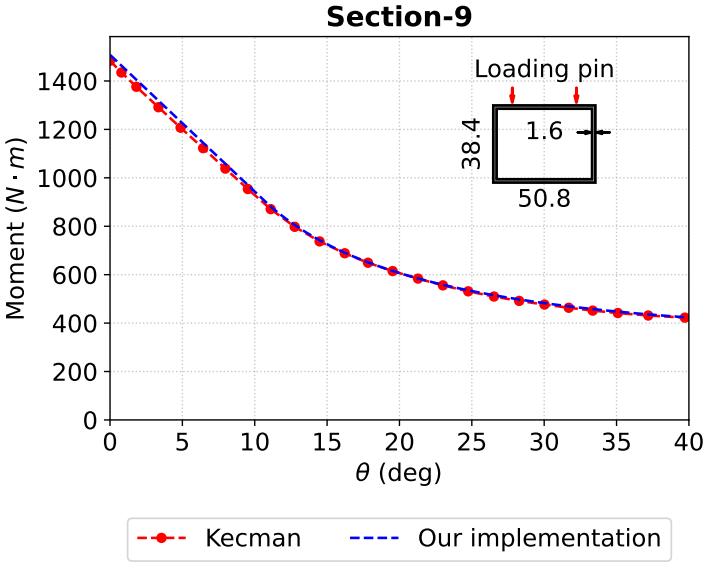

(a) Moment-rotation (θ) for section-9

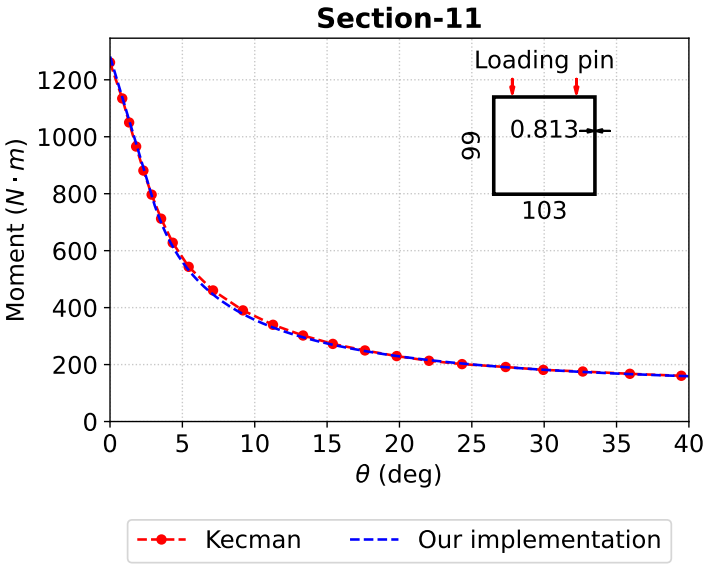

(b) Moment-rotation (θ) for section-11

Figure 3.2.: Comparison of moment-rotation curves from literature [30] and our implementation of the model

3.2.2. Wierzbicki model

Wierzbicki et al. [31] developed closed form solutions for predicting moment-rotation curves for square columns in collapse stage (Stage-III, Figure 3.1). In this model, the moment calculation is based on two unknowns: half of folding wavelength (H) and the rolling radius (r), The model relies on calculating the internal rate of change of energy with respect to change in bending angle (θ), from which moment is then calculated as a function of θ, $M(\theta)$. A mean moment is then calculated by taking the average over the entire curve. The two unknowns are calculated by minimizing the mean moment with respect to the two unknowns H and r. Finally the moment-theta curve is calculated with moment being a function of half of folding wavelength (H), the rolling radius (r) and rotation angle (θ), $M(H, r, \theta)$.

In their work, Kim and Reid [32] noted that they were unable to reproduce the results using equations given by Wierzbicki et al. [31]. In the present work, we made two attempts to reproduce the model, both being unsuccessful.

Attempt-1: For the first attempt, equation 18 from Wierzbicki et al. [31] was implemented, H and r were calculated using equations 23 and 24 from Wierzbicki et al. [31]: $H = 1.276b^{2/3}t^{1/3}$ and $r = 0.795b^{1/3}t^{2/3}$; $\eta = 0$ was assumed for the computation. As can be seen from the results (see Figure 3.3), the results closely matched the simplified equation given by Wierzbicki et al. [31] (equation 26), validating correct implementation of the energy rate equations. However, the results from the simplified equation as well as the current implementation, deviated significantly from the results presented in Wierzbicki et al. [31]. θ was calculated using equation 31 from Wierzbicki et al. [31]: $\theta = \alpha^2$.

Attempt-2: In the second attempt, θ was calculated using the equation: $2\,tan^{-1}\left(\frac{H}{b}\,(1-\cos\alpha)\right)$, following equation 12 in Liu et al. [78], which presents a model for the bending collapse of channel cross-sections derived from the earlier work of Wierzbicki et al. [31].

The results were observed to be significantly better using this approach, see Figure 3.4. However, the results still deviate from the results presented in the original work [31].

3.2.3. Kim and Reid

Kim and Reid [32] proposed a kinematically admissible and completely analytical model, for predicting moment-theta curve for bending collapse of square and rectangular tubular structures. The method used in this model is similar in methodology to Wierzbicki et al.'s model (subsection 3.2.2). The model was implemented in the present work and was verified against the moment-rotation curves reported in literature, with the literature curves being digitized using webplotdigitizer [81]. The predicted curves showed good agreement with results published in the literature, verifying correct implementation of the model, Figure 3.5 presents the comparison for two cross-sections.

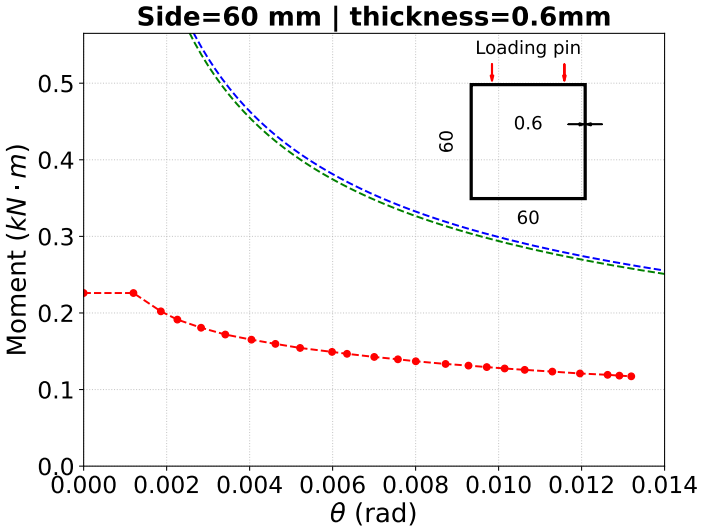

(a) Moment-rotation (θ) for t=0.6mm

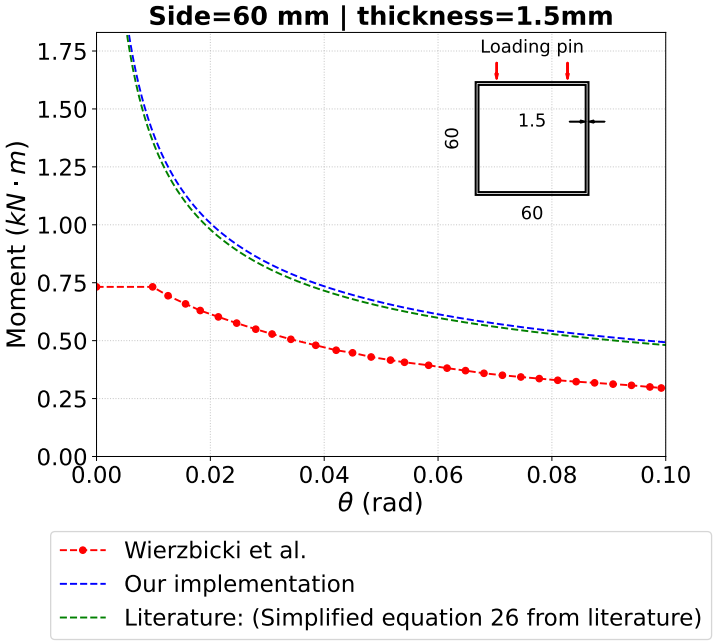

(b) Moment-rotation (θ) for t=1.5mm

Figure 3.3.: Wierzbicki attempt-1: Comparison of moment-rotation curves from Wierzbicki et al. [31] and our implementation of the model

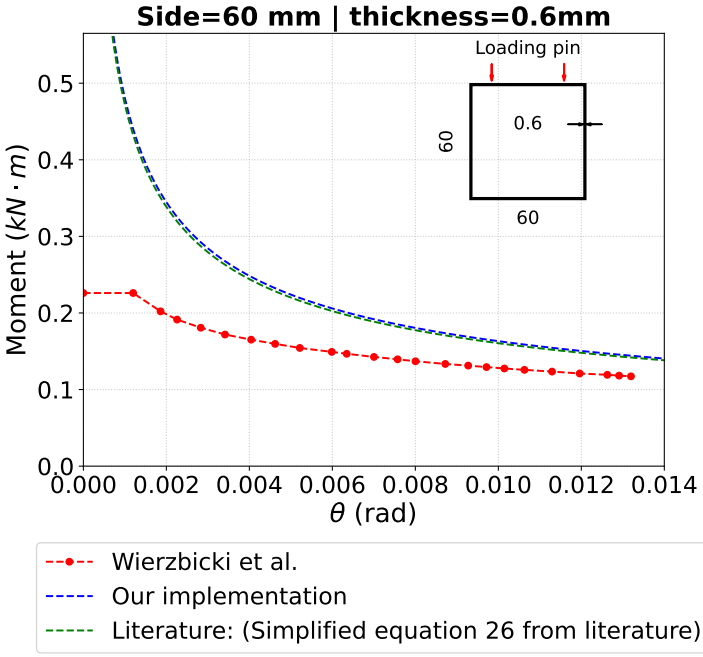

(a) Moment-rotation (θ) for t=0.6mm

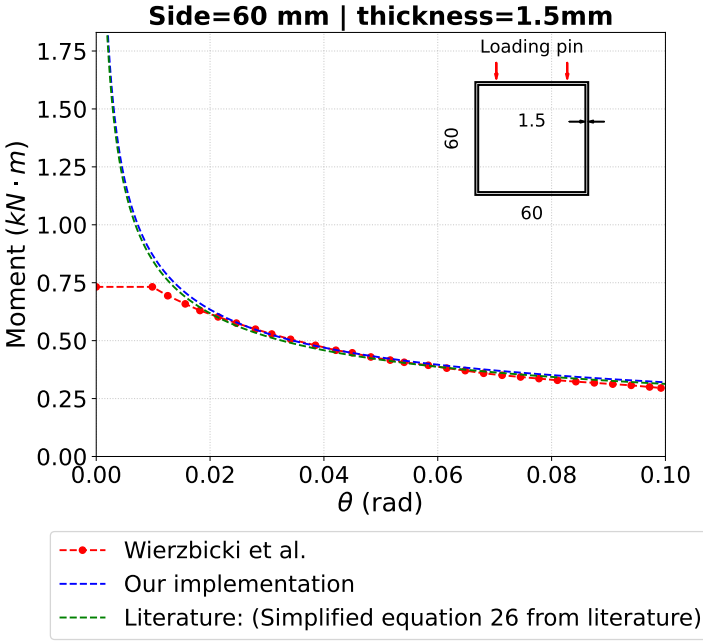

(b) Moment-rotation (θ) for t=1.5mm

Figure 3.4.: Wierzbicki attempt-2: Comparison of moment-rotation curves from Wierzbicki et al. [31] and our implementation of the model

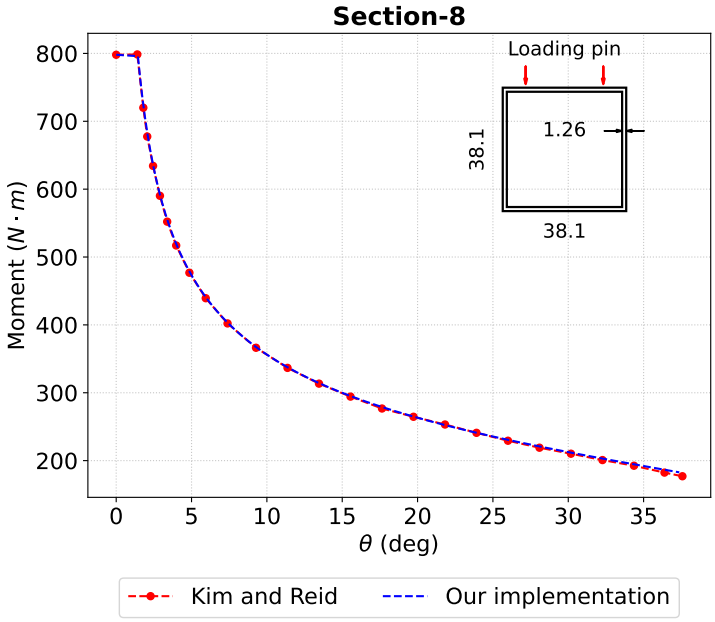

(a) Moment-rotation (θ) for section-8

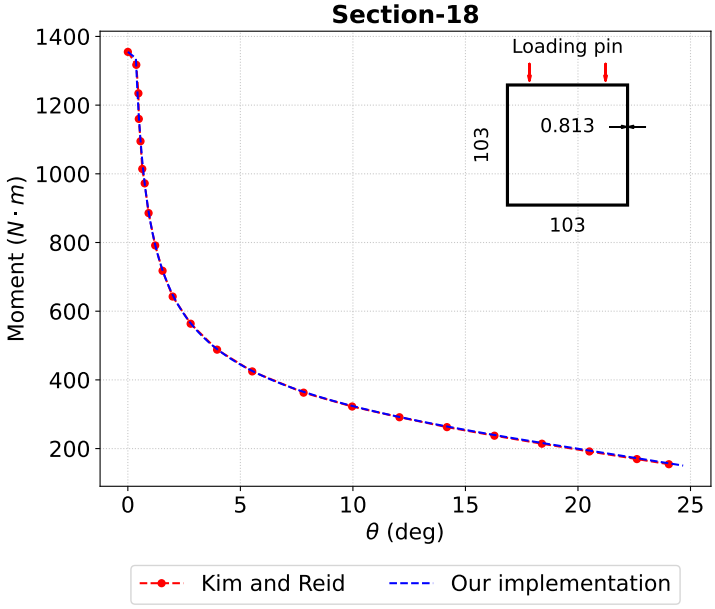

(b) Moment-rotation (θ) for section-18

Figure 3.5.: Comparison of moment-rotation curves from Kim and Reid [32] and our implementation of the model

3.3. Materials and Methods

3.3.1. Material data

The material stress-strain curves for the numerical campaign were taken from the literature and digitized using webplot digitizer [81]. Three materials were used for the numerical campaign: AL2024 [82], AL7075 [83] and S275 (material curve corresponding to the configuration: S275-25×25×1.5)[76].

3.3.2. Numerical dataset for bending simulations: Square and rectangular tubes

Finite Element Method (FEM) in Abaqus [84] was used to generate a dataset to validate the semi-analytical modelling approach presented in this paper. Simulations were carried out for square and rectangular tubular structures.

For numerical simulations, the approach is based on the 3-point bending setup used by Farfan et al. [76]. A schematic of the numerical setup is presented in Figure 3.7. The radius of loading and support pins was 15 mm and span was ten times the height of the specimen ($l_s = 10b$). The numerical model was verified against two sets of experimental data from literature [76, 85] and close agreement between the numerical and experimental results was obtained.

For the case from Farfan et al. filleted tubes were used. As noted by Farfan and Zhang [86] the fillets have influence on the maximum moment and not on the collapse stage itself. Since the numerical model uses non-filleted tubes, force values from the numerical model were multiplied by a factor to match the maximum moment with experimental force-displacement curves. The collapse part of the curve was then shifted by the difference in between the peak forces: $F_{FEM-scaled} = F_{FEM-unscaled} - (F_{max:FEM-unscaled} - F_{max:experimental})$ (Figure 3.6b).

- Configuration-1: material=AA110, a=30mm, b=30mm and t=2mm [85] (Figure 3.6a)
- Configuration-2: material=S275, a=25mm, b=25mm and t=1.5mm [76] (Figure 3.6b)

For square tubular structures, the numerical campaign was carried out using three materials: AL2024, AL7075 and S275. A total of 15 configurations were tested for each material using a combination of 5 side lengths and 3 thicknesses, resulting in a total of 45 configurations. For rectangular tubular structures a total of 10 configurations were tested with 4 configurations each for AL2024 and AL7075, and 2 configurations of S275. Dimensions and t/b ratio for all the configurations are presented in Table 3.1.

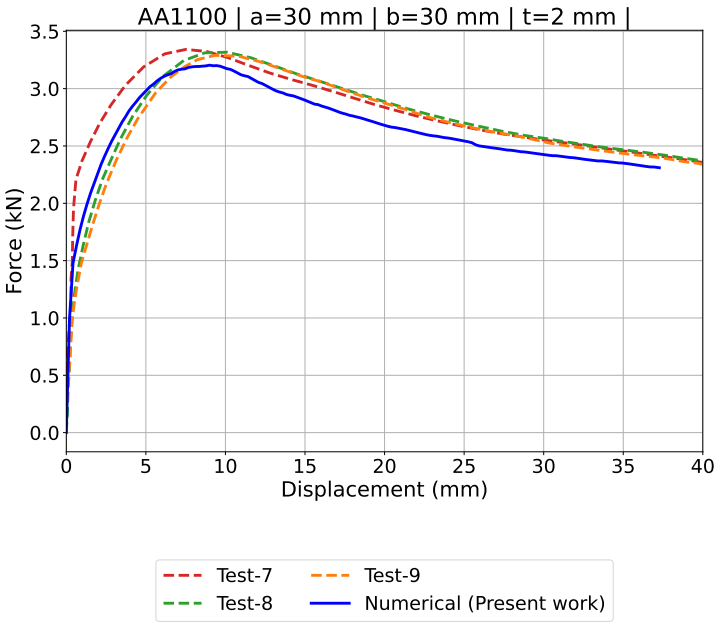

(a) AA1100 | a,b=30 | t=2mm

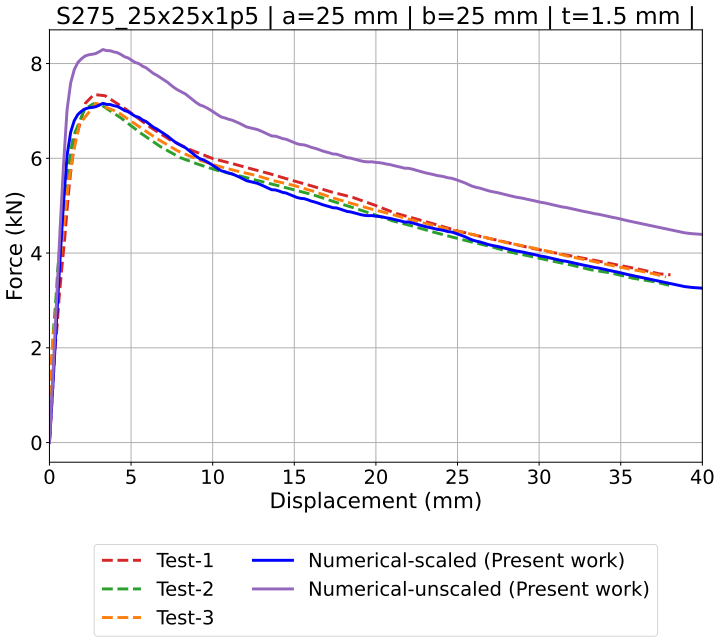

(b) S275 | a,b=25 | t=1.5mm

Figure 3.6.: Comparison between experimental force-displacement curves from literature [76, 85] and the numerical model

S.No.	Material	a	b	t	t/b	Span	S.No.	Material	a	b	t	t/b	Span
1	AL2024	15	15	1	0.07	150	**29**	AL7075	35	35	1.5	0.04	350
2		15	15	1.5	0.10	150	**30**		35	35	2	0.06	350
3		15	15	2	0.13	150	**31**	S275	15	15	1	0.07	150
4		20	20	1	0.05	200	**32**		15	15	1.5	0.10	150
5		20	20	1.5	0.08	200	**33**		15	15	2	0.13	150
6		20	20	2	0.10	200	**34**		20	20	1	0.05	200
7		25	25	1	0.04	250	**35**		20	20	1.5	0.08	200
8		25	25	1.5	0.06	250	**36**		20	20	2	0.10	200
9		25	25	2	0.08	250	**37**		25	25	1	0.04	250
10		30	30	1	0.03	300	**38**		25	25	1.5	0.06	250
11		30	30	1.5	0.05	300	**39**		25	25	2	0.08	250
12		30	30	2	0.07	300	**40**		30	30	1	0.03	300
13		35	35	1	0.03	350	**41**		30	30	1.5	0.05	300
14		35	35	1.5	0.04	350	**42**		30	30	2	0.07	300
15		35	35	2	0.06	350	**43**		35	35	1	0.03	350
16	AL7075	15	15	1	0.07	150	**44**		35	35	1.5	0.04	350
17		15	15	1.5	0.10	150	**45**		35	35	2	0.06	350
18		15	15	2	0.13	150		**Rectangular cross-sections**					
19		20	20	1	0.05	200	**1**	AL2024	25	20	1	0.05	200
20		20	20	1.5	0.08	200	**2**		25	20	2	0.10	200
21		20	20	2	0.10	200	**3**		20	25	1	0.04	250
22		25	25	1	0.04	250	**4**		20	25	2	0.08	250
23		25	25	1.5	0.06	250	**5**	AL7075	25	20	1	0.05	200
24		25	25	2	0.08	250	**6**		25	20	2	0.10	200
25		30	30	1	0.03	300	**7**		20	25	1	0.04	250
26		30	30	1.5	0.05	300	**8**		20	25	2	0.08	250
27		30	30	2	0.07	300	**9**	S275	20	25	1	0.05	250
28		35	35	1	0.03	350	**10**		20	25	2	0.10	250

Table 3.1.: Configurations used for numerical test campaign (dimensions are in mm)

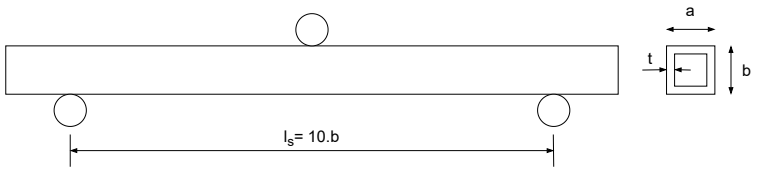

Figure 3.7.: 3-point bending setup schematic, adapted from [76]

3.4. Elastic and Elasto-plastic deformation stage (Stage-I and II)

As mentioned in the introduction, bending collapse models usually ignore computation of the elastic and elastic-plastic stages. However, since the present work is focused towards crashworthiness of aircraft in early stages of design, and because aluminum exhibits more pronounced plastic behavior than steel, a semi-analytical methodology using moment-rotation curves and spring linkage model to predict force-displacement curves for stages I and II is proposed in this section. The methodology is based on previous work from Anand et al. [87].

3.4.1. Calculation of M versus rotation curve for an element of length dx

In this work a formulation is presented for deriving a baseline moment–rotation ($M-\theta$) curve directly from discrete points along a multi-linear stress–strain law (subsection B.0.1), and scaling it using only section width and depth to model non-rectangular cross-sections via additive and subtractive rectangle operations. These equations were developed independently from first principles. To the best of the author's knowledge, this exact workflow: pre-computing a rectangular baseline from discrete test data and composing complex sections via scaled rectangular blocks evaluated at equal curvature or rotation – has not been previously documented. However, the core mechanics of this approach (e.g., area superposition, plane-sections assumption, and moment derivation from piecewise stress-strain input or curve-fits) are consistent with principles well established in the literature [88–91]. This method provides a rapid, integration-free workflow that operates directly on experimentally obtained discrete stress-strain points without curve fitting or fiber discretization. The results are therefore dependent solely on the quality and accuracy of the material test data.

First, for a given material-stress strain curve, a baseline moment and rotation are calculated. From subsection B.0.1, baseline moment can be calculated from Equation 3.2 and baseline rotation (θ) can be calculated using Equation 3.1. It must be noted that true stress-strain curves are used for the spring-linkage model.

$$\theta_{baseline} = \varepsilon_i \tag{3.1}$$

$$M_{baseline} = \frac{1}{3\varepsilon_i^2}\sum_{j=1}^{i} E_j(\varepsilon_j^3 - \varepsilon_{j-1}^3) + \frac{1}{2}\sum_{j=1}^{i}\varepsilon_{j-1}(E_{j-1} - E_j) - \frac{1}{2\varepsilon_i^2}\sum_{j=1}^{i}\varepsilon_{j-1}^3(E_{j-1} - E_j) \tag{3.2}$$

Once the baseline moment and rotation have been calculated, the moment-rotation for a complex section can be assembled. Figure 3.8 shows a hollow rectangular section with width *a*, height *b* and thickness *t*. This hollow section can be represented by a combination of 3 shapes. First a rectangle of width *a* and height *b* is considered, the moment and rotation for this shape can be calculated as follows using $z_{max} = \mathrm{b}/2$:

$$\mathbf{M_{shape-1}} = 2\mathrm{a}\left(\frac{\mathrm{b}}{2}\right)^2 M_{baseline}\ ;\ \theta_{\mathbf{shape-1}} = \frac{2dx}{\mathrm{b}}\theta_{baseline} \tag{3.3}$$

Moment and rotation for shape-2 and shape-3 are also calculated similarly:

$$\mathbf{M_{shape-2}} = 2\mathrm{a}\left(\frac{\mathrm{b}-2\mathrm{t}}{2}\right)^2 M_{baseline}\ ;\ \theta_{\mathbf{shape-2}} = \frac{2dx}{\mathrm{b}-2\mathrm{t}}\theta_{baseline} \tag{3.4}$$

$$\mathbf{M_{shape-3}} = 2(2\mathrm{t})\left(\frac{\mathrm{b}-2\mathrm{t}}{2}\right)^2 M_{baseline}\ ;\ \theta_{\mathbf{shape-3}} = \frac{2dx}{\mathrm{b}-2\mathrm{t}}\theta_{baseline} \tag{3.5}$$

Where *dx* is the length of the rigid element in the spring linkage model. This gives us 3 distinct moment-rotation curves.

Finally, to calculate $M(\theta)$ for the hollow rectangular cross-section, for a given θ_i value, corresponding moment values are gathered by interpolation from the 3 curves and they are then summed in the way shown in Figure 3.8 and Equation 3.6. Since, the strain can be approximated to be linear for a given rotation, adding or subtracting the moments for the same rotation θ_i leads to calculation of moment for the hollow rectangular section.

$$M_{hollow}(\theta_i) = M_{shape-1}(\theta_i) - M_{shape-2}(\theta_i) + M_{shape-3}(\theta_i) \tag{3.6}$$

3.4.2. Use of spring linkage method to predict elastic and elasto-plastic deformation stage

The moment-rotation curve calculated in subsection 3.4.1 is used as an input to a spring-linkage model to obtain the force-displacement response for Stage-I and Stage-II. The spring-linkage model consists of rigid links of length *dx*, connected to each other using rotational springs, as shown in Figure 3.9. For a cantilever of length *L*, divided into *N* links:

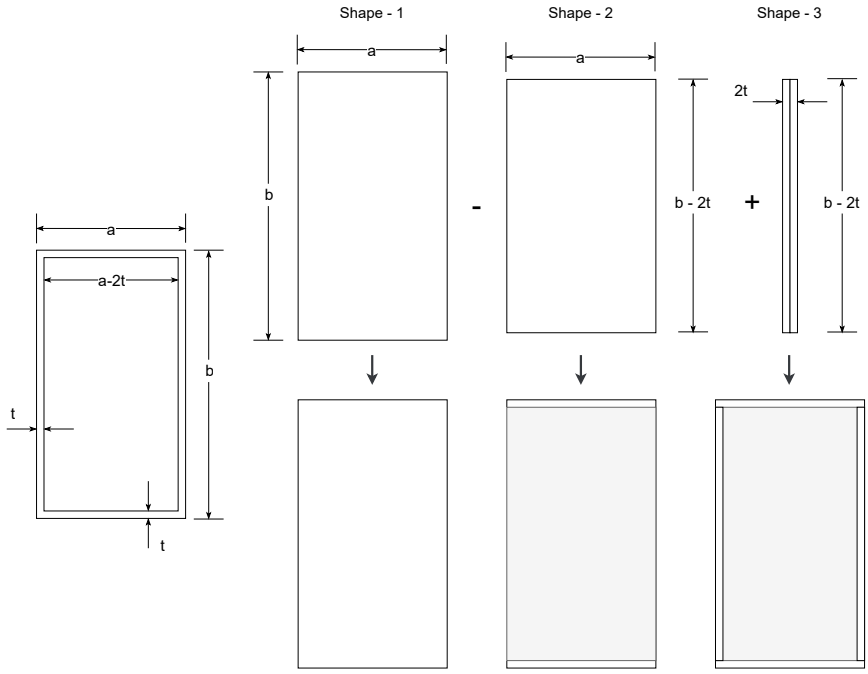

Figure 3.8.: Composite method to get moment-rotation curve for a cross-section

$$dx = \frac{L}{N} \tag{3.7}$$

The rigid links do not undergo deformation. Instead, the rotation corresponding to the bending deformation over a length dx is applied at the rotational springs. Therefore, the moment-rotation curve calculated for an element of length dx in subsection 3.4.1 is used directly as the characteristic curve for each spring:

$$M = \mathcal{M}(\theta) \tag{3.8}$$

Where $\mathcal{M}(\theta)$ represents the moment-rotation curve obtained from Equation 3.6. The same curve is assigned to all the springs since the material and cross-section remain constant along the specimen.

For a given spring rotation θ_i, the corresponding curvature over the element can be approximated as:

$$\kappa_i = \frac{\theta_i}{dx} \tag{3.9}$$

and the strain at a distance z from the neutral axis is:

$$\epsilon_i = z\kappa_i = \frac{z\theta_i}{dx} \tag{3.10}$$

This is the same strain-rotation relation used for calculating the moment-rotation curve in subsection 3.4.1.

For the 3-point bending configuration, symmetry about the loading pin is used to reduce the specimen to a cantilever with length equal to half of the span:

$$L = \frac{l_s}{2} \tag{3.11}$$

For a total force P applied at the center of the 3-point bending specimen, the reaction force at each support is:

$$F = \frac{P}{2} \tag{3.12}$$

Therefore, the half-span can be represented by a cantilever of length $L = l_s/2$, with a force $F = P/2$ applied at its free end. The equivalence can also be shown from the maximum bending moment. The moment at the fixed end of the cantilever is:

$$M_{\text{root}} = FL = \frac{P}{2}\frac{l_s}{2} = \frac{Pl_s}{4} \tag{3.13}$$

which is equal to the maximum bending moment for a simply supported beam subjected to a central point load.

For a given value of force F, the bending moment is calculated at each spring. In the undeformed configuration, if spring i is located at a distance x_i from the fixed end, the moment is:

$$M_i = F(L - x_i) \tag{3.14}$$

As the links rotate, the lever arm between each spring and the line of action of the force changes. Therefore, the lever arm is recalculated using the deformed geometry after each force increment. If r_i is the perpendicular distance between spring i and the line of action of the force, the moment at the spring is calculated as:

$$M_i = Fr_i \tag{3.15}$$

In the present implementation, the line of action of the force passes through the free end and is perpendicular to the final rigid link. If (x_i, y_i) represents the position of spring i, (x_N, y_N) represents the free end and ϕ_N is the angle of the final link, the lever arm can be written as:

$$r_i = |(x_N - x_i)\cos\phi_N + (y_N - y_i)\sin\phi_N| \tag{3.16}$$

For the initial undeformed configuration, $\phi_N = 0$, $y_i = y_N = 0$, and Equation 3.16

reduces to $r_i = L - x_i$.

Once M_i has been calculated, the corresponding local rotation of each spring is obtained from the moment-rotation curve calculated in subsection 3.4.1:

$$\theta_i = \mathcal{M}^{-1}(M_i) \tag{3.17}$$

In practice, the value of θ_i is obtained by interpolation from the discrete moment-rotation curve. Since the moment varies along the length of the cantilever, each spring has a different rotation. The largest rotation occurs close to the fixed end where the bending moment is highest.

The angle of each rigid link is then calculated by summing the rotations of the preceding springs. If ϕ_j is the angle of link j:

$$\phi_j = \sum_{i=1}^{j} \theta_i \tag{3.18}$$

For example, the angles of the first three links are:

$$\phi_1 = \theta_1, \qquad \phi_2 = \theta_1 + \theta_2, \qquad \phi_3 = \theta_1 + \theta_2 + \theta_3 \tag{3.19}$$

Once the angles of all the rigid links are known, the global coordinates of the linkage can be calculated. Taking the fixed end as $x_0 = y_0 = 0$, the coordinates of node j are:

$$x_j = \sum_{k=1}^{j} dx \cos\phi_k \tag{3.20}$$

$$y_j = \sum_{k=1}^{j} dx \sin\phi_k \tag{3.21}$$

The vertical coordinate of the final node gives the tip displacement of the cantilever:

$$\delta = |y_N| \tag{3.22}$$

The calculated force F corresponds to the reaction force for one half of the 3-point bending specimen. Therefore, the corresponding force at the loading pin is:

$$P = 2F \tag{3.23}$$

The calculation is repeated for increasing values of F. For each force value, the moment at every spring is first calculated using Equation 3.15. The corresponding spring rotations are then obtained from Equation 3.17, followed by calculation of the link angles and the global coordinates using Equations 3.18–3.21. This gives one force-displacement point (P, δ). Repeating the calculation over the complete force range gives the force-displacement curve corresponding to the elastic and

elasto-plastic deformation stages. The calculation sequence is summarized in Figure 3.9.

A comparison between the force-displacement curves obtained using the spring-linkage model and the numerical simulations is presented in Figure 3.9. Close agreement is observed for the elastic and elasto-plastic deformation stages.

A comparison of force-displacement curves obtained using this method and those obtained from numerical simulation are presented Figure 3.10. As observed, the model shows close agreement with the numerical results for elastic and elastic-plastic stages (Stage I and II).

3.5. Collapse stage (Stage-III)

This section presents the calculation for collapse stage. Samples undergo a sudden collapse followed by progressive folding of the compression flange, which is the mechanism studied by the analytical models presented in section 3.2.

3.5.1. Flow stress

All the analytical models presented in section 3.2 depend on the value of flow stress to calculate the fully plastic bending moment (M_0), which is given by the relation $M_0 = \sigma_{flow} t^2/4$ and is used to calculate the bending energy. Across the literature, various equations for flow stress have been proposed depending on the nature of the stress-strain curve. In the present work, flow stress for the aluminum samples is approximated using the average stress over the strain range, Equation 3.24 ($0 < \varepsilon < \varepsilon_u$) [92]. True stress-strain curve was used for flow stress calculations.

$$\sigma_{flow} = \frac{1}{\varepsilon_u} \int_0^{\varepsilon_u} \sigma d\varepsilon \tag{3.24}$$

For steel specimens which do not show pronounced plastic behavior a simpler formula using ultimate stress (σ_u) values is used, Equation 3.25 [38].

$$\sigma_{flow} = 0.92\sigma_u \tag{3.25}$$

3.5.2. Estimation of maximum moment

The maximum moment at which bending collapse is initiated is an important parameter for analytical calculation of the force-displacement/moment-rotation curve. Kecman [1] in their work present that maximum moment can be calculated by comparison between yield stress (σ_y) and critical stress (σ_{cr}) of the compression flange. Where σ_{cr} is given by the following equation:

$$\sigma_{cr} = \frac{\pi^2 E}{12(1-\nu^2)} \left(5.23 + 0.16\frac{a}{b}\right)\left(\frac{t}{a}\right)^2 \tag{3.26}$$

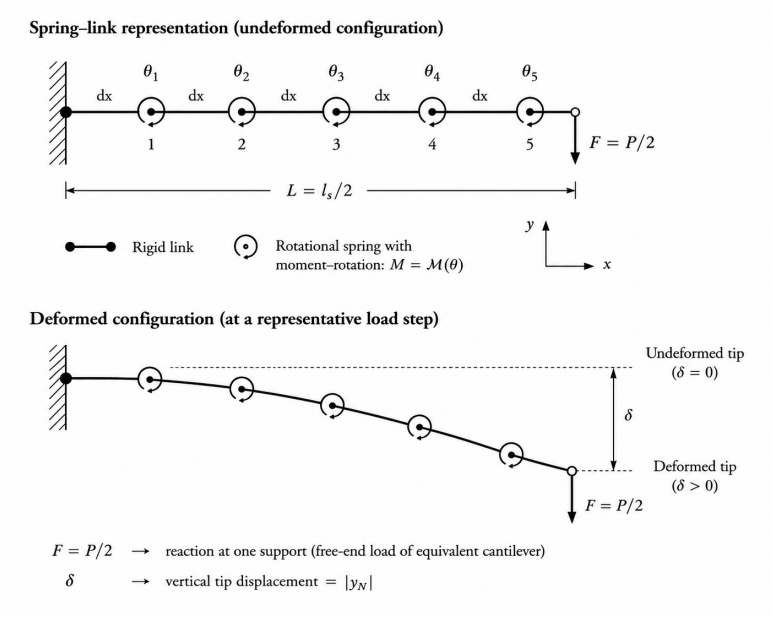

(a) Rigid-link representation of the half-span specimen.

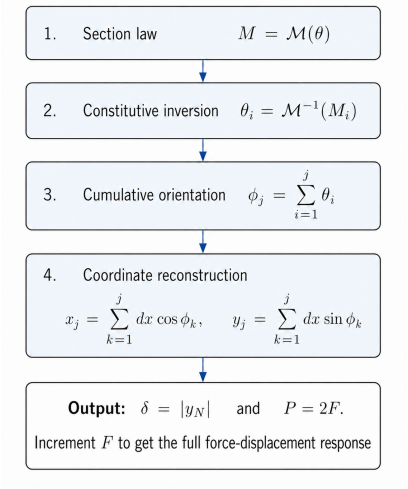

(b) Calculation sequence used in the spring-linkage model.

Figure 3.9.: Spring-linkage method used to calculate the force-displacement response for the elastic and elasto-plastic deformation stages.

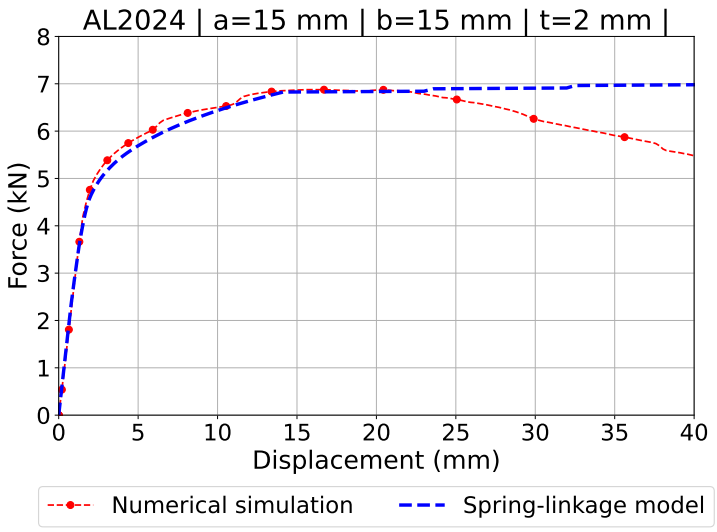

(a) AL2024: a,b=15mm and t=2mm

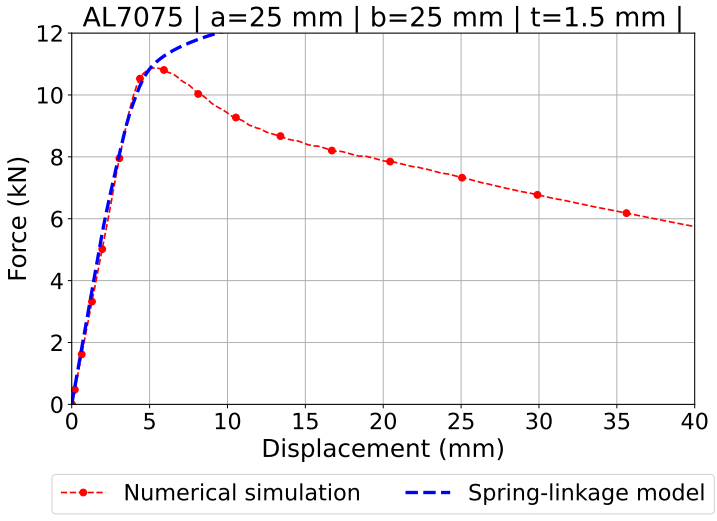

(b) AL7075: a,b=25mm and t=1.5mm

Figure 3.10.: Comparison of force-displacement curve from numerical simulation and spring-linkage model – **continued on next page**

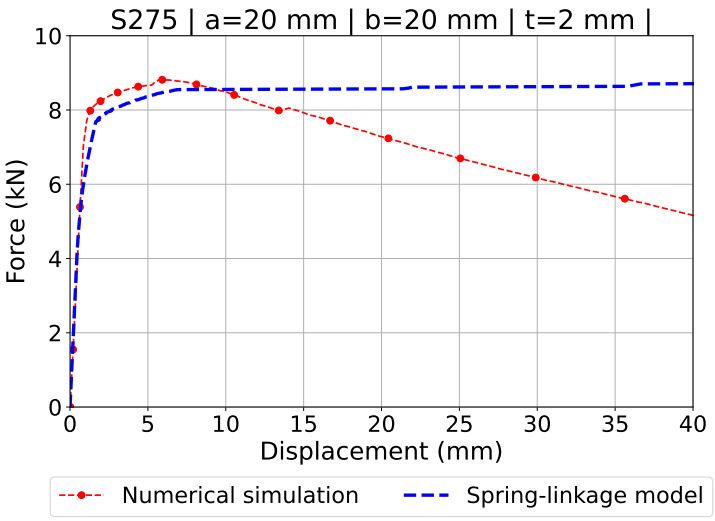

(c) S275: a,b=20mm and t=2mm

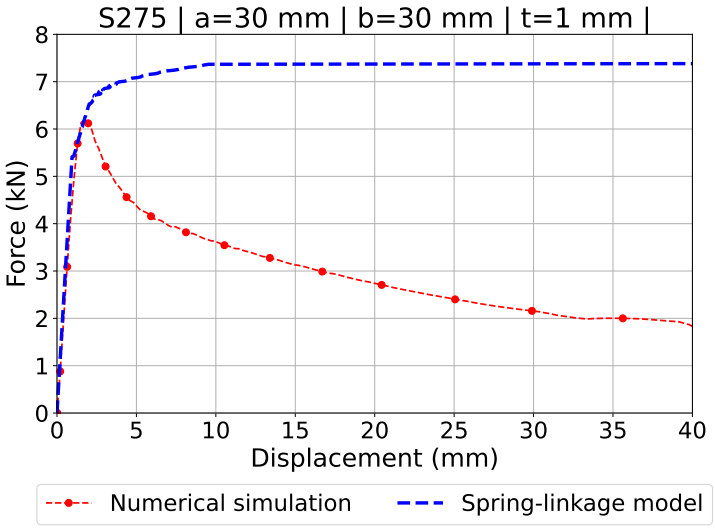

(d) S275: a,b=30 mm and t=1mm

Figure 3.10.: Comparison of force-displacement curve from numerical simulation and spring-linkage model

Three cases are then considered: $\sigma_{cr} \leq \sigma_y$, $\sigma_y < \sigma_{cr} \leq 3\sigma_y$ and $\sigma_{cr} > 3\sigma_y$. The three cases are discussed below in further detail.

Case-1 - Critical stress ≤ Yield stress ($\sigma_{cr} \leq \sigma_y$): For this case, yielding of the flanges takes place [1], a factor α_e is first calculated:

$$\alpha_e = \frac{a_e + a + 2b}{a + b}; \text{ where } a_e = a\left(0.7\frac{\sigma_{cr}}{\sigma_y} + 0.3\right) \tag{3.27}$$

If $\alpha_e \leq 2$, yielding occurs in the compressed flange first, the maximum moment and force are calculated as:

$$M'_{max} = \sigma_y t b^2 \left[\frac{2a + b + a_e((3a/b) + 2)}{3(a + b)}\right]; F'_{max} = \frac{4M'_{max}}{l_s} \tag{3.28}$$

else both flanges yield and the maximum moment and force are calculated as:

$$M'_p = \sigma_y t b\left(a + \frac{b}{3}\right); F'_{max} = \frac{4M'_p}{l_s} \tag{3.29}$$

This case was detected for 3 configurations from the numerical simulations. The results were observed to be in agreement with the numerical results and are presented in Figure 3.11.

Case-2 - Yield stress < Critical stress ≤ 3 × Yield stress ($\sigma_{yield} < \sigma_{critical} < 3\sigma_{yield}$): For critical stress values between σ_y and $3\sigma_y$, Kecman in his work suggested using an interpolation between M_p and M'_p (Equation 3.29), where M_p and F_p are calculated as:

$$M_p = \sigma_y t\left[a(b - t) + \frac{(b - 2t)^2}{2}\right]; F_p = \frac{4M_p}{l_s} \tag{3.30}$$

And the maximum force is then calculated using:

$$F_{max} = F'_p + (F_p - F'_p)\left(\frac{\sigma_{cr} - \sigma_y}{2\sigma_y}\right) \tag{3.31}$$

The corresponding results were observed to be reasonably accurate, however under-prediction was noticed for some cases, Figure 3.12.

Since the model is semi-analytical, an attempt was made to calculate the maximum moment using the semi-analytical model. M'_p in Equation 3.29 corresponds to the point where both flanges approach yielding. While calculating the rotation-moment relationship (Equation 3.6), the semi-analytical model is used to calculate the strain at the mid surface of the flange ($z_{flange} = (0.5b - 0.5t)$) using: $\varepsilon_{flange} = z_{flange}\theta_i/dx$ followed by a lookup to find the corresponding stress in the flange σ_{flange}, the moment at which stress in the flange crosses the yield stress ($\sigma_{flange} \geq \sigma_y$) is stored as $M'_{p_{SA}}$, where subscript SA is used to denote calculation

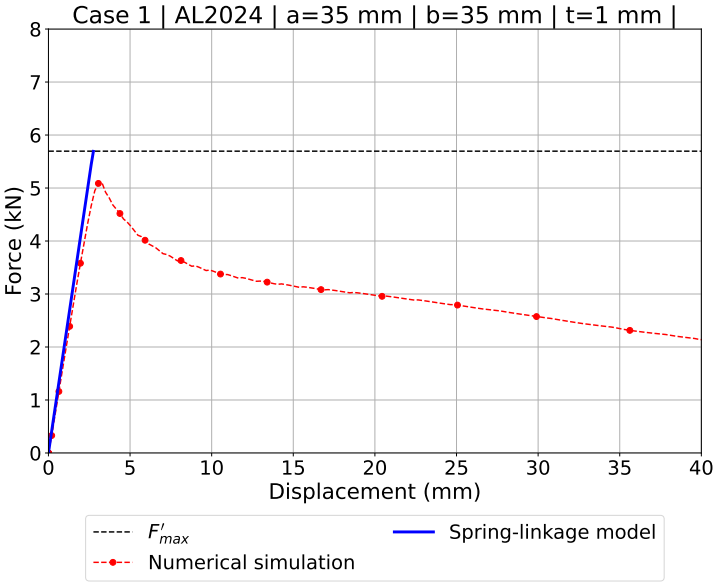

(a) AL2024 | c=35mm | t=1mm, α_e=1.97

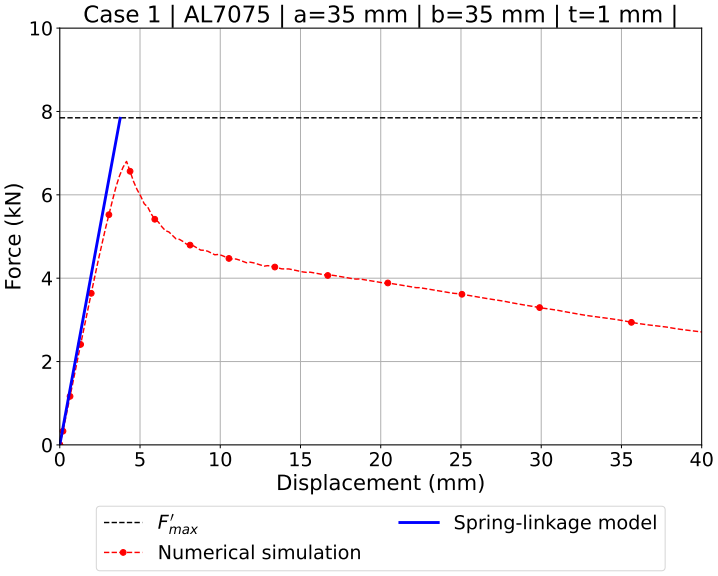

(b) AL7075 | c=35mm | t=1mm, α_e=1.85

Figure 3.11.: Comparison of numerical force-displacement curve and maximum moment (Case-1)

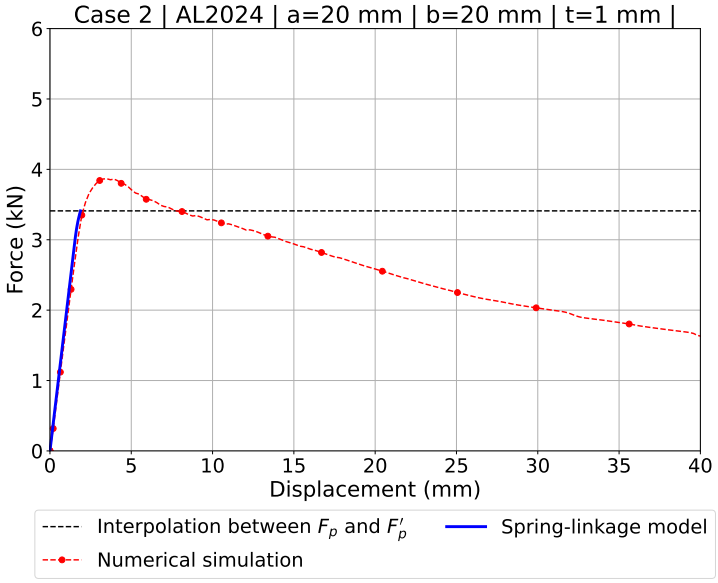

(a) AL2024 | c=20mm | t=1mm

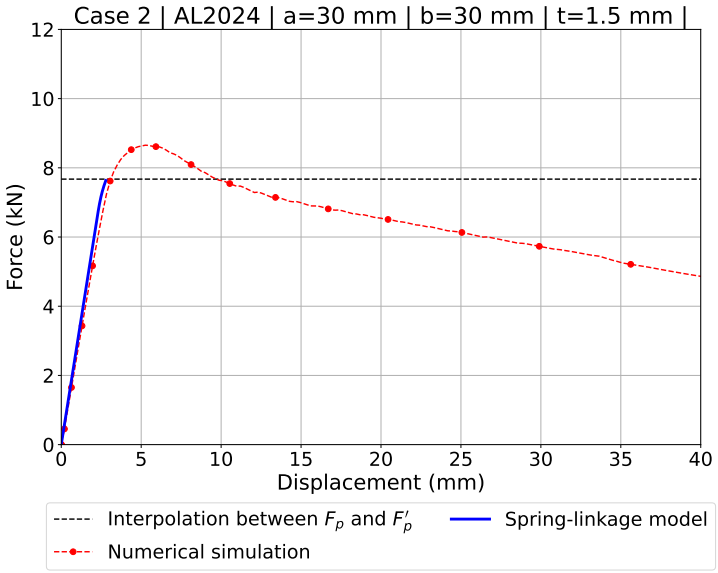

(b) AL2024 | c=30mm | t=1.5mm

Figure 3.12.: Comparison of numerical force-displacement curve and maximum moment (Case-2) – **continued on next page**

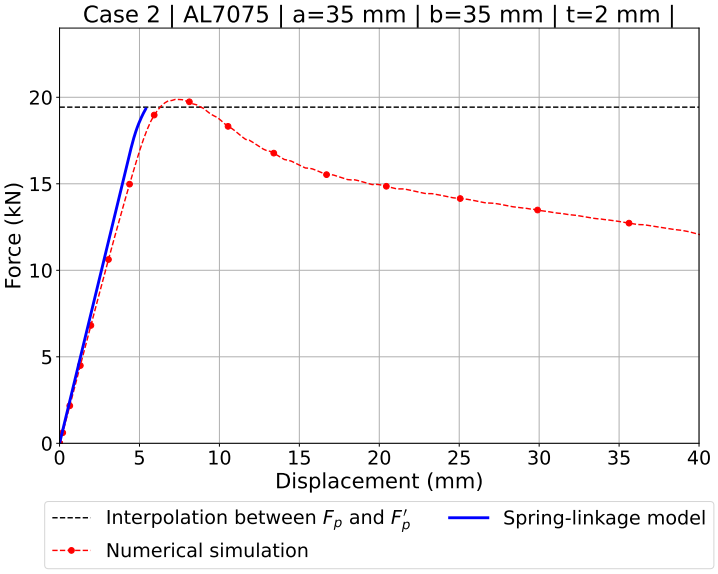

(c) AL7075: a,b=35mm and t=2mm

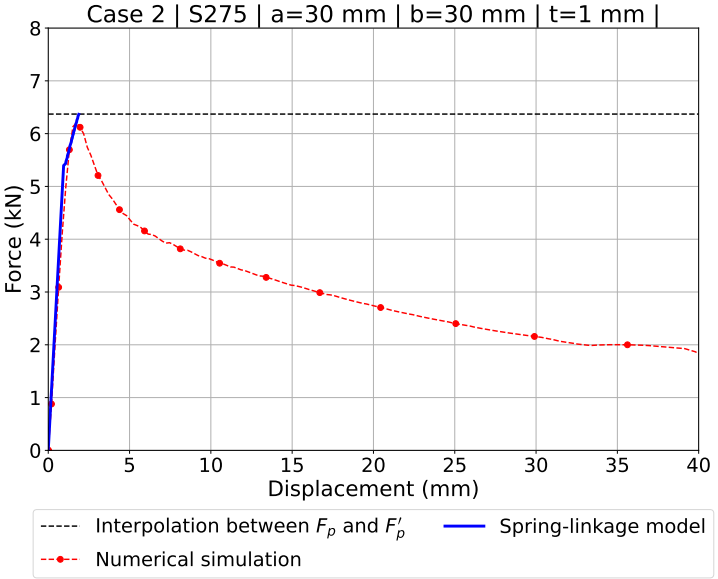

(d) S275: a,b=30 mm and t=1mm

Figure 3.12.: Comparison of numerical force-displacement curve and maximum moment (Case-2)

using semi-analytical model. When running the spring linkage model, the moment at root of the cantilever is compared against the obtained $M'_{p_{SA}}$ to return the force value ($F'_{p_{SA}}$) at which $M'_{p_{SA}}$ is reached at the root. To get the moment at which the whole section yields ($M_{p_{SA}}$), stress is calculated at 4 stations along the height and averaged: $z_1 = 0.875(b/2), z_2 = 0.625(b/2), z_3 = 0.375(b/2)$ and $z_4 = 0.125(b/2)$. The obtained stress value is then compared against the yield stress to return the Moment ($M_{p_{SA}}$) and force ($F_{p_{SA}}$) corresponding to the moment. Similar to interpolation used in Kecman model (Equation 3.31), F_{max} is then calculated using:

$$F_{max} = F'_{p_{SA}} + (F_{p_{SA}} - F'_{p_{SA}})\left(\frac{\sigma_{cr} - \sigma_y}{2\sigma_y}\right) \tag{3.32}$$

The results from semi-analytical model were observed to be in close agreement with numerical results Figure 3.13.

Case-3 - Critical stress > 3 Yield stress ($\sigma_{critical} > 3\sigma_{yield}$): If critical stress is greater than or equal to three times the yield stress ($\sigma_{cr} \geq 3\sigma_y$) then the maximum moment is equal to M_p (Equation 3.30) as per Kecman. Figure 3.14 presents the results corresponding to M_p, a discrepancy between the maximum force predicted by numerical results and Equation 3.30 was observed, with Equation 3.30 significantly under-predicting the maximum force for aluminum samples.

For aluminum samples with $\sigma_{critical} > 3\sigma_{yield}$, the peak force can vary between force corresponding to full section yielding (Equation 3.30) and the force at which the full section reaches flow stress (σ_{flow}). Based on the numerical results, it was observed that thin samples (t/b≤0.05) peak at full section yielding and thick samples (t/b≥0.1) peak at full section flow stress. An interpolation between full section yield and full section flow is proposed for $0.05 < (t/b) < 0.1$.

Similar to case-2, stress is calculated at 4 stations along the height and averaged: $z_1 = 0.875(b/2), z_2 = 0.625(b/2), z_3 = 0.375(b/2)$ and $z_4 = 0.125(b/2)$. The moment at which stress crosses yield stress is stored as $M_{p_{SA}}$ and corresponding force as $F_{p_{SA}}$. And the moment at which stress crosses flow stress is stored as $M_{p_{SA-flow}}$ and corresponding force as $F_{p_{SA-flow}}$. The maximum force can be then calculated using:

$$F_{\max} = \begin{cases} F_{p_{SA}}, & \frac{t}{b} \leq 0.05 \\ F_{p_{SA}} + \frac{F_{p_{SA-flow}} - F_{p_{SA}}}{(0.10 - 0.05)}\left(\frac{t}{b} - 0.05\right), & 0.05 < \frac{t}{b} < 0.10 \\ F_{p_{SA-flow}}, & \frac{t}{b} \geq 0.10 \end{cases} \tag{3.33}$$

The results were in close agreement with numerical results (Figure 3.15).

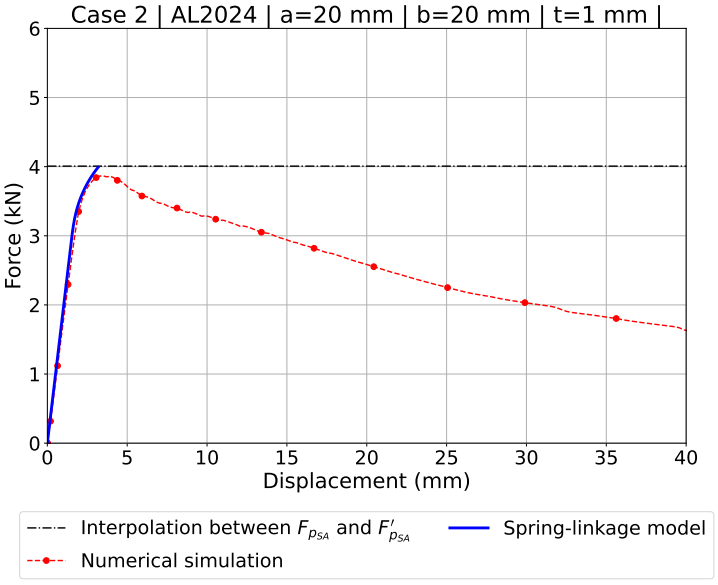

(a) AL2024 | c=20mm | t=1mm

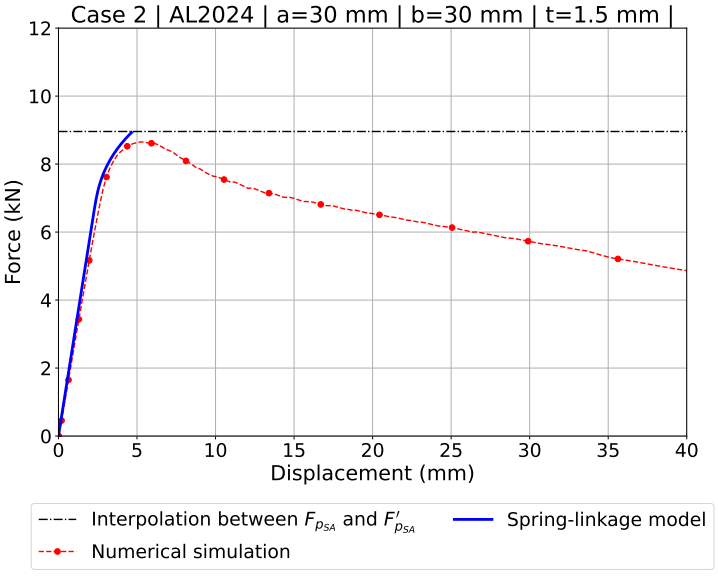

(b) AL2024 | c=30mm | t=1.5mm

Figure 3.13.: Comparison of numerical force-displacement curve and maximum moment (Case-2: Peak force obtained from semi-analytical model) – **continued on next page**

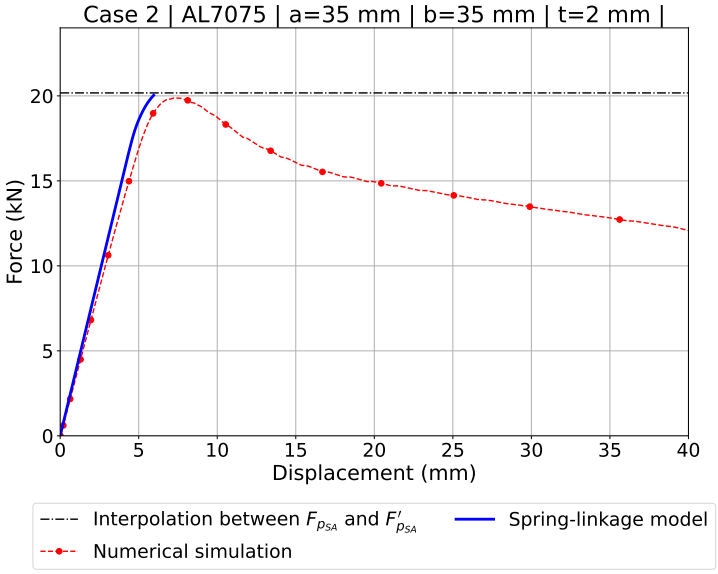

(c) AL7075: a,b=35mm and t=2mm

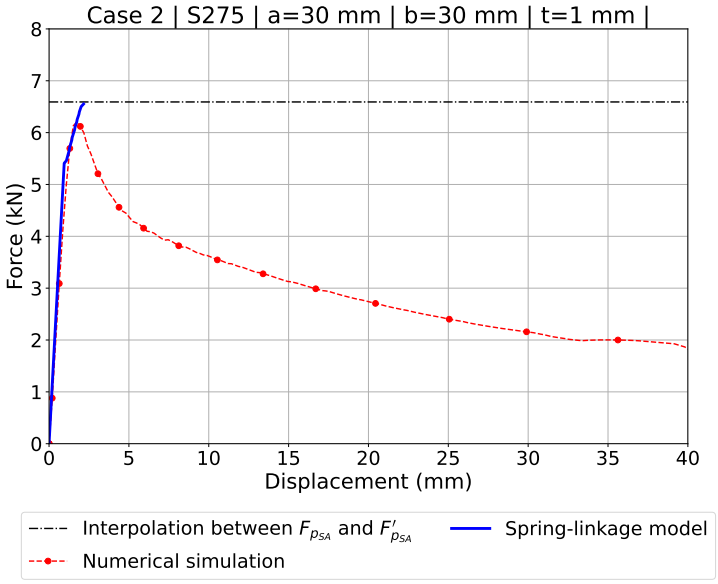

(d) S275: a,b=30 mm and t=1mm

Figure 3.13.: Comparison of numerical force-displacement curve and maximum moment (Case-2: Peak force obtained from semi-analytical model)

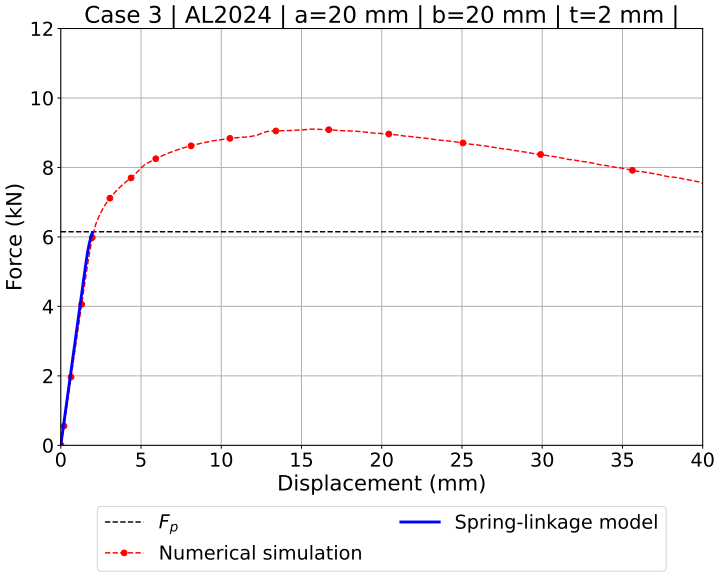

(a) AL2024 | c=20mm | t=2mm

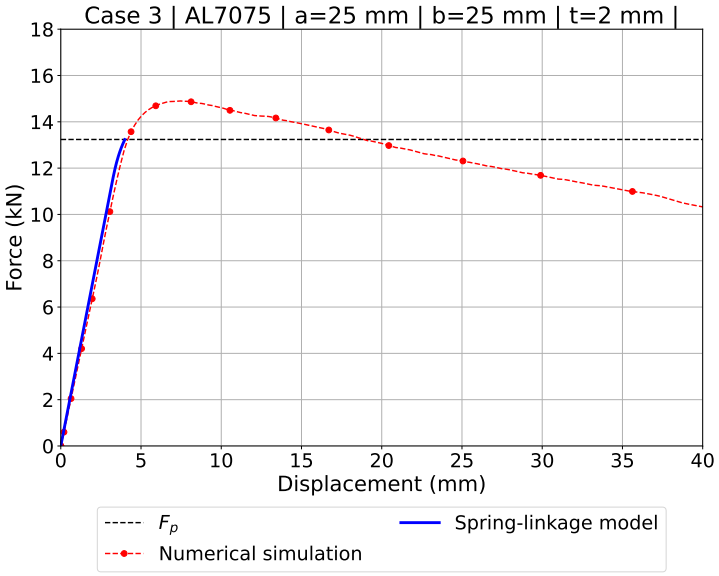

(b) AL7075 | c=25mm | t=2mm

Figure 3.14.: Comparison of numerical force-displacement curve and maximum moment (Case-3) – **continued on next page**

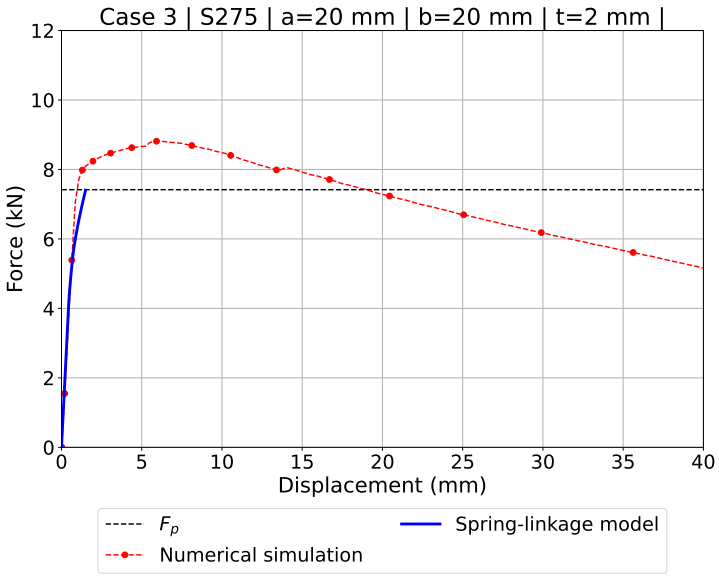

(c) S275: a,b=20mm and t=2mm

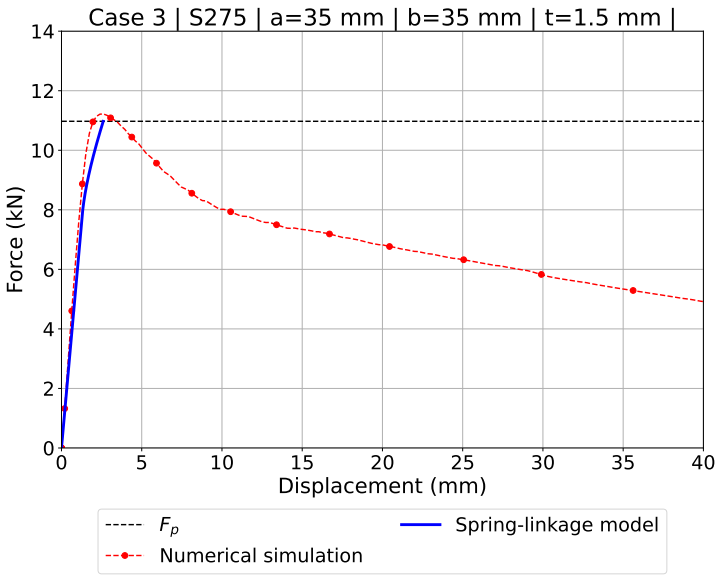

(d) S275: a,b=35 mm and t=1.5mm

Figure 3.14.: Comparison of numerical force-displacement curve and maximum moment (Case-3)

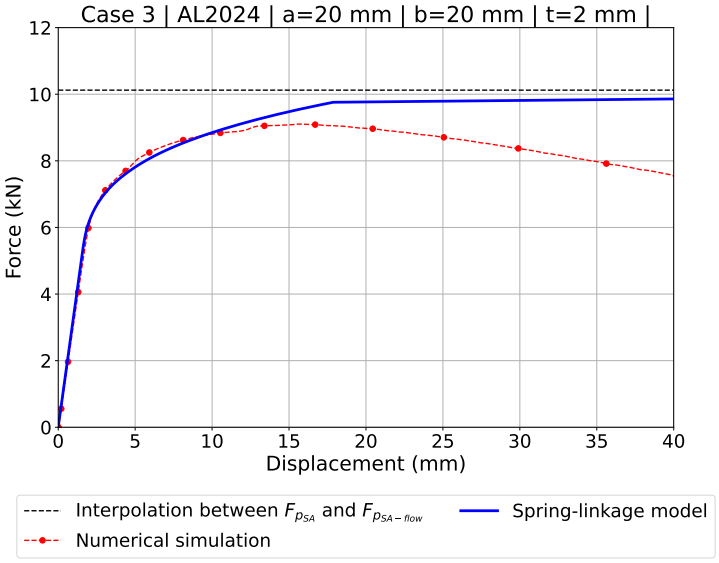

(a) AL2024 | c=20mm | t=2mm

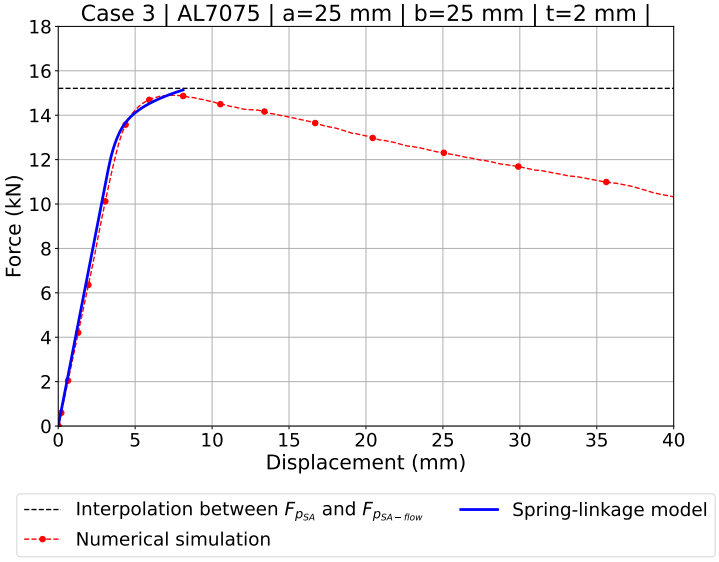

(b) AL7075 | c=25mm | t=2mm

Figure 3.15.: Comparison of numerical force-displacement curve and maximum moment (Case-3: Peak force obtained from semi-analytical model) – **continued on next page**

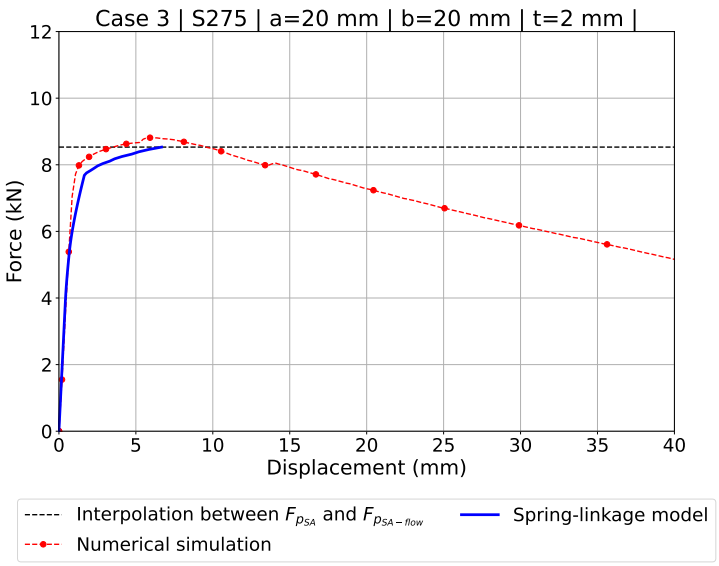

(c) S275: a,b=20mm and t=2mm

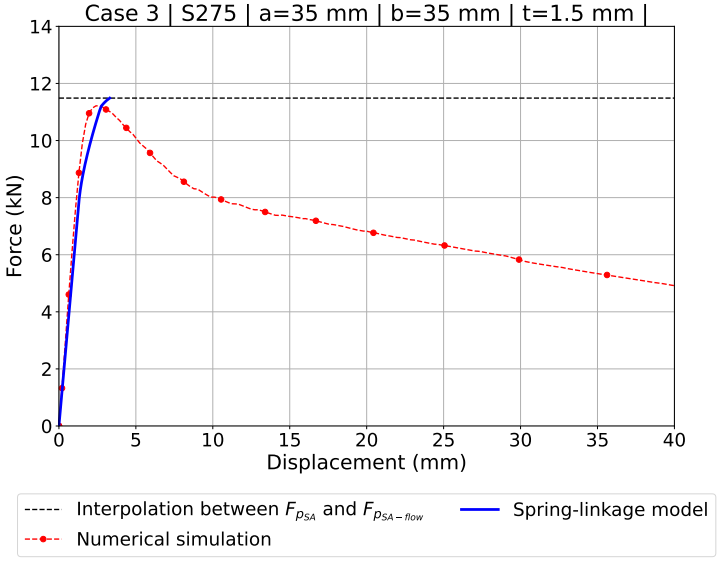

(d) S275: a,b=35 mm and t=1.5mm

Figure 3.15.: Comparison of numerical force-displacement curve and maximum moment (Case-3: Peak force obtained from semi-analytical model)

3.5.3. Model from Kecman for collapse beyond 20 degrees

Kecman [30] observed that bending collapse consists of four distinct phases:

1. **Phase-1**: Bulge creation in the webs without rolling deformation. (Initial 5-10 degrees)
2. **Phase-2**: Rolling along the yield lines (Next 20-30 degrees)
3. **Phase-3**: Initiation of jamming, termination of rolling and creation of secondary hinge.
4. **Phase-4**: Secondary hinge development.

Since, phase-2 covers most part of the collapse stage, theoretical analysis by Kecman is based on this phase. Therefore in our implementation, results from Kecman model is clipped for the 20 degrees onward region. Displacement corresponding to 20 degrees is calculated per Farfan et al. [76] $u = 0.5 l_s tan(\theta/2)$, where $\theta = 20(\pi/180)$ and l_s is the span length. A comparison between numerical results and the results from the Kecman model for beyond 20 degrees is presented in Figure 3.16, close agreement with the numerical results were observed, especially for cases with low thickness to side length ratios: Figure 3.16a (t/b=0.043)and Figure 3.16c (t/b=0.04). Flow stress was used for the calculations using Kecman model (subsection 3.5.1).

3.5.4. Transition between spring-linkage model and Kecman model

Based on the previous sections it can be concluded that Stage-I, Stage-II and trailing part of Stage-III (Figure 3.1) can be predicted using the existing analytical models and the spring-linkage model proposed in this work. However, the transition from Stage-II to trailing part of Stage-III is overestimated. This section presents a methodology to estimate the transition phase. The transition logic is presented in Figure 3.17. A total of 3 cases were observed. If OA is the curve from spring-linkage model clipped at peak force and BC is the curve from Kecman model taken for the region beyond $\theta = 20°$.

First, it is checked if point A has a lower x coordinate as compared to point B. If yes, the instantaneous slope at point B for curve BC is measured and curve BC is extended as a line with the calculated slope (line DB). Point A and B are also joined using a straight line. If slope of line AB is lesser than slope of line DB (Note: Line AB and DB have negative slopes so $m_{AB} < m_{DB}$ means line AB is steeper), transition case-1 is triggered, which signifies that a smooth drop would follow collapse initiation at point A. If slope of line DB is less than equal to slope of line AB ($m_{AB} \geq m_{DB}$), transition case-2 is triggered. If point A is found to have a higher x coordinate than point B, transition case-3 is triggered. The handling of all 3 cases is presented below:

1. **Transition case-1** ($x_A < x_B$ and $m_{AB} < m_{DB}$): For this case, the initial slope of the force vs displacement curve m_{rise} is extracted. Line AB_2 is then drawn

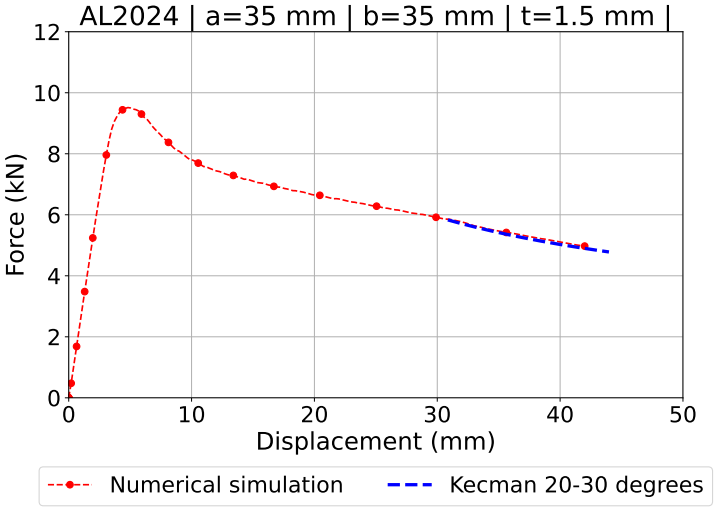

(a) AL2024: a,b=25mm and t=1.5mm

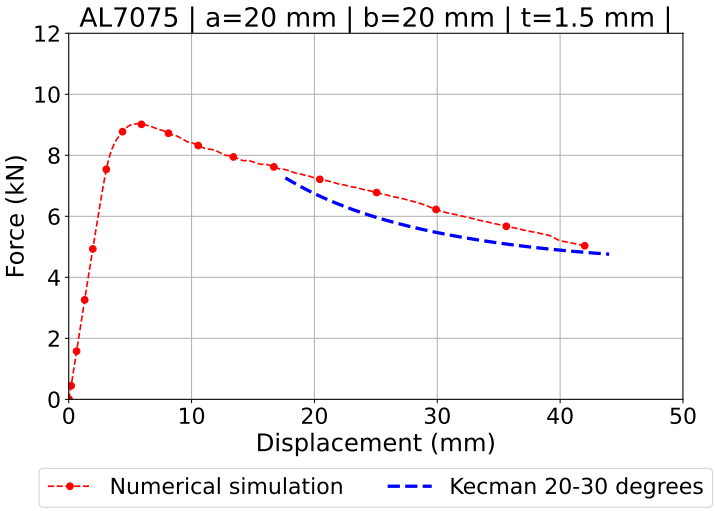

(b) AL7075: a,b=20mm and t=1.5mm

Figure 3.16.: Comparison of force-displacement curve from numerical simulation and spring-linkage model – **continued on next page**

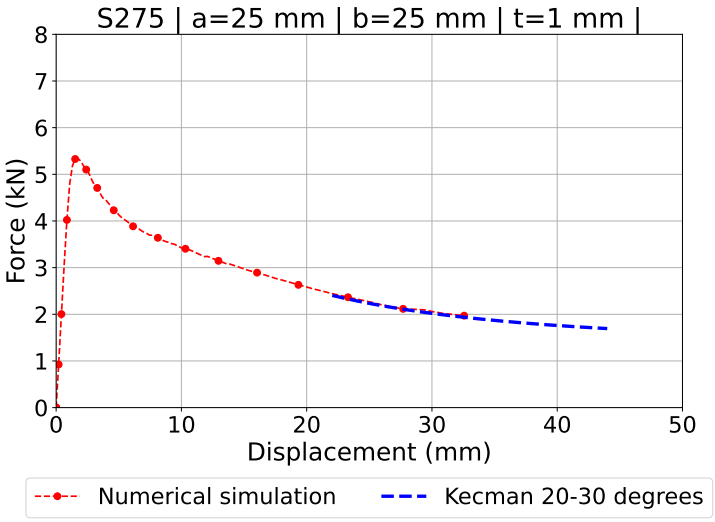

(c) S275: a,b=25mm and t=1mm

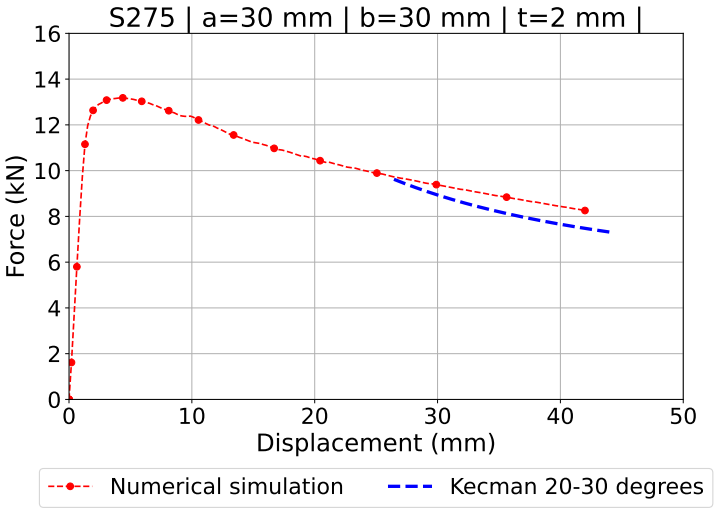

(d) S275: a,b=30 mm and t=2mm

Figure 3.16.: Comparison of force-displacement curve from numerical simulation and spring-linkage model

from point A to line DB with the slope of this line being equal to $-DFm_{rise}$, where Drop Factor (DF) is a factor with value between 0 and 1. Although DF may be chosen arbitrarily within [0,1], a value of DF=1/3 was found to be effective for curves plotted in mm and kN.

Subsequently, Point B_1 is calculated such that length(B_1B_2)=length(AB_2). Perpendiculars are then extended from point A and point B_1, and the intersection point C_{arc} is calculated. The transition is then given by arc(AB_1) followed by line B_1B.

2. **Transition case-2** ($x_A < x_B$ and $m_{AB} \geq m_{DB}$): If slope of line AB is greater than line DB, the transition is simply defined by the straight line joining point A and B (line AB).

3. **Transition case-3** ($x_A \geq x_B$: This case is generally observed for stockier samples with $t/c \geq 0.1$ which fail at peak force equal to $F_{p_{SA-flow}}$. For such cases, Kecman curve intersects curve OA. The complete force-displacement curve is then simply given by finding the x coordinate of the intersection point and trimming the curves from spring-linkage model and Kecman model such that:
   - Curve OA is trimmed by keeping values between $0 \leq x \leq x_{intersection}$.
   - Complete curve from Kecman model is trimmed by keeping values where $x \geq x_{intersection}$. The whole Kecman curve is used to ensure intersection is detected even for cases where y coordinate of point B is smaller than y coordinate of intersection ($y_B < y_{intersection}$).

Two curves are presented, one each for transition-1 Figure 3.18a and transition-2 Figure 3.18b are presented. The three parts from spring-linkage model, transition and Kecman are presented in different colors.

3.6. Results and discussions

This section presents the comparison of results between the dataset and analytical models. Subsection 3.6.1 presents a comparison between existing analytical models and dataset. Subsection 3.6.2 presents a comparison between semi-analytical model (spring-linkage, transition and Kecman model) and the dataset for square tubular structures. And Subsection 3.6.3 presents the comparison between semi-analytical model and dataset for rectangular tubular structures.

3.6.1. Comparison with existing analytical models

Numerical results were compared against analytical models presented in section 3.2. The results from the various models are discussed:

1. **Kecman model (subsection 3.2.1**): Results from Kecman model were observed to be the most accurate at higher values of displacement. The tangent method for connecting the point for maximum force with the collapse

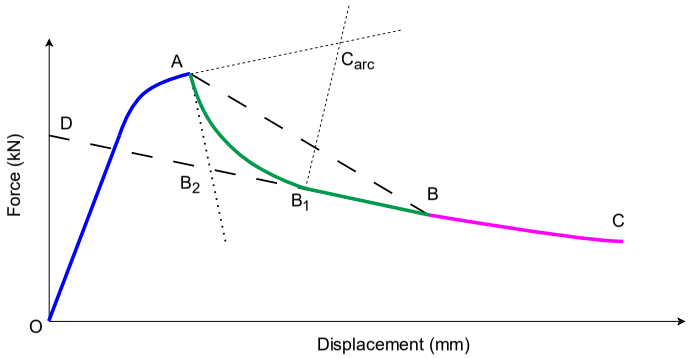

(a) Transition case-1

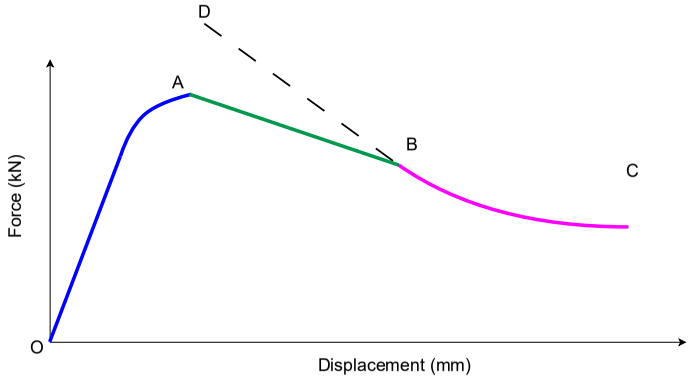

(b) Transition case-2

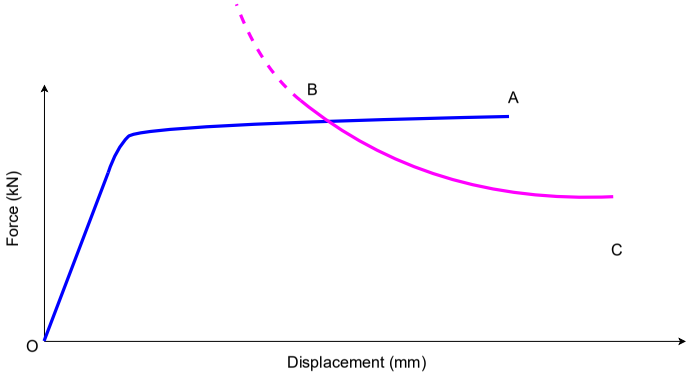

(c) Transition case-3

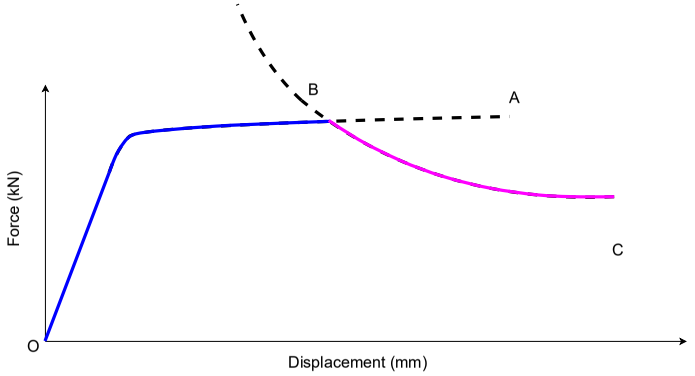

(d) Transition case-3: final curve

Figure 3.17.: Comparison of force-displacement curve from numerical simulation and spring-linkage model

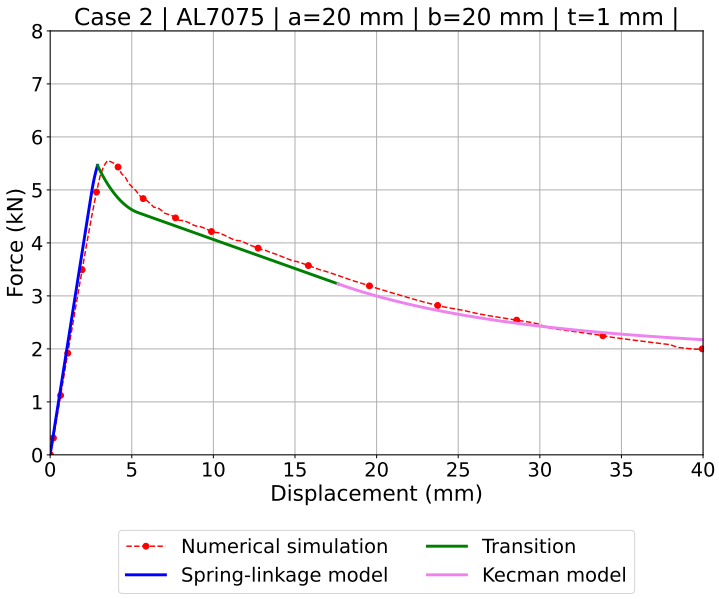

(a) AL7075 | c=20mm | t=1mm

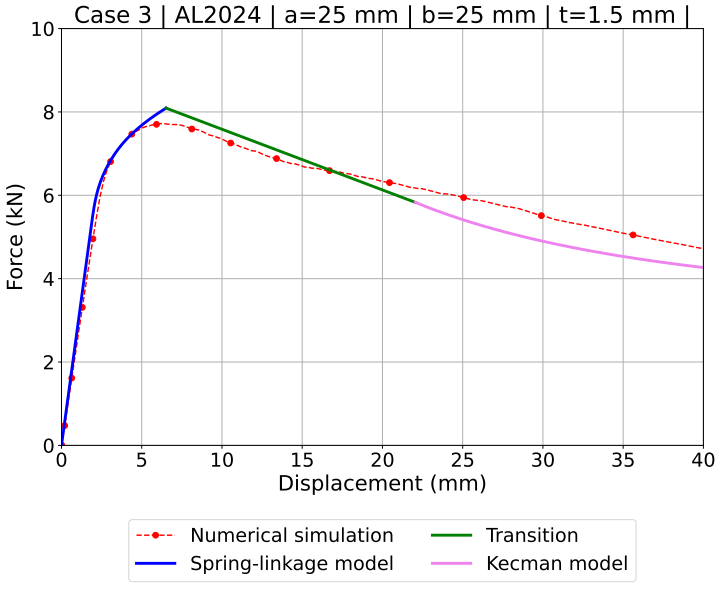

(b) AL2024 | c=25mm | t=1.5mm

Figure 3.18.: Examples for transition case-1 and case-2

curve was observed to be inconsistent, it gave good agreement with numerical data (Figures 3.19b and 3.19c), under prediction (Figures 3.19a,3.19d and 3.19e) and also over prediction for some cases (Figure 3.19f). From the results it can be seen that the model performance drops for samples which display pronounced plastic regions (Figures 3.19d and 3.19e) or cases which undergo a sharp collapse after peak (Figure 3.19f). The model fails for tubes with high t/b ratios (Figure 3.19a) because of the dominant plastic region and no modelling mechanism to capture the plastic stage.

2. **Kim and Reid model (subsection 3.2.3**): The model from Kim et al. was observed to give very similar results to the model from Kecman. With under-prediction for cases with pronounced plastic zones (Figures 3.19d and 3.19e),slight over prediction (Figures 3.19b and 3.19f) for initial collapse and good agreement with numerical results (Figure 3.19c). This model also fails for tubes with high t/b ratios (Figure 3.19a).

3. **Wierzbicki model (subsection 3.2.2**): As mentioned earlier, it was reported by Kim et al. [32] that they failed to reproduce the results given by Wierzbicki et al. [31]. Attempts made in this paper failed to reproduce the results as well subsection 3.2.2. The results from the model were also observed to be inaccurate as compared to the numerical results.

While Kim and Reid model is purely theoretical, Kecman model employs an empirical relationship for the rolling radius. Despite this difference, Kecman model was found to provide accuracy comparable to that of Kim and Reid model. However, the Kim and Reid formulation requires numerical optimization to determine the parameters H and r, resulting in higher computational cost. Given that Kecman model produced similar force–displacement predictions despite its use of an empirical rolling radius, it was therefore selected for predicting the force–displacement response for $\theta \geq 20°$.

3.6.2. Comparison between dataset and semi-analytical model for square tubular structures

Comparison of force-displacement curves obtained from the semi-analytical model and the numerical campaign are presented in Figure 3.20 (for other cases, see Table Figure B.2). Close global agreement was obtained between the numerical and semi-analytical force-versus-displacement curves.

For samples with $t/b \geq 0.1$, the plastic part is predicted with good accuracy by the spring-linkage model, however the following decrease in force is not correctly captured by the proposed model, therefore caution is advised when applying this model to tubes with high t/b ratios.

Similarly for cases where sudden collapse in force beyond peak is observed, the accuracy of drop is not exact. The drop in proposed model is controlled by the factor DF which is chosen to be a value between 0 and 1. A more detailed study of the transition zone will be required to further improve the accuracy of the model, either by better calibration of DF or more suitable transition laws.

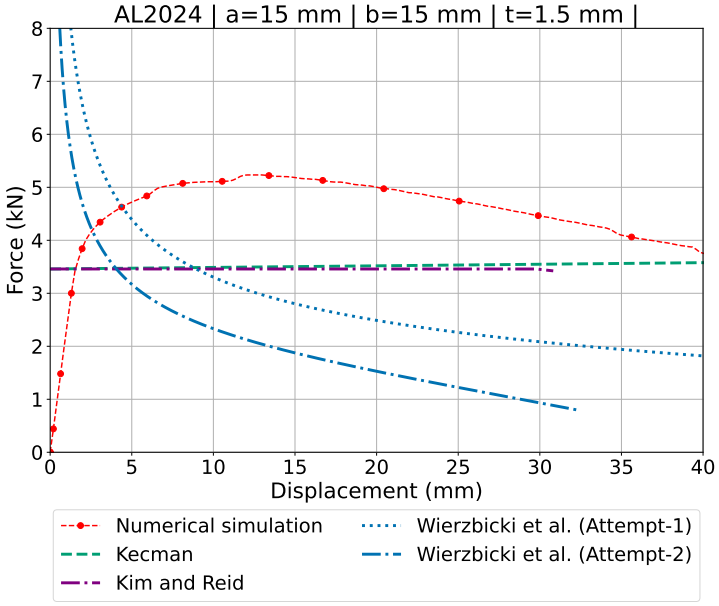

(a) AL2024 | c=15mm | t=1mm

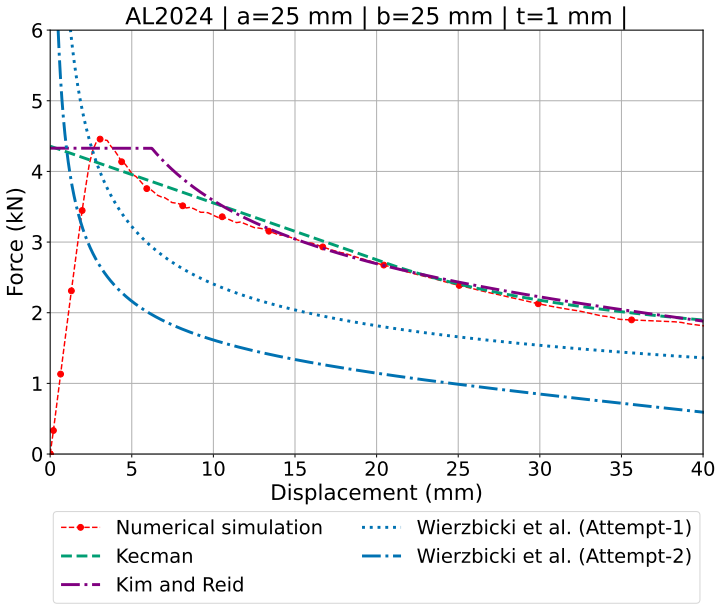

(b) AL2024 | c=25mm | t=1mm

Figure 3.19.: Comparison of numerical force-displacement curve and force-displacement curve from analytical models – **continued on next page**

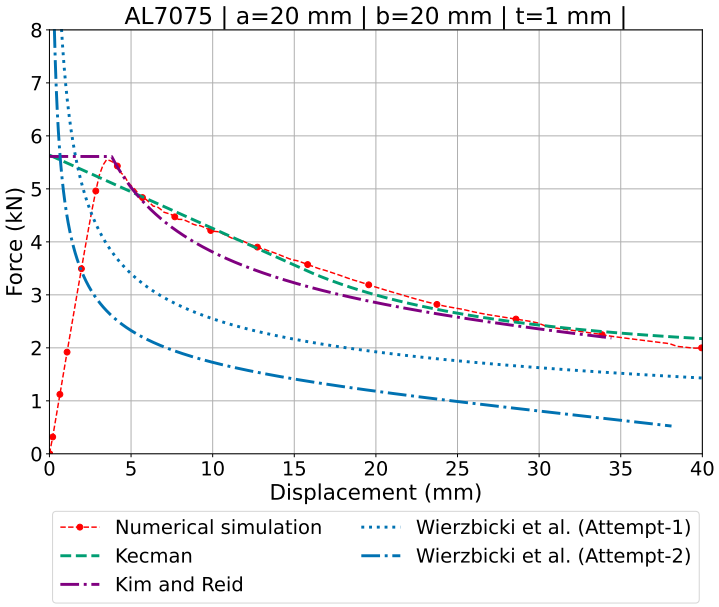

(c) AL7075: a,b=20mm and t=1mm

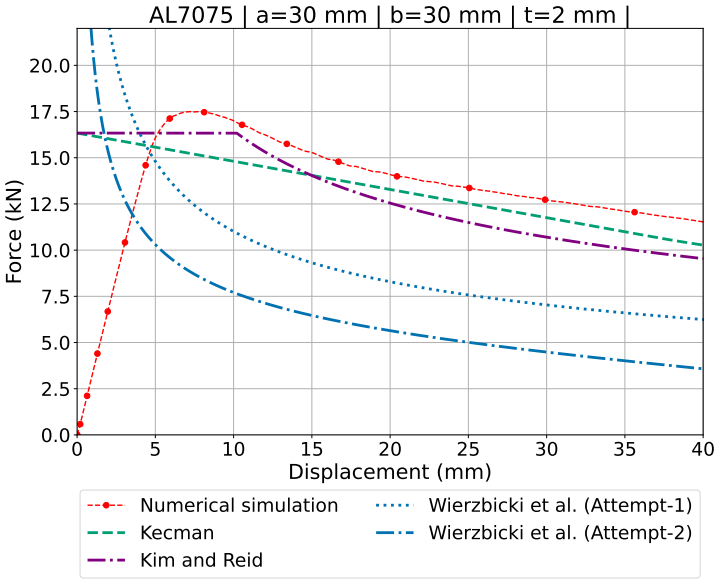

(d) AL7075: a,b=30 mm and t=2mm

Figure 3.19.: Comparison of numerical force-displacement curve and force-displacement curve from analytical models – **continued on next page**

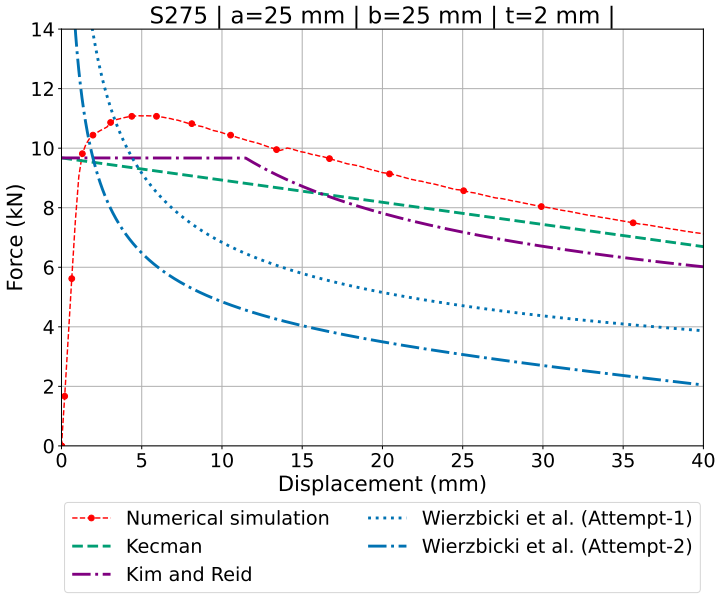

(e) S275: a,b=25mm and t=2mm

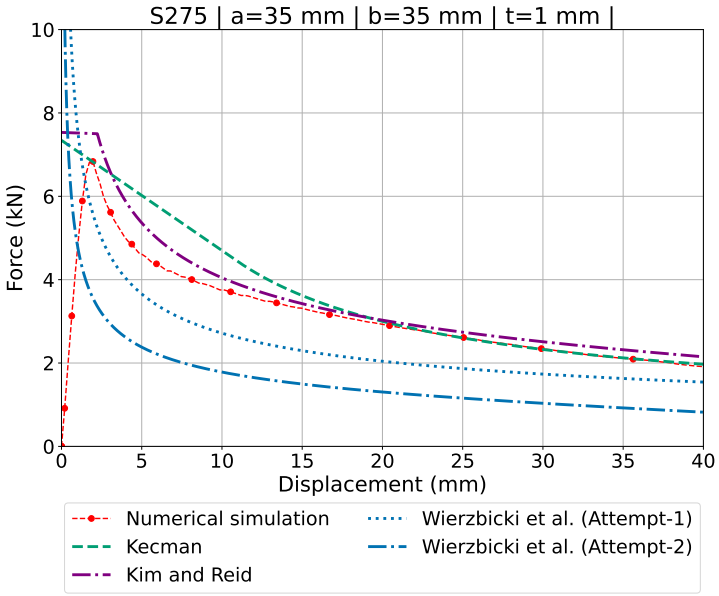

(f) S275: a,b=35 mm and t=1mm

Figure 3.19.: Comparison of numerical force-displacement curve and force-displacement curve from analytical models

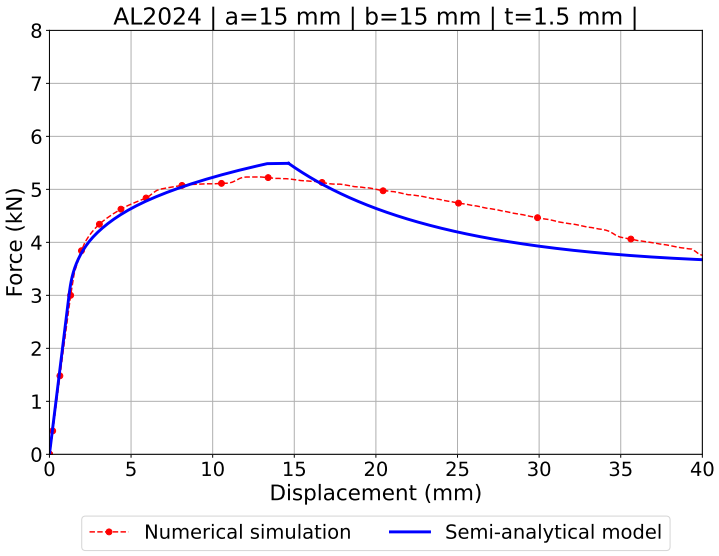

(a) AL2024 | a,b=15mm | t=1mm

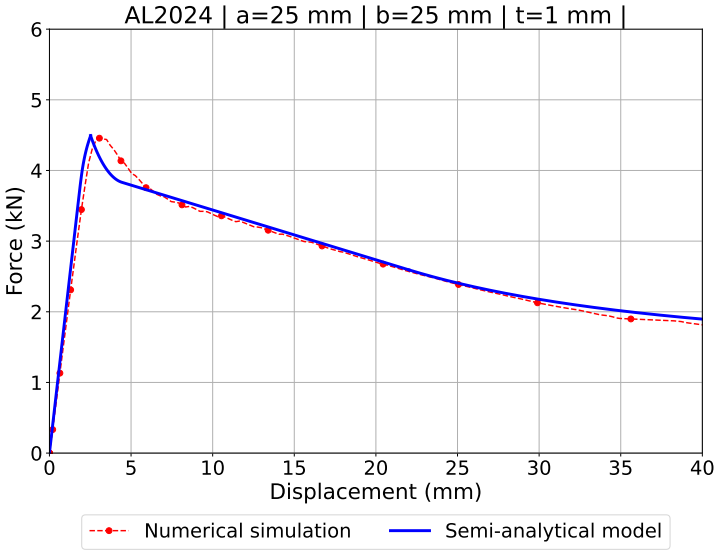

(b) AL2024 | a,b=25mm | t=1mm

Figure 3.20.: Comparison of numerical force-displacement curve and force-displacement curve from proposed semi-analytical model for square tubular structures – **continued on next page**

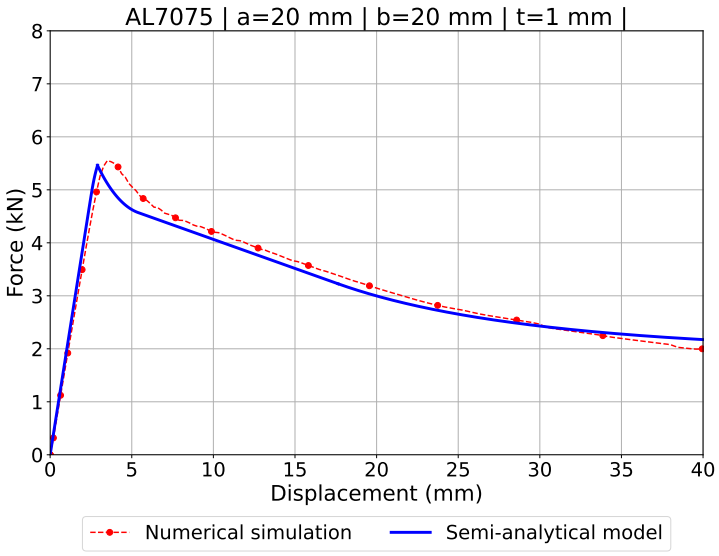

(c) AL7075: a,b=20mm and t=1mm

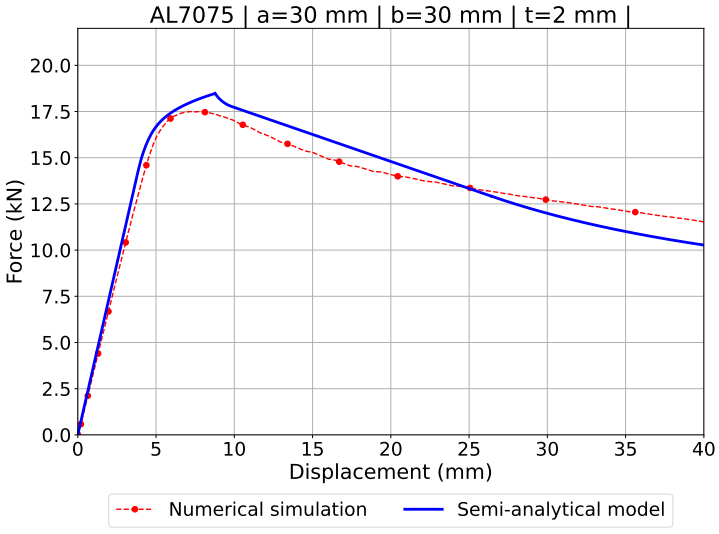

(d) AL7075: a,b=30 mm and t=2mm

Figure 3.20.: Comparison of numerical force-displacement curve and force-displacement curve from proposed semi-analytical model for square tubular structures – **continued on next page**

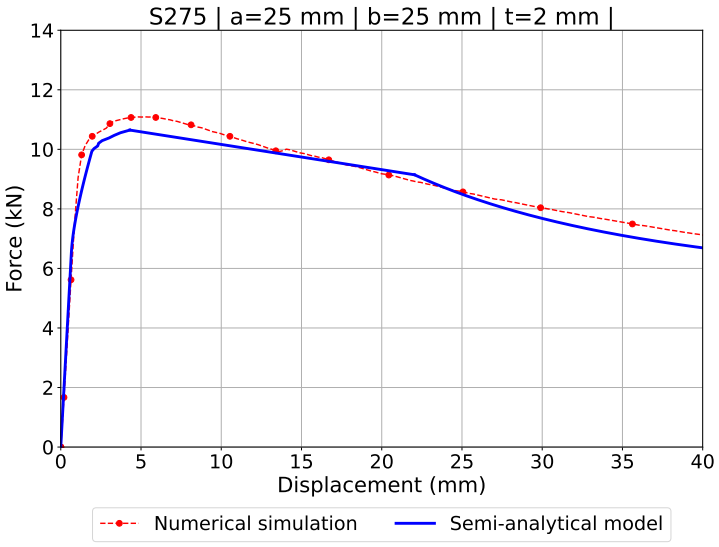

(e) S275: a,b=25mm and t=2mm

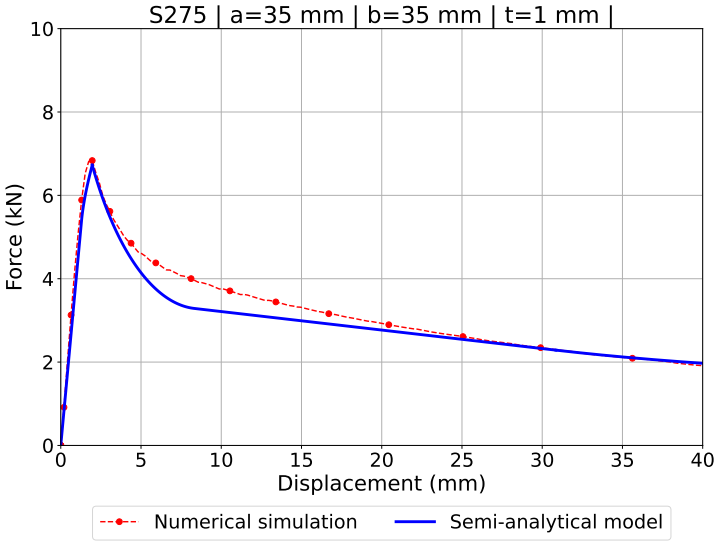

(f) S275: a,b=35 mm and t=1mm

Figure 3.20.: Comparison of numerical force-displacement curve and force-displacement curve from proposed semi-analytical model for square tubular structures

3.6.3. Comparison between dataset and semi-analytical model for rectangular tubular structures

The semi-analytical model was also compared against numerical results for rectangular tubular structures, 4 cases are presented here (for other cases refer Table Figure B.2, subfigures: p-t). Close agreement was obtained for these configurations as well (Figure 3.21). No changes were made to the model, except for geometrical inputs. Similar to the case of square tubular structures, for samples with high t/b ratios, the semi-analytical model showed good agreement up to the elastic-plastic deformation stage but deviation is observed once the drop in load initiates (Figures 3.21a and 3.21c).

3.6.4. Peak force and absorbed energy

Peak force and absorbed energy from the semi-analytical model were compared against data obtained from the semi-analytical model, a coefficient of determination R^2 value of 0.99 was observed for both cases, see Figure 3.22. The error for the majority of cases was within $\pm 10\%$ with mean error for peak force being 3.78% and absorbed energy being 4.43%.

3.6.5. Comparison between dataset and experimental results from literature

Finally, the model was compared with experimental data of 4 configurations collected from the literature to ensure the model can predict force-displacement curves for other materials which were not a part of the model development study. For this, one case was taken from Zhang et al. [85] and 3 cases from Farfan et al. [76]. While all the cases from Farfan et al. use S275, the plastic part of stress-strain curves were found to be substantially different for each case. The stress–strain and force–displacement relationships were reconstructed by digitizing figures from the literature using [81]. As a result, unlike previous cases in which both the numerical and semi-analytical models were based on identical curve definitions, discrepancies between the literature data and the semi-analytical predictions may partly arise from errors induced by the digitization process. The comparisons are presented in Figure 3.23.

For the case from Zhang et al. (Figure 3.23a), the maximum moment prediction was observed to be inaccurate which could be an outcome of the very ductile stress-strain curve for this material. However, the rest of the curve was observed to be reasonable for use in preliminary design.

As discussed in subsection 3.3.2, the results where semi-analytical model predicted a much higher peak force (Figure 3.23b), a scaling was applied to compensate for the absence of fillets in the semi-analytical model. The scaled results were found to be in agreement with the numerical results indicating that the semi-analytical model can be extended to filleted tubes if a methodology to reliably calculate the drop in peak force due to fillet can be determined.

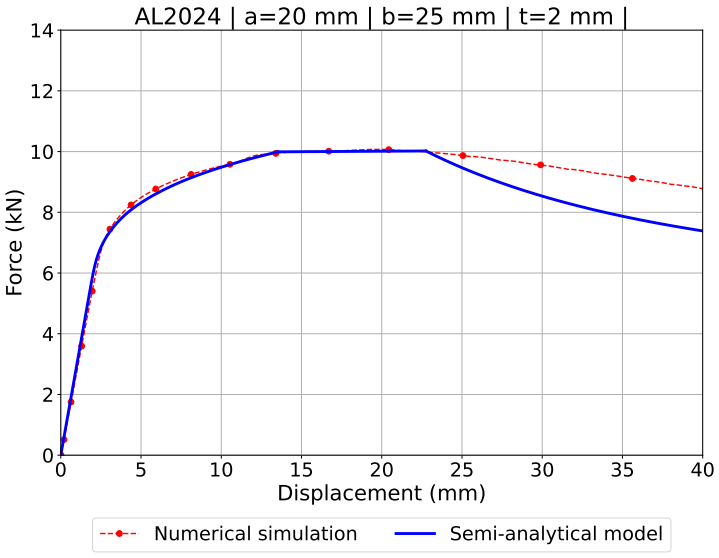

(a) AL2024 | a=20mm | b=25mm | t=2mm

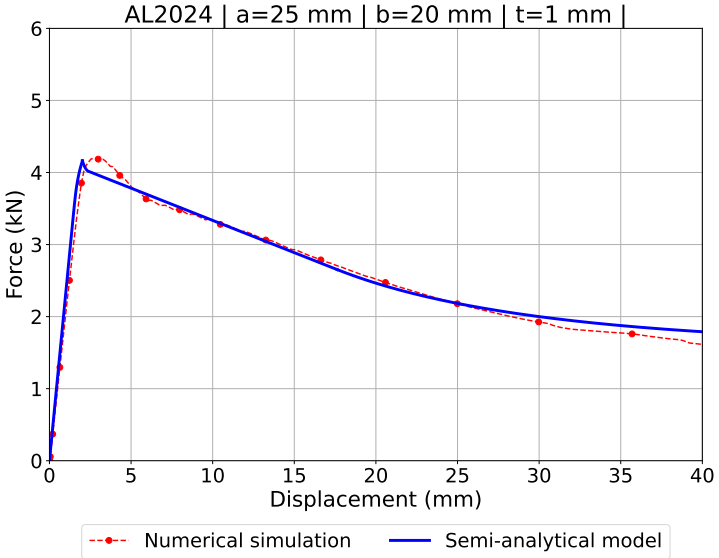

(b) AL2024 | a=25mm | b=20mm | t=1mm

Figure 3.21.: Comparison of numerical force-displacement curve and force-displacement curve from proposed semi-analytical model for rectangular tubular structures – **continued on next page**

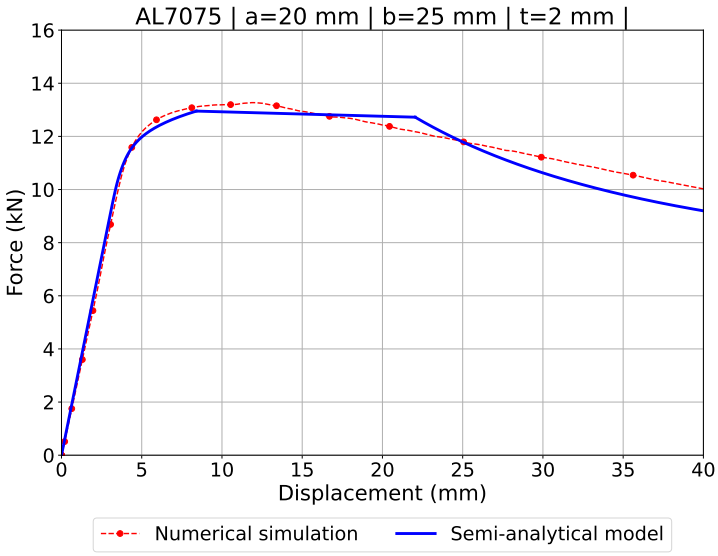

(c) AL7075: | a=20mm | b=25mm | t=2mm

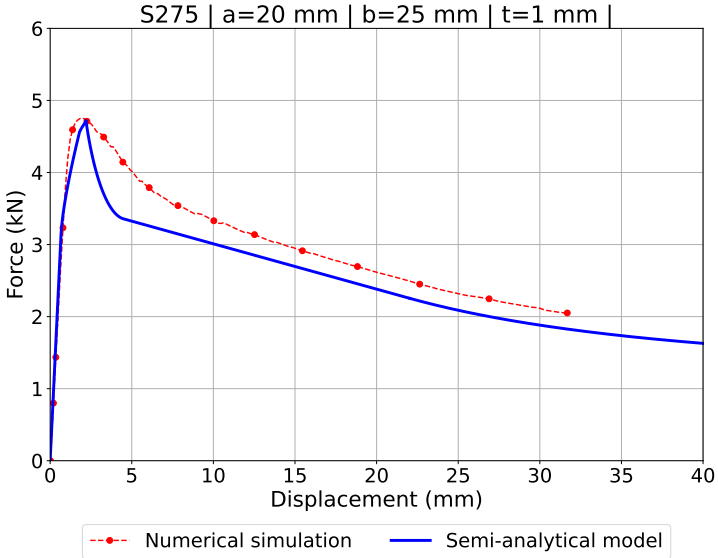

(d) S275: | a=20mm | b=25mm | t=1mm

Figure 3.21.: Comparison of numerical force-displacement curve and force-displacement curve from proposed semi-analytical model for rectangular tubular structures

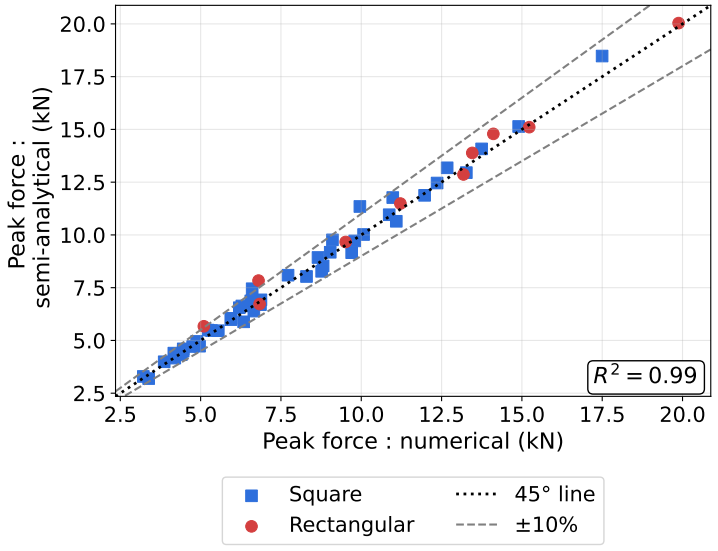

(a) Peak force comparison

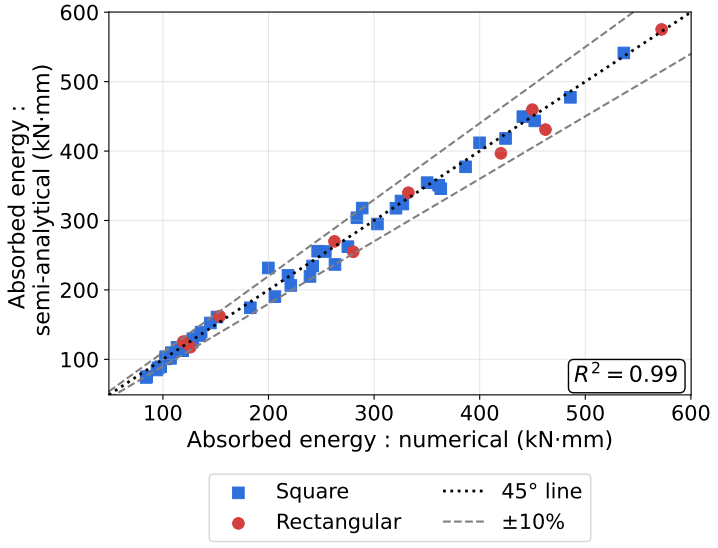

(b) Absorbed energy comparison

Figure 3.22.: Comparison between peak force and absorbed energy between semi-analytical model and numerical results

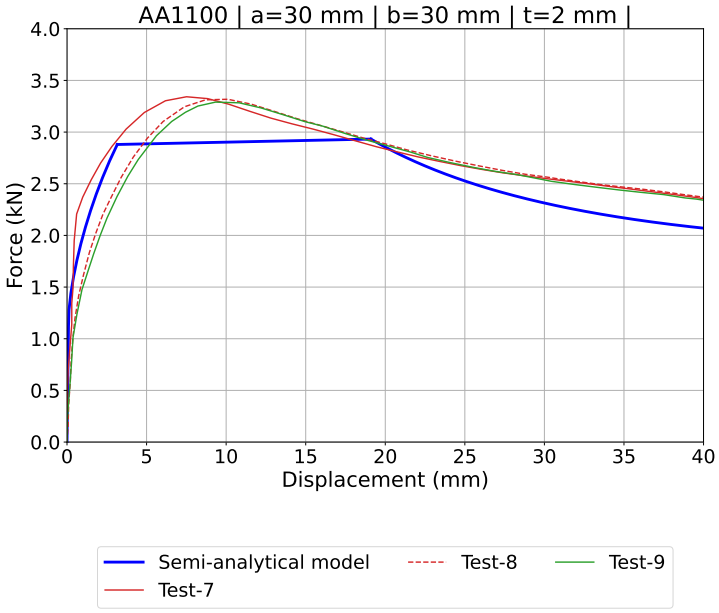

(a) AA1100 | a=30mm | b=30mm | t=2mm

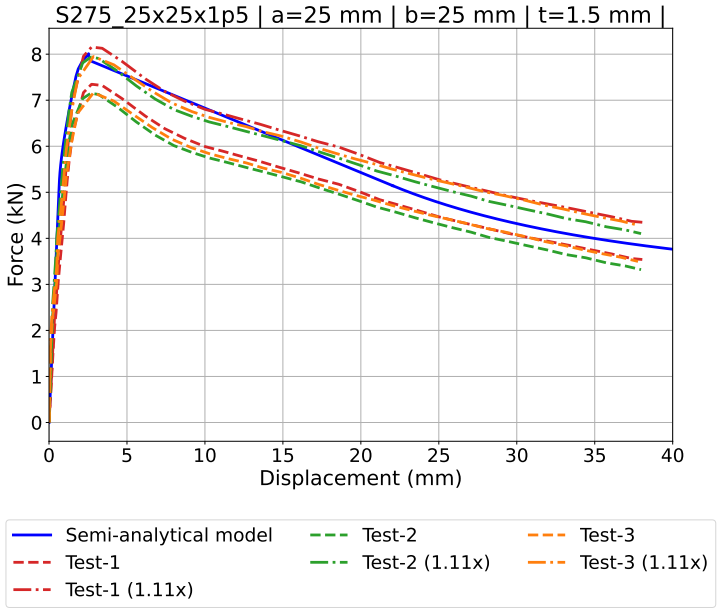

(b) S275 | a=25mm | b=25mm | t=1.5mm

Figure 3.23.: Comparison of experimental force-displacement curve from literature and force-displacement curve from proposed semi-analytical model – **continued on next page**

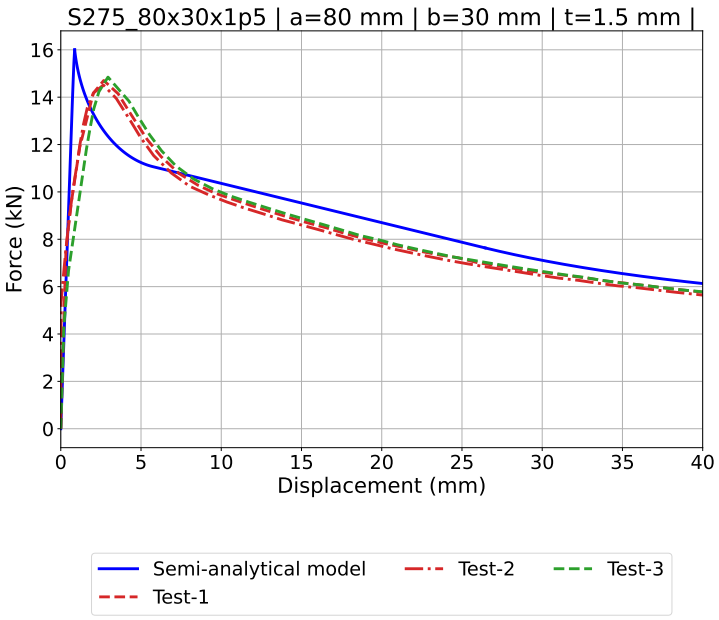

(c) S275 | a=80mm | b=30mm | t=1.5mm

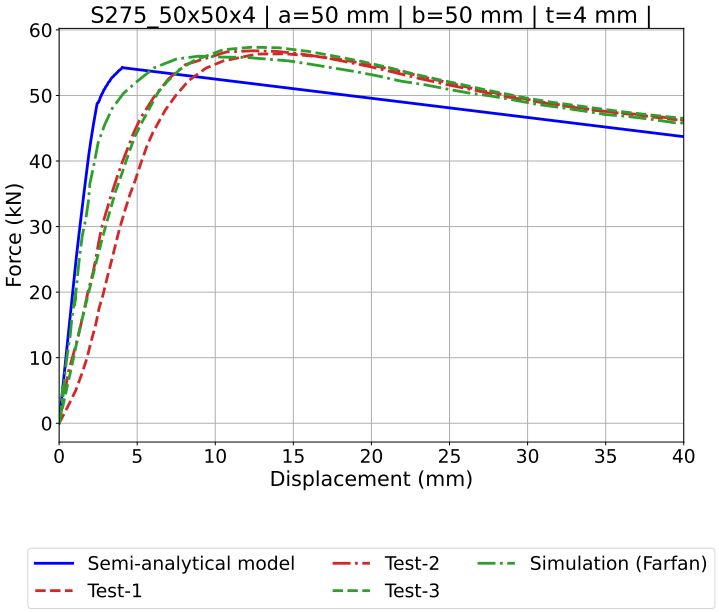

(d) S275 | a=50mm | b=50mm | t=4mm

Figure 3.23.: Comparison of experimental force-displacement curve from literature and force-displacement curve from proposed semi-analytical model

3.7. Conclusions

A study of existing models for bending collapse was conducted, the model from Kecman (subsection 3.2.1) and Kim-Reid model (subsection 3.2.3) were observed to be in close agreement with the dataset at high rotations, whereas the model from Wierzbicki (subsection 3.2.2) could not be reproduced. Since these models were intended for moment-rotation prediction for thin steel tubular structures, they were also observed to be especially inaccurate for thicker aluminum samples which display a pronounced elastic-plastic deformation stage (Figure 3.1).

In the present work, a semi-analytical model using a spring-linkage method for elastic and elasto-plastic stages, Kecman model for collapse stage and a transition algorithm has been proposed. The semi-analytical model was tested against a numerical dataset, and was shown to be more accurate than other existing analytical models at predicting force-displacement curves for collapse of square and rectangular tubular structures ($R^2 = 0.99$ for peak force and absorbed energy). However, it must be noted that for samples with $t/b \geq 0.1$, the predicted post-peak response can be inaccurate (for example: Table Figure B.2, subfigures: a,f,k and l). This discrepancy is observed because these configurations do not fail with bending collapse and instead undergo a smooth decrease in force-displacement response due to plasticity and subsequent ovalization of the cross-section.

On a standard desktop, the run time averaged between 2-3 seconds per configuration with material stress-strain curve and geometry as inputs and force-displacement response as the output. The near instantaneous run-time indicates that the model lends itself naturally to design space exploration applications in early stages of the design process.

Some areas for further possible development of semi-analytical model are listed below:

1. For thicker tubes, modelling the decrease in force-displacement response due to plasticity and ovalization.
2. Development of better transition laws for transition case-1, to remove dependence on drop factor (DF).
3. Methodology to reliably calculate the drop in peak force due to presence of fillet.

4

Three-point bending of GLARE laminates

This paper investigates 3-point bending failure of five different types of GLARE laminates (2A, 2B, 3, 4A and 4B). 73 configurations (419 specimens), with different stacking sequences and aluminum layer thicknesses are tested. Failure mechanisms, effect of stacking sequence, effect of aluminum rolling direction, effect of displacement rate and energy absorption are analyzed. Configurations with predominantly 0° *glass fiber layers fail with delamination as the major failure mode, while configurations with predominantly* 90° *glass fiber layers fail with central cracking as the major failure mode. GLARE 3, with 1:1 ratio of* 0° *and* 90° *fibers, fail with an equal mix of delamination and central cracking. A semi-analytical framework that can be used to predict the force versus displacement curve for central cracking failure is proposed and validated.*

This chapter has been copied verbatim from the paper published in Composites part-C: Open access, "Failure modes and energy absorption in Glass Reinforced aluminum (GLARE) hybrid laminates subjected to three-point bending", **Volume 18**, (October, 2025) [93]. Some additions have been made based on the recommendations of the thesis review committee.

Note on Collaboration

The experimental campaign for the GLARE laminate three-point bending tests presented in this chapter was executed by Pranshul Gupta and Nachiket Dighe, who provided technical assistance for this research. The author was responsible for the post-test documentation, the comprehensive data processing, and the development of the semi-analytical model.

Nomenclature

b	Span for 3-point bending tests
dx	Length of element in spring linkage model
$\dot{\delta}$	Displacement rate
ε_{max}	Strain at farthest fiber from neutral axis
h	Thickness of specimen
L	Length of specimen
ρ	Radius of curvature
ρ_{Al}	Density of aluminum
$\rho_{prepreg}$	Density of Uni-Directional (UD) prepreg
R^2	Coefficient of determination
SEA	Specific energy absorption
θ	Angle of rotation
w	Width of specimen
z_{max}	Distance of fiber farthest from the neutral axis

4.1. Introduction

GLARE (GLAss REinforced aluminum laminate) laminates are composed of alternating layers of aluminum and glass fiber, offering several superior properties over traditional aluminum alloys which include excellent fatigue characteristics, high strength-to-weight ratio, high corrosion resistance and a high tolerance to impact damage. These attributes have led to the usage of GLARE laminates in a variety of aerospace applications: upper fuselage skin and empennage leading edge in Airbus A380 [94], cargo liner for regional jet aircraft [94], straps for Airbus A400M fuselage frames [95] and forward bulkhead for the Learjet 45 business jet [96].

Certification for crashworthiness is a prerequisite before any aircraft can enter service, this means that an aircraft should be able to absorb impact energy while keeping the deceleration within acceptable limits. However, unconventional designs (such as the flying-V) which combine the lifting (wings) and load bearing (fuselage) structures of the aircraft to achieve higher fuel efficiency pose a difficult challenge for crashworthiness. Since, the fuselage of such aircraft shares the same structure as the wing, the fuselage needs to be "ovalized" [8] in order to maintain the airfoil shape which leads to a significant reduction in the available stroke length below the passenger floor (Figure 4.1). Due to their excellent mechanical properties, GLARE

laminates could provide an efficient solution for crashworthiness of unconventional aircraft. As bending is one of the major failure mechanisms that dissipate impact energy in event of a crash, this paper aims to evaluate the failure mechanism and energy absorption characteristics of GLARE laminates subjected to three-point bending loads.

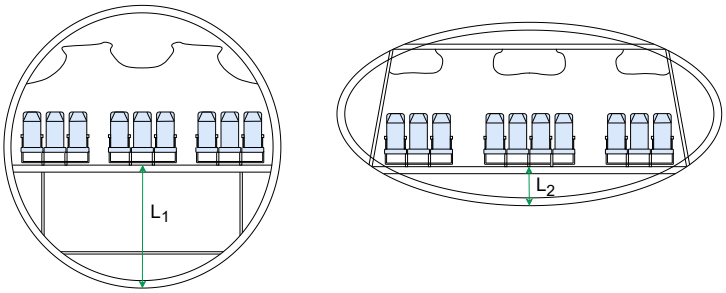

Figure 4.1.: Comparison between Airbus A350 (left) [9] and Flying-V fuselage cross section (right) [8]

Several studies have been conducted on 3-point bending of GLARE laminates. Liu et al. [97] studied the behaviour of GLARE laminates subjected to short beam 3-point bending tests with the aim of determining the interlaminar shear strength of the laminates.Liu et al. [97] used GLARE-2A, GLARE-3 and GLARE-6 specimens consisting of three aluminum alloy sheets of 0.3mm thickness and two composite layers. The authors conducted short beam bending tests for all 3 configurations, varying the span/thickness (b/h) ratio. The specimens were tested at b/h=5,8,10 and 12. At b/h=5, all specimens failed in a localized compression-deformation failure mode, however specimens with span/thickness ratio (b/h)≥8 were much more likely to exhibit local bending failure. For GLARE 2A and 6, Liu et al. [97] also report damage propagation to the end of the specimen for span/thickness ratio greater than 8.

Li et al. [98] studied the bending damage behavior of GLARE laminates by conducting three-point bending of GLARE-2A and GLARE-3 with different layer configurations (3/2, 4/3, 5/4 and 6/5, a layer configuration of 3/2 corresponds to 3 layers of aluminum with 2 glass-fiber prepreg layers). It was observed by Li et al. [98] that loading nose radius and dimension of the specimen (length and width) have no significant effect on bending strength, however b/h ratio was shown to have significant effect on both bending strength and failure mechanism. Four failure stages were observed by Li et al. [98] for bending of GLARE laminates:

1. Stage-I: Elastic stage
2. Stage-II: Plastic stage
3. Stage-III: Local failure of fiber

4. Stage-IV: Delamination stage

Kumar et al. [99] studied the effect of aluminum layer thickness on GLARE laminates and noted a 60% increase in the load bearing capacity when the thickness is increased fom 0.2mm to 0.35mm. Solyaev et al. [100] investigated thick GLARE laminates with varying b/h ratios under 3-point bending to determine elasto-plastic behavior and flexural strength, and also analyzed bending of GLARE specimens using a meso-scale finite element model. It was observed by Soyvalev et al. [100] that the main failure mechanism in slender specimens under bending is compression failure in the glass fiber layer followed by progressive delamination or instantaneous delamination-buckling.

The present study aims at characterizing the effect of various parameters (rolling direction, displacement rate and stacking sequence) on failure mechanism, peak load and energy absorption of GLARE laminates subjected to 3-point bending. A total of 419 specimens consisting of 5 types of GLARE are tested at varying displacement rates (1,10,100 and 1000 mm/min) and orientation (longitudinal and transverse), the number of specimens tested for each configuration is presented in Table 4.1.

4.2. Materials and Methods

4.2.1. Material data

Five different types of GLARE (2A, 2B, 3, 4A and 4B) with varying number of layers and aluminum layer thicknesses are tested. Table 4.1 provides a comprehensive list of GLARE configurations, also presenting the stacking sequence, number of aluminum/prepreg layers, thicknesses and main beneficial characteristics [101] of each configuration. To aid the reader in understanding the presented data, the schematic diagrams of Figure 4.2 are used to illustrate the tested orientations, and are presented as inset with the graphs. Each inset presents the laminate lay-up from the outer surface down to (but not including) the second aluminum layer. Each GLARE laminate consists of alternating aluminum and glass fiber layers, with aluminum layers on both the outermost surfaces and each glass fiber layer consisting of two or three prepregs [101]. Thickness of glass fiber plies has been calculated using the equation:

$$\text{Glass ply thickness} = \frac{\text{Specimen thickness} - \text{No. of Al layers} \times \text{Al layer thickness}}{\text{No. of Glass layers} \times \text{No. of prepregs in each layer}} \tag{4.1}$$

The density values used for the calculations are 2.77×10^{-6} kg/mm^3 for aluminum, and 1.96×10^{-6} kg/mm^3 for glass fiber layers [102].

Material properties for S2-glass fiber/FM94 epoxy resin material and the stress-strain curve for AL2024-T3 are obtained from Hagenbeek [102], with the data presented in Table 4.2 and Figure 4.3.

S.No.	Type	Stacking	Main beneficial characteristics [101]	No. of layers	No. of glass prepregs	Aluminum layer thickness (mm)	Specimen thickness (mm)	Glass ply thickness (mm)	Number of specimens tested per displacement rate (mm/min)				
									Or.	1	10	100	1000
1	2A	0°/0°	fatigue, strength	4/3	2	0.2	1.60	0.13	L	-	6	-	-
									T	-	7	-	-
2				4/3	2	0.3	2.02	0.14	L	5		-	-
									T	5		-	-
3				8/7	2	0.4	5.08	0.13	L	5	5	-	-
									T	7	7	-	-
4	2B	90°/90°	fatigue, strength	7/6	2	0.4	4.49	0.14	L	-	-	6	5
									T	-	-	6	5
5				11/10	2	0.3	6.00	0.13	L	7	6	11	5
									T	-	6	-	-
6	3	0°/90°	fatigue, impact	3/2	2	0.3	1.49	0.15	L	5	6	5	5
									T	5	5	5	5
7				5/4	2	0.4	2.98	0.12	L	5	5	6	5
									T	5	5	5	6
8				6/5	2	0.3	3.18	0.14	L	6	5	-	-
									T	7	6	-	-
9				8/7	2	0.4	5.19	0.14	L	5	5	5	5
									T	6	6	-	-
10	4A	0°/90°/0°	fatigue, strength in 0° direction	7/6	3	0.4	5.20	0.13	L	9	5	5	5
									T	5	5	5	5
11	4B	90°/0°/90°	fatigue, strength in 90° direction	4/3	3	0.4	3.01	0.16	L	-	-	7	6
									T	-	-	6	5
12				6/5	3	0.5	4.99	0.13	L	6	11	6	5
									T	6	12	6	4
13				7/6	3	0.4	5.20	0.13	L	5	5	5	5
									T	5	5	5	5
14				8/7	3	0.4	5.82	0.12	L	-	-	6	-
									T	-	-	6	-

Table 4.1.: Configurations of the tested GLARE specimens

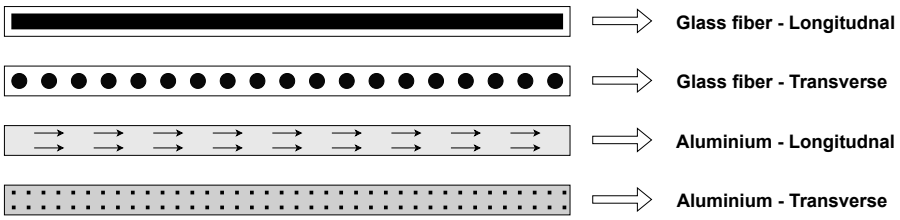

Figure 4.2.: Schematic diagrams for glass fiber and aluminum layers

Table 4.2.: Material properties for S2-glass fiber/ FM94-epoxy resin

Orientation	Young's modulus (GPa)	Ultimate stress tensile (MPa)	Ultimate stress compressive (MPa)
Longitudinal (0°)	50.6	2273	2250
Transverse (90°)	9.9	32.54	64.87

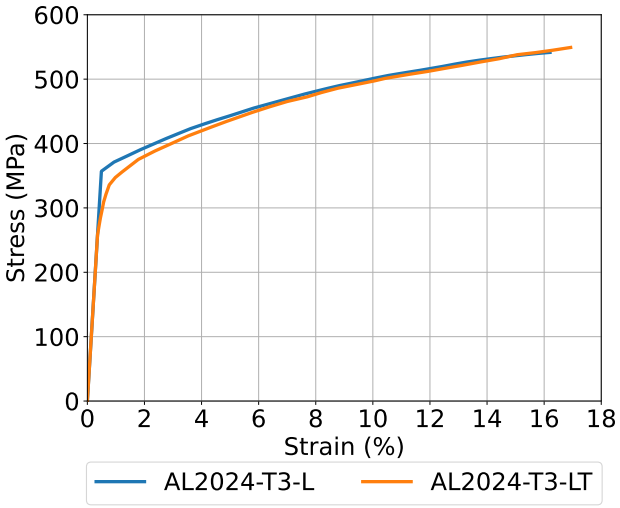

Figure 4.3.: True stress-strain curve for AL2024-T3 in laminated(L) and transverse(LT) directions, plotted using digitized data from [102]

4.2.2. Experimental setup

For 3-point bending tests on GLARE coupons, a standard set-up (single loading pin and two supporting pins), as shown in Figure 4.4, is used. The GLARE coupon is positioned on two stationary steel supporting pins, which are clamped rigidly to the mounting plate in order to eliminate any unintended lateral movement. All the pins had rounded edges with a local radius of curvature of 1.5mm. The distance between the static supports is chosen based on the span of the coupon (b). This separation

is precisely adjusted to ensure the correct span-to-thickness ratio (b/h) for each test.

The span-to-thickness ratio recommended by ASTM D790 and ASTM D7264 [103, 104] is typically in the range of 16 to 60. However, in our case, the maximum separation distance between the supporting pins of the available fixtures was 60mm, which meant that for thicker specimens a value of b/h≥16 was not possible. Due to time and cost constraints, we decided not to manufacture/procure a new fixture and instead selected a span-to-thickness ratio of 10 (b/h=10) based on the maximum thickness observed in the tested specimens (h=6.05mm). A ratio of b/h=10 is also supported by literature, where Liu et al. [97] reported that for GLARE specimens with b/h>8, the deformation is dominated by bending. The choice of b/h=10 ensured that all specimens could be tested at a consistent ratio across configurations. However, for some of the specimens a deviation from this value is possible due to experimental errors. The exact span of each configuration is presented in Appendix C.

For thin specimens, which often exhibited folding behavior, a higher span/thickness ratio is used in order to have adequate clearance with the chamfered surface of the loading pin and for such cases b is fixed to 18 mm. Also, since the maximum separation distance of the static supports is 60mm, the upper limit for b is fixed at 60mm, as shown in Equation 4.2. Load is applied on the test coupon at mid-span ($b/2$) with the loading pin moving downwards at four different displacement rates:$1\ \text{mm}\cdot\text{min}^{-1}$, $10\ \text{mm}\cdot\text{min}^{-1}$, $100\ \text{mm}\cdot\text{min}^{-1}$, and $1000\ \text{mm}\cdot\text{min}^{-1}$.

$$b = \begin{cases} 60\ \text{mm}, & \text{if } h > 6\ \text{mm} \\ 10 \times h, & \text{if } 1.8\ \text{mm} \leq h \leq 6\ \text{mm} \\ 18\ \text{mm}, & \text{if } h < 1.8\ \text{mm} \end{cases} \tag{4.2}$$

All samples were cut to approximately 150 mm in total length. Due to the large number of samples to be prepared, they were carefully cut with a band saw and then hand sanded to remove any burrs and edge flaws, reducing the risk of delamination initiating from the edges. The longer specimen length also served to minimize boundary condition effects in the test setup (e.g., specimen slipping out of the supports). Based on engineering judgment, 150 mm was found to be sufficiently long for reliable testing.

The 3-Point bending setup is installed on the Zwick 10kN/20kN Universal Testing Machine (UTM)[105] at the Delft Aerospace Structures and Materials Laboratory (DASML). A 20kN Zwick load cell is used, with sampling frequencies of up to 25Hz. A pre-load of 5N is applied for displacement rates of 100 mm/min or higher, the pre-loading rate is always carefully matched to the test loading rate. This approach prevented any undesired jerk motion of the loading support during pre-loading. Additionally, a sufficiently large grip separation distance is maintained to ensure the loading support moved downward at a constant vertical speed, without acceleration.

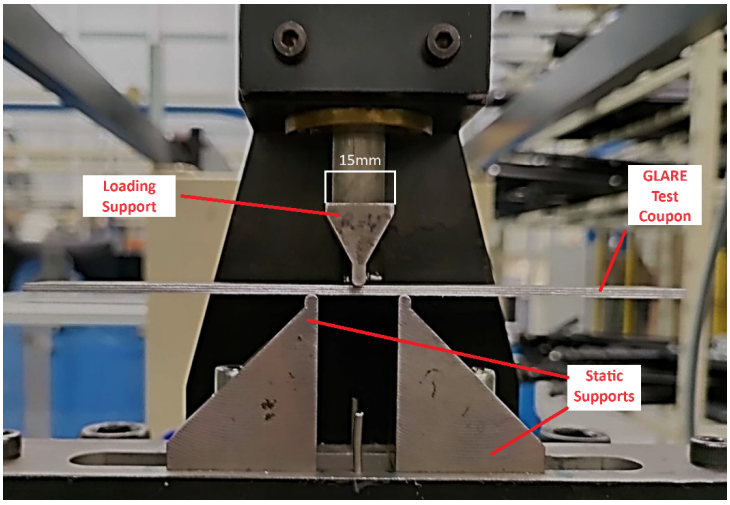

(a) Actual

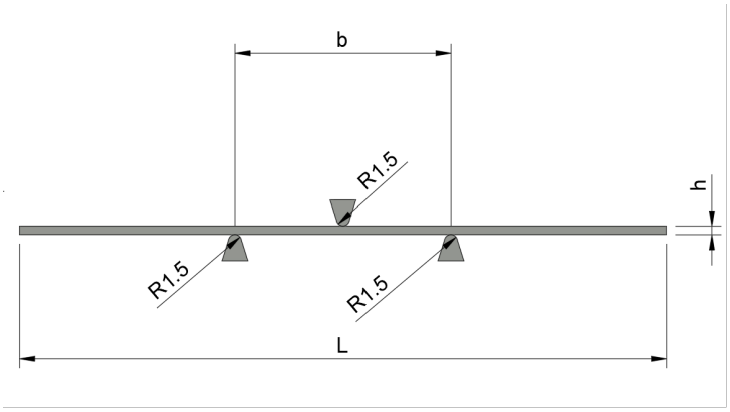

(b) Schematic

Figure 4.4.: 3-Point Bending Test Setup

4.2.3. Semi-analytical model

The finite element method (FEM) is the most commonly used method to simulate 3-point bending of GLARE laminates in the literature [98, 106, 107]. However, such models are computationally expensive and need a more detailed geometry as starting point, being therefore not efficiently suitable as part of a preliminary design and optimization scheme. We propose a fast running semi-analytical model to predict force-displacement curves for GLARE laminates subjected to 3-point bending. The model draws its basic framework from Anand et al. [87], who focused on the bending behaviour of metallic beams, combining analytical calculation of moment versus rotation curves, $M(\theta)$; with a numerical solution to assemble a

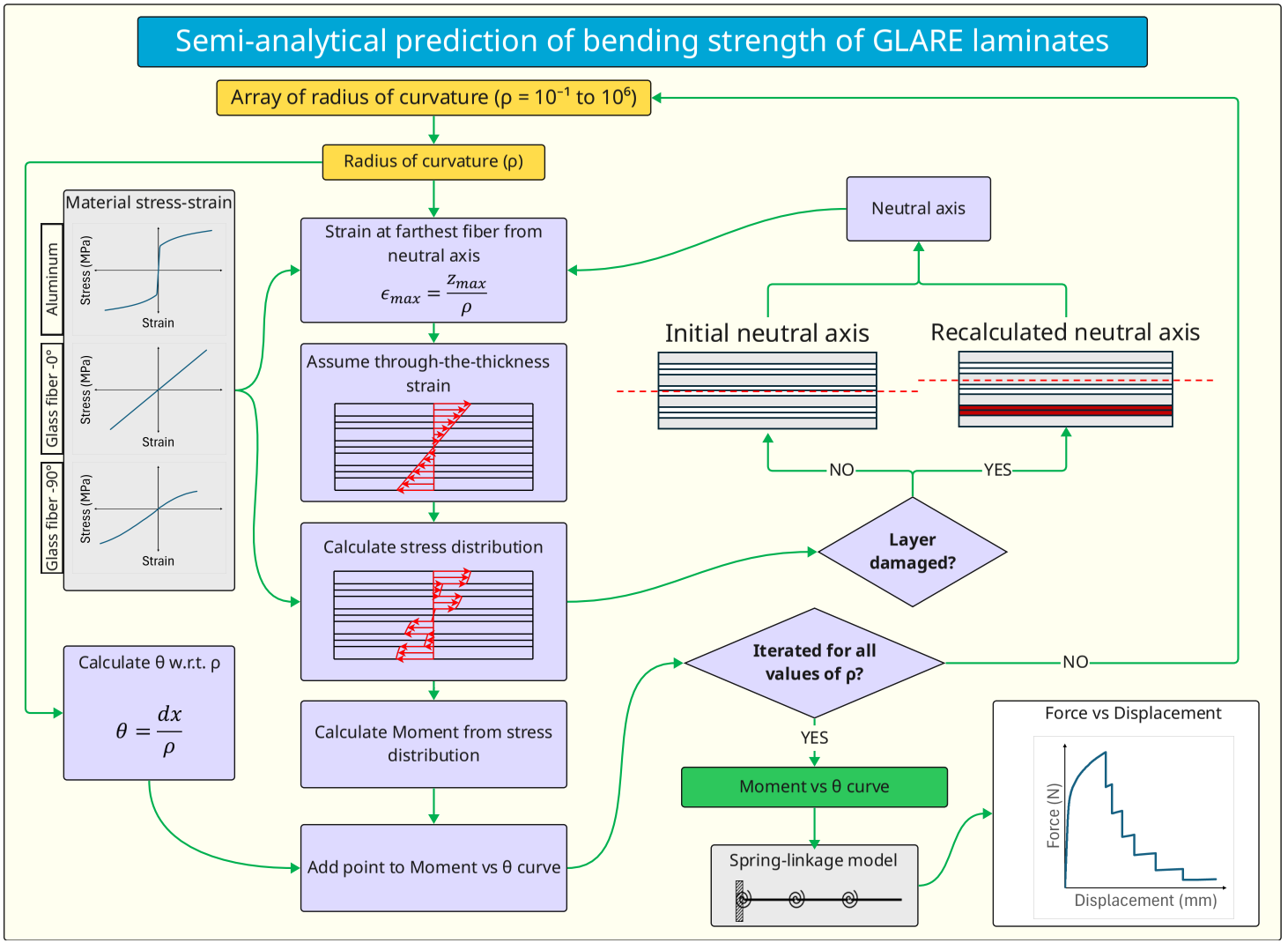

Figure 4.5.: Infographic: Semi-analytical prediction of bending strength of GLARE laminates

spring-linkage model. The model can be best understood using the info-graphic presented in Figure 4.5.

The derivation of the $M(\theta)$ curves follows the following steps:

1. The minimum value of radius of curvature is calculated using $\rho_{min} = z_{max}/\epsilon_{ult}$, where z_{max} is distance of farthest surface from the neutral axis. The maximum value of ρ is assumed to be a very high value $\approx$ 99999, effectively representing an unbent hybrid laminate. The algorithm then iterates from ρ_{min} to ρ_{max}.

2. For a given ρ:
   a) A linear strain distribution across the cross-section is assumed with $\epsilon = 0$ at neutral axis and $\epsilon = z_{max}/\rho$ at fiber farthest from the neutral axis.
   b) A stress distribution is calculated from the strain distribution using a direct lookup on stress-strain curves from aluminum or glass fiber laminate coupons. For aluminum, there is coupon data for laminated and transverse directions; whereas for glass fibers there is coupon data for each fiber orientation herein adopted, i.e. 0°, ±45° or 90°.
   c) The moment is calculated from the stress distribution, and the corresponding θ is calculated from the equation $\theta = dx/\rho$.
   d) Due to the plastic behavior of aluminum, for the aluminum layers the strain distribution is converted to true strain using $\sigma_{true} = ln(1 + \varepsilon_{eng})$, the lookup is then performed using true stress-strain curves, with the area used for the moment calculation adjusted using $Area = A_0/(1 + \varepsilon_{eng})$.

3. Step 2 is repeated for all values of ρ to assemble the $M(\theta)$ curve. The moment at which a transverse fracture of a layer occurs is recorded along with the information of the layer which fails.

Spring-linkage model: In the spring-linkage model, the beam is assumed to be divided into very small rigid elements of length dx. These rigid elements are interconnected using torsional springs. The calculation of the force-displacement curve then follows the steps enumerated below:

1. For a given configuration, the neutral axis is calculated using all the undamaged layers assuming elastic young's modulus for each layer.

2. Based on the calculated position of neutral axis, the moment-theta relationship is calculated following the methodology outlined earlier.

3. A ramp force is then applied to a cantilever beam, varying from 0 to F_{max}.

4. At each time step, a moment is calculated on all the springs by estimating the lever arm and based on the applied moment, rotation for each spring is calculated.

5. Based on the calculated rotation, the new position of each rigid element is calculated and the tip displacement is estimated.

6. The point is added to the force versus displacement curve, since the experimental studies are conducted using 3-point bending, the force values from the python model are doubled as the spring-linkage model uses a cantilever beam.

7. If no additional transverse fracture of a layer occurs, the algorithm loops back and repeats the steps. If, instead, the moment reaches the value that triggers transverse failure in any layer (Step 4), the simulation halts. The affected layer is flagged as damaged, the Moment-versus-theta curve is rebuilt taking all existing failed layers into account and the analysis restarts from t=0.

After all the force-versus displacement curves are obtained, they are assembled together to get the complete force versus displacement response. From the first run (undamaged laminate), Force-versus-displacement from 0 to $F_{failure-1}$ is considered. Then from the second run (1 layer damaged) Force-versus-displacement from $F_{failure-1}$ (Force at which failure occurs in 1st run) to $F_{failure-2}$ (Force at which transverse failure of a layer occurs in 2nd run) is considered. A vertical drop is assumed between the curves, and is shown by vertical dotted lines in Figure 4.6.

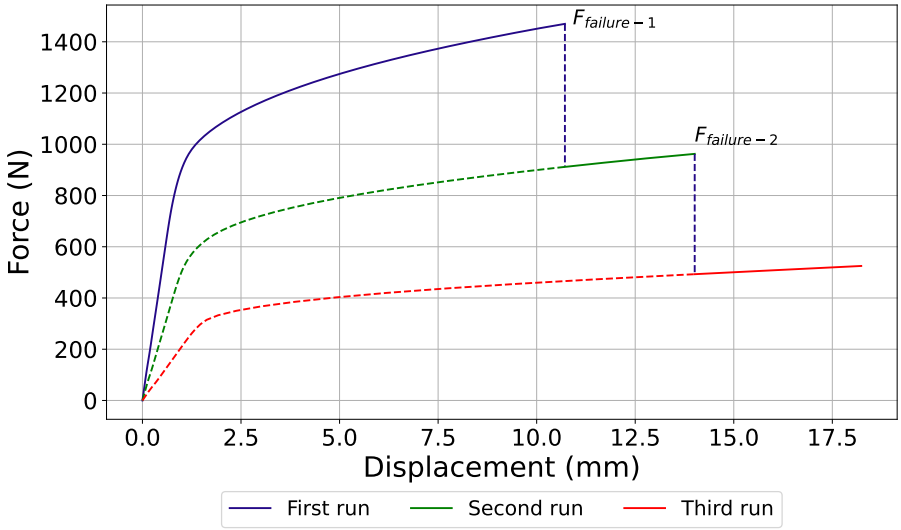

Figure 4.6.: Example force versus displacement curve with vertical drops after transverse failure of layers indicated with dotted lines

Assumptions and limitations for the semi-analytical model:

1. Only quasi-static loading is considered; rate effects have not been included.

2. Perfect bonding is assumed between the layers.
3. Shear effects are neglected. *Note:* An energy based shear correction routine is implemented in the model. Users can enable shear correction by adjusting a variable (Capture_shear). Minimal impact on the results was observed for the cases considered in this study. It is important to note that the results for shear have not been verified or validated. However, the implemented algorithm for the model included in the dataset contains the shear correction routine as part of the code for future verification, correction or extension by other researchers.
4. The model does not account for slippage over the supporting pins, consequently the span remains constant.
5. Delamination mechanics or mixed mode failure are not modeled.
6. Partial degradation of the ply is not considered, a ply is marked as failed only when the entire ply exceeds the strain limit.
7. Geometric non-linearity is ignored, except for plastic thinning in aluminum layers.

4.3. Results

4.3.1. Experimental results

Appendix C.5 reports the specific energy absorption (SEA) (kJ/kg), peak force (kN), and bending modulus (GPα) for all GLARE configurations. A more detailed dataset containing all the experimentally collected data, curves, and images can be found in the public dataset of Anand et al. [108].

The equations used for the calculation of SEA and bending modulus are enumerated below:

1. SEA (kJ/kg): the energy absorbed per unit mass of the laminate, calculated as:

$$\text{SEA} = \frac{\text{Energy absorbed}}{M} \tag{4.3}$$

where M is the mass of the specimen calculated using:

$$M = n_{Al} \cdot \rho_{Al} \cdot (L \cdot w \cdot h_{Al}) + n_{prepreg} \cdot \rho_{prepreg} \cdot (L \cdot w \cdot h_{prepreg}) \tag{4.4}$$

with:

n_{Al}	=	Number of aluminum layers
$n_{prepreg}$	=	Number of glass fiber layers
h_{Al}	=	Thickness of aluminum layers
$h_{prepreg}$	=	Thickness of glass fiber layers
ρ_{Al}	=	Density of aluminum (2.77×10^{-6} kg/mm^3) [102]
$\rho_{prepreg}$	=	Density of UD prepreg (1.96×10^{-6} kg/mm^3) [102]
L	=	Length of the specimen
w	=	Width

It is important to note that Specific Energy Absorption (SEA) values reported in this study are calculated based on the total length of the specimen, which is constant across all specimens (≈ 150mm), to ensure consistent comparison across the tested laminates. However, the damaged region can vary considerably between specimens, for example only the mid-span region is damaged for central cracking cases while the region from mid-span to end of the sample is damaged for delamination cases. Therefore, the reported SEA values should be interpreted with caution. While the values should not be interpreted as a direct measure of energy absorption efficiency of the damaged region, they provide a consistent basis for comparing the relative energy absorption capability of tested GLARE configurations.

2. Bending modulus (GPa): the material's stiffness under bending load, calculated as:

$$E_{flex} = \frac{m_{elastic} \cdot b^3}{4 \cdot w \cdot h^3} \tag{4.5}$$

where:

m_{elastic}	=	Slope for elastic region of force versus displacement curve
b	=	Span
w	=	Width
h	=	Thickness

The slope for elastic region ($m_{elastic}$) was calculated by using an automated script.The script imports force versus displacement curve, applies toe compensation of 2.5% peak force, and then extracts the portion of curve from zero displacement to displacement corresponding to peak force. This extracted segment is then interpolated using a denser set of points to ensure a smooth curve. Subsequently, linear regression over the region corresponding to 20-30% (except for the very thin case : 2A-4/3-[L&T]-0.2 (10mm/min), where the window used was 10 to 30% of peak force) of peak force is performed with an (R^2) threshold of greater than 0.98 to ensure accurate value of slope for elastic region.

Some example curves for experimental 3 point bending are presented Figure 4.7, the effect of different parameters on the energy absorption and other characteristics are discussed in section 4.4.

4.3.2. Repeatability of experimental results

To assess the repeatability of experimental data the following methodology was used:

1. First, a toe compensation of 2.5% of the peak force was applied to all experimentally obtained force-versus-displacement curves to remove the initial non-linear region.

2. For each GLARE configuration:

   a) The minimum of the maximum displacements observed across all samples was identified. A displacement array was then defined from 0

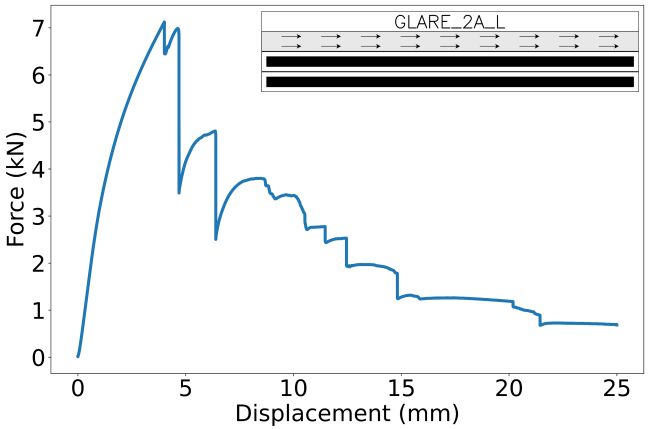

(a) 2A-8/7-L-0.4 Sample-2 (1 mm/min)

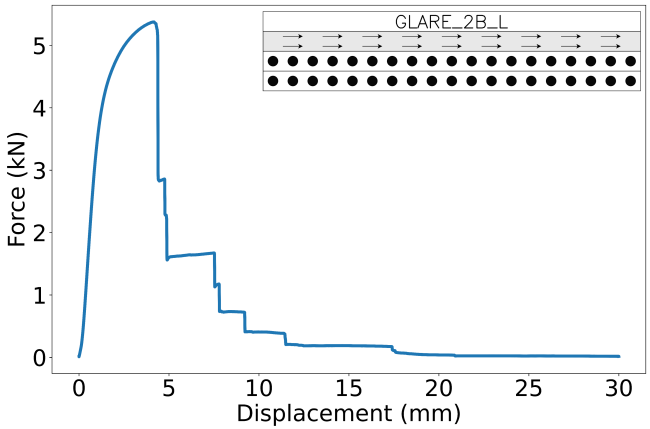

(b) 2B-11/10-L-0.3 Sample-3 (10 mm/min)

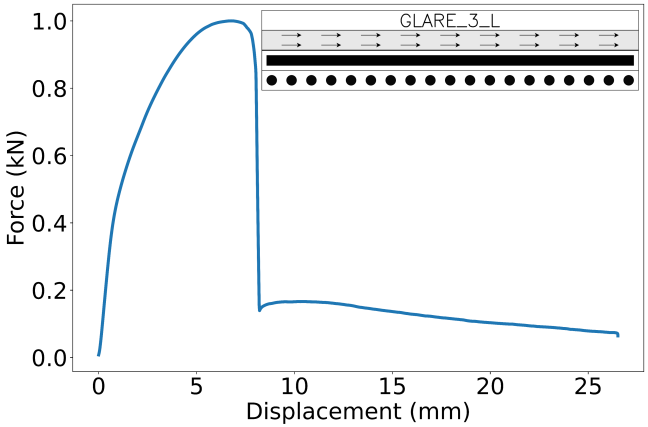

(c) 3-3/2-L-0.3 Sample-4 (100 mm/min)

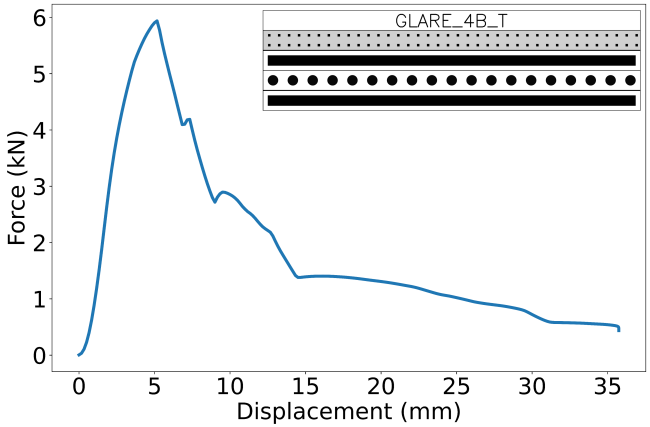

(d) 4B-6/5-T-0.5 Sample-3 (1000 mm/min)

Figure 4.7.: Experimental force versus displacement for GLARE laminates subjected to 3-point bending

to this identified displacement value, consisting of 500 equally spaced points.

b) The force-displacement curves for all the samples of that GLARE configuration was then mapped to this common displacement array ensuring standardized force-displacement curves across samples.

c) The mean force-displacement curve was calculated as point-wise average of the interpolated curves.

d) All the curves for the given configuration were then normalized, the displacement axis by dividing the common displacement array with maximum displacement value and the force axis by dividing with peak force of the mean force-displacement curve.

e) For each sample the area between its normalized curve and the normalized mean curve was calculated.

f) Finally for any given GLARE configuration, we obtain a list containing area between the normalized mean curve and the normalized sample curves. The minimum, maximum and mean of this list is then calculated.

Figure 4.8 plots the minimum, maximum and mean values of the area between normalized experimental curves and normalized mean curve observed for the tested configurations. The mean area between the curves was found to be always below 0.09 for all configurations, demonstrating that the experiments are repeatable. Repeatability of experimental data can also be observed from the graphs presented in Appendix C.6.

4.3.3. Results from semi-analytical model for central cracking

The comparison of curves from the semi-analytical model with the experimental results are presented in Appendix C.6 with only two example curves presented here, Figure 4.16. The predictions of the model were found to be significantly close to experimentally observed results and have been further discussed in subsection 4.4.5.

4.4. Discussion

The discussion is organized into the following sub-sections:

4.1 Failure mechanisms

4.2 Effect of stacking sequence

4.3 Effect of displacement rate

4.4 Effect of aluminum rolling direction

4.5 Results from semi-analytical model

4.6 Sensitivity of force-displacement curve to span

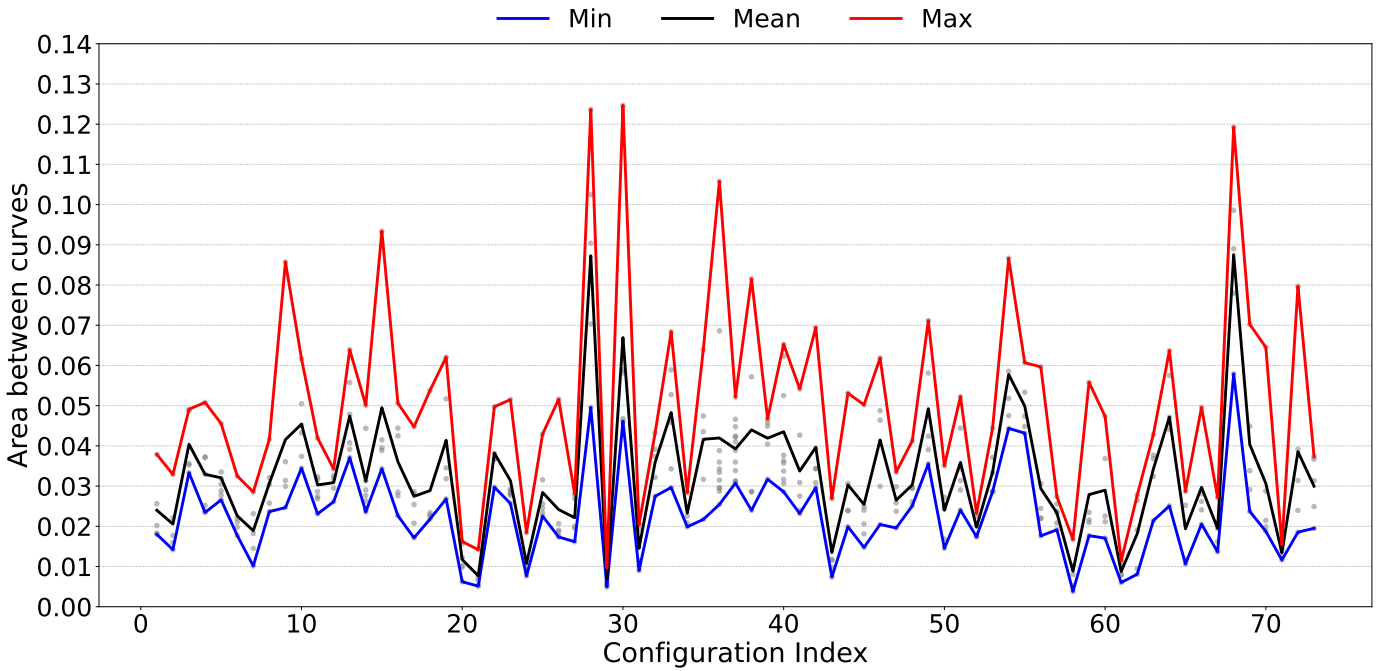

Figure 4.8.: Minimum, mean and maximum area between curves versus configuration for normalized experimental dataset

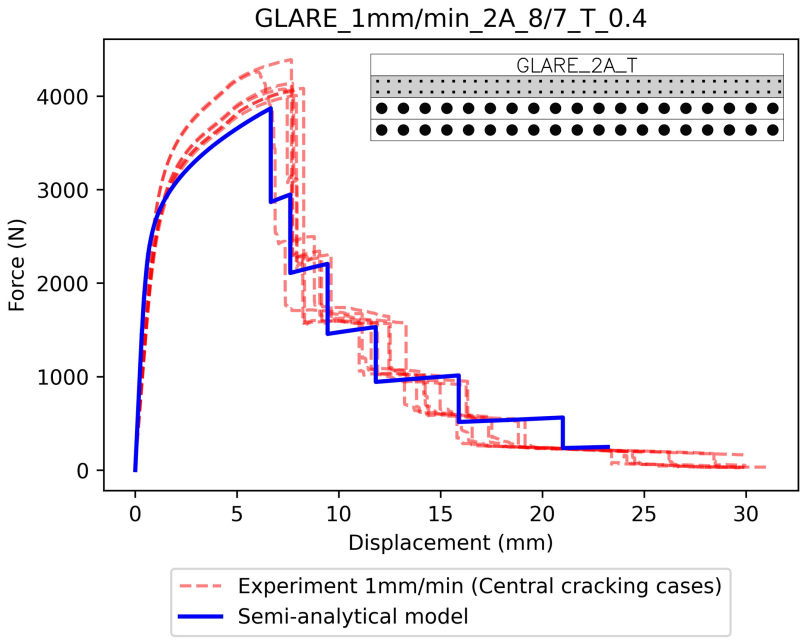

(a)

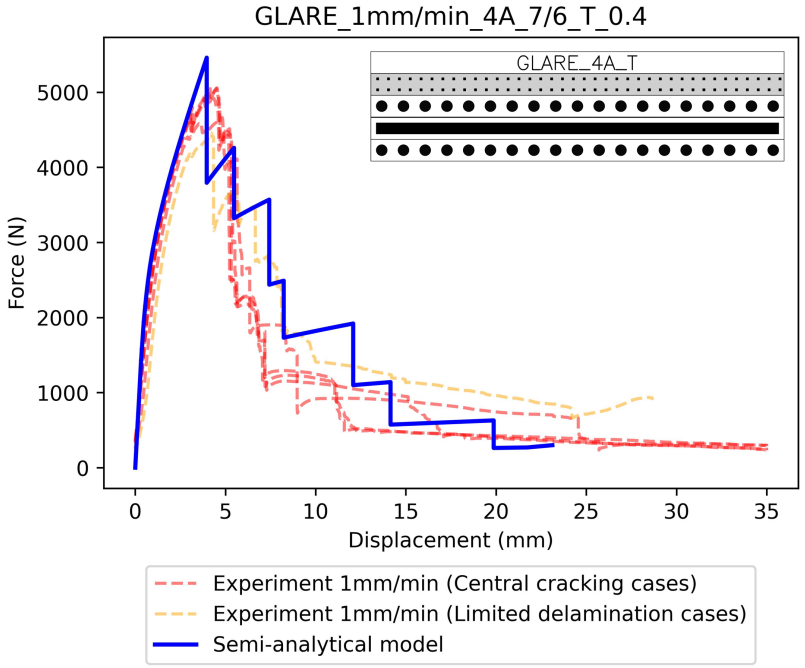

(b)

Figure 4.9.: Comparison of experimental force-versus-displacement curves with predictions from semi-analytical model

4.4.1. Failure mechanisms

From the experimental results, four failure mechanisms were observed (Figure 4.10) through which GLARE laminates fail when subjected to 3-point bending loads. These mechanisms are divided into two categories, normal stress dominated failure and shear stress dominated failure.

1. **Normal stress dominated failure mechanisms:**

   a) **Central Cracking (CC):**

   In this failure mechanism the outermost aluminum ply fractures due to an increase in tensile stress and the crack slowly progresses toward the inner layer as the laminate is loaded further. During progressive failure under bending, the local mid-surface progressively moves to the innermost ply, thus allowing tensile stresses that can grow the central crack to reach those inner plies. This failure mechanism was observed in laminates where most of glass fiber plies have a 90°orientation.

2. **Shear dominated failure mechanisms**

   a) **Delamination (D):**

   This failure mode is transverse-shear dominated, with the delamination crack initiating near the neutral axis, where the transverse shear is maximum, and then growing longitudinally all the way to the end due to the transverse shear loading. A specimen can have single or multiple delaminations (Figure 4.10b and Figure 4.10c). This failure mode is observed in laminates which have most of glass fiber plies in 0°orientation, which are more prone to transverse-shear driven failure due to high tensile and compressive failure stresses.

   b) **Limited Delamination (LD):**

   This failure mode is triggered similarly to the delamination failure mode; however, limited delamination does not progress all the way to the end of the specimen. A specimen can have single or multiple localized delaminations. Observed in laminates which have majority of glass plies in 0°orientation.

The failure modes observed for different configurations at different displacement rates are presented in Table 4.3, Table 4.4 and Table 4.5. Typical force versus displacement curves for different failure mechanisms are presented in Figure 4.11 and 4.12 along with images of the damaged specimens taken after testing. For laminates with all glass fiber plies in 90°direction, it is observed (Figure 4.11a) that the abrupt load drops for central cracking, resulting from failure of aluminum layers, are immediately followed by a plateau, a response consistent with plastic hinge formation in aluminum. For central cracking cases where the laminate has some glass fiber plies in 0°direction, similar load drops can be caused by failure of aluminum layers or failure of 0°glass fiber layers. When some aluminum and 0°glass fiber layers are still intact, a small rise in load generally follows this drop.

Figure 4.10.: Failure modes observed GLARE laminates subjected to 3 point bending

However, at higher displacements (i.e., further along the force–displacement curve), plateaus can be observed to follow the drop indicating that the plastic bending of aluminum layers governs the residual flexural resistance.

For the shear dominated cases (Figure 4.12a and 4.12b), multiple peaks and drops were observed which correspond to a combination of delamination and transverse failure of aluminum or 0°glass fiber layers. In most samples that delaminated, the bottom aluminum layer fractured transversely with further loading of the specimen after delamination.

Configuration	$\dot{\delta}$ (mm/min)	Observed failure modes		
		CC	D	LD
2A_4/3_L_0.3	1	-	-	5
2A_4/3_T_0.3	1	5	-	-
2A_4/3_L_0.2	10	-	-	6
2A_4/3_T_0.2	10	7	-	-
2A_8/7_L_0.4	1	-	5	-
	10	-	5	-
2A_8/7_T_0.4	1	7	-	-
	10	7	-	-
2B_7/6_L_0.4	100	6	-	-
	1000	5	-	-
2B_7/6_T_0.4	100	-	6	-
	1000	-	5	-
2B_11/10_L_0.3	1	7	-	-
	10	6	-	-
	100	11	-	-
	1000	5	-	-
2B_11/10_T_0.3	10	-	6	-

Table 4.3.: Failure modes observed for GLARE-2 specimens.

4.4.2. Effect of stacking sequence

Figure 4.13 presents the effect of stacking sequence on failure mechanism and specific energy absorption (SEA). From the results several observations can be made with respect to stacking sequence:

1. **Configurations where glass fiber layers are only in 90°(transverse) direction, 2A-T and 2B-L:** As illustrated in Figure 4.13, both configurations 2A-T and 2B-L failed through central cracking mechanism for all tested specimens. With increasing applied force, matrix cracking initiates in the 90°fiber layers due to the relatively low failure stress of the matrix. This is subsequently followed by yielding and tensile failure of the aluminum layers, leading to the formation of a central crack propagating upward from the bottommost layer. The average SEA for these specimens is found to be

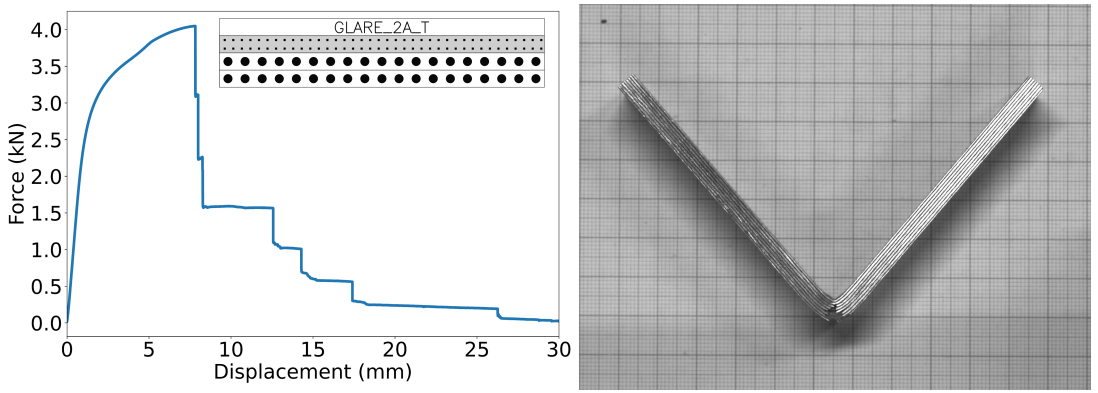

(a) Central cracking failure: GLARE-2A-8/7-T-0.4 Sample 5

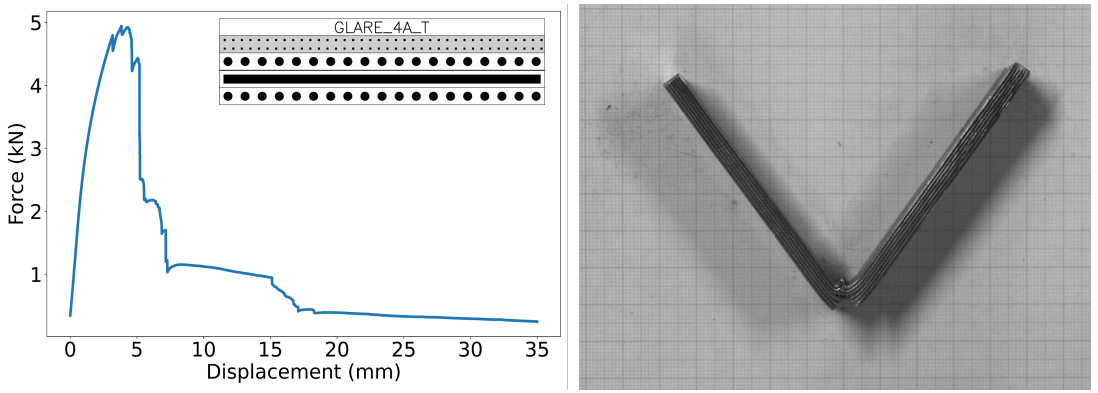

(b) Central cracking failure: GLARE-4A-7/6-T-0.4 Sample 1

Figure 4.11.: Typical force versus displacement curves for central-cracking failure mechanisms

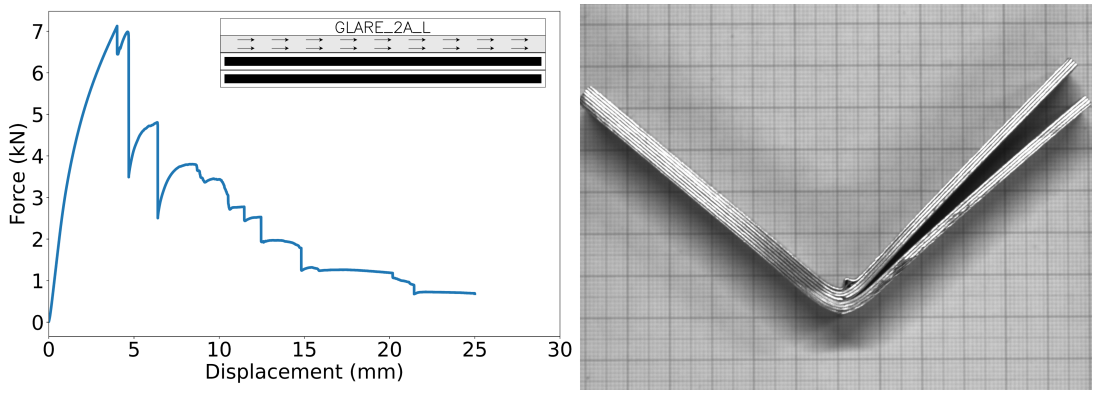

(a) Delamination failure: GLARE-2A-8/7-L-0.4 Sample 2

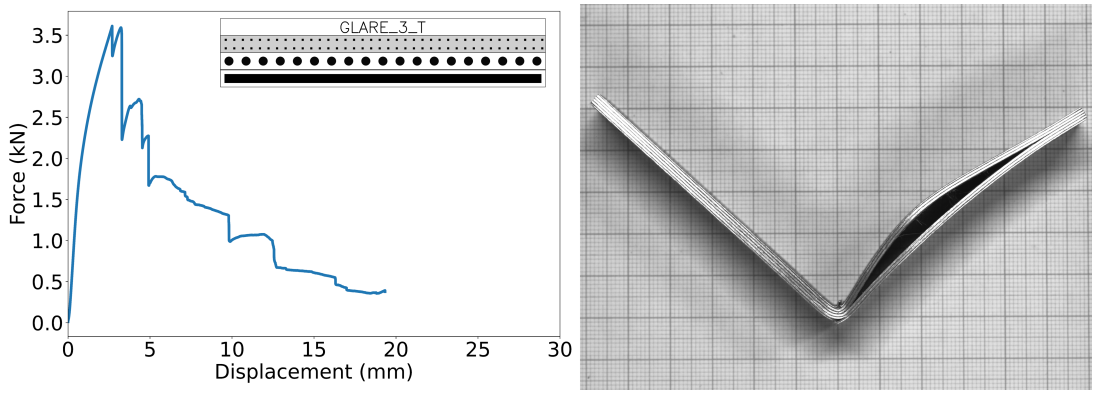

(b) Limited delamination failure: GLARE-3-6/5-T-0.3 Sample 4

Figure 4.12.: Typical force versus displacement curves for shear dominated failure mechanisms

Configuration	$\dot{\delta}$ (mm/min)	Observed failure modes		
		CC	D	LD
3_3/2_L_0.3	1	5	-	-
	10	6	-	-
	100	5	-	-
	1000	5	-	-
3_3/2_T_0.3	1	5	-	-
	10	5	-	-
	100	5	-	-
	1000	5	-	-
3_5/4_L_0.4	1	-	-	5
	10	-	-	5
	100	-	6	-
	1000	-	5	-
3_5/4_T_0.4	1	-	-	5
	10	5	-	-
	100	-	3	2
	1000	2	3	1
3_6/5_L_0.3	1	-	-	6
	10	3	-	2
3_6/5_T_0.3	1	-	-	7
	10	6	-	-
3_8/7_L_0.4	1	-	5	-
	10	-	5	-
	100	5	-	-
	1000	5	-	-
3_8/7_T_0.4	1	1	5	-
	10	2	4	-

Table 4.4.: Failure modes observed for GLARE-3 specimens.

0.69 kJ/kg. Minimum average SEA value of 0.09 kJ/kg was observed for 2A-4/3-T-0.2 specimens tested at a displacement rate of 10 mm/min and maximum average SEA value of 1.03 kJ/kg was observed for 2A-8/7-T-0.4 specimens tested at a displacement rate of 10 mm/min. (Figure C.1).

2. **Configurations where glass fiber layers are only in 0°(longitudinal) direction, 2A-L and 2B-T:** Configurations 2A-L and 2B-T, both display shear dominated failure mechanisms. For these stacking sequences, as the force increases, the aluminum layers start yielding which causes a change in slope of the force versus displacement curve. Given the relative high strength of glass fibers in the longitudinal direction as compared to transverse direction (Table 4.2), further increase in force leads to a shear dominated failure as opposed to central cracking failure observed in configurations with 90°fiber layers. As shown in Figure 4.13, all the specimens of configurations 2A-L

Configuration	$\dot{\delta}$ (mm/min)	Observed failure modes		
		CC	D	LD
4A_7/6_L_0.4	1	-	9	-
	10	-	5	-
	100	-	5	-
	1000	-	5	-
4A_7/6_T_0.4	1	4	-	1
	10	4	-	1
	100	4	1	-
	1000	5	-	-
4B_4/3_L_0.4	100	7	-	-
	1000	3	-	3
4B_4/3_T_0.4	100	6	-	-
	1000	-	4	1
4B_6/5_L_0.5	1	-	-	6
	10	9	2	-
	100	6	-	-
	1000	5	-	-
4B_6/5_T_0.5	1	-	-	6
	10	-	12	-
	100	-	6	-
	1000	-	4	-
4B_7/6_L_0.4	1	1	4	-
	10	1	4	-
	100	3	1	1
	1000	4	1	-
4B_7/6_T_0.4	1	-	4	1
	10	-	5	-
	100	-	5	-
	1000	-	4	1
4B_8/7_L_0.4	100	5	1	-
4B_8/7_T_0.4	100	-	6	-

Table 4.5.: Failure modes observed for GLARE-4 specimens.

and 2B-T failed through shear dominated failure (delamination and limited delamination). The recorded SEA values for 2A-L and 2B-T configurations are significantly higher than the configurations with all fiber layers in the 90°direction. Average SEA for the configurations 2A-4/3-L-0.2 and 2A-4/3-L-0.3, which are relatively thin, was recorded to be 1.06 kJ/kg and 0.87 kJ/kg respectively. As shown in Figure C.1, the average SEA for the other thicker configurations is recorded to be 1.83 kJ/kg with minimum and maximum values being 1.52 kJ/kg (2A-8/7-L-0.4-Sample-5, tested at 1 mm/min) and 2.22 kJ/kg (2B-7/6-T-0.4-Sample-5, tested at 1000 mm/min) respectively.

3. **Configurations with a 1:1 ratio between fibers in 90°(transverse) and 0°(longitudinal) direction, 3-L and 3-T:** Such configurations generally show a mix of central cracking and shear dominated failure modes (Figure 4.13), except for very thin configurations (3-3/2-L-0.3 and 3-3/2-T-0.3) which show central cracking followed by folding for all the 4 displacement rates (1 mm/min, 10 mm/min, 100 mm/min and 1000 mm/min). The average SEA value for GLARE-3 configurations is 1.04 kJ/kg, with minimum and maximum recorded values being 0.57 kJ/kg and 1.81 kJ/kg, also illustrated in Figure C.2.

4. **Configurations with a 2:1 ratio between fibers in 0°(longitudinal) and 90°(transverse) direction, 4A-L and 4B-T:** Configurations 4A-L and 4B-T, with a stacking orientation of 0°/90°/0°, 6 out of 89 total cases failed with central cracking failure, while the rest 83 showed shear dominated failure. This can be observed for the following cases: 4A-7/6-L-0.4, 4B-4/3-T-0.4, 4B-6/5-T-0.5, 4B-7/6-T-0.4 and 4B-8/7-T-0.4. The average SEA value for configurations 4A-L and 4B-T is 1.56 kJ/kg, with a minimum of 1.07 kJ/kg and a maximum of 1.88 kJ/kg, as shown in Figure C.3.

   For the configuration 4B-4/3-T-0.4, all six specimens tested at a displacement rate of 100 mm/min exhibited central cracking failure. However, these specimens were inadvertently tested at a span-to-thickness (b/h) ratio of 20, instead of the standard value of 10. This higher span-to-thickness ratio reduces the transverse shear stress component relative to the bending moment, thereby favoring normal stress dominated failure mechanism.

5. **Configurations with a 2:1 ratio between fibers in 90°(transverse) and 0°(longitudinal) direction, 4A-T and 4B-L:** The cases 4A-T and 4B-L, with a stacking orientation of 90°/0°/90°, tend to usually fail by central cracking, however a substantial amount of specimens also failed through shear dominated failure. 61 out of a total 87 specimens tested failed through central cracking while the rest of the specimens failed through shear dominated failure mechanisms (delamination and limited delamination). Various 4A-T and 4B-L cases are presented below:

   a) **4A-7/6-T-0.4** (Central cracking: 17 specimens, Shear dominated failure:3 specimens)

      Delamination for 1 specimen at 100 mm/min and limited delamination for 1 specimen each is observed for 1 and 10 mm/min, the peak force and SEA for these specimens with shear dominated failure was found to be in the same range (Peak force range: 4.45 to 4.73 kN, SEA range: 0.91 to 1.37 kJ/kg) as other specimens that failed through central cracking (peak force range: 4.49 to 5.47 kN, SEA range: 0.97 to 1.30 kJ/kg) indicating that the energy required for these failure mechanisms are similar.

   b) **4B-8/7-L-0.4** (Central cracking: 5 specimens, Shear dominated failure:1 specimens)

GLARE-4B-8/7-L specimens are only tested at 100 mm/min due to lack of material of this type, for 6 tested specimens, 5 failed through central cracking and delamination was observed for 1 case. The peak force was observed to be about 5.7% lower for delamination case (6.09 kN) as compared to peak force for central cracking cases (Average peak force = 6.46 kN), while SEA for delamination failure was found to be higher (1.51 kJ/kg) than for central cracking failure (Average SEA = 1.24 kJ/kg).

c) **4B-4/3-L-0.4** (Central cracking: 10 specimens, Shear dominated failure:3 specimens)

The specimens for 4B-4/3-L-0.4 were inadvertently tested at two different spans for 100 and 1000 mm displacement rates, with specimens for 100 mm/min tested at b/h ratio of 20 instead of 10, while specimens for 1000 mm/min were tested at b/h ratio of 12. 3 specimens tested at 1000 mm/min displacement rate failed through central cracking mechanism while rest 3 fail through limited delamination failure. However, all specimens tested at a 100 mm/min displacement rate and higher span ($b/h = 20$) failed through central cracking.

d) **4B-6/5-L-0.5** (Central cracking: 20 specimens, Shear dominated failure:8 specimens)

For 1 mm/min displacement rate, all specimens showed limited delamination failure; however, there is an error in the span for these specimens and from the results it is evident that these specimens were tested at a b/h ratio significantly lesser than 10. Between the rest 22 specimens tested at displacement rates of 10, 100 and 1000 mm/min, 2 at 10 mm/min failed through delamination, while the rest of the specimens failed through central cracking.

e) **4B-7/6-L-0.4** (Central cracking: 9 specimens, Shear dominated failure:11 specimens)

For all displacement rates a combination of central cracking and shear dominated failure is observed with the number of specimens showing central cracking increasing with an increase in displacement rate. Among the specimens with shear dominated failure, 1 specimen showed limited delamination failure and rest showed delamination failure. The average peak force is a bit lower, while the average SEA is higher for shear dominated failure cases. (Central cracking failure: average peak force = 5.29 kN, average SEA= 1.26 kJ/kg and shear dominated failure: average peak force = 4.95 kN, average SEA = 1.47 kJ/kg).

From the results for 4B-7/6-L-0.4 (Figure 4.15), it can be seen that the number of specimens for which central cracking was observed increases with increase in displacement rate. This switch to central cracking with the increase in displacement rate is further discussed in subsection 4.4.3.

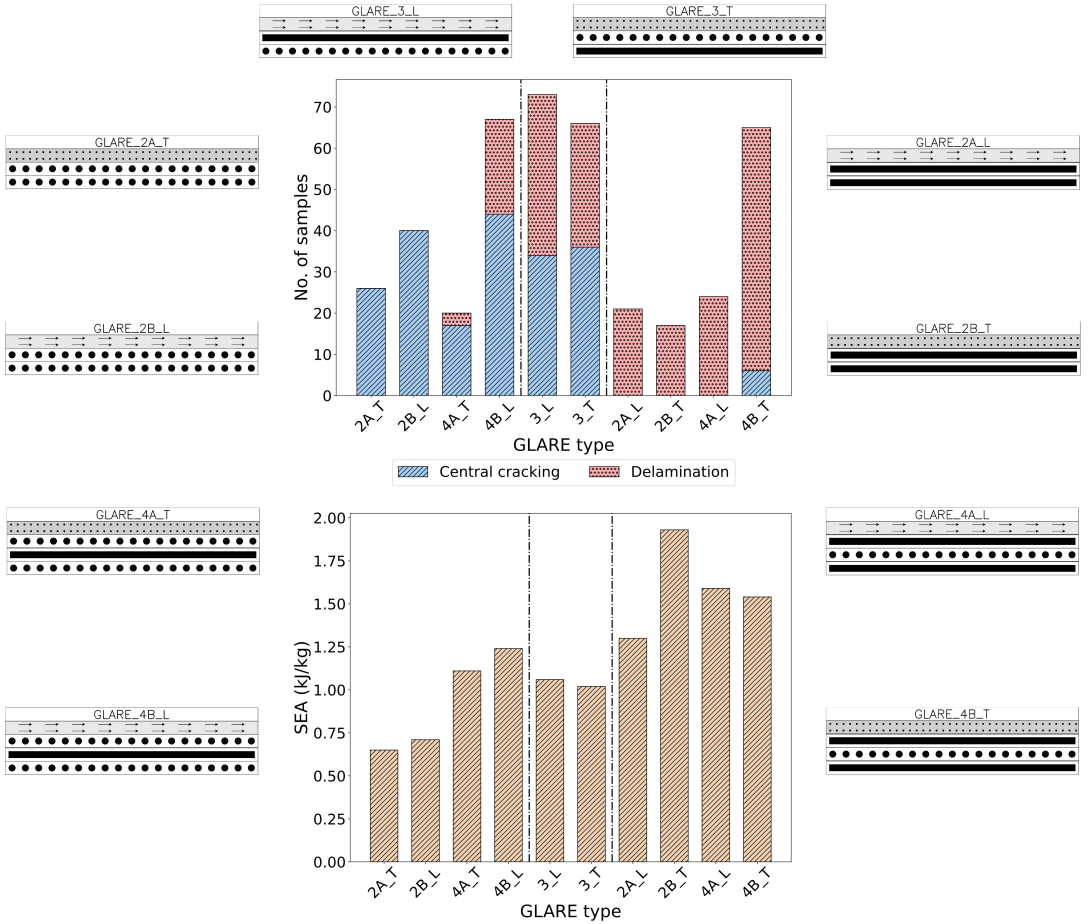

Figure 4.13.: Effect of stacking sequence on failure mode and specific energy absorption (SEA)

4.4.3. Effect of displacement rate

Bending tests were carried out at 4 different displacement rates (1 mm/min, 10 mm/min, 100 mm/min and 1000 mm/min) to study the effect of displacement rate on failure mechanism and energy absorption of the GLARE samples. For most of the cases, the effect of displacement rate on the results is found to be minimal (Figure 4.14 shows two examples), except for cases where a shift in the failure mechanism is observed. For the two examples presented in Figure 4.14, the initial non-linear toe region is removed by applying a toe compensation at 2.5% of the observed peak load. It can then be observed from Figure 4.14 that the effect of change in displacement rate was minimal, an increase in peak force with increase in displacement rate can be observed, however, the envelope boundaries for the peak are not well defined and there was overlap between the envelopes for different displacement rates.

For the exceptions, a switch from shear dominated failure (delamination and limited delamination) to central cracking is observed, with specimens failing in shear dominated failure recording a higher SEA compared to specimens failing with central cracking (Appendix C). This switch can be explained by an increase in interlaminar fracture toughness with increasing the displacement rate [109], such that the force threshold for shear dominated failure failure exceeds the force threshold for central cracking failure. Figure 4.15 shows a comparison of number of specimens that failed through central cracking and shear dominated failure mechanisms. A clear trend of increasing central-cracking failures with increase in displacement rates is observed.

4.4.4. Effect of aluminum rolling direction

To study the effect of rolling direction, a comparison can be made between the specimens 4A-7/6-L-0.4, 4A-7/6-T-0.4, 4B-7/6-L-0.4 and 4B-7/6-T-0.4. These specimens are chosen because the only difference between 4A-7/6-T-0.4 and 4B-7/6-L-0.4, and between 4A-7/6-L-0.4 and 4B-7/6-T-0.4, is the aluminum rolling direction. The comparison for both the combinations are presented below:

1. **Comparison between 4A-7/6-L-0.4 and 4B-7/6-T-0.4:**
   For both the configurations shear dominated failure is the primary failure mechanism. As observed from Figure 4.16a, while there is no significant change in bending stiffness, a slight increase in mean peak force is observed for the case with longitudinal aluminum rolling direction (4A-7/6-L-0.4: 6.38 kN and 4B-7/6-T-0.4: 5.49 kN). The average SEA is found to be similar for both configurations, 4A-7/6-L-0.4: 1.59 kJ/kg and 4B-7/6-T-0.4: 1.68 kJ/kg.

2. **Comparison between 4A-7/6-T-0.4 and 4B-7/6-L-0.4:**
   As shown in Figure 4.16b, no significant change in bending stiffness is observed, however, a slight increase in mean peak force was recorded (4A-7/6-T-0.4: 4.92 kN and 4B-7/6-L-0.4: 5.11 kN). An increase in the SEA is also observed from 1.12 kJ/kg for 4A-7/6-T-0.4 (transverse aluminum rolling direction) to 1.38 kJ/kg for 4B-7/6-L-0.4 (longitudinal aluminum rolling direction). Most of the specimens failed through central cracking (26 out of

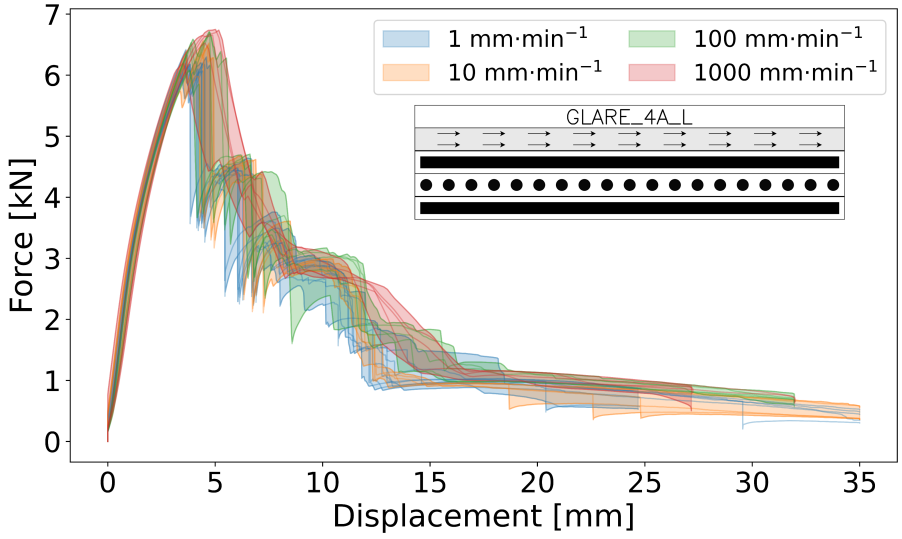

(a) F vs disp. envelopes:4A-7/6-L-0.4

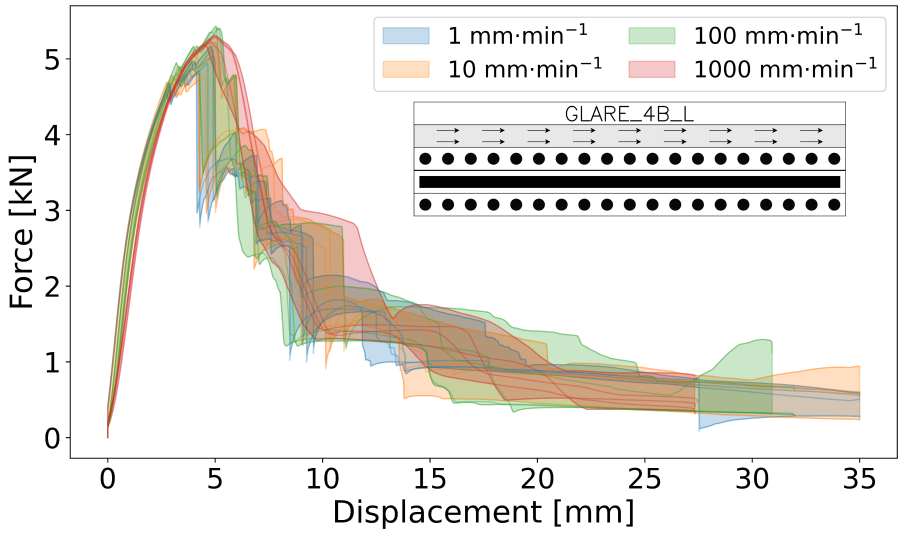

(b) F vs disp. envelopes:4B-7/6-L-0.4

Figure 4.14.: Comparison of experimental force-versus-displacement envelopes for specimens with change in displacement rate

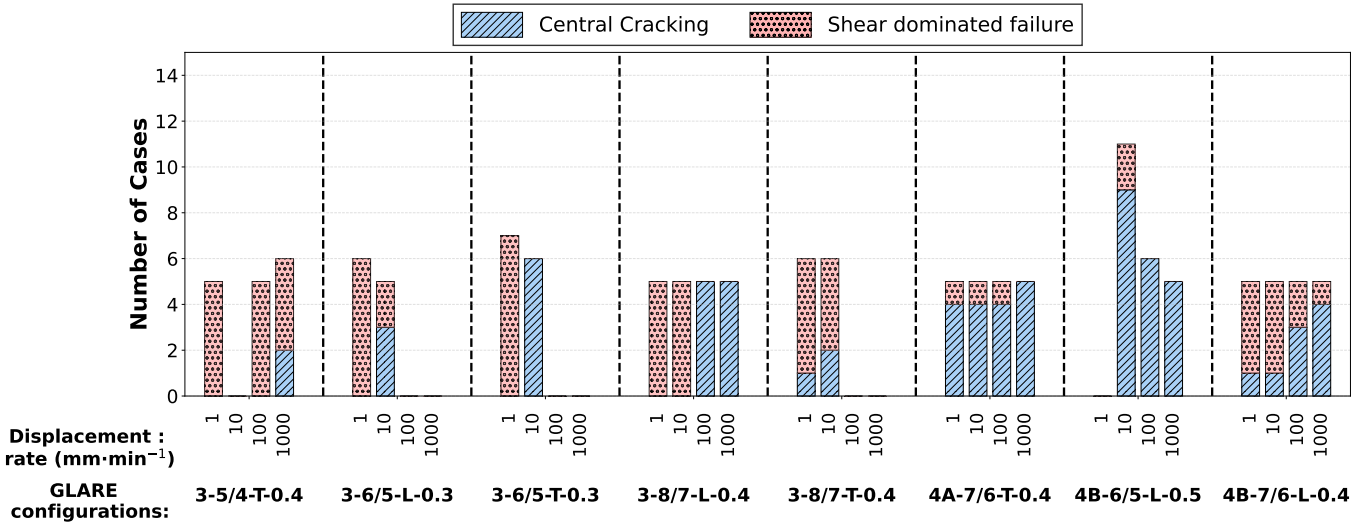

Figure 4.15.: Effect of displacement rate on failure modes

40); however, it is important to note that configurations which showed an increase in SEA failed with shear dominated failure (delamination and limited delamination) as the major failure mode.

4.4.5. Results from semi-analytical model

This section is divided into two parts, the first sub-subsection compares the predictions of the semi-analytical model with experimental results for central cracking cases, the model should be more accurate for these cases as central cracking cases are driven by tensile and compressive failure of layers which are both taken into account in the model. The second sub-subsection compares the predictions of the model against experimental data for shear dominated failure cases, while delamination and shear are not captured by the model, the model should still be able to capture the initial part of the force vs displacement curve before a major delamination appears.

Semi-analytical model: Central cracking

For central cracking of 2A-T or 2B-L laminates, which have all glass fiber plies oriented in the 90° direction, the semi-analytical model predicts the slope accurately up to the failure of the first aluminum layer and is able to also capture the subsequent load drops with reasonable accuracy. For cases where the laminate includes a mix of 0° and 90° plies, the model still predicts the force-versus-displacement response well up to the failure of the first aluminum or 0° glass fiber layer. While the load drops are not predicted as precisely as in the 2A-T and 2B-L cases, the fit remains sufficiently accurate to yield reasonable energy absorption estimates—which are the primary design driver for crash structure applications. The discrepancies in load drop predictions can be attributed to the model's assumptions and limitations, particularly its inability to account for partial damage within a ply. For thin samples exhibiting central cracking failure—such as 3-3/2-L-0.3—the semi-analytical model accurately predicts the initial stiffness (slope) up to a certain point. Beyond this point, the experimental force-displacement curve begins to smooth out and drop (see Figure 4.17b). This behavior is likely due to slippage at the supporting pins during the test, which effectively increases the span as the experiment progresses. As a result, both the peak load and the energy absorption capacity appear reduced compared to the model predictions. An example for a laminate with all plies in 90° direction is presented in Figure 4.17a and examples of laminates with plies in both 0° and 90° directions are presented in Figure 4.17b to 4.17d.

Peak force and SEA predicted by the semi-analytical model for central-cracking are found to be close to experimental values, coefficient of determination $R^2_{\text{Peak-force}} = 0.94$ and $R^2_{\text{SEA}} = 0.88$ (Figure 4.18).

Semi-analytical model: Shear dominated failure

For the two shear dominated failure mechanisms herein identified, i.e. delamination and limited delamination; the proposed model still predicts the initial slope accurately

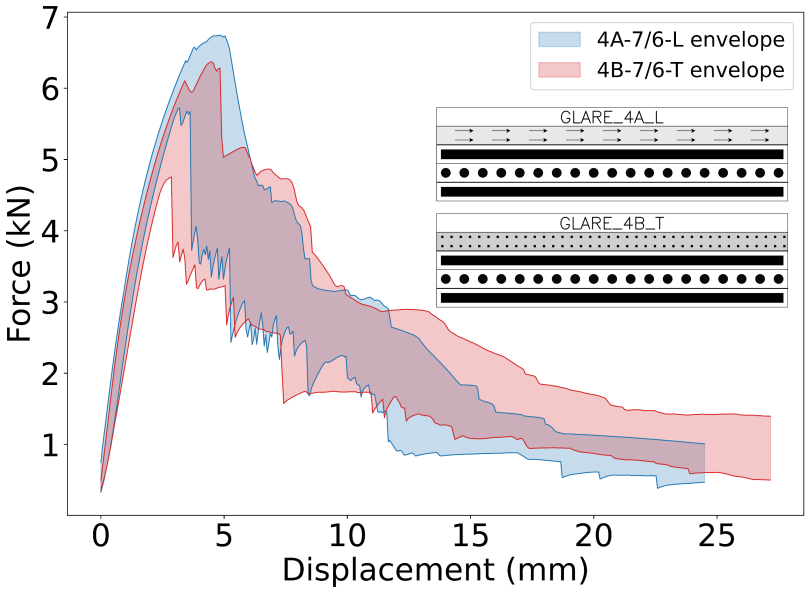

(a) F vs disp. envelopes:4A-7/6-L-0.4 and 4B-7/6-T-0.4

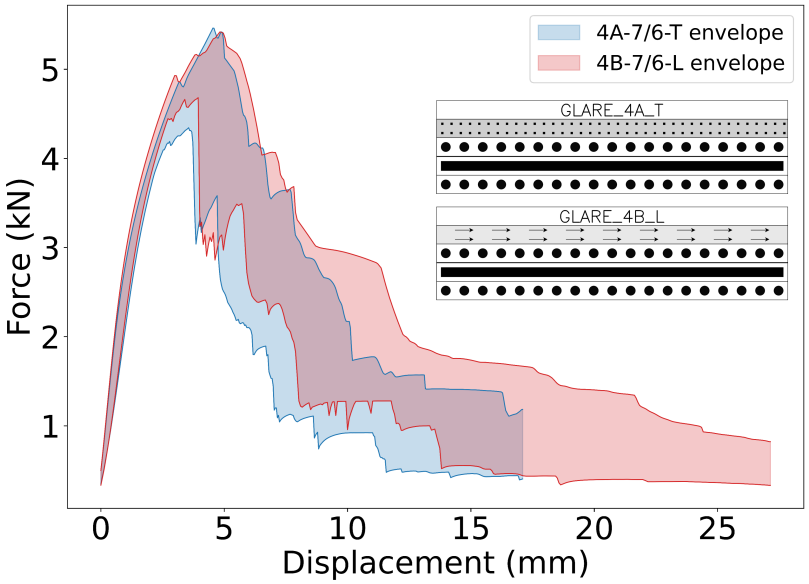

(b) 4A-7/6-T-0.4 and 4B-7/6-L-0.4

Figure 4.16.: Comparison of experimental force-versus-displacement envelopes for specimens with change in aluminum rolling direction

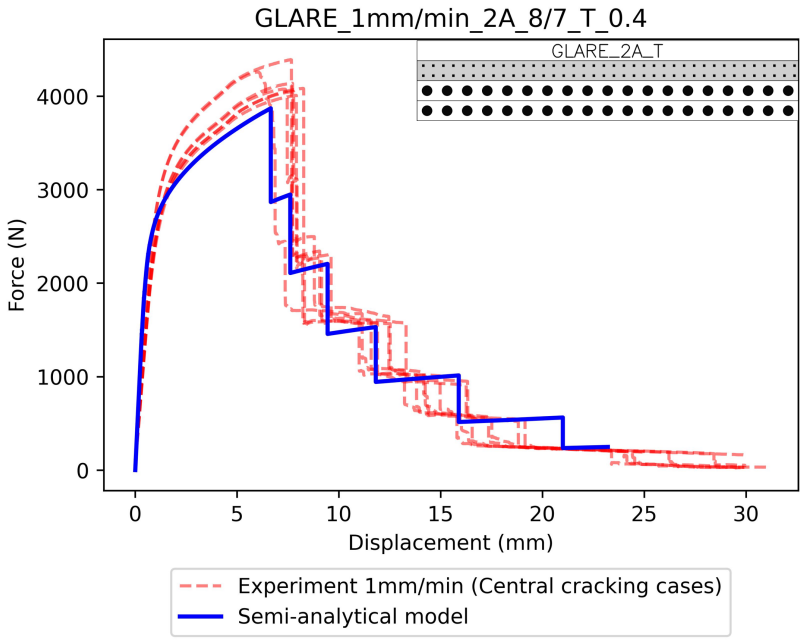

(a) 2A-8/7-T-0.4 (1 mm/min)

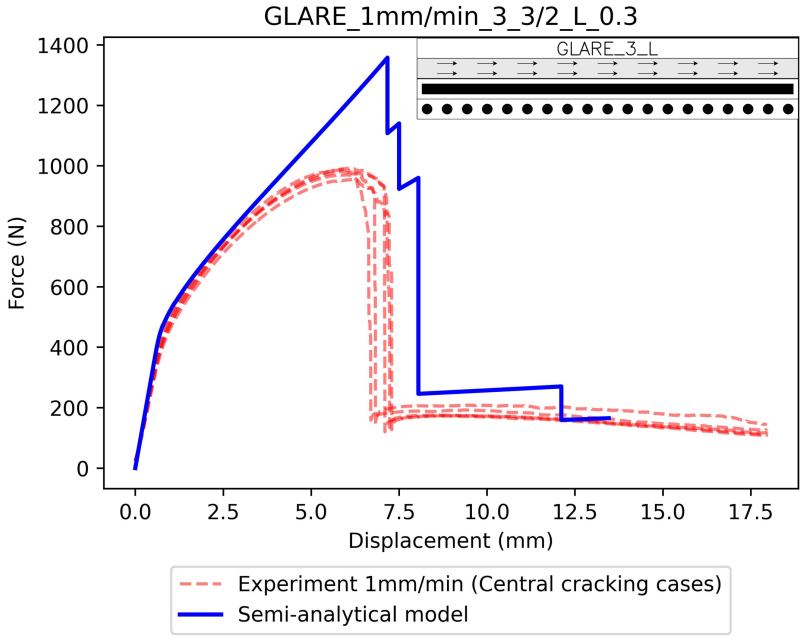

(b) 3-3/2-L-0.3 (1 mm/min)

Figure 4.17.: Comparison of experimental force-versus-displacement curves with predictions from semi-analytical model – **continued on next page**

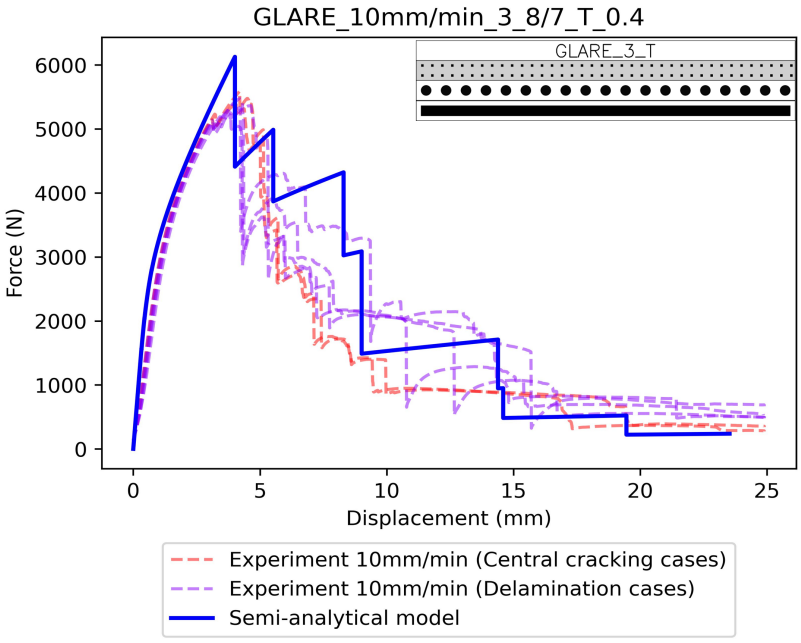

(c) 3-8/7-T-0.4 (10 mm/min)

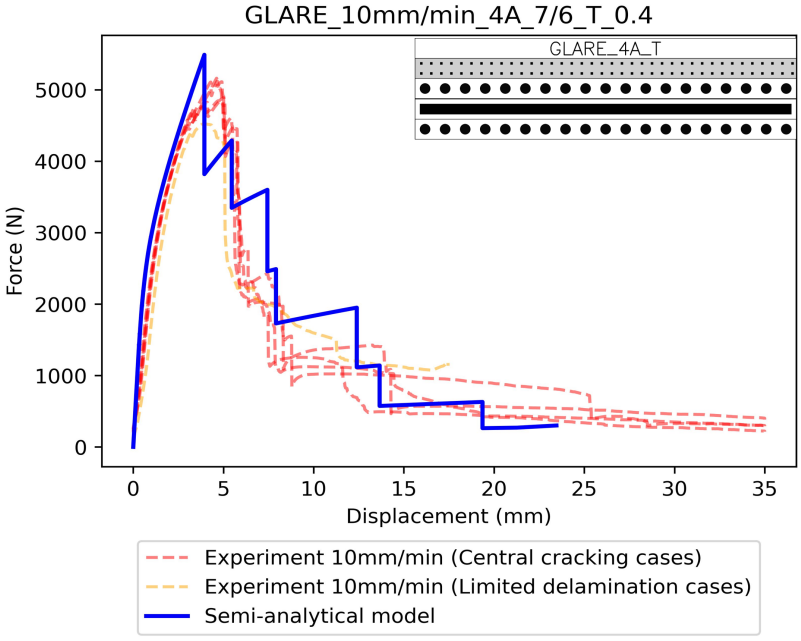

(d) 4A-7/6-T-0.4 (10 mm/min)

Figure 4.17.: Comparison of experimental force-versus-displacement curves with predictions from semi-analytical model – **continued on next page**

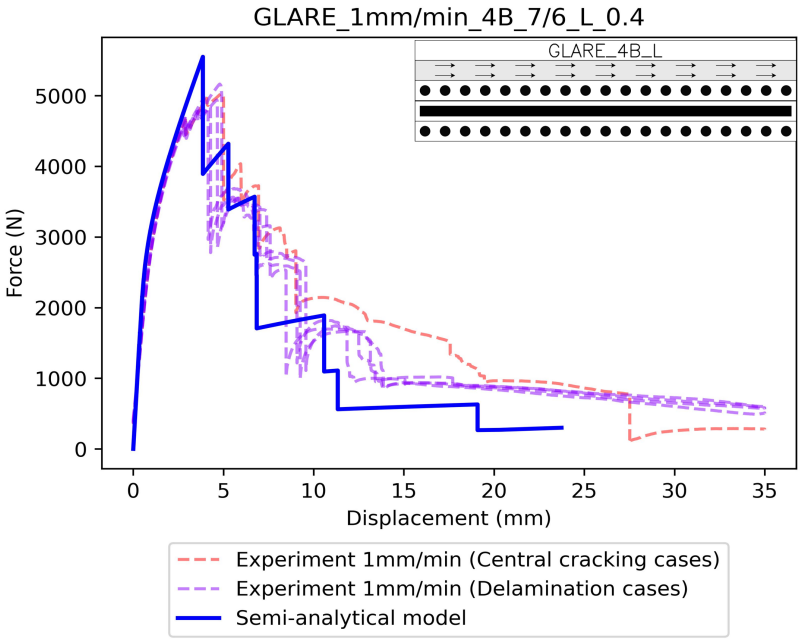

(e) 4B-7/6-L-0.4 (1 mm/min)

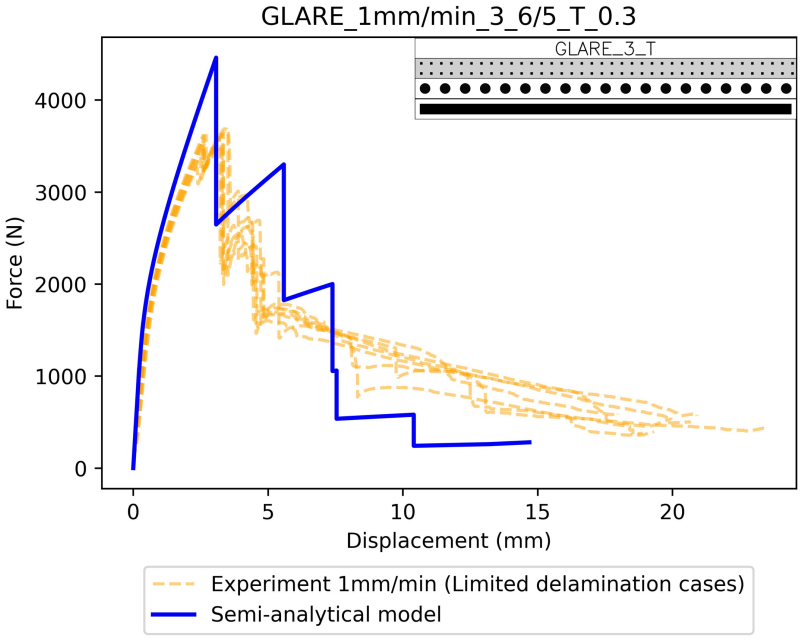

(f) 3-6/5-T-0.3 (1 mm/min)

Figure 4.17.: Comparison of experimental force-versus-displacement curves with predictions from semi-analytical model

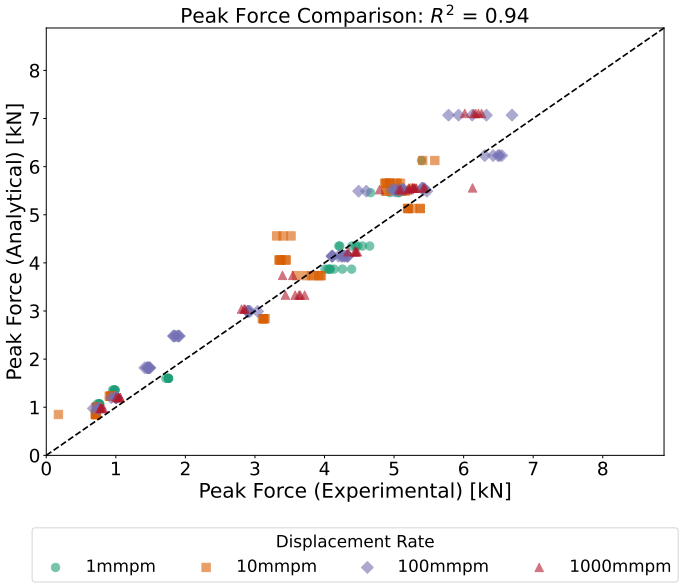

(a)

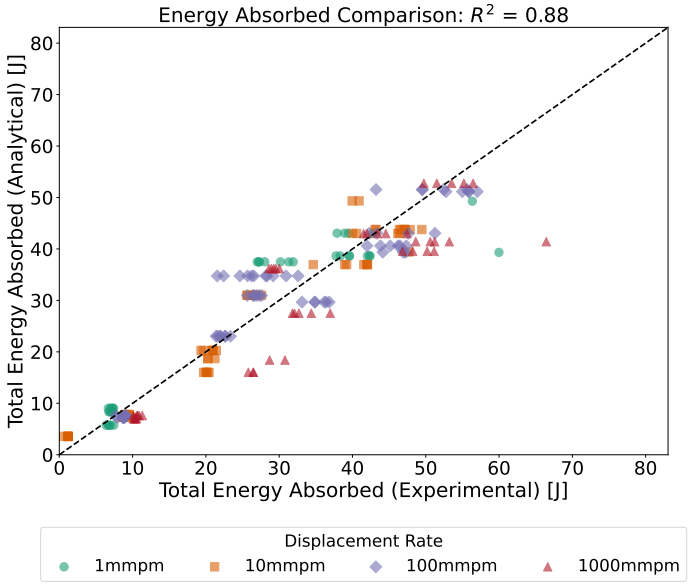

(b)

Figure 4.18.: Comparison of analytical and experimental values for peak force and total energy absorbed, only central cracking cases are considered. Dotted lines represent ideal correlation, experimental=analytical.

(Figure 4.17e and 4.17f). However, as anticipated, the peak force and load drops are not accurately captured as the model does not account for shear and delamination failure. The ability of the model to predict the initial stiffness suggests its potential applicability for bending calculations in cases where damage evolution is not considered.

4.4.6. Sensitivity of force-displacement curve to span

During the 3-point bending tests, an error of only 2 mm in the test setup can result in a variation of about ±10% in span for some of the configurations. Additionally, during the bending process, slippage at the support pins can add to errors in the force-displacement curves. In view of the reasons highlighted above, it is important to use the semi-analytical model for studying the sensitivity of force-displacement curve to span. In this section four cases are studied, for all the four cases the span was varied by ±10% and the force-versus-displacement curves were plotted (Figure 4.19). A decrease in span length (-10%) leads to an increase in peak force but a reduction in total energy absorption, whereas an increase in span length (+10%) shows the opposite trend. Notably, the relative change in peak force approximately mirrors the span variation in magnitude but with an opposite sign, indicating almost linear sensitivity of peak force to the span length.

Configuration	Span change (%)	Max Force (kN)	Energy (J)
2A-4/3-T-0.3	0	1.60	5.74
	-10	1.78 (+11.25%)	5.36 (-6.62%)
	+10	1.45 (-9.38%)	6.43 (+12.02%)
2A-8/7-T-0.4	0	3.87	38.64
	-10	4.30 (+11.11%)	35.88 (-7.14%)
	+10	3.51 (-9.30%)	41.80 (+8.18%)
3-3/2-L-0.3	0	1.36	8.36
	-10	1.51 (+11.03%)	7.91 (-5.38%)
	+10	1.24 (-8.82%)	9.04 (+8.13%)
4A-7/6-T-0.4	0	5.46	43.06
	-10	6.06 (+10.99%)	38.97 (-9.50%)
	+10	4.95 (-9.34%)	45.17 (+4.90%)

Table 4.6.: Effect of span variation on maximum force and total energy absorbed. Values in parentheses represent percentage change relative to the 0% span.

4.5. Conclusions

Following conclusions can be made from the discussions:

1. Dependence on stacking sequence:

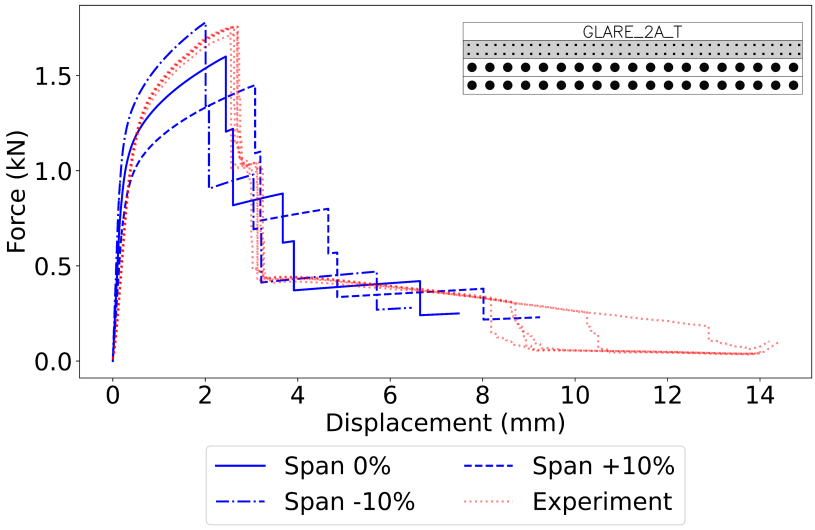

(a) 2A-4/3-T-0.3 Sample-2 (1 mm/min)

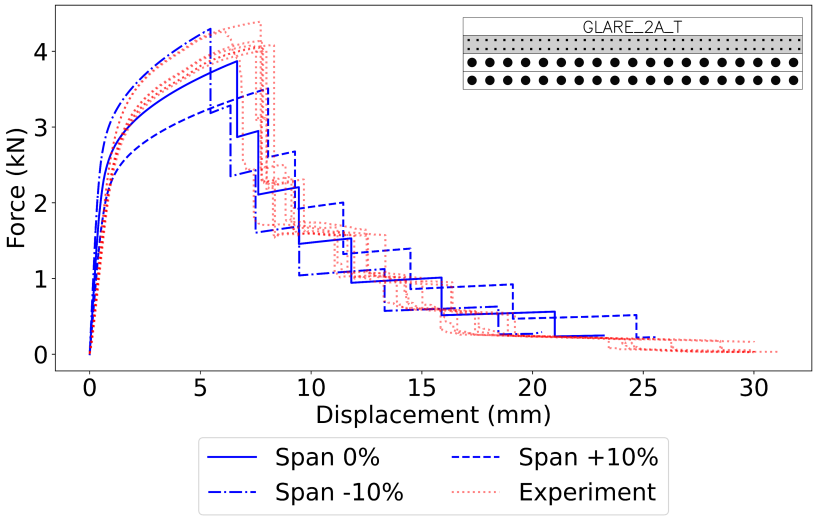

(b) 2A-8/7-T-0.4 (1 mm/min)

Figure 4.19.: Sensitivity of force versus displacement curves to span – **continued on next page**

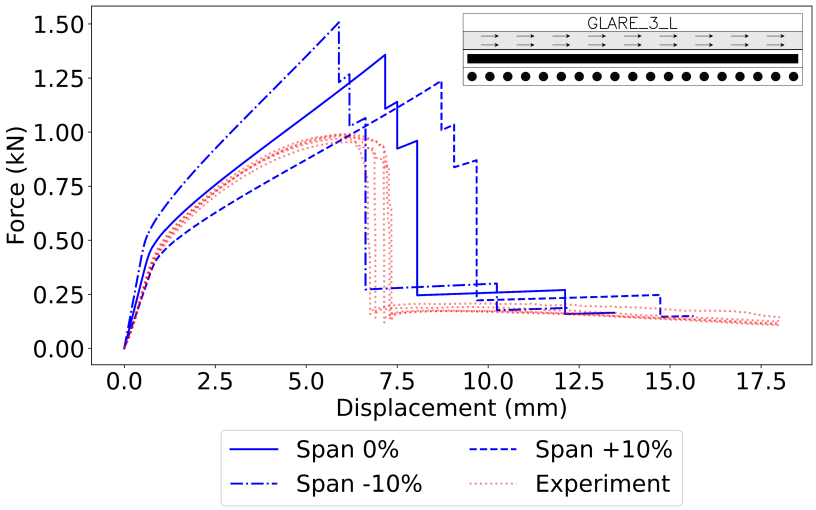

(c) 3-3/2-L-0.3 (1 mm/min)

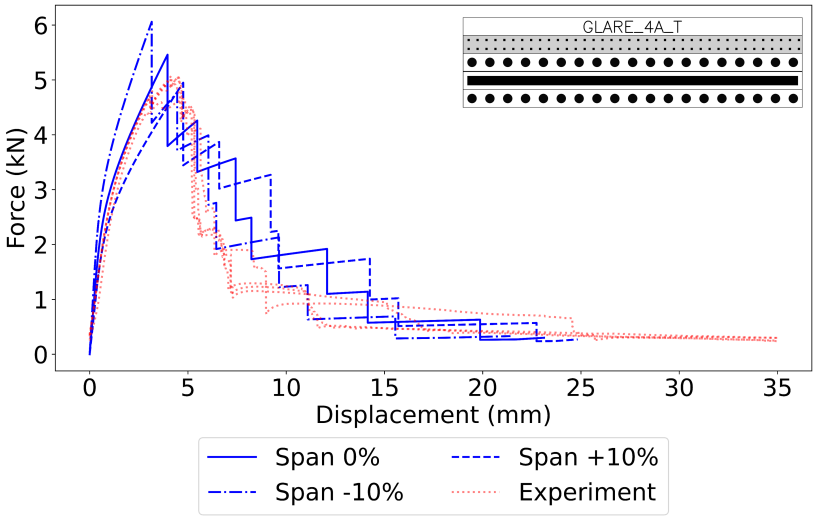

(d) 4A-7/6-T-0.4 (1 mm/min)

Figure 4.19.: Sensitivity of force versus displacement curves to span

a) GLARE 2 has either all plies in 0°or in 90°. Specimens with all glass fiber plies in 0° show shear dominated failure (delamination and limited delamination) for all specimens; and specimens with all glass fiber plies in 90° show central cracking failure. Configurations with all glass fibers in 0° direction show a much higher average SEA as compared to configurations with all glass fibers in 90° direction.

b) GLARE 3 specimens, consisting of an equal ratio of 0° and 90° plies, exhibited two distinct failure modes. Approximately half of the specimens failed through shear dominated failure mechanisms, while the other half failed due to central cracking.

c) GLARE 4A and 4B specimens 2:1 ratio between fibers in 0° (longitudinal) and 90° (transverse) direction exhibit shear dominated failure mechanism. Central cracking however observed for one case which was tested at *b/h* ratio of 20 instead of 10. This indicates that an increase in *b/h* ratio can result in a switch from shear dominated failure to central cracking due to a decrease in shear forces.

d) GLARE 4A and 4B specimens 2:1 ratio between fibers in 90° (transverse) and 0°(longitudinal) direction exhibit a combination of central cracking and shear dominated failure mechanisms.

2. Most of the cases were found to be displacement rate insensitive for the tested displacement rates (1,10,100 and 1000 mm/min), recording minimal changes as a result of change in displacement rate. However, for some configurations a shift from shear dominated failure to central cracking was observed with increase in displacement rate which can be explained by an increase in interlaminar fracture toughness with an increase in displacement rate, resulting in the threshold for shear dominated failure exceeding the threshold for central cracking failure.

3. For specimens with longitudinal aluminum rolling direction, a slight increase in peak force was observed as compared to specimens with transverse rolling direction. For cases where majority of the fibers had a 90° orientation (4A-7/6-T-0.4 and 4B-7/6-L-0.4), a shift from central cracking to shear dominated failure was observed at lower displacement rates for specimens with longitudinal aluminum rolling direction. However, it is important to note that these two conclusions are based on the results from the two comparative cases that have been evaluated in this experimental campaign, additional data is therefore required to validate these findings.

4. The proposed semi-analytical model can be used to predict the Force-versus-displacement response of GLARE laminates under 3-point bending, when central cracking is the main failure mechanism. Improving the shear module should extend this model to cases with shear dominated failure, enabling accurate predictions of the peak load.

5
Discussion

5.1. Axial crushing of metallic tubular structures

The ideal force–displacement response for a tubular structure subjected to axial crushing consists of an initial peak crushing force followed by a plateau region. As the structure is loaded, the force increases up to a peak value. At this point, the material yields and plastic collapse begins. The structure then transitions into a progressive folding mechanism, which can be represented by a mean crushing force (see Figure 2.3). For cases where no triggering mechanism is used, the peak crushing force and the corresponding displacement can be calculated as a function of yield stress and length of the tube:

$$P_{peak} = \sigma_y \times A \tag{5.1}$$

$$\delta_{peak} = \frac{P_{peak} L}{AE} = \frac{\sigma_y L}{E} \tag{5.2}$$

Where A is the cross-sectional area, L is length of the tubular structure, E is the young's modulus and σ_y is the yield stress. Figure 5.1 presents a comparison between the analytical predictions and numerical results for the peak crushing force of three 150mm long AISI-316 tubes with a 30 mm side length and varying wall thicknesses (yield strength = 467 MPa, E=193,000 MPa).

While the peak crushing force governs the onset of collapse, it represents only a small portion of the total absorbed energy during axial crushing. As shown in Figure 5.1, the peak occurs at relatively small displacements, after which the structure transitions into a progressive folding regime. Therefore, the majority of the energy absorption capacity of a tubular structure lies within this post-peak plateau region, which can be characterized by the mean crushing force. For this reason, the present work focused on modelling and evaluating the mean crushing force.

Multiple models for calculating the mean crushing force have been proposed in literature for circular, square, hexagonal and octagonal tubular structures [22, 24–29, 41]. All of these proposed models claimed close agreement with the test data.

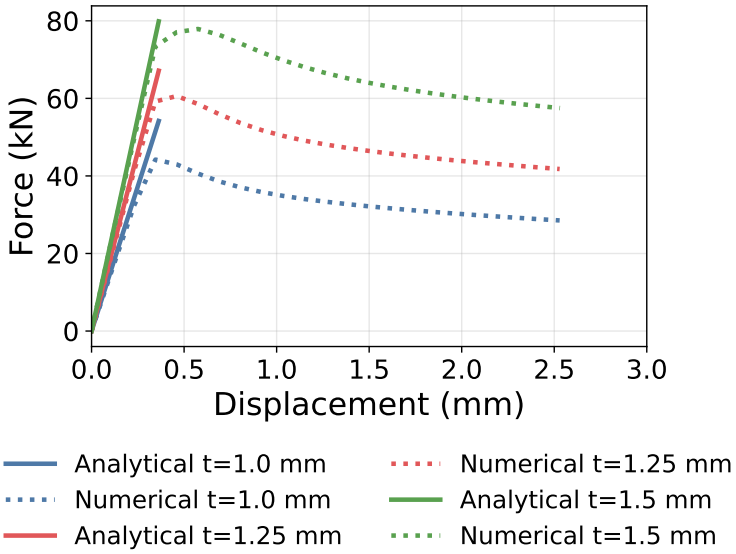

Figure 5.1.: Comparison between analytical and numerical peak crushing force

However, for the purpose of preliminary design, it was important that these models were compared against a common multi-material and multi-geometry dataset.

In chapter 2, a multi-material dataset consisting of numerical simulations and experimental data collected from literature was created for metallic tubular structures subjected to axial crushing. Various proposed models were then evaluated against this dataset and their accuracy was reported. This exercise led to a deeper understanding of how the various models performed for a given configuration and crushing mode.

Alexander [22] noted that circular tubular structures can be considered as infinitely wide beams, leading to largely plane strain and incompressible conditions. Under such conditions, using the Von Mises criterion results in a stress value of $(2/\sqrt{3})\sigma_0$. This change in flow stress was incorporated into the model of Tabacu et al. [29], and an even better correlation (increase from $R^2 = 0.91$ to $R^2 = 0.94$) between the dataset and the predicted mean force values was observed. For inextensional crushing of hexagonal and octagonal tubular structures, the model of Zhang and Zhang [42] was calibrated against the dataset created in this work. An increase in the correlation was observed for both hexagonal (increase from $R^2 = 0.86$ to $R^2 = 0.97$) and octagonal (increase from $R^2 = 0.90$ to $R^2 = 0.98$) tubular structures.

Finally, based on the comparisons and improvements made, a generalized equation for predicting mean crushing force was proposed. The equation applies to circular tubular structures and to both extensional and inextensional collapse modes

of polygonal tubular structures. The proposed generalized equation has the form:

$$P_m = \frac{M_0}{\kappa} \cdot X \cdot N_c^Y \cdot \left(\frac{c}{h}\right)^z \tag{5.3}$$

The coefficient of determination (R^2) for the generalized equation across various cross-sections and failure modes was demonstrated to be 0.97, using the dataset created in this thesis that combines experimental and high-fidelity simulation data. A comparison between the mean force from the proposed equation and the datasets was presented in Figure 2.22.

The strength of the proposed generalized expression lies in its instant runtime and ability to handle various geometries and crushing modes through simple modification of the coefficients. This flexibility enables engineers to assess multiple configurations efficiently, thereby facilitating faster and broader design space exploration.

It is important to note that the proposed model predicts the mean crushing force (P_{mean}), see Figure 2.3. However, the force-displacement response for axial crushing is characterized by successive peaks and troughs. While the proposed model can accurately predict the absorbed energy for a given displacement value, it lacks the ability to capture the detailed variation in force with respect to displacement. Accurate modelling of the peaks and troughs analytically is non-trivial because the fold formation is not strictly sequential; the second fold often initiates before the first is fully completed. Therefore, while calculating the mean crushing force using energy required to form one complete fold results in predictions with a high coefficient of determination ($R^2 = 0.97$), this approach provides an averaged representation, and not a discrete one, of the underlying crushing process. Therefore, while the model is suited for use as a preliminary design tool, engineers must remain aware that the actual structure can cause momentary spikes and drops in the global force-versus-displacement response.

The dataset created as part of this work, containing input files and results from numerical simulations for 112 different configurations consisting of 2 different materials and 4 cross-sectional shapes, was made openly available [61].

5.2. Plastic bending for metallic tubular structures

Kecman [1, 30] proposed the first analytical model for bending collapse of rectangular tubular structures. The use case for Kecman model was roll-over and falling-object protective structures for automotive applications. The bending collapse model from Kecman uses an empirical relation for rolling radius. Wierzbicki et al. [31] extended the Super-Folding Element proposed for axial crushing to bending collapse and proposed a closed-form solution for moment-rotation prediction. Subsequently, Kim and Reid [32] studied both the models from Kecman and Wierzbicki and proposed an improvement to the bending collapse model from Kecman.

While these models were shown to be accurate in their respective publications, two important gaps were observed:

1. The models focused on steel specimens and did not account for the elastic-plastic deformation stage. However, the objective of the present work was to employ these models for preliminary crashworthiness in early stages of aircraft design, which predominantly use aluminum alloys and therefore reliable prediction of elasto-plastic stage in addition to bending collapse was necessary.

2. Similarly to the case of axial crushing, a verification of the models against a varied multi-material (both steel and aluminum) and multi-geometry dataset was necessary.

In chapter 3, the existing models were first implemented and then compared against a numerically generated dataset consisting of three different materials (AL2024, AL7075 and S275). Based on the obtained results, a new model was proposed employing a semi-analytical approach composed of spring-linkage model for elastic/elasto-plastic part, the Kecman model for bending collapse beyond 20 degrees and a transition algorithm to predict the initial bending collapse zone of the force-displacement curve.

The spring-linkage model is based on the calculation of the moment-rotation curve, taking only the geometry and true stress-strain curve of the material as input. Maximum moment predictions based on calculations from the spring-linkage model were also proposed. Results from the semi-analytical model were compared against data from literature, and high-fidelity numerical simulations for square and rectangular tubes; which showed that the results from semi-analytical model were in close agreement with the datasets. The accuracy, however, dropped for tubes with high b/t ratio because the force drop in force-displacement curve for these tubes is due to plasticity and ovalization of the cross-section. Some results are presented in Figure 3.20.

The coefficient of determination (R^2) for both the peak force and energy absorption (between semi-analytical model and numerical results) was observed to be 0.99.

While the predictions from the semi-analytical model are reliable (mean error = 3.78% for peak force and 4.43% for absorbed energy), the model has room for further improvement. Currently, the model uses a drop factor (DF) multiplied with the initial slope to obtain the drop in transition case-1, which is a working assumption and not a robust physics based approach. Therefore, better transition algorithms based on the actual collapse process are required. Secondly, the model currently under-predicts post-peak force response for stockier tubes. The under-prediction for stockier tubes is a consequence of the fact that stockier tubes do not undergo bending collapse but undergo smooth decrease in force due to plasticity and subsequent ovalization of the cross-section.

The dataset created as part of this work, containing numerical simulation input files, corresponding results, the script for the semi-analytical model, the implementation of the Kecman model [1], the implementation of the model from Kim and Reid [32], and the implementation of the Wierzbicki et al. model [31], was made openly available [80].

5.3. Bending of GLARE laminates

In chapter 4, the failure modes were studied for 3 point bending of GLARE laminates. A large experimental dataset was collected for 73 different configurations and a total of 419 specimens, consisting of 5 GLARE types (2A,2B, 3, 4A and 4B) tested at 4 different strain rates (1 mm/min, 10 mm/min, 100 mm/min and 1000 mm/min). Based on the experimental results, three distinct failure modes were identified, namely central cracking, delamination, and limited delamination.

A semi-analytical framework similar to chapter 3 was also proposed, the moment-rotation curve was calculated based on a layer-wise discretization assuming linear strain through the thickness and looking up against the stress-strain curves for aluminum and glass fiber prepreg. Progressive damage was tracked based on the tensile and compressive ultimate strain, with layers marked as damaged as soon as a strain greater than ultimate strain is detected. The neutral axis was then shifted and the moment-rotation curves were updated based on the new configuration, while taking into account damaged layers.

The results from the proposed model were in close agreement with experimental results for samples failing through central cracking, including the progressive damage phase. For samples that failed through delamination, the predictions from the proposed semi-analytical model showed good agreement up to the peak force but deviated subsequently, as the semi-analytical model does not account for interlaminar shear stress. In bending of laminates, normal stresses dominate central-cracking failure, whereas delamination is primarily driven by shear stresses at the layer interfaces. Since interlaminar shear is not modeled, the post-peak response associated with delamination cannot be accurately captured. Some results are presented in Figure 4.16.

The proposed model showed that semi-analytical approaches could be extended further to composite materials. However, further development considering shear-based failure and more complex geometries is required.

A dataset containing the experimental results for 73 different configurations (419 specimens) and Python script implementing the semi-analytical model for 3-point bending of GLARE laminates was made openly available [108].

6

Conclusion

As outlined in chapter 1, this thesis addresses three research questions. The questions and their corresponding conclusions are presented below.

1. **What computationally inexpensive methods suitable for early-stage design can be developed to predict force–displacement curves for the axial crushing of metallic structures?**

   Axial crushing of metallic tubular structures consists of two failure modes: extensional and inextensional. A generalized expression, which accounts for crushing mode and cross-section shape, has been proposed in this thesis to predict the mean crushing force.

   The mean crushing force is obtained by selecting appropriate coefficients based on the geometry and collapse mode, calculating the fully plastic bending moment using the material flow stress, substituting these quantities into the generalized expression and evaluating the resulting closed-form expression for the mean crushing force. Regression analysis comparing the mean crushing force predicted by the generalized expression with the combined experimental–numerical dataset resulted in an R^2 value of 0.97, indicating strong predictive capability.

2. **What computationally inexpensive methods suitable for early-stage design can be developed to predict force–displacement curves for the bending collapse of metallic structures?**

   A combination of spring-linkage based elastic-plastic prediction, transition algorithm and Kecman model has been proposed for quick ($\approx$ 3 seconds) prediction of force-displacement curve for bending of metallic tubular structures.

   The proposed method requires the cross-sectional dimensions (width, height, and thickness), the span, and the true stress–strain curve provided as discrete data points in CSV format. Between simulations, only the geometric parameters

and the path to the material data file need to be updated, while the underlying code remains unchanged. This input-based structure readily enables automated batch processing. Furthermore, the use of discrete stress–strain data allows experimentally obtained material curves to be used with minimal post-processing.

The proposed model for predicting force-displacement curves was verified against numerical simulations and found to be consistent across geometries and materials. The coefficient of determination (R^2) for both peak force and absorbed energy was observed to be 0.99. The mean error for peak force was observed to be 3.78% and mean error for absorbed energy was observed to be 4.43%.

3. **How can analytical and semi-analytical models be extended to hybrid structures?**

   The spring-linkage model was further extended to hybrid material laminates (GLARE). The model uses the same framework as in the case of bending collapse of metallic structures but includes layer-wise damage based on maximum strain, corresponding shift in neutral axis and moment-rotation curve calculation combining aluminum and glass-fiber layers. The model was shown to be able to predict the force-displacement curve, including progressive failure, for cases where laminates failed with central cracking as the main mechanism.

This work demonstrates that, while it is not possible to obtain exact force-displacement curves for axial crushing and bending collapse analytically or semi-analytically given the complex nature of these mechanisms, curves that are well suited for early stage design exploration can be generated rapidly ($R^2 = 0.97$ for mean crushing force in axial crushing and $R^2 = 0.99$ for peak force and absorbed energy in bending). These methods can be integrated into multi-body or linkage-kinematic joint models to enable efficient exploration of the design space.

Such frameworks have the potential to equip engineers with a structured process that can inform their understanding of the design space with respect to crashworthiness and help them to strategically scope numerical simulations and experimental campaigns to maximize return on investment. A framework with geometry and material curves as the sole input is especially helpful for unconventional designs where historical crash data is absent and rules of thumb do not exist.

7

Recommendations

This chapter outlines future possible research directions which can possibly be pursued as continuation of present work. Some preliminary thoughts are presented alongside these directions and are based on the author's experience gained during the course of the present work.

7.1. Axial crushing of open sections

A small numerical campaign consisting of 10 simulations was conducted by the author on the axial crushing of C-shaped sections. The simulated geometries and obtained mean crushing force values are presented in Table 7.1. The corresponding force-displacement plots are presented in Figure 7.2.

It was observed that, instead of following a consistent fold wavelength, the structure folds with varying wavelengths for a c-shaped section of 200 mm height, as illustrated in Figure 7.1. The prediction of mean crushing force using analytical equations depends on the minimization of mean crushing force with respect to the wavelength. The biggest gap towards having robust analytical models for axial crushing of open sections, therefore, is the development of a method to estimate these wavelengths, following which similar methods can be developed to solve for the mean crushing force of c-shaped sections.

7.2. Post-peak response for stockier tubes with $t/b > 0.1$

As discussed previously in chapter 3, the proposed semi-analytical model for bending in this work underpredicts post-peak force for tubes with $t/b > 0.1$, which is because such tubes undergo plasticity and ovalization instead of bending collapse, as illustrated in Figure 7.3. Therefore, for stockier tubes, an analytical/semi-analytical model based on ovalization is required. A possible method for such cases could be to predict the central cross-section shape, assume undeformed cross sections away

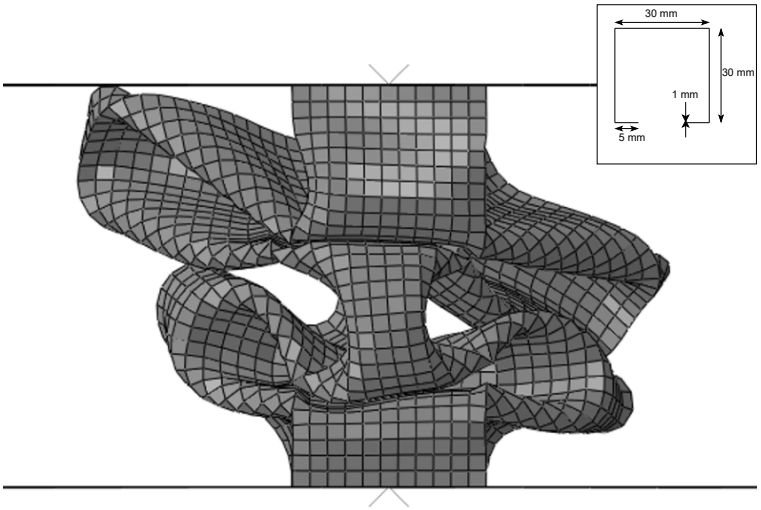

(a) Deformed c-shaped section subjected to axial loading, side length=30mm, flange length=5mm and thickness=1mm

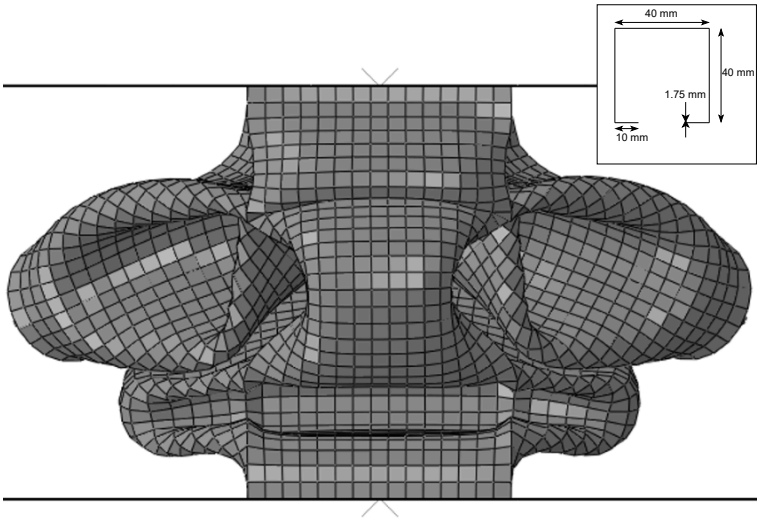

(b) Deformed c-shaped section subjected to axial loading, side length=40mm, flange length=10mm and thickness=1.75mm

Figure 7.1.: Deformed c-shaped sections submitted to axial crushing, different fold widths can be clearly observed indicating varying fold wavelength

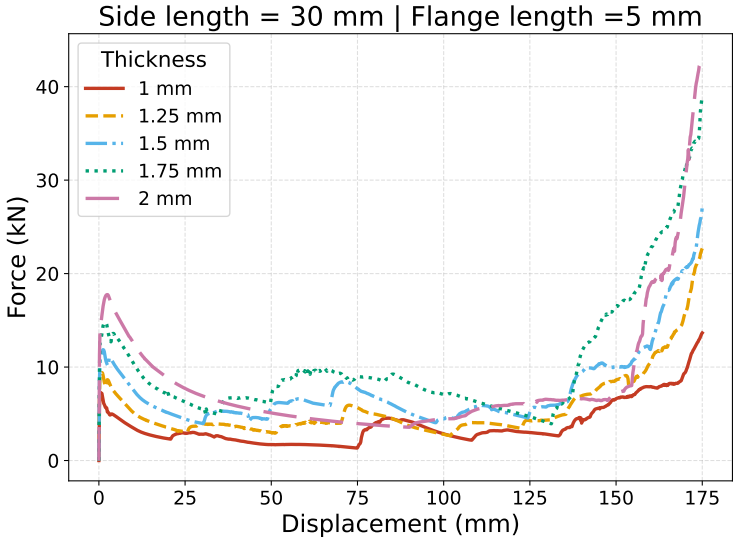

(a) Force-displacement plot for c-shaped section: Side length=30mm and Flange length=5mm

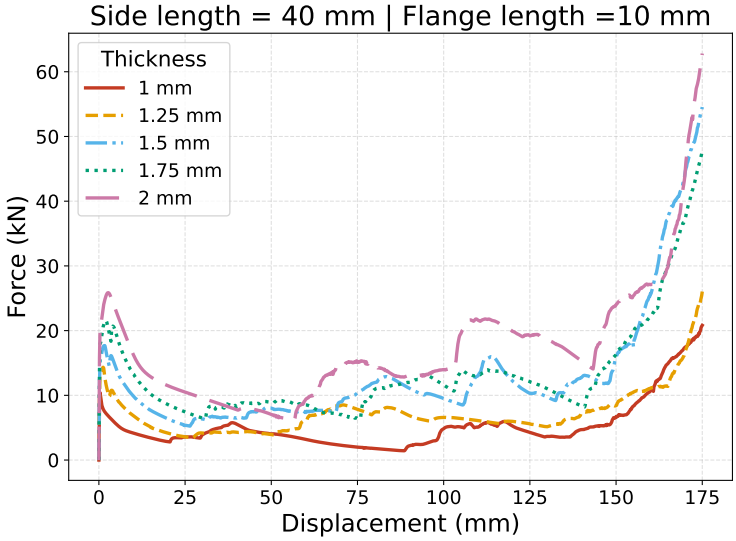

(b) Force-displacement plot for c-shaped section: Side length=40mm and Flange length=10mm

Figure 7.2.: Force-displacement plots for c-shaped section

S.No.	Side length (mm)	Flange length (mm)	Thickness (mm)	Mean crushing force (kN)
1	30	5	1	2.66
2	30	5	1.25	3.89
3	30	5	1.5	5.68
4	30	5	1.75	7.37
5	30	5	2	global buckling
6	40	10	1	3.72
7	40	10	1.25	5.98
8	40	10	1.5	9.60
9	40	10	1.75	10.28
10	40	10	2	14.45

Table 7.1.: Experimental results for mean crushing force of C-shaped sections

from the center, use splines passing through equally spaced points along the cross-sections to obtain the deformed surface and finally calculate corresponding change in energy. Works from Światkowski and Stachowicz [110] and Kut and Stachowicz [111] could serve as a starting point for such a model.

7.3. Bending for varied cross sections

A composite method for approximating the moment–rotation curve up to the plastic stage has been presented in chapter 3. This method was shown to produce decent results for I-section beams as well [87], up to the plastic deformation stage. However, the model does not account for twisting and out-of-plane displacements. In addition, for an actual fuselage structure under vertical impact, the frame bending must account for the combined geometry consisting of the frame section, shear clip, and fuselage skin, which requires a semi-analytical implementation accounting for neutral axis shift, regional collapse, and multiple materials. The study on GLARE laminates as part of this work (chapter 4) accounted for neutral axis shift, damaged layers, and multiple materials, providing a promising basis for the extension of semi-analytical methods to more geometrically complex and multi-material configurations.

7.4. Oblique impact

For cases of oblique impact, depending on the impact angle and length of the specimen, the specimen could either undergo axial crushing or buckling. A possible method to account for oblique impact could be to evaluate the direction of the resultant force and activate rotational springs informed using moment-rotation curves for bending collapse if buckling conditions are detected. Of-course an understanding of conditions which shift collapse from crushing to bending collapse is a pre-requisite.

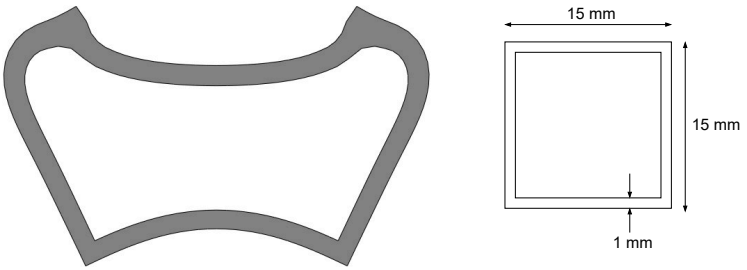

(a) Deformed cross-section for a tube with t/b<0.1, a=15mm, b=15mm and t=1mm

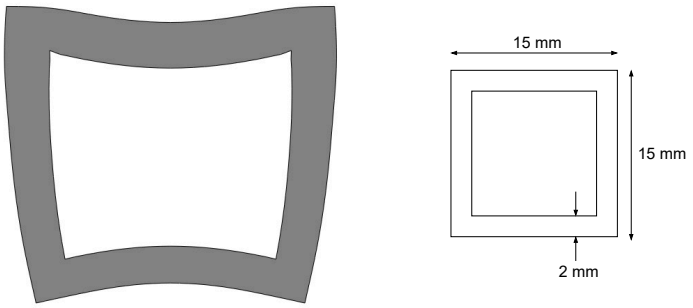

(b) Deformed cross-section for a tube with t/b>0.1, a=15mm, b=15mm and t=2mm

Figure 7.3.: Deformed cross-section for a tube with t/b<0.1 and a tube with t/b>0.1 at loading pin displacement of 20mm

7.5. Inclusion of shear for GLARE bending

The current model was shown to be capable of predicting force-displacement curves for the central cracking cases, however, since the model lacks implementation of shear it failed to reproduce delamination driven failure. However, because the model is layer-wise and semi-analytical, it should be possible to extend the model further to evaluate shear loads and therefore predict delamination failures. If a delamination all the way to the end is observed, the force-displacement curve beyond this point can be approximated as the some total of two laminates, with layers above the delaminated interface forming the first laminate and the layers below forming the second.

7.6. Extension of GLARE bending model to other composite materials

Based on the results obtained for bending of GLARE laminates , it would be of interest to extend the model and evaluate its applicability to other composite materials like Carbon fiber reinforced aluminum laminate (CARALL) and Carbon Fiber Reinforced Polymer (CFRP).

7.7. Analytical models for axial crushing of composite structures

Most analytical models for composite structures currently assume splaying of fibers with creation of a debris wedge. However, the behavior of crushing front is not consistent and can vary based on the laminate sequence. Pinho et al. [112] similarly identify axial splitting, delamination, intralaminar damage, frond formation and friction as interacting mechanisms governing the crushing response of composite tubes. For example in one of the previous works from the author, it was observed using meso-scale models that 90° layers (along the hoop direction) in composite tubes can constraint the inner 0° layers (along the crushing direction), preventing them from splaying and promoting progressive crushing failure leading to higher specific energy absorption (SEA) values [113], see Figure 7.4.

Therefore to develop analytical/semi-analytical models that can work for composite structures without resorting to parameter fitting, effort needs to be pointed towards understanding the effect of layup, geometry and boundary conditions on the development of crushing front, following which semi-analytical methods can be implemented to calculate the change in energy by accounting for friction, delamination, progressive crushing and splaying.

Delamination itself involves both initiation and progressive propagation under potentially mixed-mode loading [114, 115], while interaction between intralaminar cracking and delamination has also been highlighted in literature [116]. These observations indicate that an extension of the present analytical approach to composite crushing would also require the interaction between the dominant damage mechanisms to be accounted for while calculating the energy absorbed during crushing.

7.8. Extension towards full-aircraft crashworthiness assessment

The original motivation for the present work was the development of a computationally inexpensive crashworthiness tool that could be used during the early design of unconventional aircraft configurations such as Blended-Wing-Body aircraft. At this stage of the design process, the structural layout, materials, and dimensions can change repeatedly, while sufficiently detailed finite element models may either not be available or may be too computationally expensive for large design-space studies. A reduced-order aircraft representation based on rigid or elastic members connected

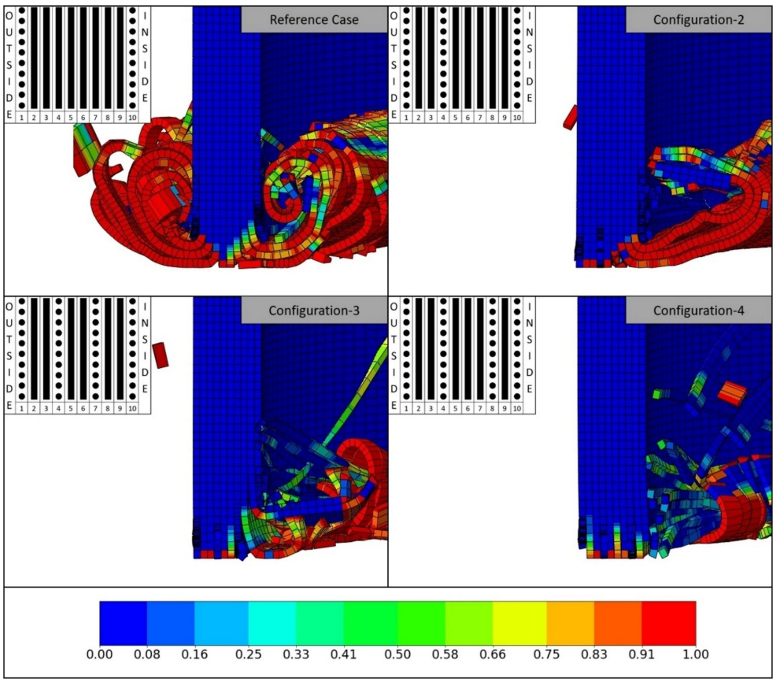

Figure 7.4.: Crushing front development in composite tube under axial loading. Reprinted from *Stacking sequence optimization of composite tubes submitted to crushing using the discrete ply model (DPM)*, S. Anand, J.-E. Chambe, C. Bouvet, and S. Rivallant, *Composite Structures*, © 2022 Informa UK Limited, trading as Taylor & Francis Group. Reprinted by permission of Informa UK Limited, trading as Taylor & Francis Group, `http://www.tandfonline.com`. [113]

through kinematic joints therefore offers a possible route for early crashworthiness assessment.

This approach has previously been demonstrated at structural and vehicle level. Nikravesh et al. [17] represented plastically deforming structures using rigid components connected through joint-spring combinations, with bending represented through revolute joints and torsional springs. Sousa et al. [19] subsequently used kinematic joints representing different deformation modes in an automotive crash model, while Tay et al. [20] applied a spring-linkage multi-body approach to an aircraft fuselage section. A common requirement in these approaches is the availability of suitable force-displacement and moment-rotation characteristics for the individual joints. Nikravesh et al. obtained these characteristics from experiments, while more recent approaches have generally relied on component-level finite element simulations.

The initial idea behind this thesis was therefore to develop analytical models for the principal energy-absorbing mechanisms in metallic structures and use these models to provide the characteristic curves required by such a multi-body aircraft model.

Composite and hybrid material systems were intended as a subsequent extension. However, it became evident that even for relatively simple metallic tubular structures, the available analytical model space was fragmented. Different formulations were applicable to different cross-sections, materials, and deformation mechanisms, and a general approach for obtaining the required force-displacement or moment-rotation response was not readily available. Consequently, a substantial part of the present work was directed towards resolving this component-level problem before proceeding to the full-aircraft model. This is reflected in Chapters 2 and 3 through the development of generalized axial-crushing and bending-collapse approaches, followed by the first extension towards hybrid materials in Chapter 4.

A logical continuation of the present work is therefore to integrate these component-level models into a reduced-order representation of an aircraft structure. Several developments would be required:

1. **Extension of the component-model library.** The present work covers only part of the structural behaviour required at aircraft level. Characteristic relationships would additionally be required for open-section frames, floor beams, joints, subfloor structures, combined loading conditions, and other relevant failure mechanisms.

   This component library would also need to be extended to account for different joining processes, particularly for structures combining conventional metallic materials and composites. Mechanically fastened, bonded, and hybrid joints could be represented through appropriate force-displacement or moment-rotation characteristics depending on their dominant deformation and failure mechanisms.

2. **Development of an aircraft-level kinematic model.** The structural layout would need to be represented using members connected through translational and rotational joints, with each joint assigned the appropriate constitutive response based on its geometry, material, and expected deformation mechanism. For a BWB configuration, this would include the integrated wing-fuselage structure, passenger floor, and subfloor energy-absorbing structure.

3. **Inclusion of dynamic effects and deformation-mode selection.** A full-aircraft crash simulation requires inertia, contact, strain-rate effects, and possible transitions between axial crushing, bending, buckling, and combined loading to be considered. The importance of dynamic correction of joint characteristics was already identified by Nikravesh et al. [17].

   For composite and hybrid structures, the numerical solution of such a dynamic model introduces an additional challenge due to the rapid loss of stiffness associated with damage and failure. Softening constitutive models have been shown to result in convergence difficulties in nonlinear numerical simulations [114, 115], while similar convergence limitations have also been reported for numerical simulation of progressive composite crushing [112]. From a numerical point of view, such an abrupt loss of load-carrying capacity can resemble an instability problem, and therefore the choice of numerical integration and

solution strategy would require further investigation before these constitutive relationships are implemented within a complete dynamic aircraft model.

4. **Hierarchical validation.** The reduced-order model should be validated progressively, beginning with individual components, followed by structural subassemblies, representative fuselage sections, and finally an aircraft-level configuration. Detailed finite element simulations and experiments would remain necessary for validation, but would be applied to a smaller number of selected configurations.

The eventual aircraft-level model would therefore follow the general approach demonstrated by Nikravesh et al. [17], Sousa et al. [19], and Tay et al. [20]: the global structure would be represented using a comparatively small number of members and kinematic joints, while the local structural behaviour would be contained within the constitutive characteristics assigned to those joints. The main extension envisaged from the present work is that these characteristics would, where possible, be generated directly from material and geometrical inputs using analytical and semi-analytical models rather than requiring a separate experimental or finite element campaign for every structural configuration.

Such a framework would return the work to its original objective: rapid screening of crashworthiness during preliminary aircraft design, followed by progressively higher-fidelity finite element simulations and experiments for the most promising structural concepts.

A

Appendix: Chapter 2

A.1. Experimental dataset from literature

A.1.1. Hexagonal tubular structures

S.No.	Reference	Material	c (mm)	h (mm)	P_m (kN)	$P_m(FEM)$ (kN)	Crushing mode
1	Zhang and Zhang[27]	Mild steel Q235	40	1.2	25.58	24.13	Inextensional
2			40	1.2	24.53	24.13	Inextensional
3			40	1.2	23.75	24.13	Inextensional
4	Fan et al. [47]	ASTM A36	33.2	1.5	46.6	48.84	Extensional
5	Liu et al. [117]	AA6061 - T4	15	1.2	10.2	12.78	Extensional
6	Nia and Hamedani [62]	Al 3003 H12	31.4	1.5	12.64	14.49	Extensional
7			31.4	1.5	12.62	14.49	Extensional
8			31.4	1.5	12.49	14.49	Extensional
9			31.4	1.5	12.5	14.49	Extensional

A.1.2. Octagonal tubular structures

S.No.	Reference	Material	c (mm)	h (mm)	P_m (kN)	$P_m(FEM)$ (kN)	Crushing mode
1	Zhang and Zhang[27]	Mild steel Q235	40	1.2	31.87	32.15	Mixed
2			40	1.2	32.09	32.15	Mixed
3			40	1.2	32.71	32.15	Mixed
4	Fan et al. [47]	ASTM A36	24.9	1.5	58.8	47.99	Extensional
5	Liu et al. [117]	AA6061 - T4	15	1.2	11.5	13.95	Extensional

A

A.1.3. Square tubular structures

S.No.	Reference	Material	c (mm)	h (mm)	P_m (kN)	$P_m(FEM)$ (kN)	Crushing mode
1	Zhao et al. [118]	Brass	35.00	1.50	18.00	21.08	Inextensional
2			35.00	1.50	18.09	21.08	Inextensional
3	Nia and Hamedani [62]	Al 3003 H12	47.10	1.50	10.50	10.84	Mixed
4			47.10	1.50	10.60	10.84	Extensional
5			47.10	1.50	10.40	10.84	Extensional
6			47.10	1.50	10.56	10.84	Mixed
7			47.10	1.50	10.27	10.84	Extensional
8			47.10	1.00	6.46	5.76	Inextensional
9			47.10	1.00	6.02	5.76	Inextensional
10			47.10	1.00	6.33	5.76	Inextensional
11	Zhang and Zhang [27]	Mild Steel Q235	40.00	1.20	16.01	16.08	Inextensional
12			40.00	1.20	16.72	16.08	Inextensional
13			40.00	1.20	15.60	16.08	Inextensional
14	Langseth et al. [49]	AA6060 T4	80.00	1.81	17.10	17.29	Inextensional
15			80.00	1.90	20.90	18.90	Inextensional
16			80.00	2.46	32.40	30.76	Inextensional
17		AA6060 T4*	80.00	1.81	21.80	22.50	Inextensional
18			80.00	1.90	25.80	24.29	Inextensional
19			80.00	2.45	37.90	36.54	Inextensional
20		AA6060 T6	80.00	1.81	28.10	25.81	Inextensional
21			80.00	1.97	30.80	28.19	Inextensional
22			80.00	2.46	45.50	39.98	Inextensional
23	DiPaolo and Tom [119]	A36	50.00	1.40	25.50	27.03	Inextensional
24			50.00	1.40	25.70	27.03	Inextensional
25		A513	50.00	1.51	36.50	34.58	Inextensional
26			50.00	1.51	37.00	34.58	Inextensional
27		AISI 316	50.00	1.47	46.20	44.29	Inextensional
28			50.00	1.47	46.20	44.29	Inextensional
29			50.00	1.49	36.60	45.05	Inextensional
30		AISI 304 - S2	50.00	1.49	44.60	39.94	Inextensional
31			50.00	1.49	44.00	39.94	Inextensional
32		AISI 304 - S3	50.00	1.49	50.90	44.12	Inextensional
33			50.00	1.49	51.00	44.12	Inextensional
34		AISI 304 - S4	50.00	1.49	50.60	45.31	Inextensional
35			50.00	1.49	49.30	45.31	Inextensional
36			50.00	1.49	49.20	45.31	Inextensional
37	Abramo- wicz et al. [25]	Mild Steel	49.30	1.63	35.28	29.91	Inextensional
38			49.34	1.64	36.71	29.91	Inextensional
39			37.11	1.15	20.75	15.81	Extensional
40			37.11	1.15	17.90	15.81	Inextensional
41			37.10	1.16	19.75	15.46	Inextensional
42			37.06	1.18	18.50	15.72	Inextensional

A.1.4. Circular tubular structures

S.No.	Ref.	Material	R (mm)	h (mm)	P_m (kN)	$P_m(FEM)$ (kN)	Crushing mode
1	Abramowi- cz et al. [24]	Mild Steel	27.94	1.20	32.60	-	c
2			28.10	1.20	30.16	-	c+d
3	Tabacu et al. [29]	AA6063 T6	20.00	1.23	15.80	16.36	c
4			19.50	0.90	8.74	10.07	d
5	Nia and Hamedani [62]	AL3003 H12	30.00	1.50	14.63	17.94	c+d
6			30.00	1.50	15.25	17.94	c+d
7			30.00	1.50	15.38	17.94	c+d
8			30.00	1.50	14.37	17.94	c+d
9			30.00	1.50	14.05	17.94	c+d
10			30.00	1.00	8.00	8.25	d
11			30.00	1.00	7.90	8.25	d
12			30.00	1.00	8.10	8.25	d
13	Bardi et al. [120]	AL6061 T6	15.28	1.26	21.97	19.67	c
14			15.08	1.66	33.99	32.31	c
15		AL6260 T4	28.94	2.04	42.61	-	c
16		CS 1020	15.31	1.26	42.43	-	c
17	Guillow et al. [121]	AA6060 T5	48.95	1.90	43.00	43.25	c
18			48.50	1.00	15.40	15.19	d
19			48.50	1.00	15.80	15.19	c+d
20			48.50	1.00	16.25	15.19	d
21			48.95	1.90	44.00	43.25	c+d
22			48.75	1.50	30.18	29.64	c+d
23			48.30	0.56	5.75	6.32	d
24			48.50	1.00	15.72	15.19	d
25			48.25	0.54	5.06	5.89	d
26			48.15	0.26	1.66	1.50	d
27			48.10	0.22	1.10	1.17	d
28			48.15	0.31	1.84	2.12	d
29			48.15	0.29	1.83	1.88	d
30			48.15	0.31	2.00	2.12	d
31			48.25	0.52	5.06	5.30	d
32			24.20	1.35	18.70	19.42	c+d
33			24.20	1.35	17.50	19.42	c
34			24.20	1.35	19.00	19.42	c+d
35			24.20	1.35	18.50	19.42	c+d
36			24.15	1.35	18.75	19.24	c
37			15.20	1.59	24.00	17.14	c
38			14.50	2.95	63.10	-	c
39			28.95	1.92	36.90	32.33	c
40			28.25	0.57	4.50	5.12	d
41			28.55	1.15	15.33	15.87	c+d
42			28.55	1.15	15.10	15.87	d
43			28.05	0.31	1.64	1.88	d
44			48.10	0.22	1.07	1.17	d

c=concertina crushing mode ; d=diamond crushing mode

A.2. Material data

Note: In most instances, the value of flow stress is obtained using Eq. 2.6, except when required data is unavailable. It is also important to note that stainless steel tubular structures (AISI-304 and AISI-316) can undergo martensitic transformation resulting in a change of material properties [119]. We found that the flow stress values obtained using Eq. 2.5 provide much better estimations of the mean crushing force for such cases.

S. No.	Material	Reference	σ_y (MPa)	σ_u (MPa)	σ_0: [Eq.2.6] (MPa)	σ_0: [Eq.2.5] (MPa)
1	Brass	Zhao et al. [118]	173.0	367.5	291.5	270.3
2	AL3003 H12	Nia and Hamedani. [62]	130.0	137.8	136.4	133.9
3	Mild Steel Q235	Zhang and Zhang [27]	218.5	323.3	305.5	270.9
4	AA6060 T4	Langseth et al. [49]	76.3	165.3	150.3	120.8
5	AA6060 T4*		133.3	200.3	184.6	166.8
6	AA6060 T6		188.3	212.0	205.5	200.2
7	A36	DiPaolo and Tom [119]	340.0	364.0	358.0	352.0
8	A513		400.0	448.0	431.9	424.0
9	AISI316		468.0	679.0	637.2	573.5
10	AISI304 -S2		380.0	683.0	598.1	531.5
11	AISI304 -S3		420.0	740.0	659.9	580.0
12	AISI304 -S4		439.0	761.0	677.1	600.0
13	Mild Steel	Abramowicz et al. [25]	264.5	328.5	311.4	296.5
14	Steel	Abramowicz et al. [24]	222	336	-	279
15	AA6063 T6	Tabacu et al. [29]	170	222	197	196
16	AL6061 T6	Bardi et al. [120]	300.8	-	320.1	-
17	AL6260 T4		128	-	200.4	-
18	CS 1020		537.9	-	617.6	-
19	Aluminum	Guillow et al. [121]	180	212.5	199.1	196.3
20	ASTM A36	Fan et al. [47]	265	425.8	379.7	345.4
21	AA6061 T4	Liu et al. [117]	112.4	214.2	193.7	163.3

A.3. Numerical dataset

A.3.1. Square and circular tubular structures

S.No.	2R or c (mm)	h (mm)	P_{mean} (kN)			
			Circular		Square (Inextensional)	
			AA6060 T4	AISI 316	AA6060 T4	AISI 316
1	30	1	9.24	33.40	5.36	20.94
2	30	1.25	11.68	47.66	8.03	30.70
3	30	1.5	16.30	55.49	11.08	42.53
4	30	1.75	19.31	-	14.91	-
5	30	2	23.26	-	19.59	-
6	30	2.25	-	-	24.88	-
7	30	2.5	-	-	29.97	-
8	40	1	10.27	31.89	5.68	21.50
9	40	1.25	12.45	47.29	8.03	31.41
10	40	1.5	17.47	62.31	11.21	43.38
11	40	1.75	21.14	-	15.02	-
12	40	2	25.27	-	19.20	-
13	40	2.25	-	-	23.87	-
14	40	2.5	-	-	29.58	-
15	50	1	9.63	34.04	5.56	23.61
16	50	1.25	13.53	48.34	8.24	33.00
17	50	1.5	17.24	65.47	11.38	44.16
18	50	1.75	22.05	-	14.40	-
19	50	2	26.62	-	18.89	-
20	50	2.25	-	-	24.10	-
21	50	2.5	-	-	29.95	-
22	60	1	9.99	34.95	5.44	23.87
23	60	1.25	14.44	54.43	8.13	35.97
24	60	1.5	18.39	73.74	11.46	47.32
25	60	1.75	23.22	-	15.69	-
26	60	2	28.23	-	19.68	-
27	60	2.25	-	-	24.82	-
28	60	2.5	-	-	30.85	-

Geometrical parameters:
$2R$ = diameter of circular tubular structures
c = edge length of square tubular structures
h = wall thickness
Material parameters:
AA6060 T4: κ =0.73, $\sigma_y = 76$ MPa, $\sigma_u = 165$ MPa and $\sigma_0 = 151$ MPa
AISI 316 : κ =0.77, $\sigma_y = 467$ MPa, $\sigma_u = 678$ MPa and $\sigma_0 = 624$ MPa

A.3.2. Hexagonal and octagonal tubular structures (Inextensional)

S.No.	c (mm)	h (mm)	P_{mean} (kN)			
			Hexagonal		Octagonal	
			AA6060 T4	AISI 316	AA6060 T4	AISI 316
1	30	1	7.96	31.63	11.08	42.74
2	30	1.12	-	39.21	-	53.09
3	30	1.25	12.27	48.31	-	-
4	30	1.37	-	57.00	-	-
5	30	1.5	17.57	67.44	-	-
6	30	1.75	22.66	-	-	-
7	30	2	28.57	-	-	-
8	40	1	8.52	32.03	10.55	44.44
9	40	1.12	-	39.07	-	54.39
10	40	1.25	12.24	47.54	16.25	69.15
11	40	1.37	-	57.11	-	79.98
12	40	1.5	17.37	67.05	-	-
13	40	1.75	23.09	-	-	-
14	40	2	29.05	-	-	-
15	50	1	8.09	33.08	11.26	46.43
16	50	1.12	-	43.83	-	58.54
17	50	1.25	12.52	48.89	16.22	70.92
18	50	1.37	-	57.04	-	83.02
19	50	1.5	17.61	66.98	22.56	97.97
20	50	1.75	23.13	-	-	-
21	50	2	30.29	-	-	-
22	60	1	8.77	39.45	11.01	47.81
23	60	1.12	-	46.64	-	58.29
24	60	1.25	13.20	56.76	16.93	72.47
25	60	1.37	-	61.01	-	80.32
26	60	1.5	18.43	71.70	22.39	97.01
27	60	1.75	23.66	-	29.31	-
28	60	2	29.13	-	-	-
Note: The parameters and material data are the same as subsection A.3.1						

A.3.3. Hexagonal and octagonal tubular structures (Extensional)

S.No.	c (mm)	h (mm)	P_{mean} (kN)			
			Hexagonal		Octagonal	
			AA6060 T4	AISI 316	AA6060 T4	AISI 316
1	30	1	9.11	39.22	9.75	41.05
2	30	1.5	16.63	67.97	17.95	74.95
3	30	2	28.36	-	28.35	-
4	40	1	10.19	45.18	12.27	51.20
5	40	1.5	18.13	79.36	21.80	93.80
6	40	2	27.91	-	31.41	-
7	50	1	10.34	47.56	13.36	62.49
8	50	1.5	19.75	84.75	25.62	114.23
9	50	2	30.59	-	37.86	-
10	60	1	10.89	50.73	13.96	67.03
11	60	1.5	20.21	86.36	27.81	124.4
12	60	2	34.10	-	41.78	-
Note: The parameters and material data are the same as subsection A.3.1						

B

Appendix: Chapter 3

B.0.1. Derivation for the baseline moment-rotation curve

To obtain the baseline moment-rotation curve an n-linear approximation of the stress-strain curve is used. However, in this derivation, a tri-linear curve (Figure B.1) is sufficient and the derived equation holds true for any value of n.

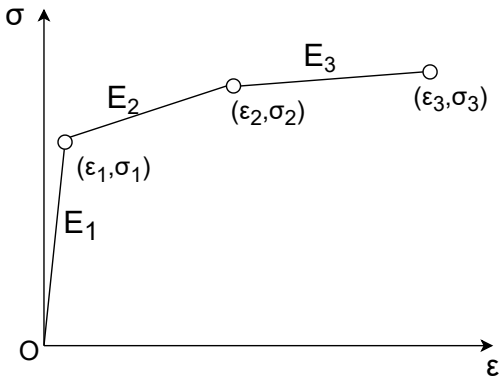

Figure B.1.: Tri-linear approximation of the stress-strain curve

We know that Moment for a given cross section Reference can be written as:

$$M = a \int_{-z_{max}}^{z_{max}} \sigma(\varepsilon_z) \cdot z \cdot dz \tag{B.1}$$

For an element of length dx taken along the axis of the beam, we know from Euler beam theory the following:

1. Radius of curvature (ρ) can be expressed as a function of element length dx and θ:

$$\rho = dx/\theta \tag{B.2}$$

2. Assuming a linear strain distribution, the strain at the farthest fiber from the neutral axis ε_{max} can be written as

$$\varepsilon_{max} = z_{max}/\rho \tag{B.3}$$

Substituting Equation B.2 in Equation B.3:

$$\varepsilon_{max} = (z_{max}/dx) \cdot \theta \tag{B.4}$$

3. Strain at any given height z from the neutral axis can be expressed as

$$\varepsilon_z = (\varepsilon_{max}/z_{max}) \cdot z \tag{B.5}$$

Substituting Equation B.5 into Equation B.1, we get:

$$M = a \int_{-z_{\max}}^{z_{\max}} \sigma\left(\frac{\varepsilon_{\max}}{z_{\max}} \cdot z\right) \cdot z \cdot dz \tag{B.6}$$

Then if ε_{max} is the maximum stress that the section is experiencing. Only segments of stress-strain curve that belong to the range $0 < \varepsilon < \varepsilon_{max}$ need to be considered to calculate the corresponding Moment. Since, the strain is assumed to be linear, different portions of the section can use different values of young's modulus (E_i) to calculate stress (σ) from strain (ε).

1. If $\varepsilon_0 < \varepsilon < \varepsilon_1$, then $\sigma = E_1 \cdot \varepsilon$. Moment can then be written as:

$$M = 2a \int_0^{z_{max}} E_1 \cdot \left(\frac{\varepsilon_{max}}{z_{max}}\right) \cdot z^2 \cdot dz \tag{B.7}$$

$$M = 2 \cdot a \cdot E_1 \cdot \varepsilon_{max} \cdot \frac{z_{max}^2}{3} \tag{B.8}$$

$$\frac{M}{2 \cdot a \cdot z_{max}^2} = \frac{E_1 \cdot \varepsilon_{max}}{3} \tag{B.9}$$

$$\frac{M}{2 \cdot a \cdot z_{max}^2} = \frac{1}{3 \cdot \varepsilon_{max}^2} \cdot E_1 \cdot \varepsilon_{max}^3 \tag{B.10}$$

Since $E_0 = 0$ and $\varepsilon_0 = 0$, Equation B.10 can be written as:

$$\frac{M}{2 \cdot a \cdot z_{max}^2} = \frac{1}{3 \cdot \varepsilon_{max}^2} \cdot E_1 \cdot (\varepsilon_{max}^3 - \varepsilon_0^3) + \varepsilon_0 \cdot (E_0 - E_1) - \frac{1}{\varepsilon_{max}^2} \cdot \varepsilon_0^3 \cdot (E_0 - E_1) \tag{B.11}$$

If $\varepsilon_{max} = \varepsilon_1$:

$$\frac{M}{2 \cdot a \cdot z_{max}^2} = \frac{1}{3 \cdot \varepsilon_1^2} \cdot E_1 \cdot (\varepsilon_1^3 - \varepsilon_0^3) + \frac{\varepsilon_0}{2} \cdot (E_0 - E_1) - \frac{(E_0 - E_1)}{2 \cdot \varepsilon_1^2} \cdot \varepsilon_0^3 \tag{B.12}$$

2. If $\varepsilon_1 < \varepsilon < \varepsilon_2$, then $\sigma = E_1 \cdot \varepsilon_1 + E_2 \cdot (\varepsilon - \varepsilon_1)$. Moment can then be written as:

$$M = 2a \int_0^{\frac{z_{max} \cdot \varepsilon_1}{\varepsilon_{max}}} E_1 \cdot \left(\frac{\varepsilon_{max}}{z_{max}} \right) \cdot z^2 \cdot dz + 2a \int_{\frac{z_{max} \cdot \varepsilon_1}{\varepsilon_{max}}}^{z_{max}} [E_1 \cdot \varepsilon_1 + E_2 \cdot (\varepsilon - \varepsilon_1)] \cdot z \cdot dz \tag{B.13}$$

$$\frac{M}{2 \cdot a} = \frac{E_1 \cdot \varepsilon_{max}}{z_{max}} \left[\frac{z^3}{3} \right]_0^{\frac{z_{max} \cdot \varepsilon_1}{\varepsilon_{max}}} + \int_{\frac{z_{max} \cdot \varepsilon_1}{\varepsilon_{max}}}^{z_{max}} (E_1 - E_2) \cdot \varepsilon_1 \cdot z \cdot dz + \int_{\frac{z_{max} \cdot \varepsilon_1}{\varepsilon_{max}}}^{z_{max}} E_2 \cdot \varepsilon \cdot z \cdot dz \tag{B.14}$$

$$\begin{aligned} \frac{M}{2\,a\,z_{\max}^2} = & \left[\frac{E_1}{3} \varepsilon_1^3 + \frac{(E_1 - E_2)}{2} \varepsilon_1 \left(\varepsilon_{\max}^2 - \varepsilon_1^2 \right) \right. \\ & \left. + \frac{E_2}{3} \left(\varepsilon_{\max}^3 - \varepsilon_1^3 \right) \right] \left(\frac{1}{\varepsilon_{\max}^2} \right) \end{aligned} \tag{B.15}$$

$$\begin{aligned} \frac{M}{2\,a\,z_{\max}^2} = & \frac{E_1}{3\,\varepsilon_{\max}^2} \varepsilon_1^3 + \frac{(E_1 - E_2)}{2} \varepsilon_1 \\ & + \frac{(E_1 - E_2)}{2\,\varepsilon_{\max}^2} \varepsilon_1^3 + \frac{E_2}{3\,\varepsilon_{\max}^2} \left(\varepsilon_{\max}^3 - \varepsilon_1^3 \right) \end{aligned} \tag{B.16}$$

Substituting $\varepsilon_{max} = \varepsilon_2$ and adding the terms for ε_0 and E_0 ,we get:

$$\begin{aligned} \frac{M}{2\,a\,z_{\max}^2} = & \frac{E_2}{3\,\varepsilon_2^2} \left(\varepsilon_2^3 - \varepsilon_1^3 \right) + \frac{E_1}{3\,\varepsilon_2^2} \left(\varepsilon_1^3 - \varepsilon_0^3 \right) \\ & + \frac{\varepsilon_1}{2} (E_1 - E_2) + \frac{\varepsilon_0}{2} (E_0 - E_1) \\ & - \frac{(E_1 - E_2)}{2\,\varepsilon_2^2} \varepsilon_1^3 - \frac{(E_0 - E_1)}{2\,\varepsilon_2^2} \varepsilon_0^3 \end{aligned} \tag{B.17}$$

3. Similarly if $\varepsilon_2 < \varepsilon < \varepsilon_3$, then $\sigma = E_1 \cdot \varepsilon_1 + E_2 \cdot \varepsilon_2 + E_3 \cdot (\varepsilon - \varepsilon_2)$. Moment

can then be written as:

$$\begin{aligned}\frac{M}{2\,a\,z_{max}^2} &= \frac{E_3}{3\,\varepsilon_{max}^2}\left(\varepsilon_{max}^3-\varepsilon_2^3\right)+\frac{E_2}{3\,\varepsilon_{max}^2}\left(\varepsilon_2^3-\varepsilon_1^3\right)\\ &+\frac{E_1}{3\,\varepsilon_{max}^2}\left(\varepsilon_1^3-\varepsilon_0^3\right)\\ &+\frac{\varepsilon_2}{2}\left(E_2-E_3\right)+\frac{\varepsilon_1}{2}\left(E_1-E_2\right)+\frac{\varepsilon_0}{2}\left(E_0-E_1\right)\\ &-\frac{\left(E_2-E_3\right)}{2\,\varepsilon_{max}^2}\varepsilon_2^3-\frac{\left(E_1-E_2\right)}{2\,\varepsilon_{max}^2}\varepsilon_1^3-\frac{\left(E_0-E_1\right)}{2\,\varepsilon_{max}^2}\varepsilon_0^3\end{aligned} \tag{B.18}$$

Substituting $\varepsilon_{max}=\varepsilon_3$ and adding the terms for ε_0 and E_0 ,we get:

$$\begin{aligned}\frac{M}{2\,a\,z_{max}^2} &= \frac{E_3}{3\,\varepsilon_3^2}\left(\varepsilon_3^3-\varepsilon_2^3\right)+\frac{E_2}{3\,\varepsilon_3^2}\left(\varepsilon_2^3-\varepsilon_1^3\right)\\ &+\frac{E_1}{3\,\varepsilon_3^2}\left(\varepsilon_1^3-\varepsilon_0^3\right)\\ &+\frac{\varepsilon_2}{2}\left(E_2-E_3\right)+\frac{\varepsilon_1}{2}\left(E_1-E_2\right)+\frac{\varepsilon_0}{2}\left(E_0-E_1\right)\\ &-\frac{\left(E_2-E_3\right)}{2\,\varepsilon_3^2}\varepsilon_2^3-\frac{\left(E_1-E_2\right)}{2\,\varepsilon_3^2}\varepsilon_1^3-\frac{\left(E_0-E_1\right)}{2\,\varepsilon_3^2}\varepsilon_0^3\end{aligned} \tag{B.19}$$

Based on Equations B.7 to B.18, we can write the equations for Moment versus rotation as a function of i where i represents the ith point on n-linear stress-strain curve :

$$\begin{aligned}\frac{M}{2\,a\,z_{max}^2} &= \frac{1}{3\,\varepsilon_i^2}\sum_{j=1}^{i}E_j\left(\varepsilon_j^3-\varepsilon_{j-1}^3\right)\\ &+\frac{1}{2}\sum_{j=1}^{i}\varepsilon_{j-1}\left(E_{j-1}-E_j\right)\\ &-\frac{1}{2\,\varepsilon_i^2}\sum_{j=1}^{i}\varepsilon_{j-1}^3\left(E_{j-1}-E_j\right)\end{aligned} \tag{B.20}$$

$$\theta\cdot\left(\frac{z_{max}}{dx}\right)=\varepsilon_i \tag{B.21}$$

Therefore, using n-linear approximation, we can obtain Equation B.20 and Equation B.21 where the right hand side of equation is purely dependent on n-linear stress-strain curve of the material and therefore can be pre-calculated. For any

rectangular cross-section having a width "a" and distance to farthest fiber "z_{max}", we can write :

$$M = A \cdot f(\text{material properties}) \textbf{ and } \theta = B \cdot f(\text{material properties}) \quad \text{(B.22)}$$

where, $A = (2 \cdot a \cdot z_{max}^2)$ and $B = dx/z_{max}$. For a rectangular section $z_{max} = h/2$ where h is the height of the cross-section.

B.0.2. Comparison between numerical data and semi-analytical model for square cross-sections

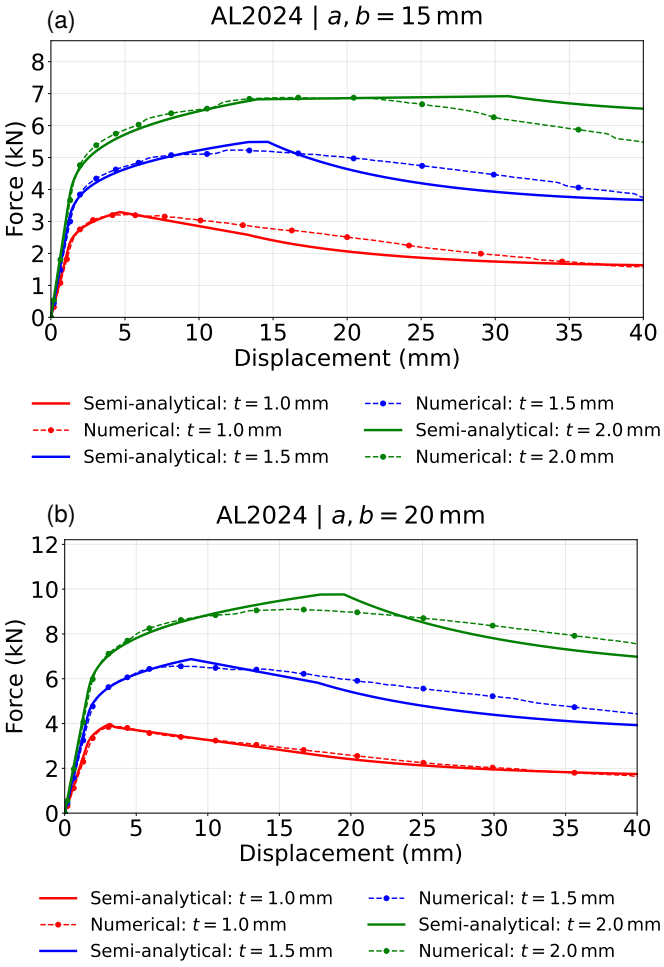

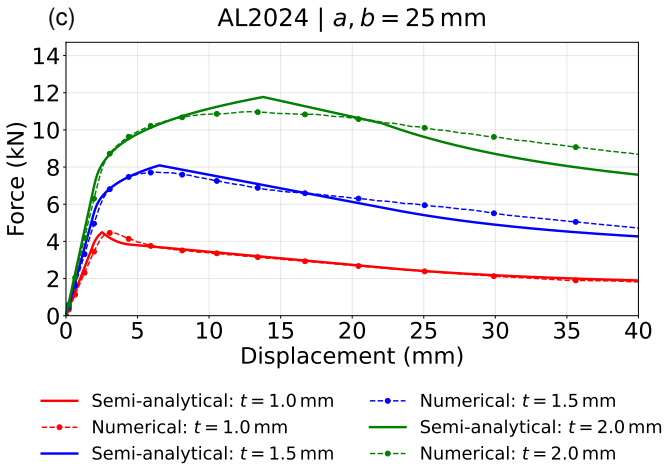

Semi-analytical: $t = 1.0$ mm
Numerical: $t = 1.0$ mm
Semi-analytical: $t = 1.5$ mm
Numerical: $t = 1.5$ mm
Semi-analytical: $t = 2.0$ mm
Numerical: $t = 2.0$ mm

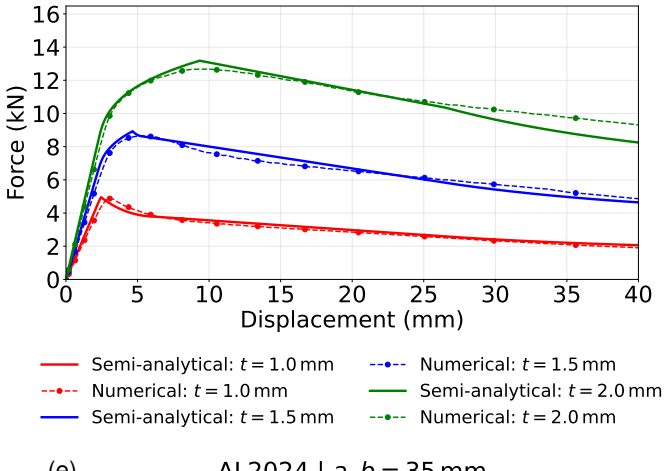

Semi-analytical: $t = 1.0$ mm
Numerical: $t = 1.0$ mm
Semi-analytical: $t = 1.5$ mm
Numerical: $t = 1.5$ mm
Semi-analytical: $t = 2.0$ mm
Numerical: $t = 2.0$ mm

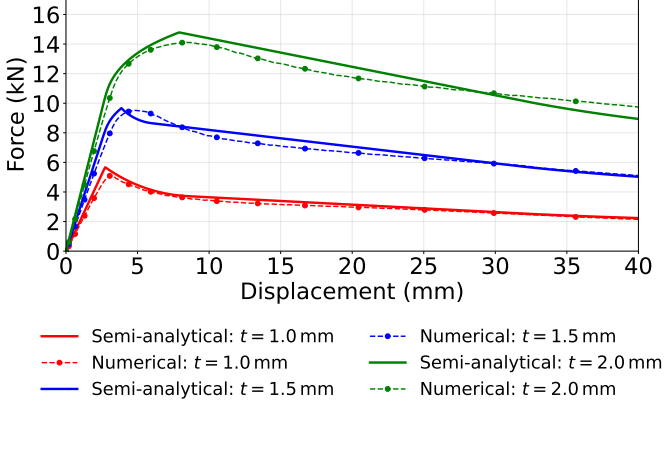

Semi-analytical: $t = 1.0$ mm
Numerical: $t = 1.0$ mm
Semi-analytical: $t = 1.5$ mm
Numerical: $t = 1.5$ mm
Semi-analytical: $t = 2.0$ mm
Numerical: $t = 2.0$ mm

(f)

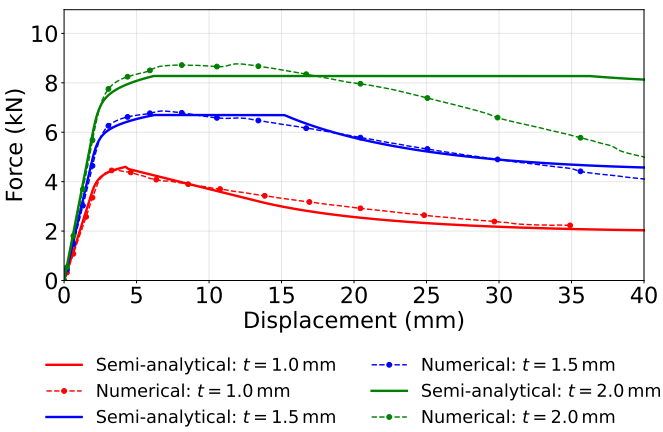
AL7075 | a, b = 15 mm
Force (kN)
Displacement (mm)
0
2
4
6
8
10
0
5
10
15
20
25
30
35
40
Semi-analytical: t = 1.0 mm
Numerical: t = 1.0 mm
Semi-analytical: t = 1.5 mm
Numerical: t = 1.5 mm
Semi-analytical: t = 2.0 mm
Numerical: t = 2.0 mm

(g)

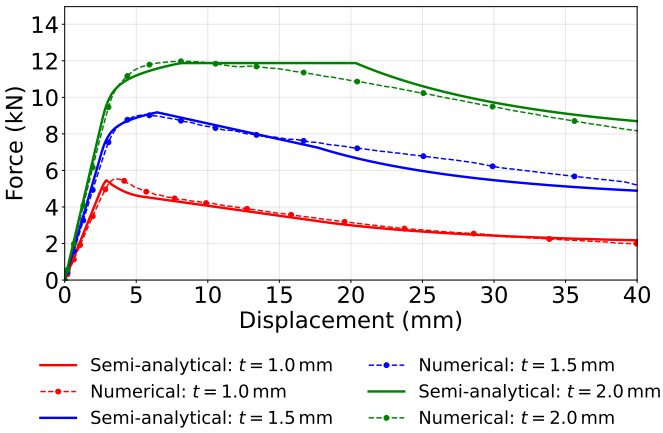
AL7075 | a, b = 20 mm
Force (kN)
Displacement (mm)
0
2
4
6
8
10
12
14
0
5
10
15
20
25
30
35
40
Semi-analytical: t = 1.0 mm
Numerical: t = 1.0 mm
Semi-analytical: t = 1.5 mm
Numerical: t = 1.5 mm
Semi-analytical: t = 2.0 mm
Numerical: t = 2.0 mm

(h)

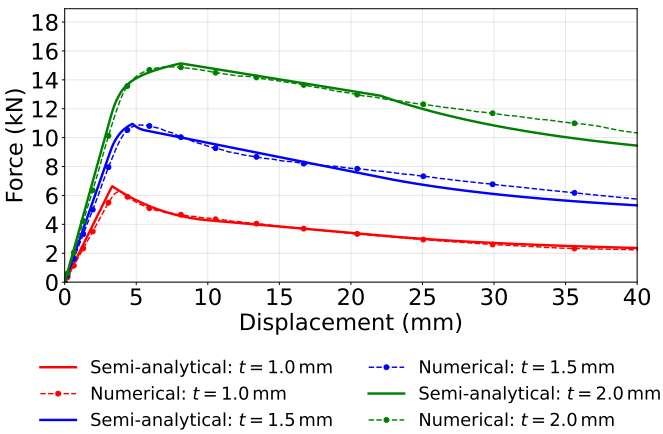
AL7075 | a, b = 25 mm
Force (kN)
Displacement (mm)
0
2
4
6
8
10
12
14
16
18
0
5
10
15
20
25
30
35
40
Semi-analytical: t = 1.0 mm
Numerical: t = 1.0 mm
Semi-analytical: t = 1.5 mm
Numerical: t = 1.5 mm
Semi-analytical: t = 2.0 mm
Numerical: t = 2.0 mm

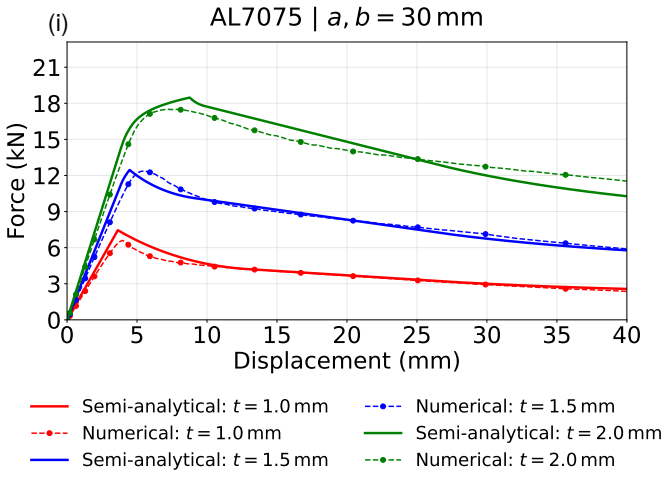
(i)
AL7075 | $a, b = 30$ mm
Force (kN)
Displacement (mm)
0 3 6 9 12 15 18 21
0 5 10 15 20 25 30 35 40
Semi-analytical: $t = 1.0$ mm
Numerical: $t = 1.0$ mm
Semi-analytical: $t = 1.5$ mm
Numerical: $t = 1.5$ mm
Semi-analytical: $t = 2.0$ mm
Numerical: $t = 2.0$ mm

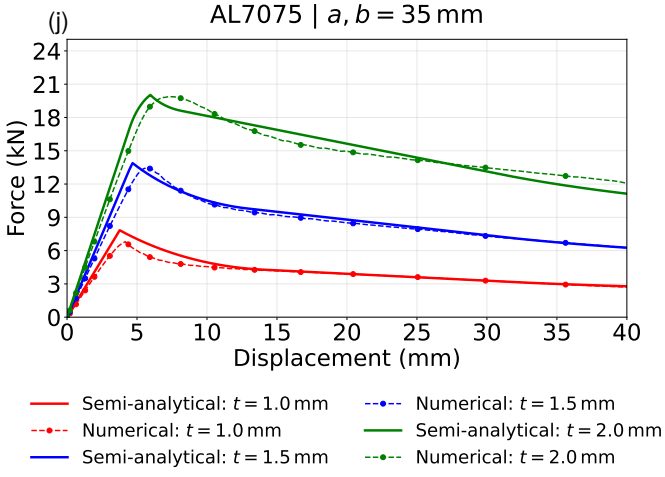
(j)
AL7075 | $a, b = 35$ mm
Force (kN)
Displacement (mm)
0 3 6 9 12 15 18 21 24
0 5 10 15 20 25 30 35 40
Semi-analytical: $t = 1.0$ mm
Numerical: $t = 1.0$ mm
Semi-analytical: $t = 1.5$ mm
Numerical: $t = 1.5$ mm
Semi-analytical: $t = 2.0$ mm
Numerical: $t = 2.0$ mm

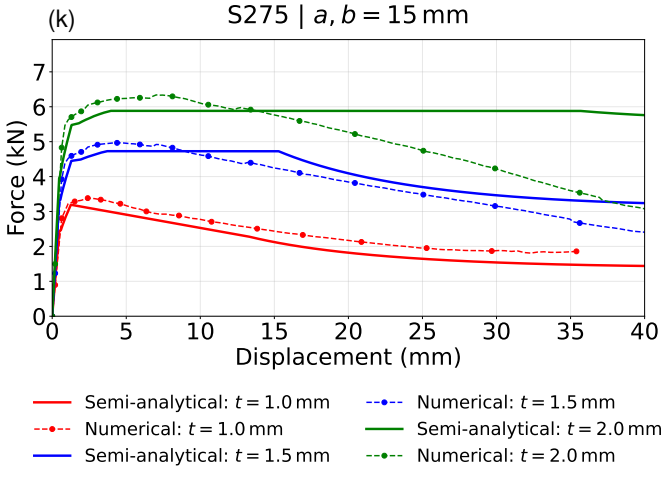
(k)
S275 | $a, b = 15$ mm
Force (kN)
Displacement (mm)
0 1 2 3 4 5 6 7
0 5 10 15 20 25 30 35 40
Semi-analytical: $t = 1.0$ mm
Numerical: $t = 1.0$ mm
Semi-analytical: $t = 1.5$ mm
Numerical: $t = 1.5$ mm
Semi-analytical: $t = 2.0$ mm
Numerical: $t = 2.0$ mm

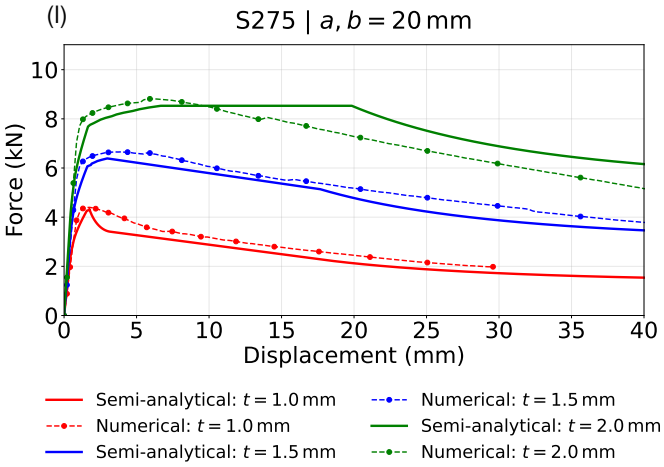
(l)
S275 | a, b = 20 mm
Force (kN)
Displacement (mm)
0
2
4
6
8
10
0
5
10
15
20
25
30
35
40
Semi-analytical: t = 1.0 mm
Numerical: t = 1.0 mm
Semi-analytical: t = 1.5 mm
Numerical: t = 1.5 mm
Semi-analytical: t = 2.0 mm
Numerical: t = 2.0 mm

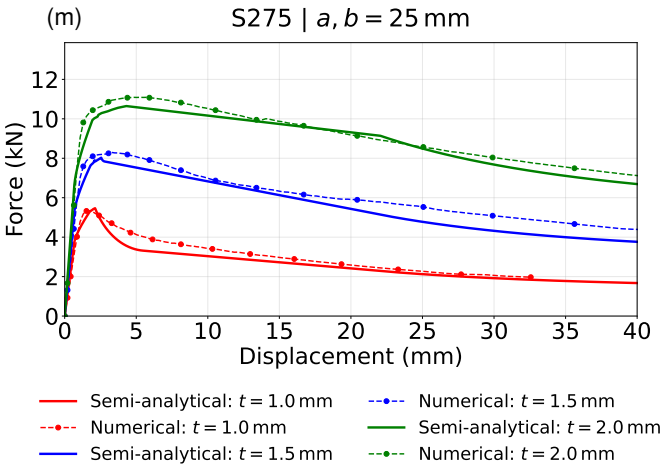
(m)
S275 | a, b = 25 mm
Force (kN)
Displacement (mm)
0
2
4
6
8
10
12
0
5
10
15
20
25
30
35
40
Semi-analytical: t = 1.0 mm
Numerical: t = 1.0 mm
Semi-analytical: t = 1.5 mm
Numerical: t = 1.5 mm
Semi-analytical: t = 2.0 mm
Numerical: t = 2.0 mm

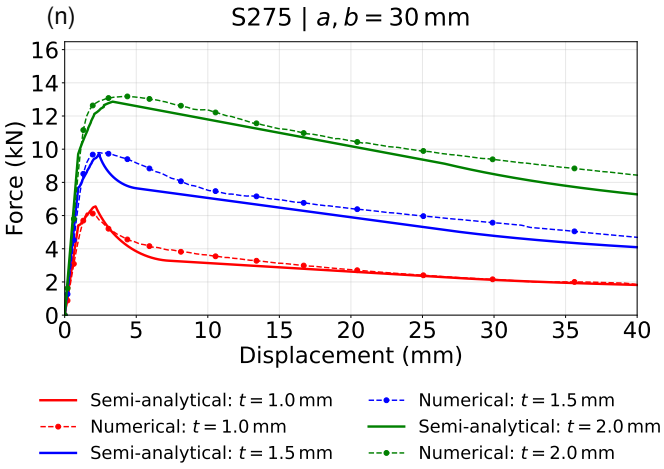
(n)
S275 | a, b = 30 mm
Force (kN)
Displacement (mm)
0
2
4
6
8
10
12
14
16
0
5
10
15
20
25
30
35
40
Semi-analytical: t = 1.0 mm
Numerical: t = 1.0 mm
Semi-analytical: t = 1.5 mm
Numerical: t = 1.5 mm
Semi-analytical: t = 2.0 mm
Numerical: t = 2.0 mm

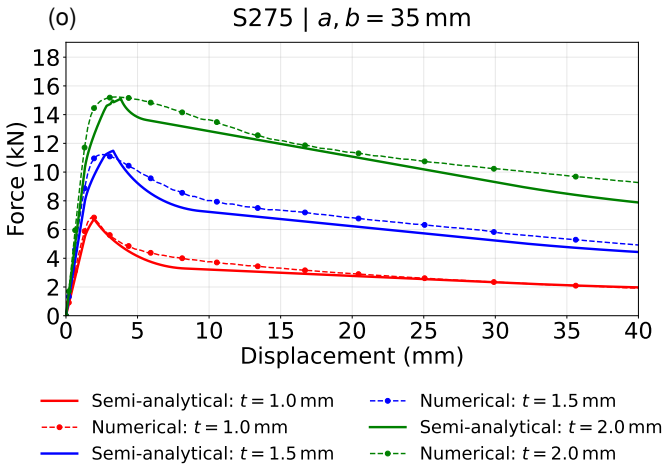
(o)
S275 | $a, b = 35$ mm
Force (kN)
Displacement (mm)
Semi-analytical: $t = 1.0$ mm
Numerical: $t = 1.0$ mm
Semi-analytical: $t = 1.5$ mm
Numerical: $t = 1.5$ mm
Semi-analytical: $t = 2.0$ mm
Numerical: $t = 2.0$ mm

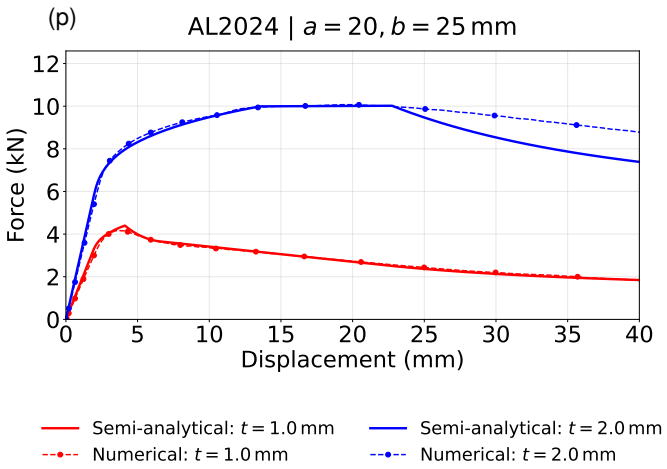
(p)
AL2024 | $a = 20, b = 25$ mm
Force (kN)
Displacement (mm)
Semi-analytical: $t = 1.0$ mm
Numerical: $t = 1.0$ mm
Semi-analytical: $t = 2.0$ mm
Numerical: $t = 2.0$ mm

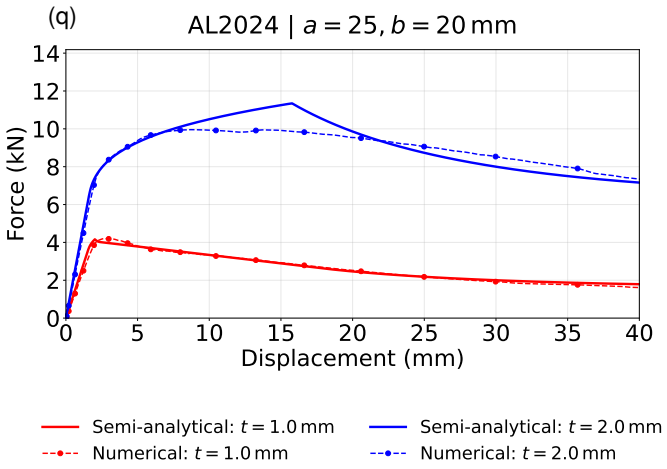
(q)
AL2024 | $a = 25, b = 20$ mm
Force (kN)
Displacement (mm)
Semi-analytical: $t = 1.0$ mm
Numerical: $t = 1.0$ mm
Semi-analytical: $t = 2.0$ mm
Numerical: $t = 2.0$ mm

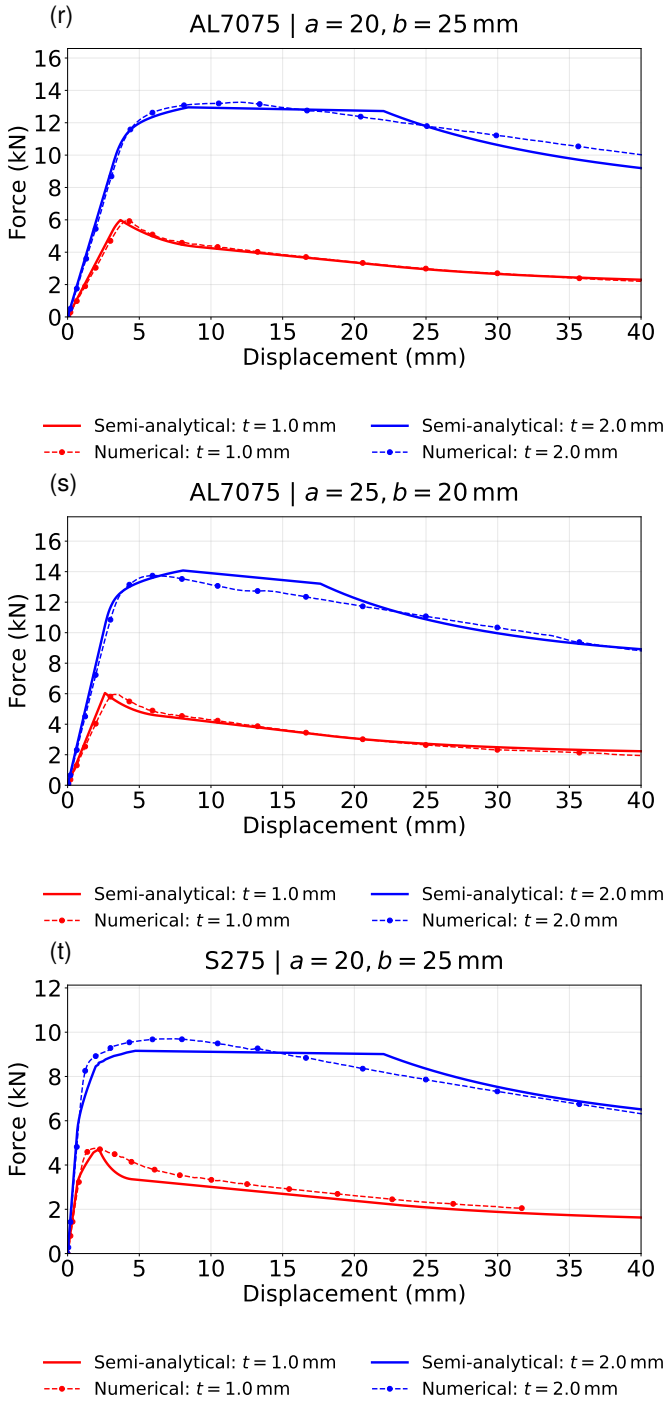

Figure B.2.: Comparison of numerical and semi-analytical force–displacement responses.

C

Appendix: Chapter 4

Datasets for the tested configurations at different displacement rates along with their dimensions are presented in Appendix C.1 to C.4. STR in tables below stands for Span-to-Thickness Ratio.
Span values listed under "Span (mm)" in the tables correspond to span values calculated per Equation 4.2 whereas "Span-analytical (mm)" refers to values used for the semi-analytical model. Discrepancy between "Span (mm)" and "Span-analytical (mm)" can be observed for some of the tested configurations listed below. The discrepancy in these two quantities can be attributed to errors made during experimentation or data reporting, which lead to significant errors in the initial slope predicted by the semi-analytical model when compared against experimental data- suggesting an error in reported span. Notable examples include the cases 1mm/min-3-3/2-0.3-L and 1mm/min-3-3/2-0.3-T, where the analytical model indicates a Span-to-Thickness Ratio (STR) of 20 instead of 10 given by Equation 4.2. For consistency, span-analytical values have been used for calculation of bending strength, energy absorption and bending modulus in Appendix C.5. However, due to the absence of test video recordings, these span values approximated using the proposed semi-analytical model could not be independently verified, and should therefore be interpreted with caution.

C.1. Configurations tested at displacement rate = 1 mm/min

S.No.	Configuration	No. of specimens	Average dimensions (mm)			Span (mm)	Span-analytical (mm)	STR
			Length	Width	Thickness			
1	2A-4/3-0.3-L	5	148.81	21.49	2.02	20.20	22.00	10.89
2	2A-4/3-0.3-T	5	151.31	21.85	2.02	20.20	20.20	10.00
3	2A-8/7-0.4-L	5	151.97	21.86	5.08	50.80	55.00	10.83
4	2A-8/7-0.4-T	7	150.97	21.32	5.08	50.80	50.80	10.00
5	2B-11/10-0.3-L	7	151.86	21.57	6.05	60.00	55.00	9.09
6	3-3/2-0.3-L	5	149.25	20.10	1.62	18.00	32.40	20.00
7	3-3/2-0.3-T	5	148.98	20.29	1.62	18.00	32.40	20.00
8	3-5/4-0.4-L	5	150.03	20.67	3.00	30.00	30.00	10.00
9	3-5/4-0.4-T	5	149.84	20.05	3.00	30.00	30.00	10.00
10	3-6/5-0.3-L	6	150.17	21.91	3.20	32.00	32.00	10.00
11	3-6/5-0.3-T	7	150.16	21.97	3.20	32.00	32.00	10.00
12	3-8/7-0.4-L	5	149.49	20.72	5.11	51.10	51.10	10.00
13	3-8/7-0.4-T	6	149.95	20.71	5.11	51.10	51.10	10.00
14	4A-7/6-0.4-L	9	151.01	20.87	5.20	52.00	52.00	10.00
15	4A-7/6-0.4-T	5	150.70	20.79	5.20	52.00	52.00	10.00
16	4B-6/5-0.5-L	6	151.48	21.26	4.99	49.90	36.00	7.21
17	4B-6/5-0.5-T	6	150.33	21.26	4.99	49.90	40.00	8.02
18	4B-7/6-0.4-L	5	149.82	20.95	5.20	52.00	52.00	10.00
19	4B-7/6-0.4-T	5	149.74	20.86	5.20	52.00	52.00	10.00

Table C.1.: Configurations tested at a displacement rate of 1 mm/min.

C.2. Configurations tested at displacement rate = 10 mm/min

S.No.	Configuration	No. of specimens	Average dimensions (mm)			Span (mm)	Span-analytical (mm)	STR
			Length	Width	Thickness			
1	2A-4/3-0.2-L	6	149.72	21.09	1.58	18.00	20.20	12.78
2	2A-4/3-0.2-T	7	149.35	21.35	1.58	18.00	20.20	12.78
3	2A-8/7-0.4-L	5	149.59	20.87	5.08	50.80	55.00	10.83
4	2A-8/7-0.4-T	7	149.76	20.63	5.08	50.80	50.80	10.00
5	2B-11/10-0.3-L	6	151.87	21.03	6.02	60.00	45.00	7.48
6	2B-11/10-0.3-T	6	150.07	20.47	6.02	60.00	60.20	10.00
7	3-3/2-0.3-L	6	149.81	21.57	1.45	18.00	29.00	20.00
8	3-3/2-0.3-T	5	148.86	21.54	1.45	18.00	29.00	20.00
9	3-5/4-0.4-L	5	149.42	20.91	2.71	27.10	30.00	11.07
10	3-5/4-0.4-T	5	149.57	21.38	2.71	27.10	30.00	11.07
11	3-6/5-0.3-L	5	150.22	20.63	3.17	31.70	31.70	10.00
12	3-6/5-0.3-T	6	149.85	20.40	3.17	31.70	31.70	10.00
13	3-8/7-0.4-L	5	149.61	20.74	5.11	51.10	51.10	10.00
14	3-8/7-0.4-T	6	149.77	20.70	5.11	51.10	51.10	10.00
15	4A-7/6-0.4-L	5	150.70	20.79	5.20	52.00	52.00	10.00
16	4A-7/6-0.4-T	5	148.87	20.96	5.20	52.00	52.00	10.00
17	4B-6/5-0.5-L	11	149.86	21.35	5.10	51.00	51.00	10.00
18	4B-6/5-0.5-T	12	149.87	21.27	5.10	51.00	51.00	10.00
19	4B-7/6-0.4-L	5	149.88	20.95	5.20	52.00	52.00	10.00
20	4B-7/6-0.4-T	5	149.76	20.87	5.20	52.00	52.00	10.00

Table C.2.: Configurations tested at a displacement rate of 10 mm/min.

C.3. Configurations tested at displacement rate = 100 mm/min

S.No.	Configuration	No. of specimens	Average dimensions (mm)			Span (mm)	Span-analytical (mm)	STR
			Length	Width	Thickness			
1	2B-7/6-0.4-L	6	149.55	20.99	4.49	44.90	50.00	11.14
2	2B-7/6-0.4-T	6	147.62	21.24	4.49	44.90	55.00	12.25
3	2B-11/10-0.3-L	11	149.82	20.95	5.98	59.80	55.00	9.20
4	3-3/2-0.3-L	5	150.00	21.10	1.45	18.00	29.00	20.00
5	3-3/2-0.3-T	5	149.23	21.09	1.45	18.00	29.00	20.00
6	3-5/4-0.4-L	6	149.80	21.08	3.10	31.00	31.00	10.00
7	3-5/4-0.4-T	5	150.00	21.06	3.10	31.00	31.00	10.00
8	3-8/7-0.4-L	5	149.94	21.12	5.28	52.80	52.80	10.00
9	4A-7/6-0.4-L	5	150.51	20.82	5.20	52.00	52.00	10.00
10	4A-7/6-0.4-T	5	149.39	20.97	5.20	52.00	52.00	10.00
11	4B-4/3-0.4-L	7	149.54	21.41	3.01	30.10	60.20	20.00
12	4B-4/3-0.4-T	6	149.50	21.35	3.01	30.10	60.20	20.00
13	4B-6/5-0.5-L	6	149.67	21.14	4.98	49.80	49.80	10.00
14	4B-6/5-0.5-T	6	149.67	21.36	4.98	49.80	49.80	10.00
15	4B-7/6-0.4-L	5	149.86	20.96	5.20	52.00	52.00	10.00
16	4B-7/6-0.4-T	5	149.74	20.80	5.20	52.00	52.00	10.00
17	4B-8/7-0.4-L	6	149.76	21.22	5.82	58.20	58.20	10.00
18	4B-8/7-0.4-T	6	149.87	21.17	5.82	58.20	58.20	10.00

Table C.3.: Configurations tested at a displacement rate of 100 mm/min.

C.4. Configurations tested at displacement rate = 1000 mm/min

S.No.	Configuration	No. of specimens	Average dimensions (mm)			Span (mm)	Span-analytical (mm)	STR
			Length	Width	Thickness			
1	2B-7/6-0.4-L	5	149.48	21.01	4.49	44.90	44.90	10.00
2	2B-7/6-0.4-T	5	147.80	21.09	4.49	44.90	55.00	12.25
3	2B-11/10-0.3-L	5	149.77	21.34	5.98	59.80	55.00	9.20
4	3-3/2-0.3-L	5	148.59	21.05	1.45	18.00	29.00	20.00
5	3-3/2-0.3-T	5	149.20	21.02	1.45	18.00	29.00	20.00
6	3-5/4-0.4-L	5	149.64	21.01	3.10	31.00	31.00	10.00
7	3-5/4-0.4-T	6	149.33	21.03	3.10	31.00	31.00	10.00
8	3-8/7-0.4-L	5	149.86	21.20	5.28	52.80	52.80	10.00
9	4A-7/6-0.4-L	5	150.70	20.84	5.20	52.00	52.00	10.00
10	4A-7/6-0.4-T	5	149.50	21.10	5.20	52.00	52.00	10.00
11	4B-4/3-0.4-L	6	149.76	21.39	3.01	30.10	36.00	11.96
12	4B-4/3-0.4-T	5	149.57	21.29	3.01	30.10	36.00	11.96
13	4B-6/5-0.5-L	5	149.60	21.28	4.98	49.80	49.80	10.00
14	4B-6/5-0.5-T	4	149.58	21.21	4.98	49.80	49.80	10.00
15	4B-7/6-0.4-L	5	149.86	20.91	5.20	52.00	52.00	10.00
16	4B-7/6-0.4-T	5	149.78	20.83	5.20	52.00	52.00	10.00

Table C.4.: Configurations tested at a displacement rate of 1000 mm/min.

C

C.5. Specific Energy Absorption (SEA), Peak force (kN) and Bending modulus (GPa) for experimental 3-point bending

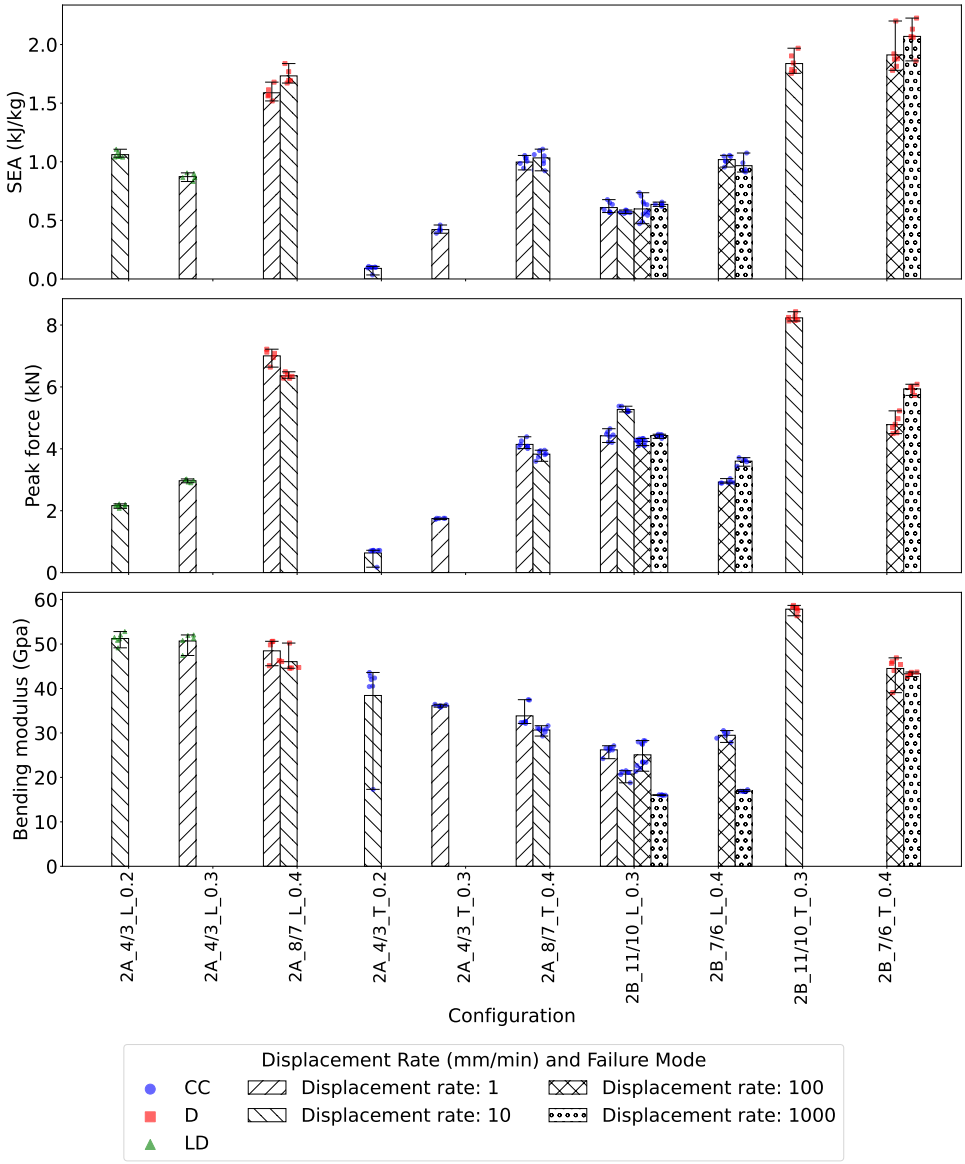

Figure C.1.: Specific Energy Absorption (SEA), Peak force (kN) and Bending modulus (GPa) for GLARE-2

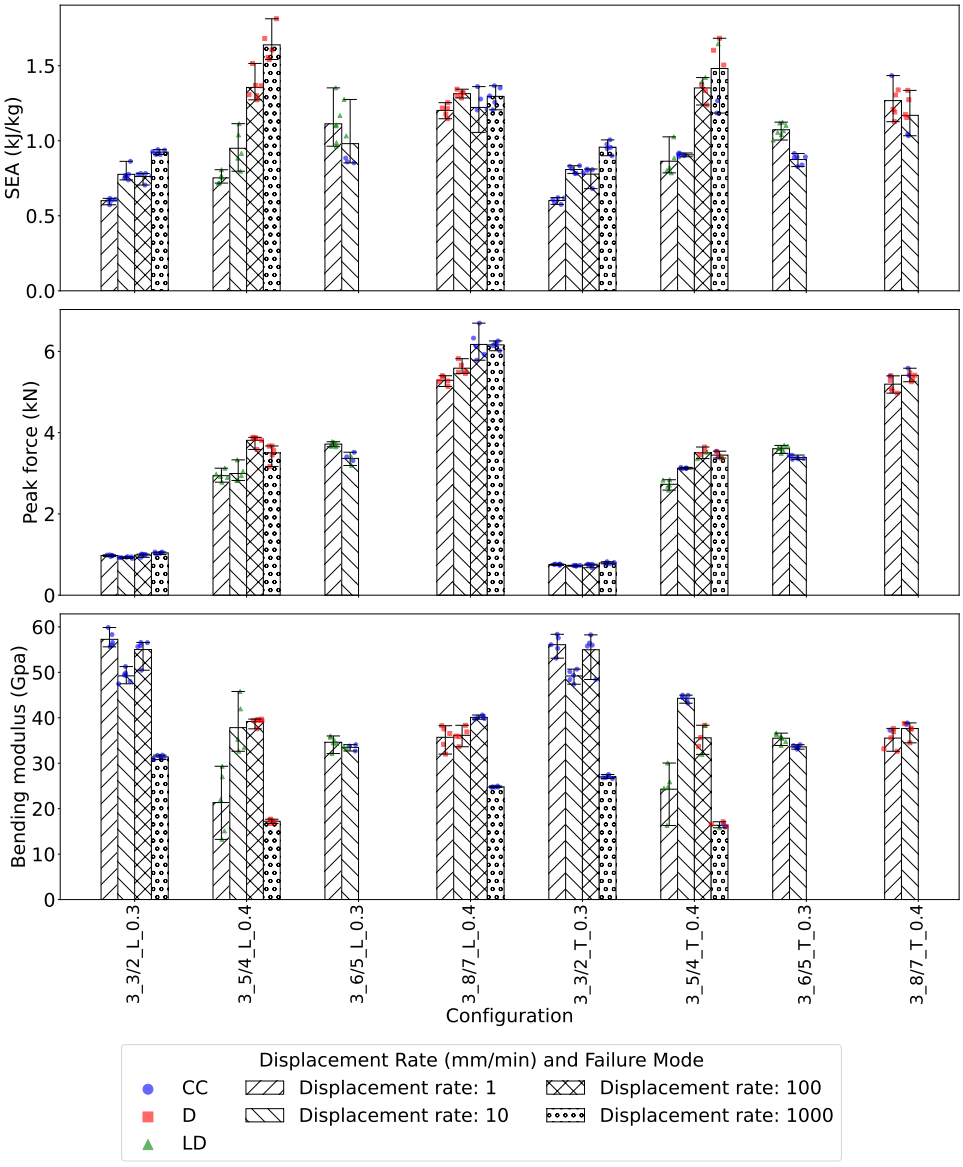

Figure C.2.: Specific Energy Absorption (SEA), Peak force (kN) and Bending modulus (GPa) for GLARE-3

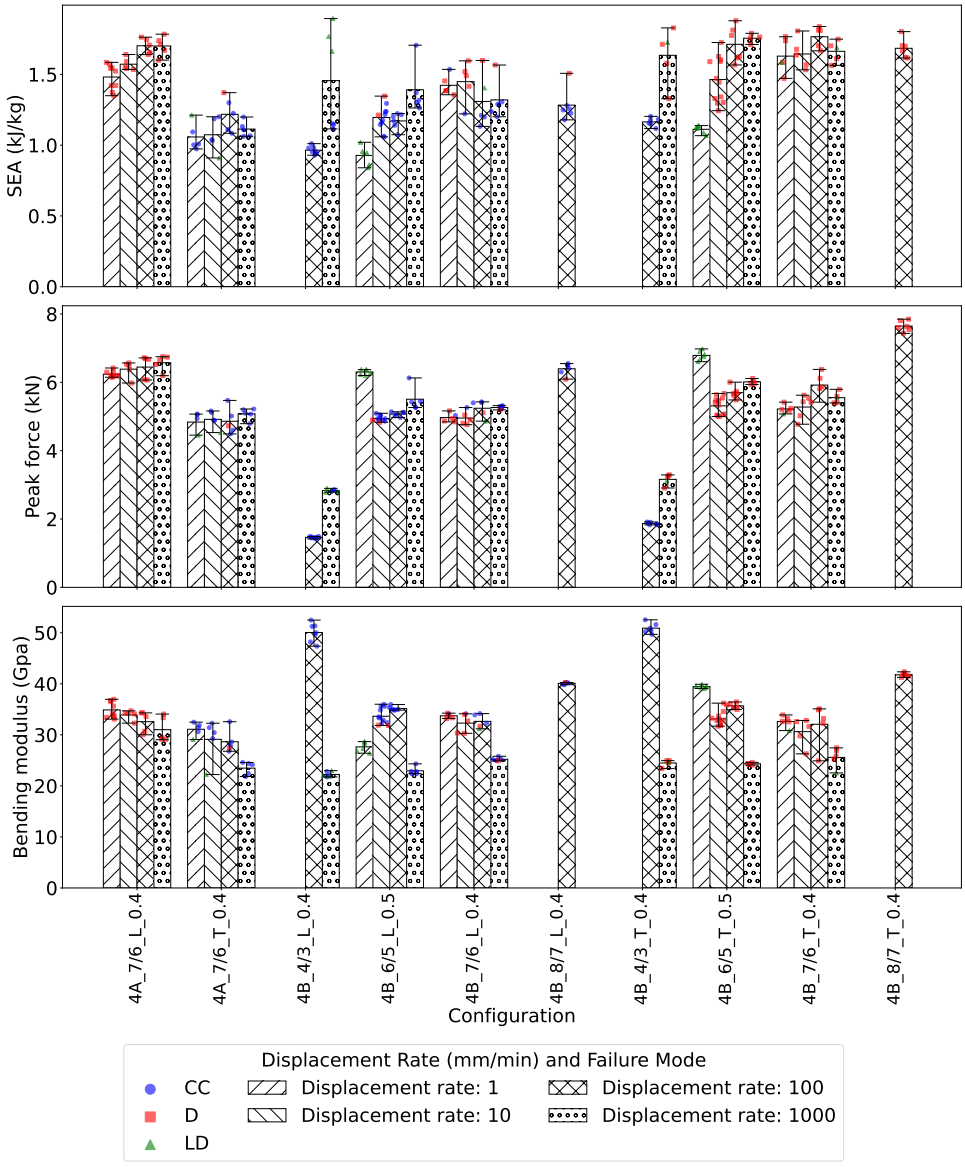

Figure C.3.: Specific Energy Absorption (SEA), Peak force (kN) and Bending modulus (GPa) for GLARE-4

C.6. Comparison of results from semi-analytical model to experimental results

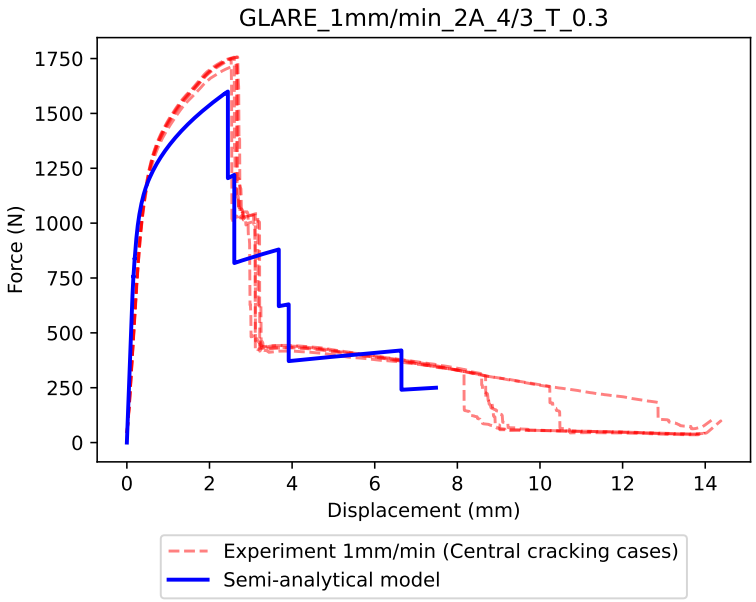

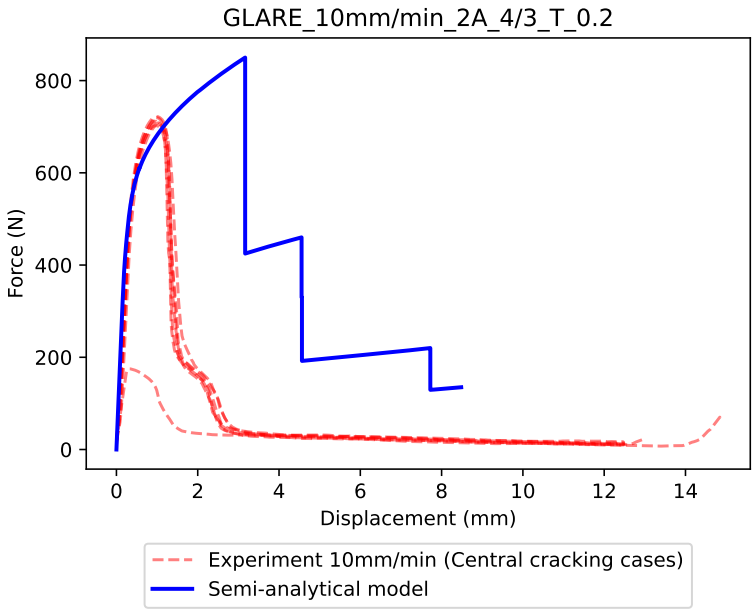

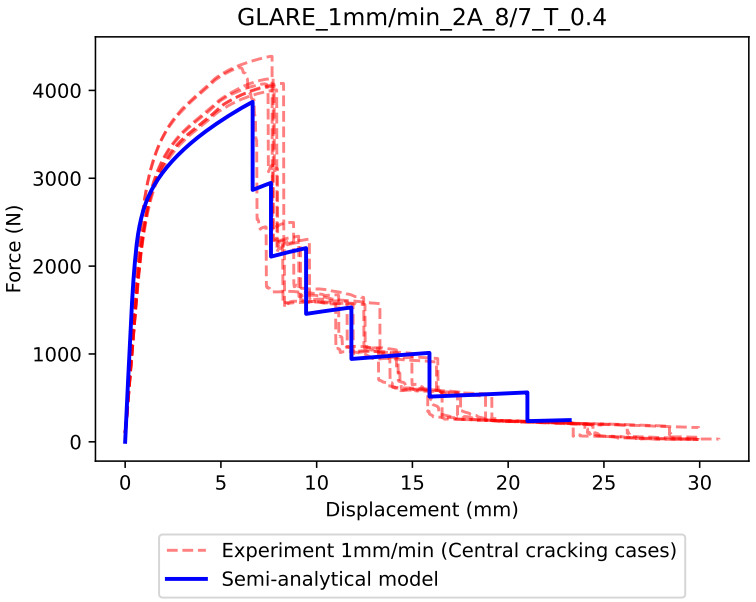
GLARE_1mm/min_2A_8/7_T_0.4
Force (N)
Displacement (mm)
Experiment 1mm/min (Central cracking cases)
Semi-analytical model

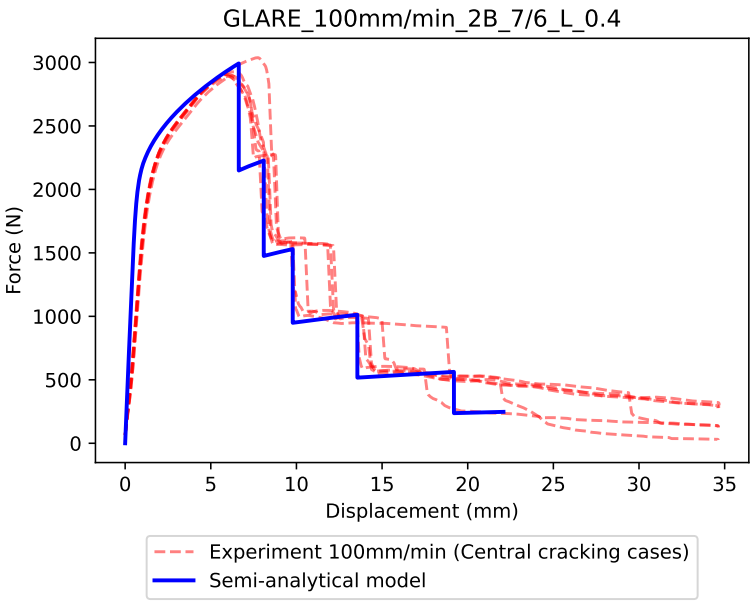
GLARE_100mm/min_2B_7/6_L_0.4
Force (N)
Displacement (mm)
Experiment 100mm/min (Central cracking cases)
Semi-analytical model

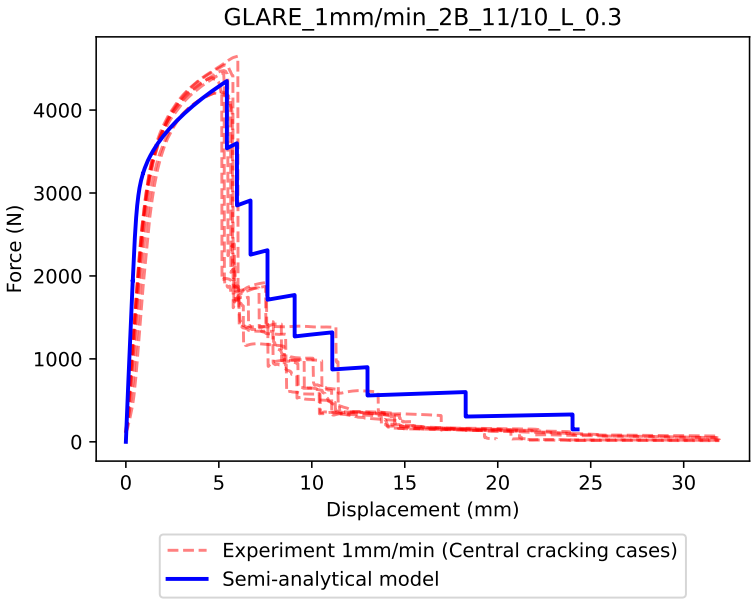
GLARE_1mm/min_2B_11/10_L_0.3
Force (N)
4000
3000
2000
1000
0
0
5
10
15
20
25
30
Displacement (mm)
Experiment 1mm/min (Central cracking cases)
Semi-analytical model

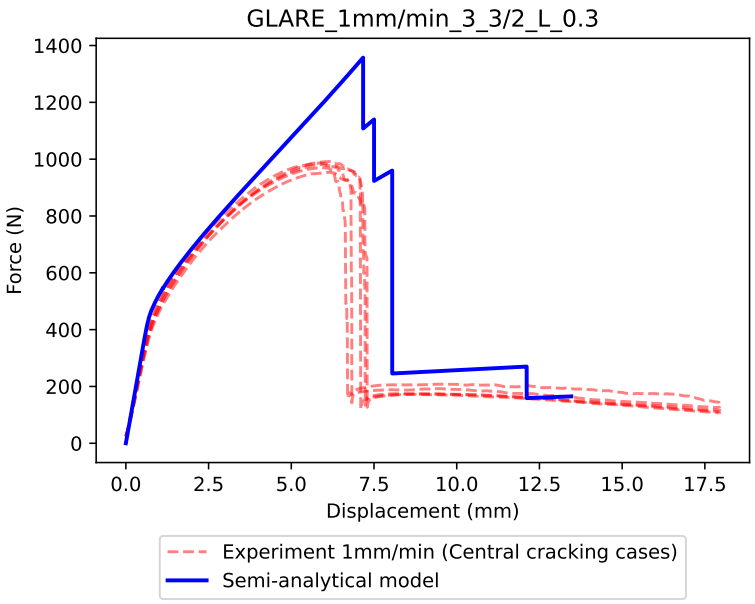
GLARE_1mm/min_3_3/2_L_0.3
Force (N)
1400
1200
1000
800
600
400
200
0
0.0
2.5
5.0
7.5
10.0
12.5
15.0
17.5
Displacement (mm)
Experiment 1mm/min (Central cracking cases)
Semi-analytical model

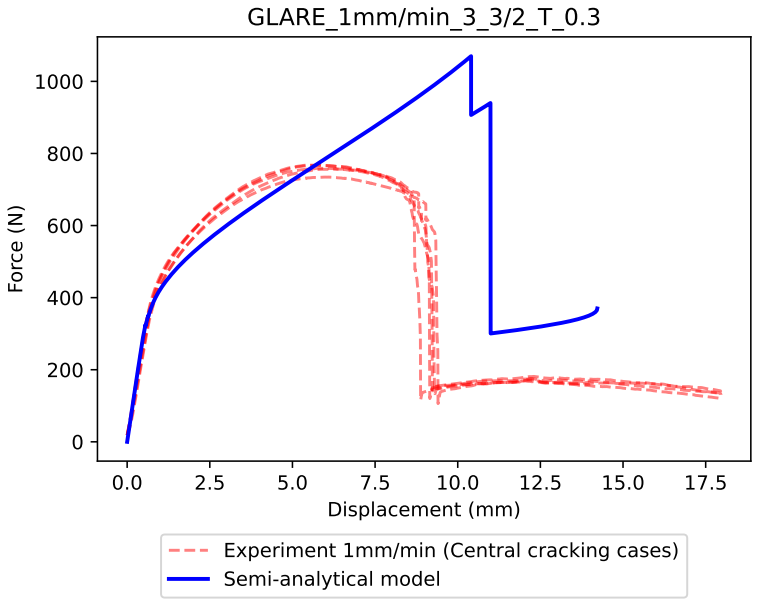
GLARE_1mm/min_3_3/2_T_0.3
Force (N)
1000
800
600
400
200
0
0.0
2.5
5.0
7.5
10.0
12.5
15.0
17.5
Displacement (mm)
Experiment 1mm/min (Central cracking cases)
Semi-analytical model

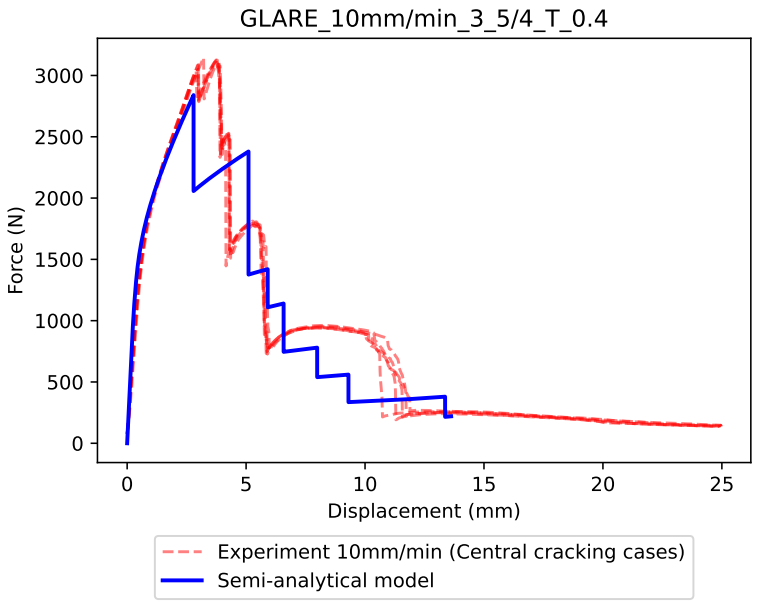
GLARE_10mm/min_3_5/4_T_0.4
Force (N)
3000
2500
2000
1500
1000
500
0
0
5
10
15
20
25
Displacement (mm)
Experiment 10mm/min (Central cracking cases)
Semi-analytical model

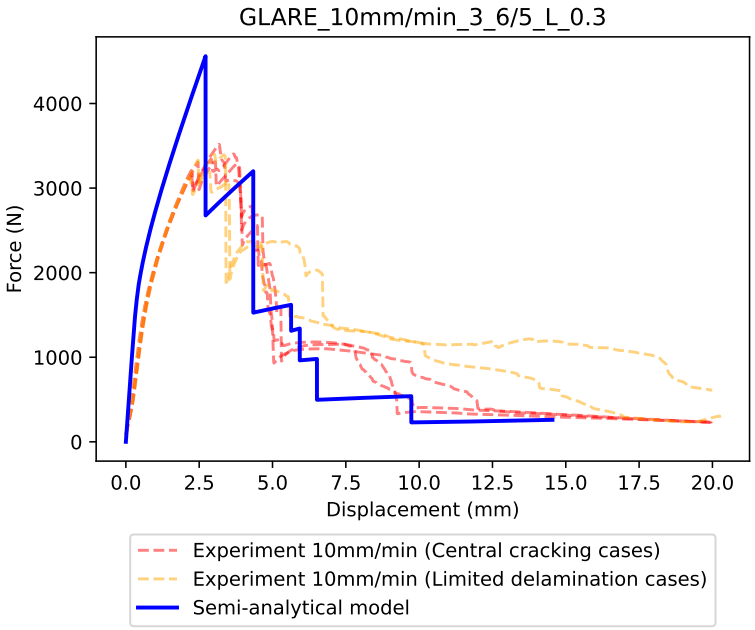
GLARE_10mm/min_3_6/5_L_0.3
Force (N)
4000
3000
2000
1000
0
0.0
2.5
5.0
7.5
10.0
12.5
15.0
17.5
20.0
Displacement (mm)
Experiment 10mm/min (Central cracking cases)
Experiment 10mm/min (Limited delamination cases)
Semi-analytical model

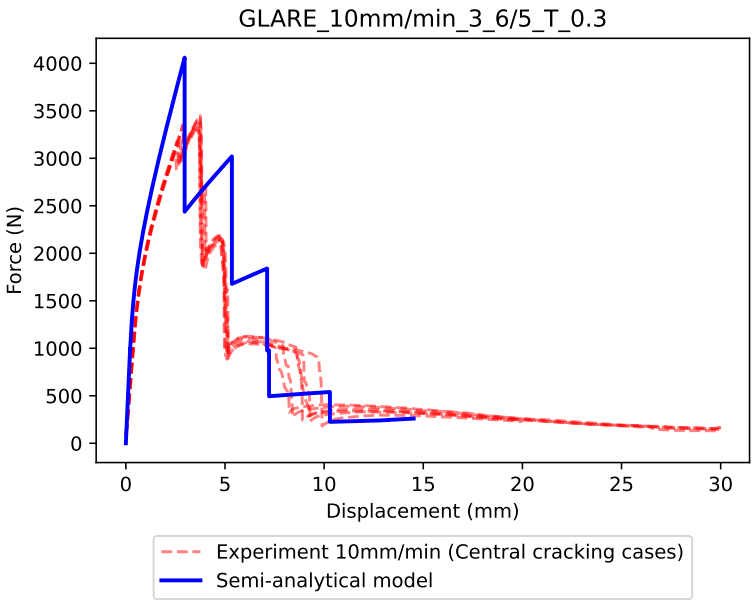
GLARE_10mm/min_3_6/5_T_0.3
Force (N)
4000
3500
3000
2500
2000
1500
1000
500
0
0
5
10
15
20
25
30
Displacement (mm)
Experiment 10mm/min (Central cracking cases)
Semi-analytical model

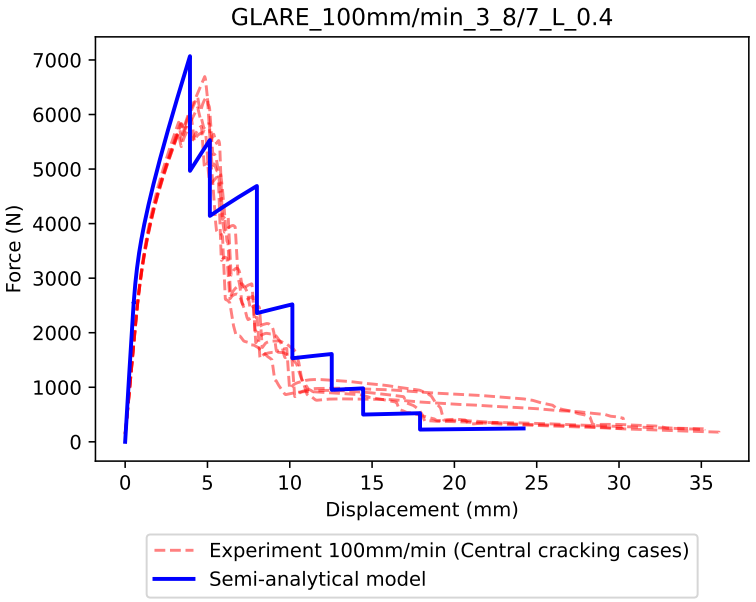
GLARE_100mm/min_3_8/7_L_0.4
Force (N)
Displacement (mm)
Experiment 100mm/min (Central cracking cases)
Semi-analytical model

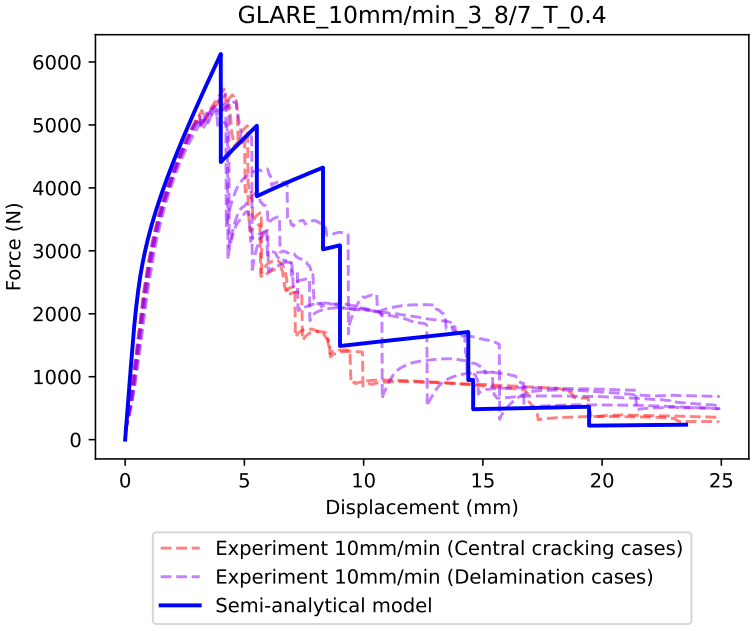
GLARE_10mm/min_3_8/7_T_0.4
Force (N)
Displacement (mm)
Experiment 10mm/min (Central cracking cases)
Experiment 10mm/min (Delamination cases)
Semi-analytical model

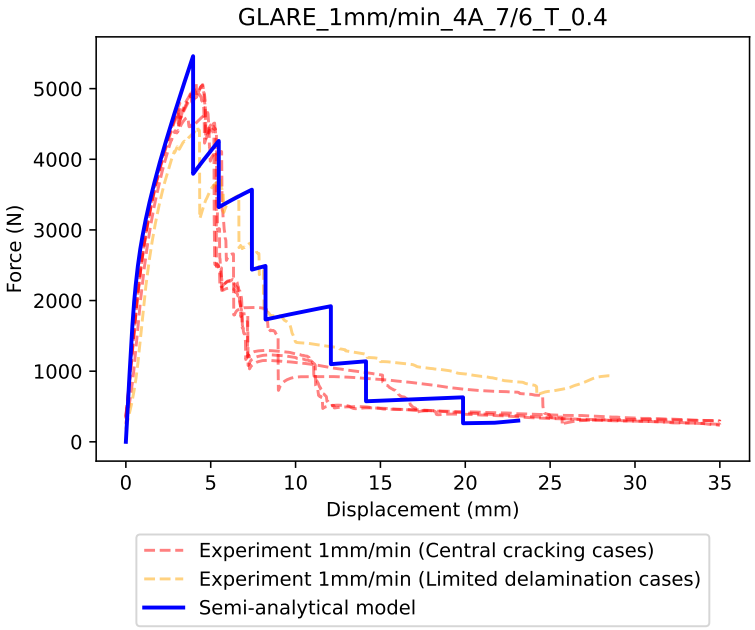
GLARE_1mm/min_4A_7/6_T_0.4
Force (N)
Displacement (mm)
Experiment 1mm/min (Central cracking cases)
Experiment 1mm/min (Limited delamination cases)
Semi-analytical model

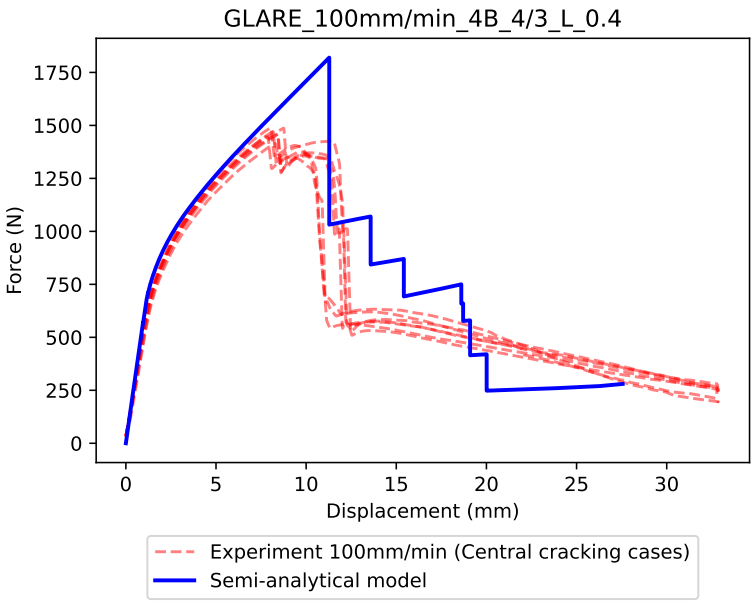
GLARE_100mm/min_4B_4/3_L_0.4
Force (N)
Displacement (mm)
Experiment 100mm/min (Central cracking cases)
Semi-analytical model

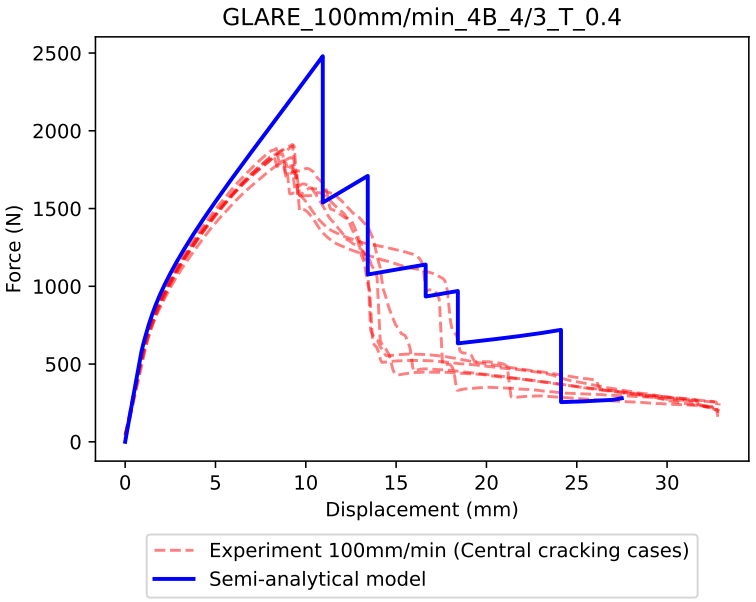
GLARE_100mm/min_4B_4/3_T_0.4
Force (N)
Displacement (mm)
Experiment 100mm/min (Central cracking cases)
Semi-analytical model

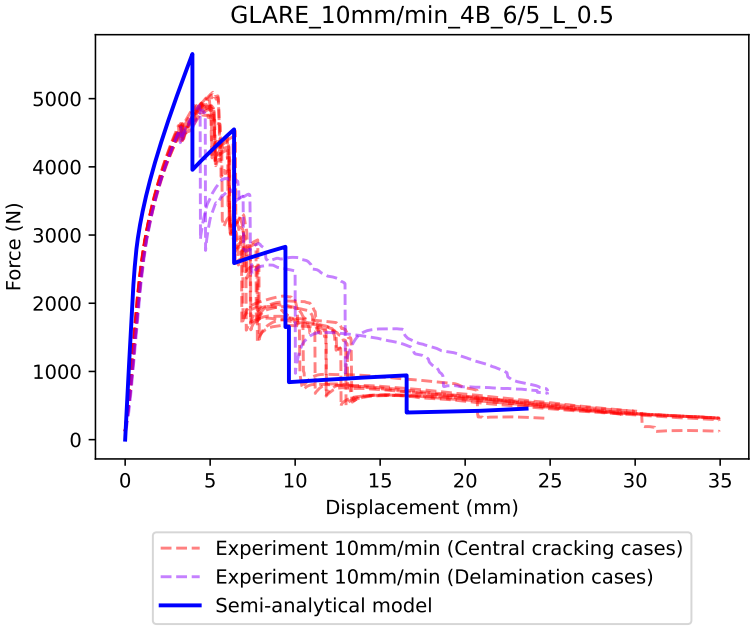
GLARE_10mm/min_4B_6/5_L_0.5
Force (N)
Displacement (mm)
Experiment 10mm/min (Central cracking cases)
Experiment 10mm/min (Delamination cases)
Semi-analytical model

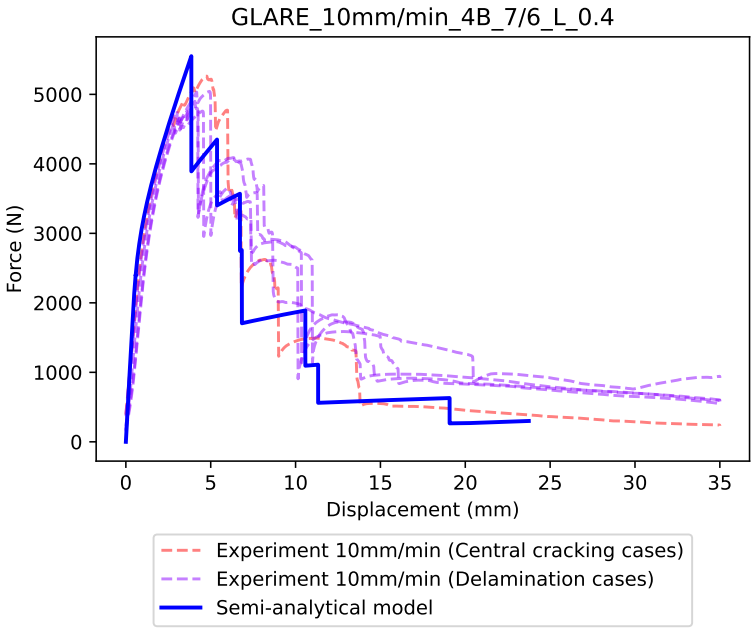

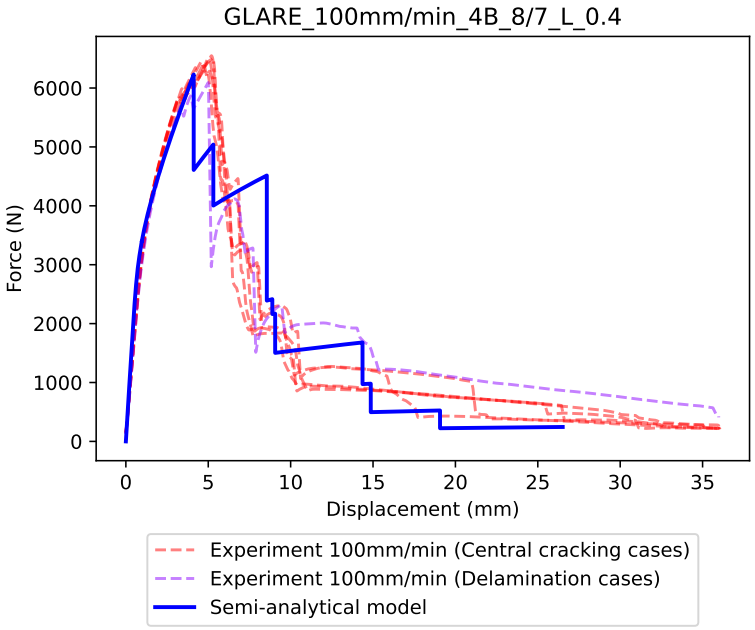

Figure C.4.: Force versus displacement curves: Experiment versus semi-analytical model

Bibliography

[1] D. Kecman. 'Bending collapse of rectangular and square section tubes'. In: *International Journal of Mechanical Sciences* 25.9 (1983). Special Issue Structural Crashworthiness Conference, pp. 623–636. DOI: 10.1016/0020-7403(83)90072-3.

[2] H. Ritchie. 'What share of global CO_2 emissions come from aviation?' In: *Our World in Data* (2024). https://ourworldindata.org/global-aviation-emissions.

[3] The Boeing Company. *Commercial Market Outlook 2025–2044*. Tech. rep. Boeing, 2025.

[4] The Boeing Company. *Current Market Outlook 2009–2028*. Tech. rep. Boeing Commercial Airplanes, 2009.

[5] T. B. Company. *Commercial Market Outlook 2022–2041*. Tech. rep. Boeing, 2022.

[6] IEA. *Carbon dioxide (CO_2) direct emissions from the aviation sector worldwide from 2000 to 2021, by flight type (in million metric tons)*. Statista. Graph, retrieved August 21, 2025. 2022. URL: https://www.statista.com/statistics/1189331/carbon-dioxide-emissions-air-passenger-flight-type/.

[7] 'Resolution on the industry's commitment to reach net zero carbon emissions by 2050'. In: (Oct. 2021). URL: https://www.iata.org/en/pressroom/pressroom-archive/2021-releases/2021-10-04-03/.

[8] W. Oosterom and R. Vos. 'Conceptual Design of a Flying-V Aircraft Family'. In: *AIAA AVIATION 2022 Forum*. American Institute of Aeronautics and Astronautics, June 2022. DOI: 10.2514/6.2022-3200.

[9] *AIRBUS A350 AIRCRAFT CHARACTERISTICS AIRPORT AND MAINTENANCE PLANNING AC*. July 2021. URL: https://www.airbus.com/sites/g/files/jlcbta136/files/2021-11/Airbus-Commercial-Aircraft-AC-A350-900-1000.pdf.

[10] C. Kindervater, D. Kohlgruber and A. Johnson. 'Composite vehicle structural crashworthiness - A status of design methodology and numerical simulation techniques'. In: *International Journal of Crashworthiness* 4.2 (1999), pp. 213–230. DOI: 10.1533/cras.1999.0101. eprint: https://doi.org/10.1533/cras.1999.0101.

[11] G. Wittlin and M. A. Gamon. *A Method of Analysis for General Aviation Airplane Structural Crashworthiness*. Tech. rep. FAA-RD-76-123. Final Report. Prepared for the U.S. Department of Transportation. Available through the National Technical Information Service (NTIS), Springfield, VA 22161. AD No. ADA032415. Washington, DC: Federal Aviation Administration, Sept. 1976.

[12] G. Wittlin, D. J. Ahrens and A. W. Bloedel. *Experimental Verification of Program KRASH-A Mathematical Model for General Aviation Structural Crash Dynamics*. SAE Technical Paper 790589. Presented at the Business Aircraft Meeting and Exposition. Sponsored by the Federal Aviation Administration. SAE International, Feb. 1979, p. 16. DOI: 10.4271/790589.

[13] G. Wittlin and B. LaBarge. *KRASH Dynamics Analysis Modeling – Transport Airplane Controlled Impact Demonstration Test*. Tech. rep. DOT/FAA/CT-85/9. Final Report. Revised March 1986. Prepared by Lockheed-California Company, Burbank, CA. Available through the National Technical Information Service (NTIS), Springfield, VA 22161. Atlantic City International Airport, NJ: Federal Aviation Administration, May 1985.

[14] W. on Computational Methods for Crashworthiness, A. Noor, H. Carden, U. S. N. Aeronautics, S. Administration, L. R. Center and U. of Virginia. Center for Computational Structures Technology. *Computational Methods for Crashworthiness: Proceedings of a Workshop Sponsored by the National Aeronautics and Space Administration, Washington, D.C., and the University of Virginia Center for Computational Structures Technology, Hampton, Virginia, and Held at Langley Research Center, Hampton, Virginia, September 2-3, 1992*. NASA conference publication. National Aeronautics, Space Administration, Office of Management, Scientific and Technical Information Program, 1993. URL: https://books.google.nl/books?id=XPf_F2skMjkC.

[15] C. Kindervater, D. Kohlgrüber and M. Lützenburger. 'Crash Simulation Methodologies for Aircraft Structures used within European Crashworthiness Research'. In: *FAA " Int. Aircraft Fire and Cabin Safety Res. Conf." Atlantic City, NJ(USA), 16-20 Nov. 1998*. LIDO-Berichtsjahr=1999, 1998. URL: https://elib.dlr.de/14667/.

[16] R. H. W. M. Frijns, G. Wittlin and A. de Boer. *A Preliminary Model to Simulate the Impact of a Frangible Approach Light Structure by an Aircraft Wing Section*. Tech. rep. NLR-TP-98227. Based on a presentation at the International Crashworthiness Conference ICRASH'98, Dearborn, Michigan, USA. Netherlands: National Aerospace Laboratory NLR, May 1998.

[17] P. E. Nikravesh, I. S. Chung and R. L. Benedict. 'Plastic Hinge Approach to Vehicle Crash Simulation'. In: *Computers & Structures* 16.1–4 (1983), pp. 395–400. DOI: 10.1016/0045-7949(83)90178-5.

[18] J. A. C. Ambrósio and P. E. Nikravesh. 'Elastic-Plastic Deformations in Multibody Dynamics'. In: *Nonlinear Dynamics* 3 (1992), pp. 85–104. DOI: 10.1007/BF00118987.

[19] L. Sousa, P. Veríssimo and J. Ambrósio. 'Development of generic multibody road vehicle models for crashworthiness'. In: *Multibody System Dynamics* 19 (Feb. 2008), pp. 133–158. DOI: 10.1007/s11044-007-9093-z.

[20] Y. Y. Tay, P. Flores and H. Lankarani. 'Crashworthiness analysis of an aircraft fuselage section with an auxiliary fuel tank using a hybrid multibody/plastic hinge approach'. In: *International Journal of Crashworthiness* 25 (Jan. 2019), pp. 1–11. DOI: 10.1080/13588265.2018.1524547.

[21] P. Schatrow and M. Waimer. 'Crash concept for composite transport aircraft using mainly tensile and compressive absorption mechanisms'. In: *CEAS Aeronautical Journal* 7 (July 2016). DOI: 10.1007/s13272-016-0203-6.

[22] J. M. Alexander. 'An approximate analysis of the collapse of thin cylindrical shells under axial loading'. In: *The Quarterly Journal of Mechanics and Applied Mathematics* 13 (1 Jan. 1960), pp. 10–15. DOI: 10.1093/QJMAM/13.1.10.

[23] C. Magee and P. Thornton. 'Design Considerations in Energy Absorption by Structural Collapse'. In: *Trans SAE* (1978), pp. 2041–55. DOI: 10.4271/780434.

[24] W. Abramowicz and N. Jones. 'Dynamic axial crushing of circular tubes'. In: *International Journal of Impact Engineering* 2 (3 Jan. 1984), pp. 263–281. DOI: 10.1016/0734-743X(84)90010-1.

[25] W. Abramowicz and N. Jones. 'Dynamic axial crushing of square tubes'. In: *International Journal of Impact Engineering* 2 (2 Jan. 1984), pp. 179–208. DOI: 10.1016/0734-743X(84)90005-8.

[26] W. Abramowicz and T. Wierzbicki. 'Axial Crushing of Multicorner Sheet Metal Columns'. In: *Journal of Applied Mechanics* 56 (1 Mar. 1989), pp. 113–120. DOI: 10.1115/1.3176030.

[27] X. Zhang and H. Zhang. 'Experimental and numerical investigation on crush resistance of polygonal columns and angle elements'. In: *Thin-Walled Structures* 57 (Aug. 2012), pp. 25–36. DOI: 10.1016/J.TWS.2012.04.006.

[28] Y. Maalej, F. Chaari, B. Zouari and E. Markiewicz. 'Closed form solution for the collapse of polygonal thin-walled columns in the axial crushing case'. In: *Journal of Theoretical and Applied Mechanics* 52 (Aug. 2014), pp. 707–718. URL: http://jtam.pl/pdf-102150-33710?filename=Closed%20form%20solution%20for.pdf.

[29] S. TABACU and C. DUCU. 'An analytical solution for the estimate of the mean crushing force of structures with polygonal and star-shaped cross-sections subjected to axial load'. In: *International Journal of Mechanical Sciences* 161-162 (Oct. 2019), p. 105010. DOI: 10.1016/J.IJMECSCI.2019.105010.

[30] D. Kecman. 'Bending collapse of rectangular section tubes in relation to the bus roll over problem'. In: (1979).

[31] T. Wierzbicki, L. Recke, W. Abramowicz, T. Gholami and J. Huang. 'Stress profiles in thin-walled prismatic columns subjected to crush loading-II. Bending'. In: *Computers & Structures* 51.6 (1994), pp. 625–641. DOI: 10.1016/S0045-7949(05)80002-1.

[32] T. Kim and S. Reid. 'Bending collapse of thin-walled rectangular section columns'. In: *Computers & Structures* 79.20 (2001), pp. 1897–1911. DOI: 10.1016/S0045-7949(01)00089-X.

[33] S. Anand, R. Alderliesten and S. G. Castro. 'Crashworthiness in preliminary design: Mean crushing force prediction for closed-section thin-walled metallic structures'. In: *International Journal of Impact Engineering* 188 (2024), p. 104946. DOI: 10.1016/j.ijimpeng.2024.104946.

[34] S. Anand, R. Alderliesten and S. G. Castro. 'Corrigendum to "Crashworthiness in preliminary design: mean crushing force prediction for closed-section thin-walled metallic structures" [International Journal of Impact Engineering, Volume 188, June 2024, 104946]'. In: *International Journal of Impact Engineering* 194 (2024), p. 105086. DOI: 10.1016/j.ijimpeng.2024.105086.

[35] H. Ritchie, M. Roser and P. Rosado. 'CO_2 and Greenhouse Gas Emissions (revision August 2020)'. In: *Our World in Data* (2020). URL: https://ourworldindata.org/co2-and-greenhouse-gas-emissions.

[36] IATA. 'Net Zero Resolution Fact Sheet'. In: (June 2022). URL: https://www.iata.org/en/iata-repository/pressroom/fact-sheets/fact-sheet---iata-net-zero-resolution/.

[37] EIA. 'International Energy Outlook 2021'. In: (2021). URL: www.eia.gov/outlooks/ieo/.

[38] T. Wierzbicki, S. U. Bhat, W. Abramowicz and D. Brodkin. 'Alexander revisited—A two folding elements model of progressive crushing of tubes'. In: *International Journal of Solids and Structures* 29 (24 Jan. 1992), pp. 3269–3288. DOI: 10.1016/0020-7683(92)90040-Z.

[39] A. A. Singace, H. Elsobky and T. Y. Reddy. 'On the eccentricity factor in the progressive crushing of tubes'. In: *International Journal of Solids and Structures* 32 (24 1995), pp. 3589–3602. DOI: 10.1016/0020-7683(95)00020-B.

[40] Y. Liu and M. L. Day. 'Development of simplified finite element models for straight thin-walled tubes with octagonal cross section'. In: *International Journal of Crashworthiness* 12.5 (2007), pp. 503–508. DOI: 10.1080/13588260701483557.

[41] Y. Liu and M. L. Day. 'Axial Crushing of Thin-Walled Columns with Octagonal Section: Modeling and Design'. In: *Advances in Computational Algorithms and Data Analysis*. Ed. by S.-I. Ao, B. Rieger and S.-S. Chen. Dordrecht: Springer Netherlands, 2009, pp. 365–379. ISBN: 978-1-4020-8919-0. DOI: 10.1007/978-1-4020-8919-0_25.

[42] X. Zhang and H. Zhang. 'Theoretical and numerical investigation on the crush resistance of rhombic and kagome honeycombs'. In: *Composite Structures* 96 (2013), pp. 143–152. DOI: 10.1016/j.compstruct.2012.09.028.

[43] X. Zhang and H. Zhang. 'Axial crushing of circular multi-cell columns'. In: *International Journal of Impact Engineering* 65 (Mar. 2014), pp. 110–125. DOI: 10.1016/J.IJIMPENG.2013.12.002.

[44] A. G. Mamalis, D. E. Manolakos, M. B. Ioannidis, P. K. Kostazos and C. Dimitriou. 'Finite element simulation of the axial collapse of metallic thin-walled tubes with octagonal cross-section'. In: *Thin-Walled Structures* 41 (10 Oct. 2003), pp. 891–900. DOI: 10.1016/S0263-8231(03)00046-6.

[45] F. Tarlochan, F. Samer, A. M. S. Hamouda, S. Ramesh and K. Khalid. 'Design of thin wall structures for energy absorption applications: Enhancement of crashworthiness due to axial and oblique impact forces'. In: *Thin-Walled Structures* 71 (Oct. 2013), pp. 7–17. DOI: 10.1016/J.TWS.2013.04.003.

[46] M. Yamashita, M. Gotoh and Y. Sawairi. 'Axial crush of hollow cylindrical structures with various polygonal cross-sections: Numerical simulation and experiment'. In: *Journal of Materials Processing Technology* 140 (1-3 Sept. 2003), pp. 59–64. DOI: 10.1016/S0924-0136(03)00821-5.

[47] Z. Fan, G. Lu and K. Liu. 'Quasi-static axial compression of thin-walled tubes with different cross-sectional shapes'. In: *Engineering Structures* 55 (Oct. 2013), pp. 80–89. DOI: 10.1016/J.ENGSTRUCT.2011.09.020.

[48] T. Wierzbicki. 'Crushing analysis of metal honeycombs'. In: *International Journal of Impact Engineering* 1 (2 Jan. 1983), pp. 157–174. DOI: 10.1016/0734-743X(83)90004-0.

[49] M. Langseth and O. S. Hopperstad. 'Static and dynamic axial crushing of square thin-walled aluminium extrusions'. In: *International Journal of Impact Engineering* 18 (7-8 Oct. 1996), pp. 949–968. DOI: 10.1016/S0734-743X(96)00025-5.

[50] A. G. Hanssen, M. Langseth and O. S. Hopperstad. 'Static crushing of square aluminium extrusions with aluminium foam filler'. In: *International Journal of Mechanical Sciences* 41 (8 Aug. 1999), pp. 967–993. DOI: 10.1016/S0020-7403(98)00064-2.

[51] P. D. Yang and J. B. Caldwell. 'Collision energy absorption of ships' bow structures'. In: *International Journal of Impact Engineering* 7 (2 Jan. 1988), pp. 181–196. DOI: 10.1016/0734-743X(88)90025-5.

C

[52] W. Abramowicz and T. Wierzbicki. 'AXIAL CRUSHING OF FOAM-FILLED COLUMNS'. In: *Int. J. Mech. Sc* 30 (1988), pp. 263–271. DOI: 10.1016/0020-7403(88)90059-8.

[53] T. Wierzbicki and J. Huang. 'Initiation of plastic folding mechanism in crushed box columns'. In: *Thin-Walled Structures* 13 (1-2 Jan. 1992), pp. 115–143. DOI: 10.1016/0263-8231(92)90005-H.

[54] Y. Ohkubo, T. Akamatsu and K. Shirasawa. 'Mean Crushing Strength of Closed-Hat Section Members'. In: *SAE Transactions* 83 (1974), pp. 223–232. DOI: 10.4271/740040. (Visited on 17/01/2024).

[55] A. Wimmer. 'Einfluss der Belastungsgeschwindigheit auf das Festigkeitsund Verformungsverhaten von Blechkonstruktionen am Beispiel von Kraftfahrzengen'. In: *ATZ* 77 (1975), pp. 281–286.

[56] T. Akerstrom and T. Wierzbicki. 'Dynamic Crushing of Strain Rate Sensitive Box Columns'. In: *2nd International Conference on Vehicle Structural Mechanics*. SAE International, Feb. 1977. DOI: 10.4271/770592.

[57] T. Wierzbicki and W. Abramowicz. 'CRUSHING OF THIN-WALLED STRAIN RATE SENSITIVE STRUCTURES.' In: *Rozprawy Inzynierskie* 29.1 (1981). Cited by: 10, pp. 153–163. URL: https://www.scopus.com/inward/record.uri?eid=2-s2.0-0019651247&partnerID=40&md5=88feb31ce3434472bf2f5be919b0da0d.

[58] N. Jones. 'Dynamic progressive buckling'. In: *Structural Impact*. Cambridge University Press, 1990, pp. 385–431. DOI: 10.1017/CBO9780511624285.010.

[59] M. Fauziah, I. K. Azwan, A. Masniezam, Y. Sazali and I. Othman. 'Dynamic Axial Crushing of Empty and Foam-Filled Conical Aluminium Tubes: Experimental and Numerical Analysis'. In: *Applied Mechanics and Materials* 566 (2014), pp. 305–309. DOI: 10.4028/WWW.SCIENTIFIC.NET/AMM.566.305.

[60] M. Malawat, D. A. Sumarsono, J. Istiyanto, G. Prayogo and F. Dionisius. 'Theoretical prediction of dynamic axial crushing on a square tube with eight holes used as a crush initiator'. In: *International Journal of Technology* 10 (5 2019), pp. 1042–1055. DOI: 10.14716/IJTECH.V10I5.2297.

[61] S. Anand, R. Alderliesten and S. G. P. Castro. *Dataset for Crashworthiness in preliminary design: mean crushing force prediction for closed-section thin-walled metallic structures*. Jan. 2024. DOI: 10.5281/zenodo.10522974.

[62] A. A. Nia and J. H. Hamedani. 'Comparative analysis of energy absorption and deformations of thin walled tubes with various section geometries'. In: *Thin-Walled Structures* 48 (12 Dec. 2010), pp. 946–954. DOI: 10.1016/J.TWS.2010.07.003.

[63] X. Zhang and H. Huh. 'Crushing analysis of polygonal columns and angle elements'. In: *International Journal of Impact Engineering* 37 (4 2010), pp. 441–451. DOI: 10.1016/j.ijimpeng.2009.06.009.

[64] 'Abaqus/CAE User's Guide'. In: *SIMULIA User Assistance 2021* (). URL: https://help.3ds.com/2021/English/DSSIMULIA_Established/SIMACAECAERefMap/simacae-c-ov.htm?contextscope=all&id=7d6038c876dd40b984c8f7cd798ba0b8.

[65] A. Kumar. 'Experimental Investigations with Crush Box Simulations for Different Segment Cars using LS-DYNA'. In: *International Journal of Current Engineering and Technology* 2 (2 Jan. 2013), pp. 670–676. DOI: 10.14741/IJCET/SPL.2.2014.127.

[66] M. Harhash, M. Kuhtz, J. Richter, A. Hornig, M. Gude and H. Palkowski. 'Trigger geometry influencing the failure modes in steel/polymer/steel sandwich crashboxes: Experimental and numerical evaluation'. In: *Composite Structures* 262 (Apr. 2021), p. 113619. DOI: 10.1016/J.COMPSTRUCT.2021.113619.

[67] D. F. Shanahan. 'Human Tolerance and Crash Survivability'. In: *RTO-EN-HFM-113* (2004). URL: https://www.sto.nato.int/publications/STO%20Educational%20Notes/RTO-EN-HFM-113/EN-HFM-113-06.pdf.

[68] X. Yang, J. Ma, D. Wen and J. Yang. 'Crashworthy design and energy absorption mechanisms for helicopter structures: A systematic literature review'. In: *Progress in Aerospace Sciences* 114 (Apr. 2020), p. 100618. DOI: 10.1016/J.PAEROSCI.2020.100618.

[69] A. Airoldi and G. Janszen. 'A design solution for a crashworthy landing gear with a new triggering mechanism for the plastic collapse of metallic tubes'. In: *Aerospace Science and Technology* 9 (5 July 2005), pp. 445–455. DOI: 10.1016/J.AST.2005.04.001.

[70] W. Abramowicz and N. Jones. 'Dynamic progressive buckling of circular and square tubes'. In: *International Journal of Impact Engineering* 4.4 (1986), pp. 243–270. DOI: 10.1016/0734-743X(86)90017-5.

[71] T. Wierzbicki and W. Abramowicz. 'On the Crushing Mechanics of Thin-Walled Structures'. In: *Journal of Applied Mechanics* 50 (4a Apr. 1983), pp. 727–734. DOI: 10.1115/1.3167137.

[72] M. Desiderio, M. Schuurman, R. Alderliesten and S. G. P. Castro. 'Crashworthiness of the Flying-V Aircraft Concept with Vertical Drop Test Simulations'. In: (Feb. 2024). DOI: 10.31224/3034.

[73] T. F. Costa, S. G. Castro, C. Rans and A. Villa. 'Crashworthiness Assessment of the Flying-V Under Complex Crash Scenarios With Partially Detailed Structures'. In: *AIAA SCITECH 2025 Forum*. American Institute of Aeronautics and Astronautics, Jan. 2025. DOI: 10.2514/6.2025-0622.

[74] Y.-L. Lo, T.-L. Ho, J.-L. Chen, R.-S. Lee and T.-C. Chen. 'Linkage-spring model in analyzing wirebonding loops'. In: *IEEE Transactions on Components and Packaging Technologies* 24.3 (2001), pp. 450–456. DOI: 10.1109/6144.946493.

[75] Y.-L. Lo, T.-C. Chen and T.-L. Ho. 'Design in triangle-profiles and T-profiles of a wirebond using a linkage-spring model'. In: *IEEE Transactions on Components and Packaging Technologies* 24.3 (2001), pp. 457–467. DOI: 10.1109/6144.946494.

[76] D. Lavayen-Farfan, M. J. L. Boada and J. A. Rodriguez-Hernandez. 'Bending collapse analysis for thin and medium-thin-walled square and rectangular hollow shapes'. In: *Thin-Walled Structures* 165 (2021), p. 107934. DOI: 10.1016/j.tws.2021.107934.

[77] S. Timoshenko and J. Gere. *Theory of Elastic Stability*. Dover Civil and Mechanical Engineering. Dover Publications, 2009. ISBN: 978-0-486-47207-2. URL: https://books.google.nl/books?id=rAk_AwAAQBAJ.

[78] Y. C. Liu and M. L. Day. 'Bending collapse of thin-walled beams with channel cross-section'. In: *International Journal of Crashworthiness* 11 (3 2006), pp. 251–262. DOI: 10.1533/IJCR.2005.0408.

[79] Y. Liu and M. L. Day. 'Bending collapse of thin-walled circular tubes and computational application'. In: *Thin-Walled Structures* 46 (4 Apr. 2008), pp. 442–450. DOI: 10.1016/J.TWS.2007.07.014.

[80] S. Anand, R. Alderliesten and S. G. P. Castro. *Dataset for Crashworthiness in preliminary design: Semi-analytical modeling for bending collapse of square and rectangular tubular structures*. Zenodo, Feb. 2026. DOI: 10.5281/zenodo.18632098.

[81] A. Rohatgi. *WebPlotDigitizer*. Version 5.2. URL: https://automeris.io.

[82] F. Esmaeili, M. Zehsaz, T. Chakherlou and S. Barzegar. 'Fatigue life estimation of double lap simple bolted and hybrid (bolted/bonded) joints using several multiaxial fatigue criteria'. In: *Materials & Design* 67 (2015), pp. 583–595. DOI: 10.1016/j.matdes.2014.11.003.

[83] J. Frutos, R. Ambriz, C. J. García and D. Jaramillo. 'Orthogonal impact load in 6061-T651 and 7075-T651 aluminum alloy plates'. In: *Journal of Materials Research and Technology* 26 (2023), pp. 4245–4262. DOI: 10.1016/j.jmrt.2023.08.174.

[84] Dassault Systèmes Simulia Corp. *Abaqus/CAE 2024*. RI, USA, 2023.

[85] X. Zhang, H. Zhang and Z. Wang. 'Bending collapse of square tubes with variable thickness'. In: *International Journal of Mechanical Sciences* 106 (2016), pp. 107–116. DOI: 10.1016/j.ijmecsci.2015.12.006.

[86] X. Zhang, H. Zhang and W. Ren. 'Bending collapse of folded tubes'. In: *International Journal of Mechanical Sciences* 117 (2016), pp. 67–78. DOI: 10.1016/j.ijmecsci.2016.07.016.

[87] S. Anand, R. Alderliesten and S. G. Castro. 'Low-fidelity crashworthiness assessment of unconventional aircraft: Modelling of plastic bending'. In: *AIAA SCITECH 2024 Forum*. American Institute of Aeronautics and Astronautics, Jan. 2024. DOI: 10.2514/6.2024-0833.

[88] G. Szuladzinski. 'Bending of Beams with Nonlinear Material Characteristics'. In: *Journal of Mechanical Design* 102.4 (Oct. 1980), pp. 776–780. DOI: 10.1115/1.3254821. eprint: https://asmedigitalcollection.asme.org/mechanicaldesign/article-pdf/102/4/776/5747056/776_1.pdf.

[89] M. Yekani Fard, A. Chattopadhyay and Y. Liu. 'Multi-linear stress–strain and closed-form moment curvature response of epoxy resin materials'. In: *International Journal of Mechanical Sciences* 57.1 (2012), pp. 9–18. DOI: 10.1016/j.ijmecsci.2012.01.009.

[90] C. Pleesudjai and B. Mobasher. 'Analytical moment-curvature solutions for generalized textile-reinforced concrete sections'. In: *Engineering Structures* 276 (2023), p. 115317. DOI: 10.1016/j.engstruct.2022.115317.

[91] A. Szwed, I. Kamińska and C. Ajdukiewicz. 'Full-Range Moment–Curvature Relationships for Beams Made of Low-Hardening Aluminium Alloys'. In: *Materials* 17.22 (2024). DOI: 10.3390/ma17225545.

[92] W. Chen and T. Wierzbicki. 'Relative merits of single-cell, multi-cell and foam-filled thin-walled structures in energy absorption'. In: *Thin-Walled Structures* 39.4 (2001), pp. 287–306. DOI: 10.1016/S0263-8231(01)00006-4.

[93] S. Anand, N. Dighe, P. Gupta, R. Alderliesten and S. G. Castro. 'Failure modes and energy absorption in Glass Reinforced aluminum (GLARE) hybrid laminates subjected to three-point bending'. In: *Composites Part C: Open Access* 18 (2025), p. 100651. DOI: 10.1016/j.jcomc.2025.100651.

[94] C. Rans. '2 - Bolted joints in glass reinforced aluminium (Glare) and other hybrid fibre metal laminates (FML)'. In: *Composite Joints and Connections*. Ed. by P. Camanho and L. Tong. Woodhead Publishing Series in Composites Science and Engineering. Woodhead Publishing, 2011, pp. 35–76. ISBN: 978-1-84569-990-1. DOI: 10.1533/9780857094926.1.35.

[95] M. Plokker, D. Daverschot and T. Beumler. 'Hybrid Structure Solution for the A400M Wing Attachment Frames'. In: *ICAF 2009, Bridging the Gap between Theory and Operational Practice*. Ed. by M. J. Bos. Dordrecht: Springer Netherlands, 2009, pp. 375–385. ISBN: 978-90-481-2746-7. DOI: 10.1007/978-90-481-2746-7_22.

[96] A. Vlot. 'Glare in Europe — a long, long runway (1988–1997)'. In: *Glare: history of the development of a new aircraft material*. Dordrecht: Springer Netherlands, 2001, pp. 111–139. ISBN: 978-0-306-48398-1. DOI: 10.1007/0-306-48398-X_4.

[97] C. Liu, D. Du, H. Li, Y. Hu, Y. Xu, J. Tian, G. Tao and J. Tao. 'Interlaminar failure behavior of GLARE laminates under short-beam three-point-bending load'. In: *Composites Part B: Engineering* 97 (2016), pp. 361–367. DOI: 10.1016/j.compositesb.2016.05.003.

[98] H. Li, Y. Xu, X. Hua, C. Liu and J. Tao. 'Bending failure mechanism and flexural properties of GLARE laminates with different stacking sequences'. In: *Composite Structures* 187 (2018), pp. 354–363. DOI: 10.1016/j.compstruct.2017.12.068.

[99] M. H. Kumar, N. R. Mathivanan and S. Kumar. 'Experiment investigations of effect of laminate thickness on flexural properties of GLARE and GFRP laminates'. In: *Materials Research Express* 6 (2 Feb. 2019). DOI: 10.1088/2053-1591/aaf066.

[100] Y. Solyaev, S. Lurie, O. Prokudin, V. Antipov, L. Rabinskiy, N. Serebrennikova and V. Dobryanskiy. 'Elasto-plastic behavior and failure of thick GLARE laminates under bending loading'. In: *Composites Part B: Engineering* 200 (2020), p. 108302. DOI: 10.1016/j.compositesb.2020.108302.

[101] A. Vlot and J. Gunnink. *Fibre Metal Laminates: An Introduction*. Springer Netherlands, 2001. ISBN: 978-94-010-0995-9. DOI: 10.1007/978-94-010-0995-9.

[102] M. Hagenbeek. 'Characterisation of Fibre Metal Laminates under Thermomechanical Loadings'. PhD thesis. Delft University of Technology, Nov. 2005.

[103] *Standard Test Methods for Flexural Properties of Unreinforced and Reinforced Plastics and Electrical Insulating Materials*. ASTM International, 2017. DOI: 10.1520/D0790-17.

[104] *Standard Test Method for Flexural Properties of Polymer Matrix Composite Materials*. ASTM International, 2021. DOI: 10.1520/D7264_D7264M-21.

[105] Zwick Roell Group. *Proline Technical Datasheet*. 2014. URL: %7Bhttps://www.zwickroell.com/products/static-materials-testing-machines/universal-testing-machines-for-static-applications/proline/%7D.

[106] H. Li, J. Tian, W. Fei, Z. Han, G. Tao, Y. Xu, X. Xu and J. Tao. 'Springback and failure characteristics of roll bending of GLARE laminates'. In: *Materials Research Express* 6 (8 May 2019), 0865b2. DOI: 10.1088/2053-1591/ab2109.

[107] Y. Solyaev and A. Babaytsev. 'Direct observation of plastic shear strain concentration in the thick GLARE laminates under bending loading'. In: *Composites Part B: Engineering* 224 (Nov. 2021), p. 109145. DOI: 10.1016/J.COMPOSITESB.2021.109145.

[108] S. Anand, N. Dighe, P. Gupta, R. Alderliesten and S. G. P. Castro. 'Dataset for Glass Reinforced aluminum (GLARE) Laminates subjected to three-Point Bending'. In: (July 2025). DOI: 10.6084/m9.figshare.29590073.v1.

[109] X. Hua, H. Li, Y. Lu, Y. Chen, L. Qiu and J. Tao. 'Interlaminar fracture toughness of GLARE laminates based on asymmetric double cantilever beam (ADCB)'. In: *Composites Part B: Engineering* 163 (2019), pp. 175–184. DOI: 10.1016/j.compositesb.2018.11.040.

[110] K. Swiatkowski and F. Stachowicz. 'Analysis of the cross-sectional deformation of box profiles subjected to bending'. In: *Journal of Mechanical Working Technology* 10.1 (1984), pp. 103–116. DOI: 10.1016/0378-3804(84)90082-2.

[111] S. Kut and F. Stachowicz. 'Cross-Section Deformation and Bending Moment of a Steel Square Tubular Section'. In: *Materials* 13.22 (2020). DOI: 10.3390/ma13225170.

[112] S. T. Pinho, P. P. Camanho and M. F. de Moura. 'Numerical Simulation of the Crushing Process of Composite Materials'. In: *International Journal of Crashworthiness* 9.3 (2004), pp. 263–276. DOI: 10.1533/ijcr.2004.0287.

[113] S. Anand, J.-E. Chambe, C. Bouvet and S. Rivallant. 'Stacking sequence optimization of composite tubes submitted to crushing using the discrete ply model (DPM)'. In: *Mechanics of Advanced Materials and Structures* 31.4 (2024), pp. 820–833. DOI: 10.1080/15376494.2022.2123579.

[114] P. P. Camanho, C. G. Dávila and M. F. de Moura. 'Numerical Simulation of Mixed-Mode Progressive Delamination in Composite Materials'. In: *Journal of Composite Materials* 37.16 (2003), pp. 1415–1438. DOI: 10.1177/0021998303034505.

[115] A. Turon, P. P. Camanho, J. Costa and C. G. Dávila. 'A Damage Model for the Simulation of Delamination in Advanced Composites under Variable-Mode Loading'. In: *Mechanics of Materials* 38.11 (2006), pp. 1072–1089. DOI: 10.1016/j.mechmat.2005.10.003.

[116] C. Bouvet, B. Castanié, M. Bizeul and J.-J. Barrau. 'Low Velocity Impact Modelling in Laminate Composite Panels with Discrete Interface Elements'. In: *International Journal of Solids and Structures* 46.14–15 (2009), pp. 2809–2821. DOI: 10.1016/j.ijsolstr.2009.03.010.

[117] W. Liu, Z. Lin, N. Wang and X. Deng. 'Dynamic performances of thin-walled tubes with star-shaped cross section under axial impact'. In: *Thin-Walled Structures* 100 (Mar. 2016), pp. 25–37. DOI: 10.1016/J.TWS.2015.11.016.

[118] H. Zhao, S. Abdennadher and R. Othman. 'An experimental study of square tube crushing under impact loading using a modified large scale SHPB'. In: *International Journal of Impact Engineering* 32.7 (2006), pp. 1174–1189. DOI: 10.1016/j.ijimpeng.2004.09.013.

[119] B. P. DiPaolo and J. G. Tom. 'A study on an axial crush configuration response of thin-wall, steel box components: The quasi-static experiments'. In: *International Journal of Solids and Structures* 43 (25-26 Dec. 2006), pp. 7752–7775. DOI: 10.1016/J.IJSOLSTR.2006.03.028.

[120] F. C. Bardi, H. D. Yun and S. Kyriakides. 'On the axisymmetric progressive crushing of circular tubes under axial compression'. In: *International Journal of Solids and Structures* 40 (12 June 2003), pp. 3137–3155. DOI: 10.1016/S0020-7683(03)00111-2.

[121] S. R. Guillow, G. Lu and R. H. Grzebieta. 'Quasi-static axial compression of thin-walled circular aluminium tubes'. In: *International Journal of Mechanical Sciences* 43 (9 Sept. 2001), pp. 2103–2123. DOI: 10.1016/S0020-7403(01)00031-5.

List of Publications

Journal publications

1. S. Anand, R. Alderliesten and S. G. Castro. 'Crashworthiness in preliminary design: Mean crushing force prediction for closed-section thin-walled metallic structures'. In: *International Journal of Impact Engineering* 188 (2024), p. 104946. DOI: 10.1016/j.ijimpeng.2024.104946
   Corrigendum:
   S. Anand, R. Alderliesten and S. G. Castro. 'Corrigendum to "Crashworthiness in preliminary design: mean crushing force prediction for closed-section thin-walled metallic structures" [International Journal of Impact Engineering, Volume 188, June 2024, 104946]'. In: *International Journal of Impact Engineering* 194 (2024), p. 105086. DOI: 10.1016/j.ijimpeng.2024.105086
   Corresponding Dataset:
   S. Anand, R. Alderliesten and S. G. P. Castro. *Dataset for Crashworthiness in preliminary design: Mean crushing force prediction for closed-section thin-walled metallic structures*. Zenodo, July 2024. DOI: 10.5281/zenodo.12773062

2. Dataset:
   S. Anand, R. Alderliesten and S. G. P. Castro. *Dataset for Crashworthiness in preliminary design: Semi-analytical modeling for bending collapse of square and rectangular tubular structures*. Zenodo, Feb. 2026. DOI: 10.5281/zenodo.18632098

3. S. Anand, N. Dighe, P. Gupta, R. Alderliesten and S. G. Castro. 'Failure modes and energy absorption in Glass Reinforced aluminum (GLARE) hybrid laminates subjected to three-point bending'. In: *Composites Part C: Open Access* 18 (2025), p. 100651. DOI: 10.1016/j.jcomc.2025.100651
   Corresponding Dataset:
   S. Anand, N. Dighe, P. Gupta, R. Alderliesten and S. G. P. Castro. 'Dataset for Glass Reinforced aluminum (GLARE) Laminates subjected to three-Point Bending'. In: (July 2025). DOI: 10.6084/m9.figshare.29590073.v1

Conference publications

1. *A Review of Analytical Models for Determining the Behavior of Metallic Tubular Structures Submitted to Axial Crushing*. Vol. ASME 2023 Aerospace Structures, Structural Dynamics, and Materials Conference. Aerospace Structures, Structural Dynamics, and Materials Conference. June 2023, V001T01A016. DOI: 10.1115/SSDM2023-108398. eprint: https://asmedigitalcollection.asme.org/ssdm/proceedings-pdf/SSDM2023/87141/V001T01A016/7052470/v001t01a016-ssdm2023-108398.pdf

2. S. Anand, R. Alderliesten and S. G. Castro. ‘Low-fidelity crashworthiness assessment of unconventional aircraft: Modelling of plastic bending’. In: *AIAA SCITECH 2024 Forum*. American Institute of Aeronautics and Astronautics, Jan. 2024. DOI: 10.2514/6.2024-0833

Acknowledgements

Doing a PhD has been one of the most rewarding experiences and a truly valuable learning opportunity. First and foremost, I am immensely grateful to the Kingdom of the Netherlands for providing a stable and secure environment in which academic inquiry can flourish. The protection of its institutions and the reliability of its public systems created the essential foundation for this work. I am equally thankful to Delft University of Technology (TU Delft) for fostering an inspiring academic atmosphere and for providing the resources and institutional support necessary to carry out this research.

My deepest thanks go to my supervisor, Professor Saullo G. P. Castro, for his continuous guidance and unwavering support throughout this journey. His friendly and approachable nature, constant encouragement, availability, and clear communication made this PhD experience both enjoyable and deeply fulfilling. I feel truly fortunate to have had the opportunity to pursue my doctoral studies under such a knowledgeable and caring supervisor.

In addition, I would like to sincerely thank my promotor, Professor René Alderliesten, for consistently guiding me with his profound expertise and for steering me in the right direction whenever I felt uncertain. I will always remember two particularly meaningful pieces of advice he shared during my first year: “Vagueness suits a politician, not a scientist” and “Do not trust any source blindly.” As my research progressed, the depth of these statements became increasingly clear. They have profoundly shaped my scientific mindset and my approach to rigorous inquiry.

I am also very thankful to Nachiket and Pranshul for their collaboration on the GLARE laminate bending section. Their tremendous effort in the lab to run experimental tests while simultaneously managing their Master’s coursework was truly inspiring. Without their dedication to this experimental campaign, the dataset investigation and the resulting semi-analytical model would not have been possible.

I would like to express my deepest gratitude to my wife for her unwavering support throughout the many ups and downs of this PhD journey. Her patience, encouragement, and constant belief in me gave me the strength to persevere during challenging moments. In addition to her emotional support, she generously devoted her time to helping in practical ways, from helping me check the completeness of my datasets to proofreading drafts. I am profoundly grateful to have had her by my side throughout this journey.

During the course of this PhD, I enjoyed countless discussions with Siddharth on defense and geopolitics. It was truly a pleasure to have an office mate who shared a

strong interest in topics I enjoy exploring beyond my research. I found Srikanth to be a very supportive colleague, and our early discussions on the state of academia were particularly engaging. I am also grateful to all my colleagues for fostering and maintaining a friendly and supportive working atmosphere.

I offer my sincere gratitude to all the teachers I have had throughout my life for their knowledge and guidance, which have shaped my intellectual development and enabled me to pursue a PhD.

I am deeply grateful to my parents and sister for their unwavering support since the beginning of my academic journey. Their teachings and guidance have shaped my understanding of the world's complexity and the importance of clarity in thought and action. Last but not least, I am also grateful to Lord Shiva, my guru, whose guidance has sustained me and fostered my growth throughout this journey.

Curriculum Vitæ

Shreyas Anand

09-09-1996 Born in Ranchi, Jharkhand, India.

Education

2002–2014 Delhi Public School
Ranchi, Jharkhand

2014–2018 Bachelor of Technology in Aeronautical Engineering
Manipal Institute of Technology
Manipal, Karnataka, India

2019-2021 Master of Science in Aerospace Engineering
Institut supérieur de l'aéronautique et de l'espace (ISAE-SUPAERO)
Toulouse, Occitania, France

2021-2026 PhD in Aerospace structures
Technische Universiteit Delft (TU-DELFT)
Delft, Zuid-Holland, Netherlands

Thesis: Analytical and semi-analytical models for crash-worthiness in preliminary design
Supervisor: Prof. dr. Saullo Giovanni Periera Castro
Promotor: Prof. dr. René Alderliesten

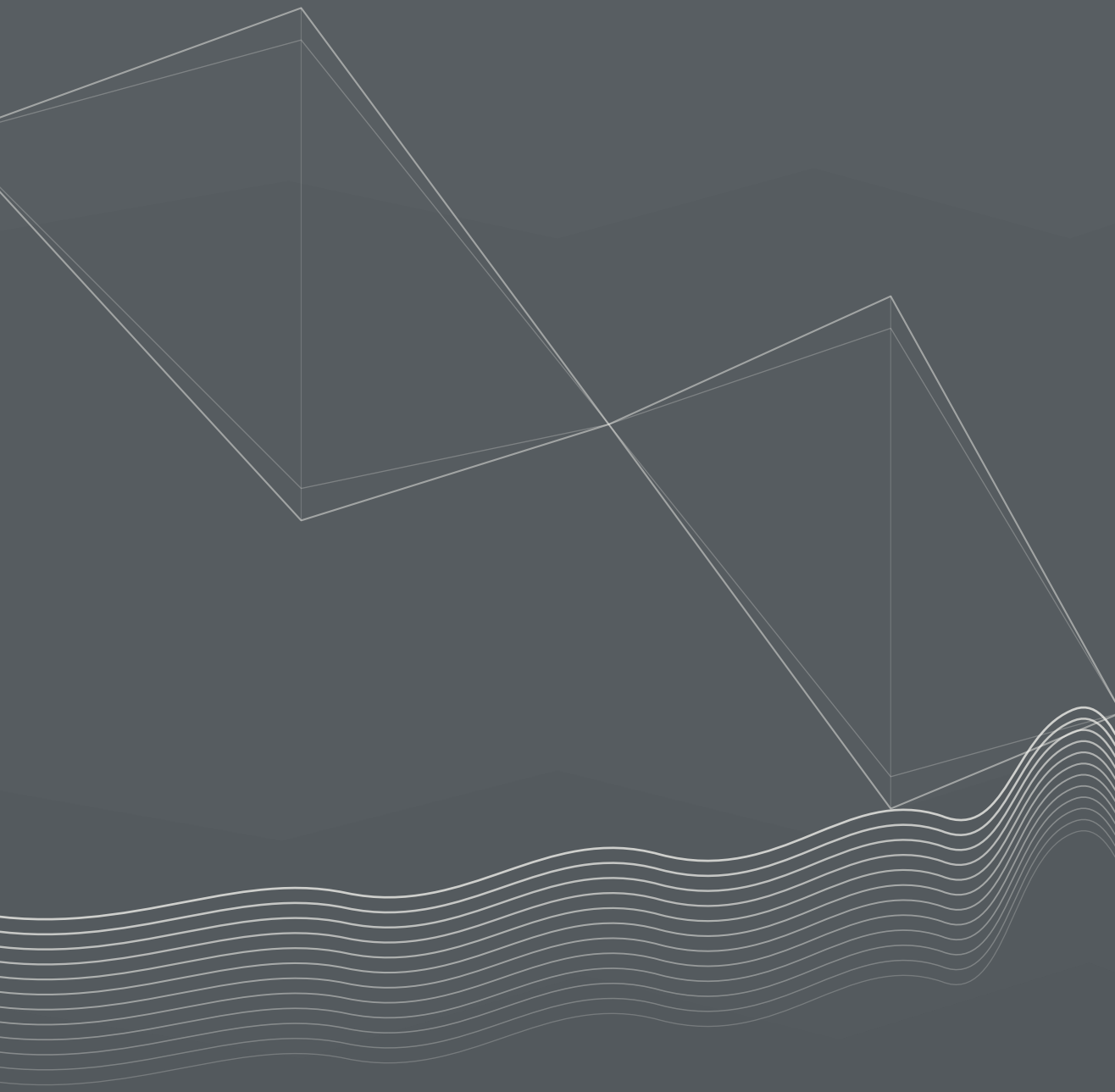

ISBN 978-94-6518-412-8